UNIVERSITY OF STRATHCLYDE

DEPARTMENT OF PHYSICS

Investigations of Fast Electron Transport in Intense Laser-Solid Interactions

by

Mark N. Quinn

A thesis presented in fulfilment of the requirements for
the degree of Doctor of Philosophy

2011

Declaration of Authorship

This thesis is the result of the author's original research. It has been composed by the author and has not been previously submitted for examination which has led to the award of a degree.

Signed: 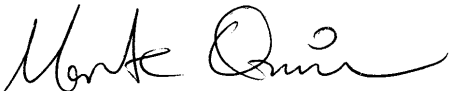

Date: 29 September 2011

Abstract

This thesis reports on experimental investigations of relativistic ('fast') electron transport in solid density plasma. Intense laser pulses, $> 10^{19}\,\mathrm{W/cm^2}$, interacting with solid targets generate a front surface plasma from which a mega-ampere relativistic electron beam is created. The transport of this fast electron beam through the target is occluded from direct measurement. Novel diagnostic methods involving proton emission are developed to investigate the effects of magnetic pinching, filamentation and refluxing on fast electron transport.

Results of the effect of self-generated kilo-tesla magnetic fields on fast electron transport in solid aluminium targets are reported. For target thickness of 25 μm to 1.4 mm, the maximum energies of protons are measured to infer changes in the fast-electron density and therefore the divergence of the fast-electron beam. If the electron transport was purely ballistic, a much faster decrease in the maximum proton energy with increasing target thickness would be expected. This implies that some degree of 'global' magnetic pinching is occurring, particularly in the case of thick ($> 400\,\mu$m) targets. Numerical simulations show that the magnetic pinching effect is significantly reduced in thin targets where enhanced electron refluxing can disrupt the magnetic field growth.

Results of the influence of beam scattering and material resistivity on electron beam filamentation are reported. This phenomena is diagnosed in solids targets ranging from $50 - 1200\,\mu$m in thickness using proton beam uniformity measurements. Electron and proton beam uniformity are correlated using a 3D analytical model. In targets of similar initial resistivity, it is found that increasing the target Z (and therefore scattering) produces no measurable effect on electron beam filamentation. Simulations suggest that target resistivity in the low temperature regime and self-induced magnetic pinching are significant influences on beam filamentation in sold targets.

Results of an investigation of fast electron refluxing within solid targets are reported. Refluxing occurs when the fast electrons are reflected by the sheath potentials formed at the front and rear surfaces. The number of times the fast electrons reflux through a Cu fluorescence layer is controlled by varying the thickness of a second layer comprised of plastic (CH). Enhancements in the K_α x-ray yield and source size are measured as the thickness of the CH layer is decreased. Comparison with analytical and numerical modelling confirms that significant refluxing occurs. This work highlights the importance of considering this phenomenon when deriving information on fast electron transport in thin solid density targets.

Dedicated to my

parents
Rose and Frank,
for their support and love,

brothers,
Francis, Liam, Ciarán,
who are the easiest of company,

sisters,
Marcella, Linda, Caroline, Mairéad, Mary-Rose,
who always inspire,

best friend,
Shane,
who says it as it is,

and partner,
Olivia,
who has made this journey worth-it.

Acknowledgements

This thesis is the culmination of over three years of research. A number of individuals have made enduring contributions to this experience and are deserving of special mention and appreciation.

First and foremost I wish to sincerely thank my PhD supervisor Prof. Paul McKenna. I am indeed most fortunate to have worked with such an exemplary scientist, a paragon of leadership and professionalism who has consistently provided me with guidance, support and opportunities. I also gratefully acknowledge the funding sources awarded to Prof McKenna by the Science and Engineering Research Council which made my PhD work possible.

From the group at the University of Strathclyde I had the benefit of sharing the expertise of a number of colleagues. A ready forum for discussion on electron transport was provided by Dr Xiaohui Yuan, whose energy and work ethic inspired imitation. Dr David Carroll invariably made time for many prompt discussions and exemplified how the complexities and challenges of an experiment could be managed with patience and efficiency. Also, thanks to my fellow PhD students, Olivier, Silvia, Salima, MP, John and Richard for their comradeship and providing some relief from the toils of long office hours.

By virtue of the collaborative nature of high energy physics research, I had the fortunate experience of working alongside a number of international scientists. These included groups of researchers based at: Queen's University Belfast lead by Prof Marco Borghesi and Prof Matt Zepf, l'Ecole Polytechnique lead by Prof Julien Fuchs, University of Milan lead by Prof Dimitri Batani, University of Bordeaux lead by Dr. João Jorge Santos, the Beijing National Laboratory lead by Prof Yutong Li, the PHELIX Department at GSI Germany lead by Prof Thomas Kuehl and finally groups based at the U.K's Central Laser Facility lead by Prof Peter Norreys and Prof David Neely.

The experimental campaigns, conducted at national facilities, involved a number of support staff for whose assistance I am most grateful. Particular mention to the link scientists: Rob Clarke, Margaret Notley and Kate Lancaster at Vulcan Petawatt and Bernhard Zielbauer at Phelix; thank you sincerely for investing a good amount of your energy and many late evenings in helping to bring the experiments online. Thanks also to the dedicated laser technicians at the respective facilities who made each laser shot possible. Special thanks goes to the target fabrication wizards at the CLF for their excellent foils and prompt service. Much deserved appreciation to the engineering support staff at Vulcan, particularly Phil and Toby, for their assistance in tackling the myriad mechanical challenges encountered in a typical experiment.

Computing resources were provided by STFC's e-Science facility at RAL and also the PCRI computer cluster at the University of Strathclyde. Special thanks to Dr. Alex Robinson in providing access and support to the LEDA numerical code and also to Prof Roger Evans regarding the Pollux code. Other valuable technical support was provided by Dr Ricky Martin and Dr Raoul Trines.

Last but most certainly not least I am indebted to my family, key friends and my partner who have suffered me over these past few years and who are selflessly encouraging even now as I move onwards. Please accept the dedication of this work as modest proof of my heartfelt gratitude.

Role of the author

The author analysed most of the data presented in this thesis, had a leading role in all the experiments and contributed to writing all of the publications resulting from the work presented in this thesis.

Chapter 5: The author played a leading role in both planning and running (as deputy TAO) this experiment. The proton dosimetry film was scanned by L. Lancia during the experiment. Proton stack design and assembly was carried out by the author. Analysis of proton beam maximum energy was carried out by X. H. Yuan. The author contributed to the development of the initial sheath size model which was devised by X. H. Yuan. Analytical modelling of ballistic transport was carried out by the author. Hybrid simulations were carried out by both A. P. L Robinson and the author.

Chapter 6: The author played a leading role in both planning and running (as deputy TAO) this experiment. The proton dosimetry film was scanned by L. Lancia during the experiment. Proton stack design and assembly was carried out by the author. Proton beam uniformity analysis was carried out by the author. The 3D proton beam model was written by the author. The LEDA hybrid simulations were carried out by the author assisted by A. P. L Robinson who also ran the ZEPHYROS PIC-Hybrid simulations. The calculation of the resistivity curves for lithium were carried out by M. P. Desjarlais.

Chapter 7: The author played a leading role in both planning and running (as deputy TAO) this experiment. Assembly and the running of the K_α imager diagnostic was carried out by X. X. Lin who also performed the initial analysis. Further analysis of experimental data was carried out by the author for opacity and absorption effects. The K_α emission and refluxing model was written by the author. The analysis of proton emission data was carried out by the author including the ballistic model predictions. Hybrid simulations using the LEDA code were carried out by the author, and subsequent analysis including proton emission predictions. Plasma temperature effects on K_α emission was also calculated by the author using the FLYCH code.

Publications

1. "On the investigation of fast electron beam filamentation in laser-irradiated solid targets using multi-MeV proton emission." M. N. Quinn, D. C. Carroll, X. H. Yuan, M. Borghesi, R. J. Clarke, R. G. Evans, J. Fuchs, P. Gallegos, L. Lancia, K. Quinn, A. P. L. Robinson, L. Romagnani, G. Sarri, C. Spindloe, P. A. Wilson, D. Neely and P. McKenna, *Plasma Physics and Controlled Fusion,* Accepted, to be published December 2011.

2. "Refluxing of fast electrons in solid targets irradiated by intense, picosecond laser pulses," M.N. Quinn, X.H. Yuan, X.X. Lin, D.C. Carroll, O. Tresca, R.J. Gray, M. Coury, C. Li, Y.T. Li, C.M. Brenner, a P.L. Robinson, D. Neely, B. Zielbauer, B. Aurand, J. Fils, T. Kuehl, and P. McKenna, *Plasma Physics and Controlled Fusion,* vol. 53, p. 025007, 2011.

3. "Effect of Lattice Structure on Energetic Electron Transport in Solids Irradiated by Ultraintense Laser Pulses" P. McKenna, A. P. L. Robinson, D. Neely, M.P. Desjarlais, D. C. Carroll, M.N. Quinn, X. H. Yuan, C.M. Brenner, M. Burza, M. Coury, P. Gallegos, R. J. Gray, K. L. Lancaster, Y.T. Li, X. X. Lin, O. Tresca, and C.-G. Wahlström, *Physical Review Letters,* vol. 106(18), p. 185004, 2011.

4. "Controlling the properties of ultra-intense laser-proton sources using transverse refluxing of hot electrons in shaped mass-limited targets" O. Tresca, D. C. Carroll, X. H. Yuan, B. Aurand, V. Bagnoud, C. M. Brenner, M. Coury, J. Fils, R. J. Gray, T. Kuehl, C. Li, Y. T. Li, X. X. Lin, M. N. Quinn, R. G. Evans, B. Zielbauer, M. Roth, D. Neely and P. McKenna. *Plasma Physics and Controlled Fusion,* vol. 53, p. 105008, 2011.

5. "Ballistic Focusing of Polyenergetic Protons Driven by Petawatt Laser Pulses" S. Kar, K. Markey, M. Borghesi, D.C. Carroll, P. McKenna, D. Neely, M. N. Quinn, and M. Zepf, *Physical Review Letters*, vol. 106(22), p. 225003, 2011.

6. "Hollow microspheres as targets for staged laser-driven proton acceleration," M. Burza, A. Gonoskov, G. Genoud, A. Persson, K. Svensson, M. N. Quinn, P. McKenna, M. Marklund, and C.-G. Wahlström, *New Journal of Physics*, vol. 13, p. 013030, 2011.

7. "Effect of self-generated magnetic fields on fast-electron beam divergence in solid targets," X.H. Yuan, A.P.L. Robinson, M.N. Quinn, D.C. Carroll, M. Borghesi, R.J. Clarke, R.G. Evans, J. Fuchs, P. Gallegos, L. Lancia, D. Neely, K. Quinn, L. Romagnani, G. Sarri, P.A. Wilson, and P. McKenna, *New Journal of Physics*, vol. 12(6), p. 063018, 2010.

8. "Spatially resolved X-ray spectroscopy using a flat HOPG crystal," X.H. Yuan, D.C. Carroll, M. Coury, R.J. Gray, C.M. Brenner, X.X. Lin, Y.T. Li, M.N. Quinn, O. Tresca, and B. Zielbauer, D. Neely, and P. McKenna, N*uclear Instruments and Methods in Physics Research Section A: Accelerators, Spectrometers, Detectors and Associated Equipment*, 2010.

9. "Spectral Enhancement in the Double Pulse Regime of Laser Proton Acceleration," K. Markey, P. McKenna, C. Brenner, D. Carroll, M. Günther, K. Harres, S. Kar, K. Lancaster, F. Nürnberg, M.N. Quinn, A. Robinson, M. Roth, M. Zepf, and D. Neely, *Physical Review Letters*, vol. 105(19), p. 195008, 2010.

10. "Carbon ion acceleration from thin foil targets irradiated by ultrahigh-contrast, ultraintense laser pulses," D.C. Carroll, O. Tresca, R. Prasad, L. Romagnani, P.S. Foster, P. Gallegos, J.S. Green, M.J.V. Streeter, N. Dover, C.A.J. Palmer, C.M. Brenner, F.H. Cameron, K.E. Quinn, J. Schreiber, A.P.L. Robinson, T. Baeva, M.N. Quinn, X.H. Yuan, Z. Najmudin, M. Zepf, D. Neely, M. Borghesi, and P. McKenna, New Journal of Physics, vol. 12, 2010, p. 045020.

11. "New developments in energy transfer and transport studies in relativistic laser–plasma interactions," P. A. Norreys, J.S. Green, K.L. Lancaster, A.P.L. Robinson, R.H.H. Scott, F. Perez, H.-P. Schlenvoight, S. Baton, S. Hulin, B. Vauzour, J.J. Santos, D.J. Adams, K. Markey, B. Ramakrishna, M. Zepf, M.N. Quinn, X.H. Yuan, P. McKenna, J. Schreiber, J.R. Davies, D.P. Higginson, F.N. Beg, C. Chen, T. Ma, and P. Patel, *Plasma Physics and Controlled Fusion*, vol. 52, 2010, p. 124046.

12. "Laser-Driven Fast Electron Collimation in Targets with Resistivity Boundary," B. Ramakrishna, S. Kar, A. Robinson, D. Adams, K. Markey, M.N. Quinn, X. Yuan, P. McKenna, K. Lancaster, J. Green, R. Scott, P. Norreys, J. Schreiber, and M. Zepf, *Physical Review Letters*, vol. 105(13), p. 135001 2010.

13. "Magnetic collimation of petawatt driven fast electron beam for prospective fast ignition studies," S. Kar, D. Adams, M. Borghesi, K. Markey, B. Ramakrishna, M. Zepf, K. Lancaster, P. Norreys, A.P.L. Robinson, D.C. Carroll, P. McKenna, M.N. Quinn, X.H. Yuan, C. Bellei, and J. Schreiber, *Journal of Physics: Conference Series*, vol. 244, 2010, p. 022041.

14. "Fast electron propagation in high-density plasmas created by 1D shock wave compression: Experiments and simulations," J.J. Santos, D. Batani, P. McKenna, S.D. Baton, F. Dorchies, a Dubrouil, C. Fourment, S. Hulin, E. d'Humières, P.H. Nicolaï, L. Gremillet, a Debayle, J.J. Honrubia, P. Carpeggiani, M. Veltcheva, M.N. Quinn, E. Brambrink, and V. Tikhonchuk, *Journal of Physics: Conference Series*, vol. 244, p. 022060, 2010.

15. "Fast electron propagation in high density plasmas created by shock wave compression," J.J. Santos, D. Batani, P. McKenna, S.D. Baton, F. Dorchies, A. Dubrouil, C. Fourment, S. Hulin, P. Nicolaï, M. Veltcheva, P. Carpeggiani, M.N. Quinn, E. Brambrink, M. Koenig, M. Rabec Le Glohaec, C. Spindloe, and M. Tolley, *Plasma Physics and Controlled Fusion*, vol. 51, p. 014005, 2009

16. "Dynamic control and enhancement of laser-accelerated protons using multiple laser pulses," D.C. Carroll, D. Batani, R.G. Evans, Y. Glinec, C. Homann, R. Jafer, S. Kar, F. Lindau, O. Lundh, and K. Markey, D. Neely, F. Nürnberg, A.

Persson, M.N. Quinn, A.P.L. Robinson, M. Roth, C.-G. Wahlström, X.H. Yuan, M. Zepf, and P. McKenna, *Comptes Rendus Physique*, vol. 10, p. 188-196, 2009.

17. "Observation of the transient charging of a laser-irradiated solid," K. Quinn, P. a Wilson, B. Ramakrishna, G. Sarri, L. Romagnani, A. Pipahl, O. Willi, L. Lancia, J. Fuchs, D.C. Carroll, M.N. Quinn, P. Gallegos, X.H. Yuan, P. McKenna, R.J. Clarke, D. Neely, M. Notley, A. Macchi, and M. Borghesi, *The European Physical Journal D*, vol. 55, p. 293-297, 2009.

18. "Laser-Driven Ultrafast Field Propagation on Solid Surfaces," K. Quinn, P. Wilson, C. Cecchetti, B. Ramakrishna, L. Romagnani, G. Sarri, L. Lancia, J. Fuchs, A. Pipahl, T. Toncian, O. Willi, R. Clarke, D. Neely, M. Notley, P. Gallegos, D. Carroll, M.N. Quinn, X. H. Yuan, P. McKenna, T. Liseykina, A. Macchi, and M. Borghesi, *Physical Review Letters*, vol. 102(19), p. 194801, 2009.

19. "Modified proton radiography arrangement for the detection of ultrafast field fronts.," K. Quinn, P. A. Wilson, B. Ramakrishna, L. Romagnani, G. Sarri, C. a Cecchetti, L. Lancia, J. Fuchs, A. Pipahl, T. Toncian, O. Willi, R.J. Clarke, D. Neely, M. Notley, P. Gallegos, D.C. Carroll, M.N. Quinn, X.H. Yuan, P. McKenna, and M. Borghesi, *The Review of scientific instruments*, vol. 80(11), p. 113506, 2009.

20. "Effects of front surface plasma expansion on proton acceleration in ultraintense laser irradiation of foil targets," P. McKenna, D.C. Carroll, O. Lundh, F. Nürnberg, K. Markey, S. Bandyopadhyay, D. Batani, R.G. Evans, R. Jafer, S. Kar, D. Neely, D. Pepler, M.N. Quinn, R. Redaelli, M. Roth, C.-G. Wahlström, X.H. Yuan, and M. Zepf, *Laser and Particle Beams*, vol. 26, p. 591, 2008.

Contents

List of Figures

List of Tables

List of Symbols

acceleration time	t_a	k-vector	$\mathbf{k}$
Alfvén limit	I_A	laser energy	E_L
atomic number, charge state	Z	laser incident angle	θ_L
atomic density	n_a	laser wavelength	λ_L
Avogadro's number	N_A	laser spot radius	r_L
atomic electric field	E_a	laser spot diameter	ϕ_L
Bohr radius	a_B	laser intensity	I_L
Boltzmann's constant	k_B	laser frequency	ω_L
charge density	ρ_q	laser power	P_L
collimation factor	Γ	laser pulse length	τ_L
collisional frequency	ν_{ei}	laser-electron conversion	$\eta_{L\rightarrow e}$
conductivity	κ	lorentz factor	γ
Coulomb logarithm	$\ln\Lambda$	magnetic field	B
Coulomb potential	ϕ	magnetic diffusion time	τ_d
critical density	n_c	mass density	ρ
cross section	σ	mass number	A
curl operator	$\nabla\times$	momentum vector	$\mathbf{p}$
current density	$\mathbf{J}$	max proton energy	E_{max}
Debye length	λ_D	normalised acceleration time	τ_p
degree of ionisation	Z^*	opacity	μ
distribution function	f	particle number	N
divergence operator	$\nabla.$	pedestal intensity	I_p
divergence half-angle	$\theta_{1/2}$	permittivity of free space	ε_o
electron charge	e	permeability of free space	μ_o
electron density	n_e	plasma frequency	ω_p
electric field	$\mathbf{E}$	plasma scale length	L_s
electric field peak	E_0	plasma skin depth	l_s
electron mass	m_e	ponderomotive force	F_p
electron temperature	k_BT_e	position vector	$\mathbf{r}$
energy	E	pressure	P
energy density	ϵ	proton mass	m_p
energy gain	Q	proton source size	D_p
fast electron density	n_f	refractive index	η_L
fast electron initial energy	E_{f0}	refluxing efficiency	η_r
fast electron temperature	k_BT_f	resistivity	η
fast electron beam radius	r_f	return current density	$\mathbf{j}_r$
fast electron current density	$\mathbf{j}_f$	scattering angle	θ_{ei}
fast electron current	I_f	sheath area	S_A
fluid velocity vector	$\mathbf{u}$	sheath diameter	D_e
heat capacity	C	sound speed	c_s
impact parameter	b	speed of light	c
injection angle	θ_e	stopping power	dE/ds
ion mass	m_i	target thickness	L
ionisation potential	U_k	thermal velocity	v_t
ion density	n_i	vector potential	a_0
Keldysh parameter	K	velocity	$\mathbf{v}$

List of Abbreviations

AO	Adaptive-Optics.
ASE	Amplified Spontaneous Emission.
BSI	Barrier Suppression Ionisation.
CCD	Charged Coupled device.
CH	Plastic.
CPA	Chirped Pulse Amplification.
CR39	California Resin 39.
CSDA	Continuous-Slowing-Down Approximation.
CTR	Coherent Transition Radiation.
DT	Deuterium-Tritium.
ELI	Extreme-Light-Infrastructure.
EOS	Equation Of State.
FWHM	Full Width at Half Maximum.
GSI	Gesellschaft für SchwerIonenforschung.
HEDP	High Energy Density Physics.
HIPER	High Power laser Energy Research facility.
HISAC	HIgh-Speed Sampling Camera.
ICF	Inertial Confinement Fusion.
IFAR	In-Flight Aspect Ratio.
LTE	Local Thermodynamic Equilibrium.
MCP	Multi-Channel Plate.
MHD	Magnetic-HydroDynamics.
MPI	Message Passing Interface.
NIF	National Ignition Facility.

OPCPA	Optical Parametric Chirped Pulse Amplification.
PI	Principle Investigator.
PIC	Particle In Cell.
PSL	Photo-Simulated Luminescence.
RAL	Rutherford Appleton Laboratory.
RCF	Radio-Chromic film.
RPA	Radiation Pressure Acceleration.
SRIM	Stopping and Range of Ions in Matter.
TAO	Target Area Operator.
TAP	Target Area Petawatt.
TCC	Target-Chamber-Centre.
TNSA	Target Normal Sheath Acceleration.
TP-Spec	Thomson Parabola Spectrometer.
VFP	Vlasov-Fokker-Planck.
WDM	Warm Dense Matter.

Chapter 1

Introduction

Over the past 50 years since the first demonstration of the laser [1] there have been continuous efforts to increase and harness its concentrated power to create and study high energy states of matter. The past decades have witnessed the progression to laser intensities beyond the threshold needed for material ionisation and relativistic electron acceleration to current limits where short pulse intensities greater than $10^{21}\,\mathrm{W/cm^2}$ are attainable.

With such intensities comes the realisation of generating mega-ampere electron beams propagating through dense plasma close to the velocity of light - this is hereafter referred to as **fast electron transport**. Many novel physical phenomena have become apparent in such conditions. Interesting collective effects such as the generation of 10^3 tesla magnetic fields and target heating to 10^7 degrees prevail in these most extreme terrestrial environments.

1.1 Fast electron transport

This thesis reports on a number of investigations of relativistic or fast electron transport in solid density plasmas. A simplified schematic of these investigations is shown in Figure 1.1. A petawatt ($10^{15}\,\mathrm{W}$) class laser is incident onto the front surface of a solid density target. The delivery of this power ionises the target surface creating a dense plasma with a temperature approaching that of the sun's surface. The short pulsed energy of the laser is coupled into the plasma accelerating a population of electrons to velocities close to that of light. These '**fast electrons**' are injected into the target forming a beam transporting millions of amperes of current through solid density plasma. Before the advent of sub-picosecond ultra-intense lasers, earlier transport studies in the

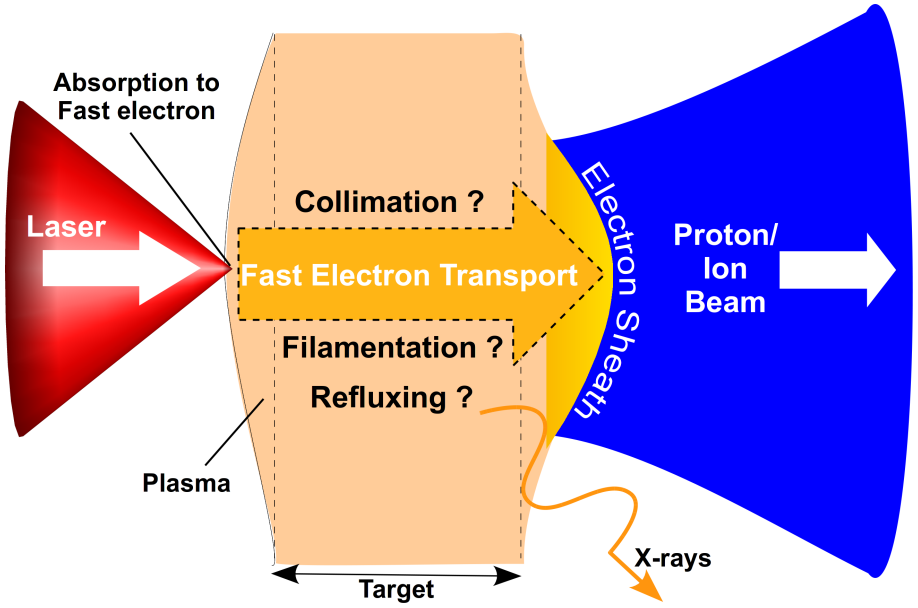

FIGURE 1.1: An illustration providing an overview of fast electron transport. The fast electron beam is created by the absorption of intense laser energy onto a solid target. The transport of this current through the dense plasma to the rear surface involve key phenomena such as collimation, filamentation and refluxing. These effects are investigated in this thesis using a combination of secondary emission involving protons and x-rays.

1970's utilised nanosecond pulsed electron beams injected via a linear accelerator into a preformed low density plasma [2–4].

In the solid density, short pulse regime, much of the specifics regarding fast electron transport physics is occluded from direct measurement by the surrounding high density plasma and the fact that the bulk of the electron beam does not escape the positively charged target. A number of fundamental features of fast electron transport remain open questions and are investigated in this thesis:

1. **Can self-generated magnetic fields reduce beam divergence**?
   Kilo-tesla magnetic fields are expected to be induced by fast electron transport. Although these fields have the potential to pinch and help collimate the fast electron beam, the extent to which they influence its transport has yet to be confirmed.

2. **What are the main factors controlling beam filamentation?**
   Electromagnetic instabilities can cause the fast electron beam to break up or filament. In solid density plasma, a number of material properties such as conductivity and atomic number are believed to be contending influences. The dominating dependence remains unclear.

3. **To what extent do the fast electrons reflux within thin solid targets?**
   Coulomb fields exceeding 10^{12} V/m are expected to prevent the majority of the fast

electrons from escaping the target. The fast electrons have millimeter ranges in solid density material and should therefore be constrained to traverse thin targets a number of times. Direct measurement of such 'refluxing' and the effects of such cross propagation have yet to be fully elucidated.

The challenge of probing these concealed ultra fast phenomena is met using the secondary emissions which are generated by the fast electrons. On propagating through the target the fast electrons excite and induce the fluorescence of x-rays from the plasma atoms [5]. At the front and rear surfaces, the formation of electron sheath fields are sufficiently strong to ionise and accelerate beams of protons and other heavier ions away from the target [6]. The spectral and spatial properties of both ion and x-ray emission are very sensitive to the properties of fast electron transport.

The experimental evidence provided by these measurements is interpreted using a combination of both numerical and analytical models to provide a description of the fast electron transport physics which can be compared with theory. The resulting picture that emerges from this work is one where all three phenomena - collimation, filamentation and refluxing - act collectively on the transport of fast electrons and create a complex inter-dependency.

1.2 The applications of fast electron transport

Fast electron transport intrinsically acts as an efficient energy carrier in coupling the intense laser energy to a range of other phenomena. A number of applications utilise this and are currently the primary drives for this field of research. Fusion energy demands plasma temperatures exceeding ten million degrees. Here a relativistic electron beam can provide the necessary heating using a scheme called **Fast Ignition** [7]. The ion beams accelerated by the fast electron sheath fields can in principle be used as a compact **oncology source** [8]. Short pulsed sources of x-rays and protons provide probes for the study of exotic states of **warm dense matter** [9, 10] characteristic of many astrophysical systems [11].

1.2.1 Fast Ignition approach to ICF

Self-sustained release of energy by nuclear fusion is presently only possible in the cores of stars. The possibility of achieving this on a smaller scale here on Earth can potentially provide a plentiful energy source. Inertial Confinement Fusion (ICF), which is summarised in Appendix A, is a possible approach involving compression and heating

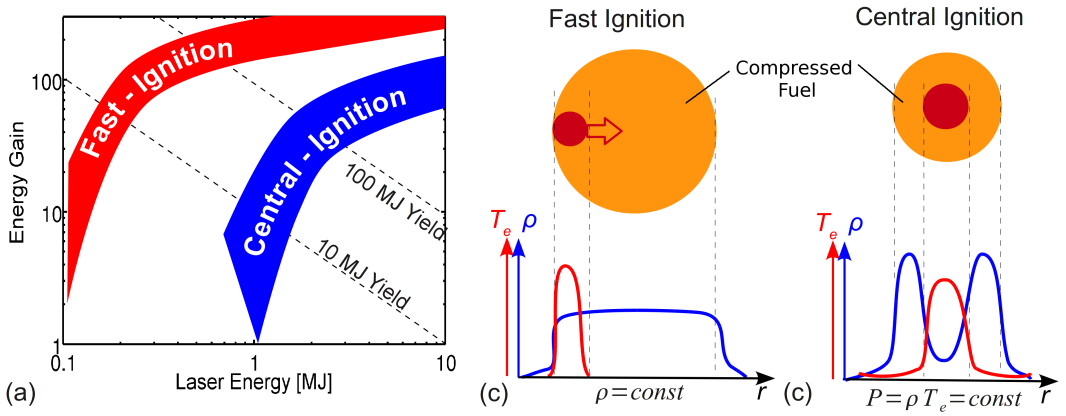

FIGURE 1.2: Comparison of Fast-Ignition and Central-Ignition in terms of: expected fusion energy gain (a) and final compression configuration, which is (b) isochoric for Fast Ignition and (c) isobaric for Central Ignition, described in terms of the fuel density, ρ, and temperature T_e.

of fuel via lasers or x-rays. Central Ignition is the conventional approach to ICF which requires compression to extreme pressures ($1000\,\mathrm{g/cm^3}$) to cause the deuterium-tritium fuel to ignite and induce a fusion chain reaction. Fast Ignition is an alternative scheme for ICF that decouples the compression and ignition stages [7]. Utilising distinct stages of compression and heating result in a much greater efficiency and also significantly eases the requirements for ICF when compared to the Central Ignition approach.

In Fast Ignition, the fuel is first compressed to densities $\rho \approx 300 - 400\,\mathrm{g/cm^3}$ and then ignited by an external source. The reduction in compression solves a number of problems. There is no longer a need to ensure perfect symmetry of compression and shock convergence. The lower density fuel means lower driver energies $200 - 300\,\mathrm{kJ}$ rather than $> 1\,\mathrm{MJ}$ and this results in higher gains. Lowering the constraints of compression means more mass can be assembled to a lower peak density. Greater fuel mass means greater fuel content and thus greater energy output. This again translates into a higher gain for a given laser energy when compared to conventional (central) ignition. This is shown in Figure 1.2(a) which provides a prediction for the performance of Fast Ignition and Central Ignition, if successful. Another distinction concerns the nature of the compression. For Fast Ignition the fuel is compressed to an isochoric state (equal density) rather than isobaric (equal pressure) as is illustrated in Figure 1.2(b-c). This has the advantage that the capsule implosion is less susceptible to hydrodynamic instabilities. The capsule design is also distinct with a smaller ratio of capsule radius to shell thickness. This parameter, is known as the In-Flight Aspect Ratio and plays an important role in stabilising the Rayleigh-Taylor instability during the implosion. The smaller IFAR means a more stable implosion compared to Central Ignition.

The solutions offered by Fast-Ignition also introduce a number of new problems such as

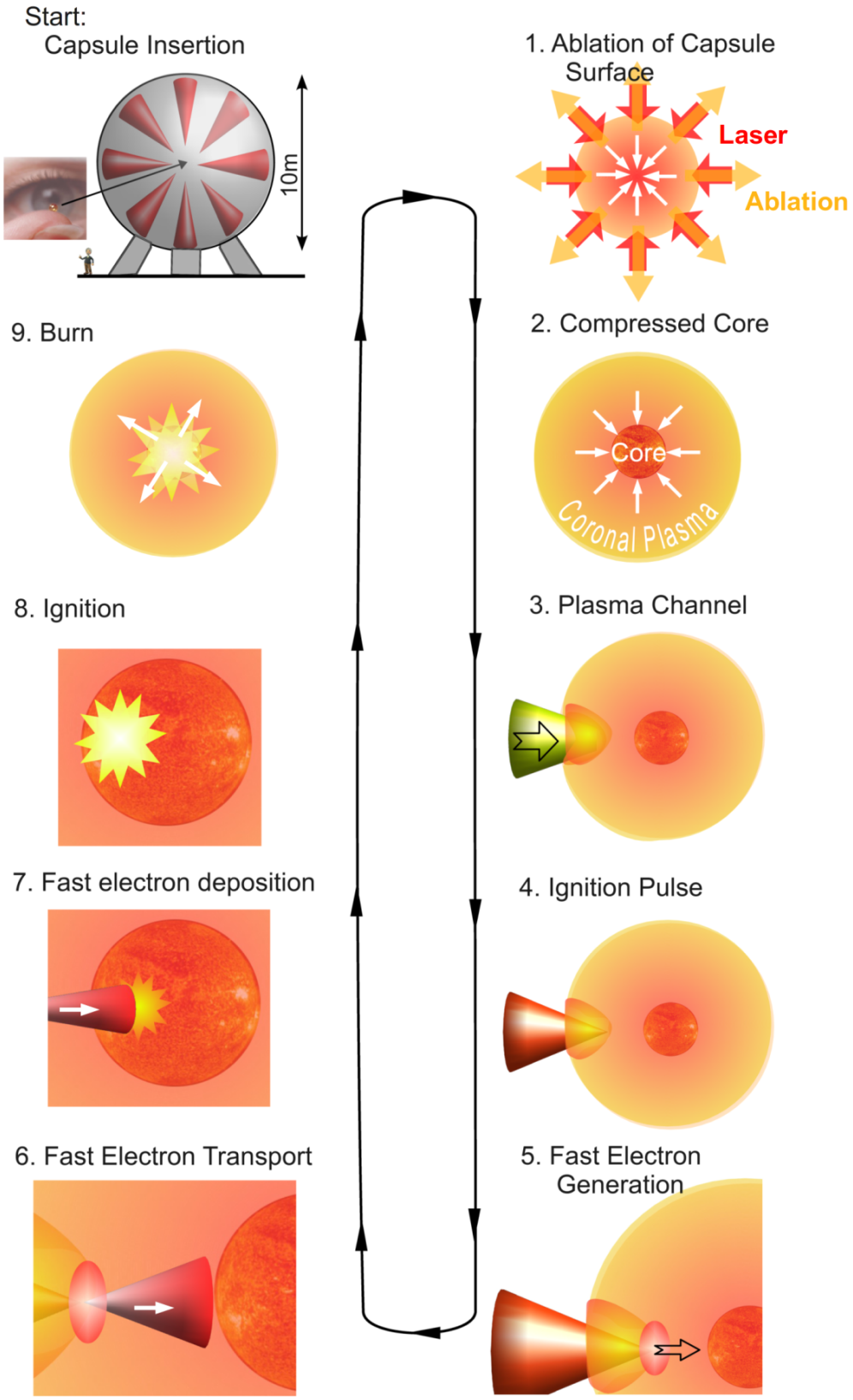

FIGURE 1.3: The production of fusion energy by Fast Ignition involves multiple stages which are discussed in the text. The physics relevant to the transport of the ignitor energy via the fast electrons is investigated in this work.

the delivery and transport of the ignitor energy. A laser accelerated beam of electrons [7] or protons [12] are possible candidates. The general sequence of events is depicted in Figure 1.3 for the electron ignitor scheme:

1. **Ablation:** The compression of the fuel is driven by ablation of the outer layer of the capsule. The ablation is induced by a number of long nano-second pulse laser beams radiating around the capsule surface. A high degree of pulse synchronisation and beam uniformity are required.

2. **Compression:** The fuel is compressed via the ablation of the outer capsule layer to approximately $300\,\mathrm{g/cm^3}$. A total laser energy of $100 - 300\,\mathrm{kJ}$ is needed for this stage.

3. **Plasma channel formation:** A clear channel must exist to facilitate the delivery of the ignitor laser pulse through the 1 mm scale length plasma surrounding the core. Two possible methods are (i) laser induced hole-boring [13] or (ii) by inserting a gold cone into the fuel assembly [14]. Both methods present significant challenges [15–19].

4. **Ignitor laser pulse:** At the moment of peak compression, a relatively short pulse laser is injected into the plasma channel. This is the ignitor pulse and it should deliver 100 kJ within 10 ps, that's 10 PW of power, when stopped in the overdense plasma some few hundred microns from the ignition zone. The focal spot of the ignitor laser should be smaller than the compressed fuel. For a spot radius of $30\,\mu m$ this corresponds to a laser intensity of $3 \times 10^{20}\,\mathrm{W/cm^2}$.

5. **Fast electron generation:** The energy of the ignitor laser pulse is absorbed by the plasma and coupled into a beam of fast electrons which are generated over 10 ps and carry a good fraction of the laser energy.

6. **Fast electron transport:** This fast electron beam must be transported through $100 - 300\,\mu\mathrm{m}$ through compressed plasma spanning a 10^3 density gradient to the ignition zone. The beam should ideally be spatially smooth and perfectly collimated.

7. **Fast electron deposition:** Collisional stopping of the fast electrons deposits the ignitor energy to the fuel core. The energy distribution of the electron beam determines their range and the efficiency of the energy coupling to the hot-spot. Electrons with energy $\approx 1\,\mathrm{MeV}$ have a mean free path close to that of the 3.5 MeV α-particles produced on the fusion of D and T.

8. **Ignition:** The delivery of the ignition energy induces temperatures and densities to meet the required fusion conditions: a temperature of $5 - 10\,\mathrm{keV}$ and areal

density of $\approx 0.3 - 0.5\,\mathrm{g/cm^2}$. The latter meets the criteria for α-particle stopping $0.25\,\mathrm{g/cm^2}$.

9. **Burn:** A self-sustained fusion burn spreads from this small region throughout the remaining compressed fuel before the fuel disassembles.

The first integrated Fast Ignition experiments with compression beams and cone-guided ignition geometry were performed at scaled down energies by Kodama *et al* [20] using the GEKKO XII facility at Osaka University in Japan. These experiments demonstrated increased rates of fusion reactions indicated by an enhanced neutron yield from 10^4 to 10^7 when the ignition pulse was delivered. While compression physics have been rigorously developed over the past 30 years for conventional ICF, the physics associated with the generation, transport and energy deposition of the fast electron beam are not well understood and represent the principal challenge facing electron based Fast Ignition [21].

The investigations reported in this thesis, regarding collimation, filamentation and refluxing, are fundamentally relevant to the understanding of transport physics in Fast Ignition. For example, the divergence or collimation of the electron beam limits the stand-off distance between the ignition laser pulse and the compressed core. The development of beam filamentation can incur significant energy losses, therefore reducing the final energy disposition at the core. Refluxing is a feature of fast electron transport in thin foil targets which if not accounted for, can lead to incorrect assumptions of beam transport in relation to Fast Ignition.

Demonstrating Fast Ignition: HiPER

HiPER[1] is a European project which aims to define the root to Inertial Fusion energy with a specific objective to develop high gain schemes such as Fast Ignition [22]. As of 2007, the baseline design for HiPER specifies $40 \times 5\,\mathrm{kJ}$ laser beam-lines to generate a total of 200 kJ compression energy and $24 \times 3\,\mathrm{kJ}$ beam-lines to generate a total of 70 kJ ignitor energy. The compression beams may also be frequency doubled or tripled, the latter puts more power into the target, but is less efficient in converting the light. Much of the specific features of the HiPER system are currently the subject of ongoing research, an effort which will eventually produce a point design for the project. HiPER's preparatory phase concludes in 2013, this is intended to be followed by a 7-year technology development phase.

[1] HiPER: High Power laser Energy Research facility

Fast Ignition will require fundamental increases both in repetition rate and efficiency by factors of $10-100$ for petawatt type laser systems. Replacing the traditional flash lamps which pump the gain medium with diodes lasers offers a real solution to both problems of efficiency and repetition rate. Part of the HiPER framework is to build a system called PETAL to demonstrate such technology, its goal is to produce $1-10\,\mathrm{kJ}$ laser shots up to 10 times per second [23]. This relatively new technology of diode-pumping laser media is currently operating at energies $\leqslant 100\,\mathrm{J}$ such as for the MERCURY system at Livermore. The Extreme-Light-Infrastructure (ELI) project is a key European initiative to push the development of a $200\,\mathrm{PW}$ laser using diode technology to attain high repetition pulses [24].

If the HiPER facility is built and demonstrates sustained high gain fusion at high repetition rates the next step will be to deliver a design for a prototype fusion power plant. This post-HiPER project would include research to address numerous challenges such a system to carry the heat out of the target chamber for electricity production, protecting the device from the neutron flux generated by the fusion reactions, and the production of tritium from this flux in order to produce more fuel for the reactor.

1.2.2 Ion acceleration

Ion emission is one of the key secondary processes resulting from fast electron transport and is described in detail in Section 3.8. The acceleration is the result of intense electric fields setup by the fast electron sheath across the surfaces of the target. The electrostatic potential at the rear surface can exceed $10^{12}\,\mathrm{V/m}$ and can effectively accelerate ions to multi-MeV energies over a few microns. The acceleration process is known as Target Normal Sheath Acceleration (TNSA) [25]. The geometry of the acceleration mechanism results in ion beams emitted normal to the surface of the target. Key characteristics of these beams include a compact source size both spatially (tens of microns) and temporally (ps at source) and very low transverse emittance. Having the largest charge to mass ratio, protons are accelerated more effectively than other heavier ions. At present, the maximum energy of protons accelerated by this method is $\approx 60\,\mathrm{MeV}$ [26], although recent reports have been made of $67.5\,\mathrm{MeV}$ [27]. The total transfer of energy between the laser ion beam via the fast electrons can reach 10% [26].

Ion beams of such good quality are adaptable to a number of applications. As an oncology source for destroying cancer, the ion beams offer a localised energy deposition at a given depth. This contrasts with x-rays and electrons which deposit more energy continuously over their respective range. However, for treatment of deep seated tumors the challenge is to deliver monochromatic pulses of protons with energies approaching

250 MeV [8]. While this is currently beyond the range of TNSA methods, the development of radiation pressure acceleration (RPA) can potentially satisfy these goals [28] . The discrete energy deposition can also be applied to act as the ignitor energy transport in Fast Ignition requiring presently achievable beam energies [12, 29].

Laser accelerated proton beams have also been applied to provide fast heating of secondary solid targets in proof of principle experiments [9, 30] which supports their use as tools for studies of warm dense matter (WDM) and high energy density physics (HEDP). Laser accelerated protons can also be used to probe lower density plasmas [31]. Furthermore, the multi-MeV per nucleon energies are sufficient to induce nuclear reactions so that laser systems could be used in nuclear physics experiments as well as medical isotope production e.g for positron emission tomography (PET) [32, 33].

1.2.3 Ultra-fast x-ray science

Hard x-ray K_α sources ranging from $10-100$ keV can be produced by relativistic electrons within solid targets. There are many appealing features of such sources. The x-ray burst is very bright with up to 10^{13} photons produced per pulse with a short duration close to that of the laser and a small source size depending on the material, target thickness and intensity [34–38]. These features make it an ideal source for fast time resolved x-ray diffraction experiments in optical pump/x-ray probe setup and also for bio-medical imaging [39, 40]. Comparatively, the peak spectral brightness of laser produced x-rays is orders of magnitude greater than that from synchrotron sources, although the latter is greater in terms of time-averaged brightness [41].

1.2.4 Warm and hot dense matter studies

Many astrophysical bodies such as the interior of stars, giant planets and brown dwarfs exist in exotic material states. Since the inner workings of astronomical objects are not directly accessible, physical models must be relied upon. Specific densities and pressures can be potentially created and probed by laser plasma experiments which can provide the **equation of state** (EOS) and **opacity** measurements necessary for modelling.

A phase diagram of pressure and temperature is shown for aluminium in Figure 1.4. Regions within this diagram are defined by the coupling strength and the degeneracy of the plasma ions and electrons respectively. Both parameters are defined as ratios. The coupling strength between ions, Γ, describes the ratio of their Coulomb to kinetic energy. Electron degeneracy is defined as a ratio of the electron thermal energy to the Fermi energy. A degeneracy equal to 1 is shown in Figure 1.4 separating dense plasma and

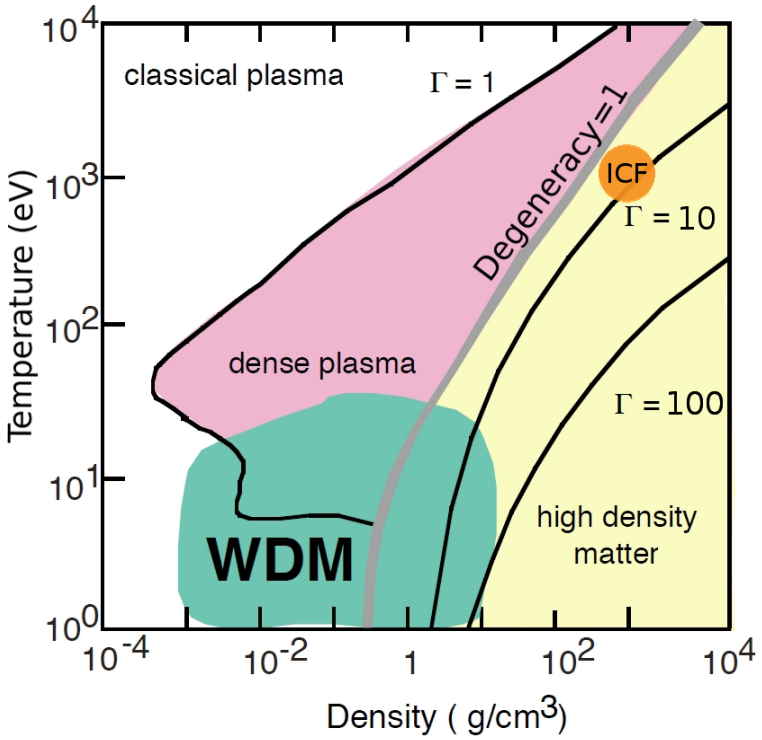

FIGURE 1.4: The temperature-density phase diagram for aluminum (adapted from Lee *et al* [42]). The location relevant to Inertial Confinement Fusion conditions is indicated as ICF.

high density matter. The convergence of these two categories define the area labelled 'WDM' for **Warm Dense Matter** which refers to material states where the ions are strongly coupled $\Gamma > 1$ and with partially degenerate electrons. Although a number of theoretical models have been developed, an adequate description of WDM over the whole parameter range is not yet available. The creation of such exotic states of matter in the laboratory provides an important tool for measuring these quantities.

Laser produced plasmas are able to reproduce states similar to those found in stars interior for certain conditions. Fast electron transport provides an efficient means of coupling the laser energy to the heating of target material up to multi-keV temperatures [43]. Short pulsed secondary emissions such as proton and x-ray beams produced by fast electrons provide additional means of providing isochoric heating of external samples. These beams can also be utilised to probe the material sample.

1.3 Thesis overview

A number of investigations regarding fast electron transport are presented in this thesis. Before doing so, a review of the background physics is provided in two chapters.

Chapter 2 contains a description of lasers and plasmas individually, progressing to their interaction and culminating in the creation and injection of the fast electron beam into the overdense target. **Chapter 3** discusses the transport of this fast electron current within the target and provides a review of progress in this field.

The methodology and results of the investigations regarding fast electron transport are reported in Chapters 4-7 as follows:

- **Chapter 4:** Methods: Experiments & Modelling
- **Chapter 5:** Effect of self-generated magnetic fields on fast electron beam divergence in solid targets
- **Chapter 6:** The effects of scattering and low temperature resistivity on electron transport instabilities
- **Chapter 7:** Refluxing of fast electrons in solid targets irradiated by intense, picosecond laser pulses

The conclusions and summary of these investigates are discussed in **Chapter 8**. A number of appendices are also included which contain notes on laser induced fusion and a description of a selection of the analytical models used in this work.

Chapter 2

Laser induced plasma and Fast electron generation

2.1 Introduction

The focusing of a petawatt of laser power (P_L) to a micron scale spot can be achieved by current laser technology resulting in intensities of over $10^{21}\,\mathrm{W/cm^2}$. This is several orders of magnitude higher than that required for ionisation of matter. The interaction of such laser intensities with solid targets is discussed in this chapter.

The sequence of events begin with the arrival of an intense sub-picosecond laser pulse onto an initially cold target in vacuum. Within tens of femtoseconds a hot plasma is formed from the ablating front surface which launches shock waves into the target which propagate over nanosecond timescales. The creation of a dense plasma during the life time of the laser pulse results in the coupling of a sizable fraction of the laser energy to the plasma electrons. A large population of electrons are relativistically accelerated by the intense laser fields to propagate into the dense target. The creation of this fast electron current completes this review chapter.

2.2 The laser

The current technological path to producing the highest intensity laser pulses is termed CPA for **Chirped Pulse Amplification** [44–46], a schematic of CPA is shown in Figure 2.1. The term chirp refers to the process of stretching or compressing the laser pulse length in time. Older technology produced limited laser intensities for the very simple fact that propagating highly intense laser pulses through the laser chain tends to

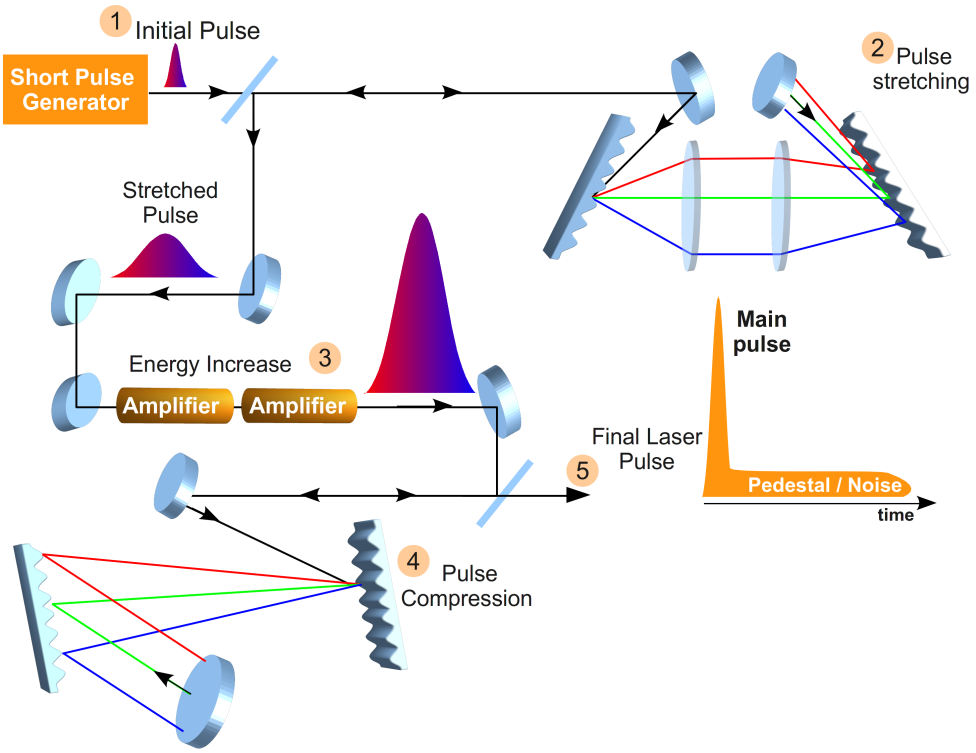

FIGURE 2.1: The laser amplification chain incorporating the stretching and compressing of the laser pulse for chirped pulse amplification. The final laser pulse which exits the laser chain is preceded by a low energy pedestal.

damage or destroy the optics and amplifiers. CPA resolves this limitation by stretching the laser pulse before the amplification media. The amplified pulse is then compressed at the end of the laser chain. The chirping is achieved using gratings which spread the different frequencies of the laser pulse out in time, stretching the initial pulse by a factor of $10^3 - 10^5$. The gain media amplify the pulse's energy by a factor of a million or more. Once amplified the stretched pulse is compressed by applying the opposite chirp to that applied by the stretcher. Compressing the pulse in time ramps its power up to the presently achievable levels of 10^{15} Watts. Compressing the pulse in space with a parabola before target focuses the pulse to a micron size spot creating intensities exceeding $10^{20}\mathrm{W/cm^2}$.

Some fraction, f_c, of the total laser energy, E_{L_0}, is lost during compression and also from the imperfect reflectivity of the focusing optic. The energy on target is therefore $E_L = E_{L_0} \times f_c$. Assuming a Gaussian spatial profile for the focused laser spot, the peak intensity on target is usually quoted using the fraction of energy, f_s, contained within the spot (FWHM) ϕ_L:

$$I_L = \frac{f_s \times E_L}{\pi(\phi_L/2)^2 \tau_L} \ [\mathrm{W/cm^2}] \tag{2.1}$$

Laser Parameters	Symbol	Units	Vulcan (c. 2008)
Energy before compressor	E_{L_0}	J	600 (max)
Energy on Target	E_L	J	360 (max)
Pulse length (FWHM)	τ_L	fs	700
Wavelength	λ_L	μm	1.06
Frequency (Angular)	ω_L	Hz	2×10^{15}
Spot Size (FWHM)	ϕ_L	μm	5
Energy in ϕ_L	f_s	%	50
Compressor Throughput	f_c	%	60
Intensity	I_L	W/cm^2	10^{21}
Irradiance	$I_L\lambda_L^2$	Wμm^2/cm^2	10^{21}
Contrast Ratio	-	-	10^8
Polarisation	p, s	-	p

TABLE 2.1: Laser parameters are listed with typical symbols. Example values are quoted for the Vulcan Petawatt laser circa 2008.

where τ_L is the laser pulse length (FWHM). The relevant laser parameters which are typically quoted for investigations are listed in Table 2.1.

Producing a single pulse of compressed laser energy is an ideal that is usually unobtainable in practice. In typical highly intense laser systems the chirped pulse arrives on target amidst a background or pedestal of optical noise termed **Amplified Spontaneous Emission** (ASE). As the laser energy is been amplified within the gain media, some leakage occurs which propagates down the laser chain, through the compressor, and arrives on to the cold target some nanoseconds before the main pulse. Gating techniques involving Pockel Cells and saturable absorbers can help limit ASE. Although not as energetic as the main pulse, the ASE pedestal is typically nanoseconds long and can deliver sufficient energy to disrupt the target itself. As a figure of merit for intense laser systems, a value relating the intensity **Contrast Ratio** between the main pulse intensity and pedestal intensity is often used to describes the noise output. The higher the contrast the cleaner the pulse. A contrast of 10^8 measured at 3 ns before a 10^{20} W/cm^2 pulse essentially means a 10^{12} W/cm^2 pedestal will arrive on target 3 ns before the main pulse. Besides the ASE pedestal, a sequence of sharp prepulses can also be present. These are the result of spurious reflections and leakage of oscillator pulses through optical shutters within the laser chain. Existing over shorter picosecond time scales, the prepulses can be nominally more intense compared to the laser pedestal.

The orientation of the laser electric field, relative to the the plane of incidence onto target, defines its polarisation. For linear polarisation, this is either 's' or 'p'. If the electric field is polarised in the plane of incidence, it is referred to as **p-polarised** light as shown in Figure 2.2 . Conversely, if the electric field is polarised perpendicular to the plane of incidence, then it is referred to as **s-polarised** light. The 's' is attributed to

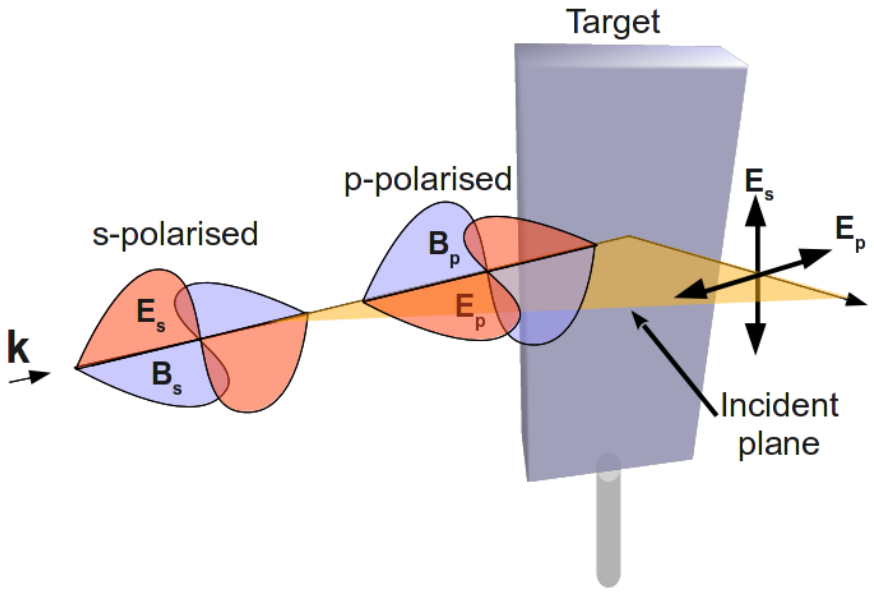

FIGURE 2.2: Polarisation is defined as the orientation of the electric field relative to incident plane. This is shown for p-polarised and s-polarised electromagnetic fields.

the German 'senkrecht' (for perpendicular).

2.3 The plasma

'A plasma is a quasi-neutral gas of charged and neutral particles which exhibits collective behavior.' [47]

Solid, liquid and gas are the familiar terrestrial states of matter. The addition of sufficient energy to heat the matter changes its state. At each stage, the additional energy supplied breaks the bonds between the constituent units of crystals (solid), molecules (liquid), or atoms (gas). Further energy can be applied and the atoms of the gas start to ionise, breaking up to their constituents electrons and ions. This is a plasma, the 4^{th} state of matter, discovered in the late 19^{th} century by William Crookes and given its current name by Irving Languir in 1928.

Plasma is the most common form of visible matter in the universe. This is true if measured both by mass or volume. A plasma is defined using the terms "quasi-neutral" and "collective behavior". The latter means that motions are not only dependant on local conditions but are also driven by long-range electromagnetic forces. For example, as charges move around within the plasma, electric fields are generated from the charge displacement which then drive currents which induces a magnetic field. These fields can affect other charged particles over a certain scale within the plasma. 'Quasi-neutrality' denotes that the plasma is neutral on a macroscopic scale. However there still exists

non-vanishing electromagnetic forces on a microscopic scale. In a plasma these fields can only penetrate locally, the rest of the plasma is shielded from their influence. Hence, the plasma is quasi-neutral.

In more technical terms, a set of criteria can be used to define a plasma [47]:

1. The shielding distance is much less than the dimension of the system.
2. A large number of particles must exist within the shielding distance.
3. The rate of collisions is small compared to the plasma oscillation frequency.

The third condition discriminates between a plasma and an ionised gas. In the case of a weakly ionised gas jet the charged particles collide so frequently with the neutral atoms that their motion is described by ordinary hydrodynamic forces rather than electromagnetic forces.

2.3.1 Describing a plasma

The two basic quantities that describe a plasma are its **free electron density** (n_e [$/m^3$]) and **temperature.** The latter is written as T_e when measured in Kelvin [K] or written as $k_B T_e$ when measured in units of energy such as Joules [J] or electron volts [eV] ($1\,\mathrm{eV} = 1.6 \times 10^{-19}\,\mathrm{J} \approx 10^4\,\mathrm{K}$). Later in this chapter a sub-population of the plasma electrons representing fast electrons will be described using n_f and $k_B T_f$ for their density and temperature respectively.

The number of free electrons per given volume is a function of the **degree of ionisation** of the plasma. This can be calculated using an analytical model presented in Appendix B. With large numbers of particles, statistics are applied to describe their motion. Here the concept of temperature is used to define the mean kinetic energy of the collection of plasma electrons.

Consider an example relevant to solid density plasma at a temperature of a few hundred eV. The electron density created in the ionisation state is given by:

$$n_e = Z^* n_i = \frac{Z^* N_A \rho}{A} \tag{2.2}$$

Using a solid density aluminium plasma as an example: the plasma temperature is $\approx$ 200 eV and the atoms have been ionised to an effective ion charge of $Z^* = 9$. The electron density can be calculated with the values for material density $\rho_{solid} = \rho = 2.3\,\mathrm{g/cm^3}$, mass number $A = 26$, and Avogadro's number $N_A = 6.02 \times 10^{23}$ which results in

$n_e = 5 \times 10^{29}$ /m^3. As a comparison, the sun's corona has an average temperature of ≈ 0.5 eV and a density of $\approx 10^{16}$ /m^3. Evidently, the conditions of a typical solid density plasma exceed those of the suns atmosphere, although conditions at the star's core are much more extreme ($n_{core} = 10^{32}$ /m^3 and $k_B T_{core} \approx$ keV).

The energetic electrons of a plasma will be pushed away from the heavier ions, creating a charge separation field which pulls them back. The electrons overshoot their equilibrium positions and oscillate back and forth in a simple-harmonic motion with **plasma frequency**:

$$\omega_{pe} = \sqrt{\frac{e^2 n_e}{\varepsilon_o \bar{\gamma} m_e}} \tag{2.3}$$

where e is the electron charge, ε_0 is the dielectric constant, $\bar{\gamma}$ is the Lorentz factor of the electrons averaged over one oscillation period and m_e is the electron mass. As an example, non-relativistic plasma electrons with density $n_e = 5 \times 10^{29}$ /m^3 will oscillate at $\omega_{pe} \approx 10^{16}$ Hz.

The shielding distance describes the thickness of plasma through which the electric fields can penetrate. This is also referred to as the **Debye length**, given by:

$$\lambda_D = \sqrt{\frac{\varepsilon_0 k_B T_e}{n_e e}} \tag{2.4}$$

written here for the case of static ions and $k_B T_e$ in units of eV. The plasma electrons shield out the electrostatic Coulomb potential, ϕ, of a charge, q, exponentially with distance, r:

$$\phi(r) = \frac{q}{4\pi\varepsilon_0 r} \exp\left(-\frac{r}{\lambda_D}\right) \tag{2.5}$$

such that only particles within a distance of λ_D will interact strongly with the charge. Beyond this scale, the plasma can be considered electrical neutral. As the electron temperature increases, the shielding becomes less effective and the fields penetrate through more plasma. For a perfectly conducting plasma, the depth to which the fields can penetrate is referred to as the collisionless **skin depth** c/ω_{pe} which is of the order of nano-metres for hot solid density plasmas. For the example of solid density Al plasma ($k_B T_e = 200$ eV and $n_e = 5 \times 10^{29}$ /m^3), field penetration is therefore minimal with $\lambda_D \approx 0.1$ nm. However, at the vacuum boundaries of such a plasma the local density can be much lower and hence the fields can penetrate to greater depths with $\lambda_D \approx \mu m$. This defines the width of a **plasma sheath** field extending across the boundary - a phenomena which will be discussed further throughout this thesis in relation to the sheath field acceleration of ions.

Kinetic and Fluids Models

The most direct method to describe plasma phenomena is to solve the equation of motion for every single particle. With well over 10^{15} particles, solving in this manner at successive intervals would be quite time consuming. However, in the **kinetic theory** of plasmas the calculations are performed instead on a statistical distribution function f_α representing a particle species α with momentum $\mathbf{p}$ or velocity $\mathbf{v}$ (where $\alpha = e, i$ denotes electrons or ions) at each spatial point $\mathbf{r}$ over time: $f_\alpha(\mathbf{r}, \mathbf{p}, t)$. Hence, the large number of particles are represented by a single distribution function which enables the large complex system to be modelled.

The **Vlasov-Fokker-Planck** equation calculates the changes of f_α at each spatial point (∂r) over time (∂t) as a function of the forces acting on the particle distribution based on Boltzmann's equation:

$$\frac{\partial f_\alpha}{\partial t} + \mathbf{v}.\frac{\partial f_\alpha}{\partial \mathbf{r}} + q_\alpha \left[\mathbf{E} + \mathbf{v} \times \mathbf{B}\right].\frac{\partial f_\alpha}{\partial \mathbf{p}} = C_{ee}(f_\alpha) + C_{ei}(f_\alpha) \tag{2.6}$$

where q_α is the charge of species α. The forces here are the electromagnetic $(\mathbf{E}, \mathbf{B})$ and the collisional terms C_{ei} and C_{ee} are the Fokker-Planck electron-ion and electron-electron operators respectively. For a sufficiently hot plasma, collisions can be neglected. For a collisionless plasma, Equation 2.6 reduces to the **Vlasov equation**:

$$\frac{\partial f_\alpha}{\partial t} + \mathbf{v}.\frac{\partial f_\alpha}{\partial \mathbf{r}} + q_\alpha \left[\mathbf{E} + \mathbf{v} \times \mathbf{B}\right].\frac{\partial f_\alpha}{\partial \mathbf{p}} = 0 \tag{2.7}$$

The Vlasov equation, coupled with Maxwell's equations to solve the fields, provides a closed system for describing a plasma. However, this is a classical system where ionisation and recombination are neglected. In real laser-solid interactions both quantum degeneracy and strong-coupling effects may be important at temperatures below a few hundred electron-volts.

A further simplification, using a **hydrodynamic** approach, can be applied if the electron dynamics need not be resolved. This method treats the plasma as a fluid of charge, with velocity $\mathbf{u}_\alpha$, and the motion of the macroscopic fluid elements are tracked. The fluid equations are derived from the Boltzmann equation by integrating over the velocity distribution $f_\alpha(\mathbf{v})$. The hydrodynamic equations consist of the **fluid continuity equation**:

$$\frac{\partial n_\alpha}{\partial t} + \frac{\partial}{\partial \mathbf{r}} n_\alpha \mathbf{u}_\alpha = 0 \tag{2.8}$$

and the **fluid force equation**, which is obtained after first multiplying the Boltzmann equation by the momentum before integrating:

$$n_\alpha \left[\frac{\partial \mathbf{u}_\alpha}{\partial t} + \left(\mathbf{u}_\alpha \cdot \frac{\partial \mathbf{u}_\alpha}{\partial \mathbf{r}} \right) \right] = \frac{n_\alpha q_\alpha}{m_\alpha} \left[\mathbf{E} + \frac{\mathbf{u}_\alpha \times \mathbf{B}}{c} \right] - \frac{1}{m_\alpha} \frac{\partial p_\alpha}{\partial \mathbf{r}} \tag{2.9}$$

An equation-of-state is required to close the system of equations. In many cases, it is sufficient to specify the ideal gas law equation of state constant temperature with pressure:

$$P = n_\alpha k_B T_\alpha \tag{2.10}$$

If the considered process is slow enough for the species to thermalise then an isothermal equation of state is assumed. Otherwise an adiabatic equation of state is used. The kind of equation of state to be used for each species depends on the comparison of the plasma frequency $\omega_{p\alpha}$ and the wave-number $\mathbf{k}$ of the phenomenon under study with the particle thermal velocity:

$$v_{t\alpha} = \sqrt{k_B T_\alpha / m_\alpha} \tag{2.11}$$

Such that when $\omega_{p\alpha}/\mathbf{k} \ll v_{t\alpha}$ the particles have enough time to thermalise the plasma causing a constant temperature. Otherwise the adiabatic equation of state is applicable for a plasma of d dimensions:

$$\frac{P}{n_\alpha^{\frac{d+2}{d}}} = \text{constant} \tag{2.12}$$

The fluid equations, augmented with the equation of state and coupled to Maxwell's equations, constitute a closed set.

The fields $\mathbf{E}$ and $\mathbf{B}$ are calculated using **Maxwell's equations** involving divergence $\nabla\cdot$ and curl $\nabla\times$ operators.

- Gauss's law for electric field generation by charges:

$$\nabla \cdot \mathbf{E} = \frac{\rho_q}{\varepsilon_0} \tag{2.13}$$

- Gauss's law for magnetic field generation by charges:

$$\nabla \cdot \mathbf{B} = 0 \tag{2.14}$$

- Faraday's law for electric field generation by induction:

$$\nabla \times \mathbf{E} = -\frac{\partial \mathbf{B}}{\partial t} \tag{2.15}$$

- Ampère's law for magnetic field generation by induction:

$$\nabla \times \mathbf{B} = \mu_0 \mathbf{J} + \frac{1}{c^2}\frac{\partial \mathbf{E}}{\partial t} \tag{2.16}$$

where μ_0 is the vacuum permeability, ρ_q is the total charge density and $\mathbf{J}$ is the total current density.

The fluid theory is sufficiently accurate to describe many important physical processes, and has the great advantage of leading to simpler equations to be solved in comparison with the kinetic approach. For instance, the main features of the propagation of electromagnetic waves in a plasma can be understood within a fluid treatment. The kinetic approach on the other hand is necessary in some cases as the fluid approximation may break down, while in other cases provides complementary information which cannot be retrieved within the fluid theory. Systems that are not in **local thermodynamic equilibrium** (LTE) cannot be described by fluid equations as no equation of state is valid. For example, some of the collisionless laser absorption mechanisms that will be presented later have an intrinsic kinetic nature.

Collisions and resistivity

Any electric field existing within the plasma will drive charged particles as a current. Since the ions are less mobile, this current can be assumed to be entirely electrons. As the electrons are driven through the plasma they suffer collisions. The resistivity within the plasma arises due to the exchange of momentum that occurs when plasma particles collide. Since momentum transfer is dominated by collisions between particles of different mass, one only needs to consider electron-ion collisions. An expression for the resistivity may be obtained by considering the plasma as a fluid of electrons and ions. The change in the momentum of the electron fluid due to collisions with ions is:

$$\Delta \boldsymbol{p}_{ei} = m_e n_e (v_e - v_i)\nu_{ei} \tag{2.17}$$

where ν_{ei} is the frequency of electron-ion collisions and is defined later in Equation 2.27. As the collisions are essentially the interaction of the Coulomb charge of the ions (eZ) and electrons (e) then the momentum transfer is proportional to the relative charges, the densities and the relative velocities of the two fluid species:

$$\Delta \boldsymbol{p}_{ei} \propto Ze^2 \times n_e^2 [v_e - v_i] \tag{2.18}$$

$$\Rightarrow \Delta \boldsymbol{p}_{ei} = \eta \times Ze^2 \times n_e^2 [v_e - v_i] \tag{2.19}$$

The proportionality constant, η, is called the **resistivity** and can be defined using Equations 2.17 and 2.19 as [47]:

$$\eta = \frac{m_e \nu_{ei}}{Z n_e e^2} \tag{2.20}$$

The **Coulomb force** between the electron and ion over distance r is:

$$\boldsymbol{F}_{ei} = -\frac{Ze^2}{4\pi\varepsilon_0 r^2} \tag{2.21}$$

and is exerted over the time that the electron is within the vicinity (b) of the ion: $t \approx b/v_e$. Therefore, the change in the electrons momentum is approximately:

$$\Delta \boldsymbol{p}_{ei} = |\boldsymbol{F}_{ei} t| \approx \frac{Ze^2}{4\pi\varepsilon_0 b v_e} \tag{2.22}$$

The Coulomb collision, as an inverse-square law force, deflects the electron in a hyperbolic trajectory. The scattering angle θ_{ei} is described by the distance of closest approach called the **impact parameter** (b):

$$\tan\frac{\theta_{ei}}{2} = \frac{Ze^2}{4\pi\varepsilon_0 m_e v_e^2 b} \tag{2.23}$$

In many situations in plasma physics, the upper limit on b is taken to be the Debye length, and the low cut-off is chosen to be the impact parameter for a 90° scatter, b_0. For such a 90° interaction, $\tan(\theta_{ei}/2) = 1$, and the change in momentum will be of the order of:

$$m_e v_e = \frac{Ze^2}{4\pi\varepsilon_0 b_0 v_e} \tag{2.24}$$

and the impact factor here is:

$$b_0 = \frac{Ze^2}{4\pi\varepsilon_0 m_e v_e^2} \tag{2.25}$$

The Coulomb **cross section** is therefore:

$$\sigma = \pi b_0^2 = \frac{Z^2 e^4}{16\pi\varepsilon_o^2 m_e^2 v_e^4} \tag{2.26}$$

and the collision frequency is:

$$\nu_{ei} = n_e \sigma v_e = \frac{n_e Z^2 e^4}{16\pi\varepsilon_0^2 m_e^2 v_e^3} \tag{2.27}$$

and finally the resistivity is:

$$\eta = \frac{m_e}{n_e e^2}\nu_{ei} = \frac{Ze^2}{16\pi\varepsilon_0^2 m_e v_e^3} \tag{2.28}$$

For the case of a Maxwellian distribution of electron velocities, the electron temperature is $k_B T_e = v_e^2 m_e$, which provides an order of magnitude estimate for resistivity and temperature:

$$\eta \approx \frac{Z\pi e^2\sqrt{m_e}}{(4\pi\varepsilon_0)^2 k_B T_e^{3/2}} \tag{2.29}$$

This equation for resistivity is of course based exclusively on large angle collisions. In reality, the long range nature of the Coulomb force makes b large resulting in small scattering angles θ_{ei}. Indeed the overall effect of many small angle deflections proves more influential in determining the angular distribution. A correction factor is applied called the **Coulomb logarithm**, $\ln\Lambda$, where Λ is the ratio of the maximum and minimum impact factors, $\Lambda = b_{max}/b_{min}$. These values are usually $b_{max} = \lambda_D$ and $b_{min} = b_0$ which are defined in Equations (2.4,2.25) respectively and combine to give [48]:

$$\ln\Lambda = \ln\left(4\pi n_e \lambda_D^3\right) = 6.6 - 0.5\ln\left(\frac{n_e}{10^{20}\,/\mathrm{m}^3}\right) + \frac{3}{2}\ln\left(\frac{k_B T_e}{\mathrm{eV}}\right) \tag{2.30}$$

As an example for a hot (200 eV) dense aluminium ($5\times10^{29}/\mathrm{m}^3$) plasma this expression gives a value of $\ln\Lambda \approx 3$. However, for an initially cold solid density plasma, the Coulomb logarithm can be very small or even negative. Quantum mechanical effects, such as degeneracy, need to be included for such conditions, and predictions by Lee and More [49] result in $\ln\Lambda \geq 2$. Incorporating this correction factor ($\ln\Lambda$) the value of η is termed the **Spitzer resistivity** [50]:

$$\eta \approx \frac{Z\pi e^2\sqrt{m_e}}{(4\pi\epsilon_0)^2 k_B T_e^{3/2}}\ln\Lambda \tag{2.31}$$

The expression defines the high temperature resistivity of a fully ionised plasma, at a few hundred eV, referred to as the Spitzer regime and is regularly written as,

$$\eta_s = 5.2\times10^{-5}\frac{Z\ln\Lambda}{k_B T_e^{3/2}} \tag{2.32}$$

which exhibits a dependence with plasma temperature and ion charge yet is independent of the plasma density. Since in this model $n_e = n_i$, any increased in plasma density will be accompanied by an increase in frictional drag with ions. These two effects cancel resulting in a constant resistivity. A simple estimate for the current density, $\mathbf{j}$, driven by an electric field, $\mathbf{E}$, in the plasma is given by Ohm's law:

$$\mathbf{E} = \eta\mathbf{j} \tag{2.33}$$

The resistivity for aluminium has been measured up to $\approx$ 100 eV by Milchberg *et al* [51], see Figure 2.3. For these measurements, the material was heated by a short

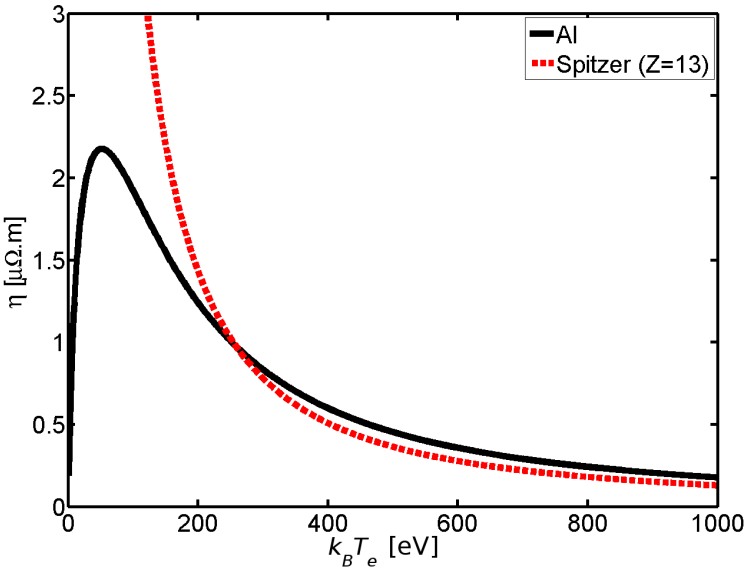

FIGURE 2.3: Resistivity curve for solid density aluminium [52] composed of measured data up to ≈ 100 eV [51] extended to higher temperatures by using the Spitzer resistivity prediction [50].

pulse laser and the plasma temperature was characterised via the reflected pulse. The expansion velocity and hence the resistivity was derived from the measured Doppler shifting of the reflected pulse. The trend in resistivity increases up to a saturation value corresponding to the minimum electron mean free path (equivalent to the inter-atomic distance) followed by a decrease with higher temperatures. Davies *et al* [52] determined a resistivity curve for aluminium from a fit to the Milchberg measurements and extending to the Spitzer regime:

$$\eta_{\mathrm{Al}} = \frac{1}{5 \times 10^6 (k_B T_e)^{-1} + 170 (k_B T_e)^{3/2} + 3 \times 10^5} \ \Omega.m \tag{2.34}$$

The resistivity equation exhibits a $k_B T_e^{-3/2}$ dependence. This inverse relationship indicates that as the plasma is heated the Coulomb cross section (σ) decreases and the resistivity drops rapidly with temperature. Heating can be simply achieved by passing a current through the plasma using ohmic I^2R (or $j^2\eta$) losses. However, heating in this manner cannot proceed indefinitely. Due to the $k_B T_e^{-3/2}$ scaling, continuous heating to thermonuclear temperatures (tens of keV) becomes progressively more difficult since plasmas as such temperatures become such good conductors that they are considered collisionless - i.e. zero resistivity. At such temperatures the distinction in resistivity between different materials becomes negligible.

The shape of the resistivity curve is the combined result of a number of material properties and hence is unique to each material. Resistivity plays a principle role in the

generation of electric (10^{12} V/m) and magnetic fields (10^{3} T) via fast electron propagation through solid density plasma. As reported in the investigations of this thesis, the collective effects from these resistively induced fields effectively dominate the transport physics of fast electrons.

2.4 Creating the plasma

In the context of this thesis the motivation for delivering intense laser pulses onto solid targets is to (i) create a controlled short-lived plasma via ionisation followed by (ii) energy absorption into fast electrons. The laser-target interaction takes place within a sealed target chamber under high vacuum. The CPA laser beam, which had been spatially expanded before compression, is now focused onto target by a large parabolic optic. The initial absorption of laser pedestal energy at the cold target surface will lead to a fast transformation of the irradiated spot. Thus, the incident main pulse does not interact with a cold solid target but rather with a preheated or even ionised plasma. Not all the main laser energy will be absorbed, some fraction will be reflected depending on the laser and target parameters.

The CPA laser pulse can in practice be cleaned to remove pedestal and prepulse components with the use of **plasma mirrors** placed before target [53–55]. This can improve the intensity contrast $> 10^{10}$ at the expense of some loss ($> 50\%$) of laser energy. While this is especially important for thin targets $< 1\,\mu$m, which can be destroyed by laser prepulse, the work of this thesis concerns relatively thick targets and some **pre-plasma** is desirable for more efficient fast-electron generation [56, 57]. Accordingly, plasma mirrors were not used for these investigations.

2.4.1 Ionisation

A front surface plasma is created from the initial break down of the target material by the laser field through the process of ionisation. As discussed previously, creating a plasma from a solid material involves a change of state which necessitates energy. This energy must be sufficient to overcome the binding energy of first the solid crystal lattice, then the molecular bonds and then the binding energy of electrons within atoms. Higher levels of ionisation require higher energies to strip electrons from inner orbitals. The energies required to free electrons from each orbital are termed the ionisation potentials (U) of the atom.

For example, ionising a ground state hydrogen atom requires $U_H = 13.6\,\text{eV}$ of energy. In this state the electron orbits at a distance of $a_B = 4\pi\varepsilon_0\hbar^2/m_e e^2 = 0.053\,\text{nm}$, the Bohr radius, from the nucleus. The electric field strength, E_a , that keeps this electron in this orbit can be calculated classically: $E_a = e/4\pi\varepsilon_0 a_B^2 = 5 \times 10^{11}\,\text{V/m}$. To overcome this ionisation potential, the laser field needs to exceeds the atomic intensity:

$$I_a = \frac{\varepsilon_0 c}{2} E_a^2 \approx 10^{16}\,\text{W/cm}^2 \tag{2.35}$$

However, a number of quantum mechanical phenomena can effectively circumvent this limit enabling very high levels of ionisation at lower laser intensities. These effects include **multi-photon** ionisation and **tunneling** or **barrier suppression** ionisation, see Figure 2.4. Work by Keldysh [58] and later Perelomov [59, 60] derived quantitative calculations to determine if ionisation from tunneling or multi-photon ionisation is more likely. Keldysh introduced the following dimensionless parameter [58]:

$$K = \frac{\text{Tunneling Time}}{\tau_L} = \omega_L \sqrt{\frac{2U}{I_L}} \quad \text{[Atomic Units]} \tag{2.36}$$

As a general rule of thumb, tunneling is dominant when $K \ll 1$, in the case of strong laser fields and long wavelengths. Multiphoton ionisation applies when $K \gg 1$ for low and moderate laser intensities. In the example of a Vulcan-type laser field, tunneling is dominant during the main picosecond pulse, whereas multi-photon ionisation will dominate during the longer nano-second duration of the ASE pedestal. However, the descriptive limits of the Keldysh parameter have been noted by Reiss [61], especially in the case of intense laser fields where tunneling is made irrelevant by barrier suppression effects. These distinct mechanisms are discussed below.

Multi-photon ionisation is induced if a sufficient quantity (n) of photons are absorbed by the bound electron 'simultaneously' (i.e. in one field cycle). This quantum mechanical effect can occur for the very high photon intensities typical of lasers. In the case where a net surplus number of photons (s) are absorbed, the kinetic energy (KE) of the electron can be larger than the photon energy: $KE = (n + s)\hbar\omega_L - U$. Ionisation of ground state hydrogen would require 12 photons within 0.5 fs in the case of a $\lambda_L = 1\,\mu$m laser where $\hbar\omega_L = 1.2\,\text{eV}$. As discussed above, this mechanism is prevalent during the laser pedestal interaction. See Burnett [62] and Freeman *et al* [63] for reviews on theoretical and experimental approaches .

Tunneling/Barrier suppression ionisation defines a lower ionisation threshold which can occur due to the distortion of the atomic binding potential from the electric field of the laser. In such cases the electric field of the laser is so strong that the Coulomb barrier is suppressed, the electron can escape freely or have a high probability of tunneling.

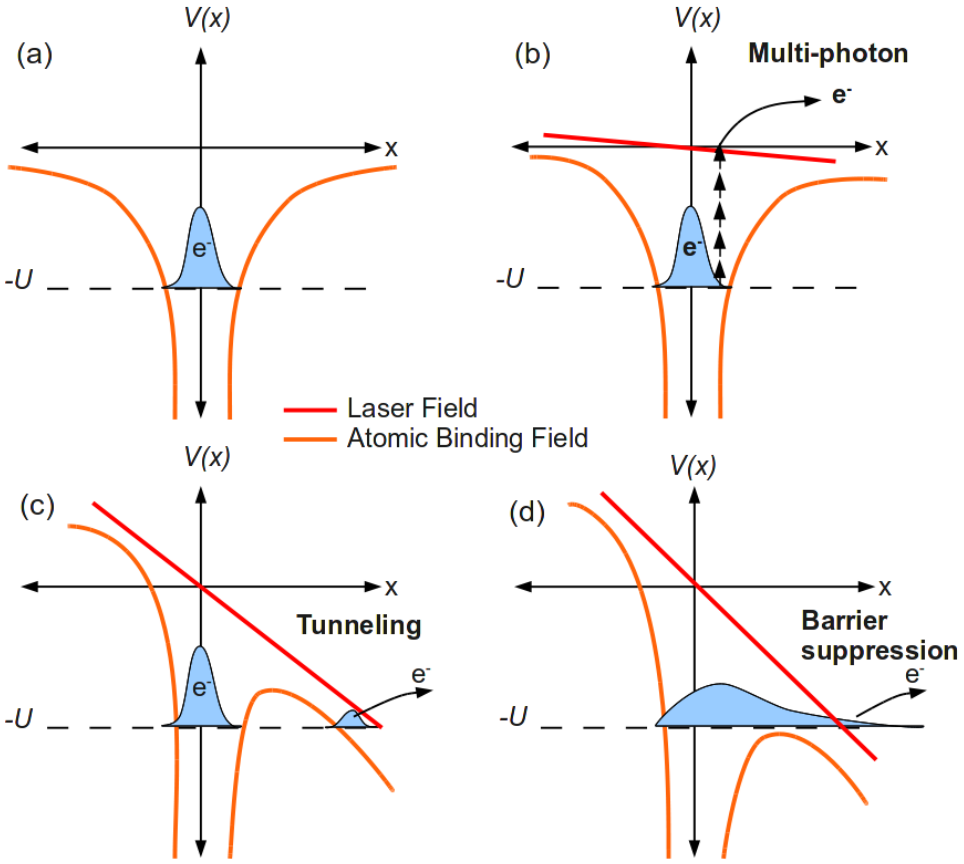

FIGURE 2.4: Ionisation mechanisms: (a) An electron, illustrated by a wave-packet, is initially bound to an atom by an electric potential U. Ionisation of this bound state can occur under the influence of an external field representing that of the laser. The electron can escape by (b) multi-photon, (c) tunneling and (d) barrier suppression ionisation.

Tunneling occurs in the limiting case of a relatively weak laser field. Barrier suppression occurs once a critical electric field strength is achieved:

$$E_k = \frac{U^2 \varepsilon_0 \pi}{e^3 Z} = 1.73 \times 10^8 \,\mathrm{V/m} \cdot \frac{U^2/\mathrm{eV}}{Z} \tag{2.37}$$

For the example of ground state hydrogen this threshold field value is $3.2 \times 10^{10}\,\mathrm{V/m}$. Including this suppression effect lowers the minimum laser intensity required for ionisation to $10^{14}\,\mathrm{W/cm^2}$.

$$I_{BSI} = \frac{U^4 c \pi^2 \varepsilon_0^3}{2 Z^2 e^6} = \frac{4 \times 10^9}{Z^2} \frac{U^4}{[\mathrm{eV}]}\,[\mathrm{W/cm^2}] \tag{2.38}$$

The **rate of ionisation** for tunneling/barrier suppression can be derived by calculating according to the Keldysh model discussed above. For hydrogen-like ions with an applied electric field, $\mathbf{E}$, this rate is given by:

$$\nu_K = 4\omega_a \left(\frac{U}{U_H}\right)^{\frac{5}{2}} \frac{E_a}{\mathbf{E}(t)} \exp\left[-\frac{2}{3}\left(\frac{U}{U_H}\right)^{\frac{3}{2}} \frac{E_a}{\mathbf{E}(t)}\right] \tag{2.39}$$

The Keldysh theory does not include any species dependence into the rate equation. Ammosov, Delone, and Krainov [64] extended this theory for larger atoms with a higher number of charge states. The **ADK ionisation rate** is given by:

$$\nu_{ADK} \approx 6.6 \times 10^{16} \frac{Z^2}{n_{ef}^{4.5}} \left[10.87 \frac{Z^3}{n_{ef}^4} \left(\frac{E_a}{\mathbf{E}(t)} \right)^{1/2} \right]^{2n_{ef}-1.5} \times \exp \left[-\frac{2Z^3}{3n_{ef}^3} \left(\frac{E_a}{\mathbf{E}(t)} \right)^{1/2} \right] \tag{2.40}$$

where Z is the charge of the created ion and $n_{ef} = Z/\sqrt{U/U_H}$. Experimentally [65], the ionisation predictions of ADK-theory has been confirmed for the noble gases helium, argon, neon and xenon for an range of short pulse laser intensities from $10^{13}\,\mathrm{W/cm^2}$ up to $10^{18}\,\mathrm{W/cm^2}$.

Collisional ionisation: Once ionised, the free electrons with sufficient kinetic energy can liberate bound electrons through collisions. All electrons with kinetic energy in excess of the ionisation energy contribute. The collisional ionisation rate can be calculated using the ionisation potentials with the electron velocity v_e, density and temperature [66, 67]:

$$\nu_C \approx n_e v_e 4\pi a_b^2 \left(\frac{U_H^2}{U\, k_B T_e} \right) \ln \left(\frac{k_B T_e}{U} \right) \tag{2.41}$$

2.4.2 Front surface plasma

The creation of a plasma by the laser energy, either via the pedestal or by the main pulse, is the first part of the picture. The laser continues to irradiate and interact with this plasma over the duration of its pulse length. There are a number of important processes such as plasma expansion and heating which require discussion.

The ionisation rapidly heats the front of the target creating a surface plasma. The plasma pressure created during heating causes the surface matter to blow off at near the sound speed:

$$c_s = \left(\frac{Z^* k_B T_e}{m_i} \right)^{\frac{1}{2}} \tag{2.42}$$

This expanding plasma can be described by a density profile that falls off exponentially for a one-dimensional isothermal expansion. At a distance z from a target for which surface density is n_0, the plasma density is:

$$n_e(z) = n_0 \exp \left(-\frac{z}{L_s} \right) \tag{2.43}$$

The steepness of the profile is described by the **density scale length** L_s. This is the distance at which the density drops by a factor of $1/e$, where e is Euler's number. The scale length characterises the amount of pre-formed plasma. This greatly effects how the

energy from the main laser pulse is absorbed. The scale length can be estimated using the sound speed and laser pulse duration giving $L_s \approx c_s \tau_L$ or:

$$L_s \simeq 3 \left(\frac{k_B T_e}{\text{keV}}\right)^{1/2} \left(\frac{Z^*}{A}\right)^{1/2} \left(\frac{\tau_L}{\text{fs}}\right) 10^{-4}\, \mu\text{m} \tag{2.44}$$

A value for the plasma temperature, $k_B T_e$, can be calculated using an expression shown later in Equation 2.50. For a laser with $\lambda_L = 1\ \mu$m, an absorbed intensity of $I_L = 10^{20}\text{W/cm}^2$ will heat the front surface of an Al target, $n_e = 6 \times 10^{29}\ /\text{m}^3$, to tens of keV resulting in a scale length of $L_s \sim \lambda_L$. Factoring in the presence of the low intensity laser pedestal with a contrast of 10^8 will result in $I_p = 10^{12}\ \text{W/cm}^2$. This intensity sustained for 3 ns will create a substantial underdense pre-plasma before the main pulse arrives resulting in a pre-plasma scalelength in the region of $L_s \sim 200\,\mu$m. Hence, there is a dramatic difference in the laser-target interaction if the inherent contrast of a laser system is ignored.

The laser pulse will only be able to propagate through the increasingly dense plasma up to a certain point. At this **critical density** the plasma becomes opaque to the laser field of frequency ω_L:

$$n_c = \frac{\varepsilon_0 \bar{\gamma} m_e}{e^2} \omega_L \approx 1.1 \times 10^{27} \left(\frac{1\mu\text{m}}{\lambda_L}\right)^2\ [/\text{m}^3] \tag{2.45}$$

Two distinct laser-plasma regimes are defined using the critical density:

1. Underdense plasma where $n_e < n_c$
2. Overdense plasma where $n_e > n_c$

Note that the critical density is inversely proportional to the square of the laser wavelength. A laser with a wavelength of 1 μm propagates up to the critical density n_c of about $10^{27}/\text{m}^3$. The location where the laser meets this density is termed the **critical surface.** In sufficiently intense laser fields the plasma electrons can be accelerated to near the speed of light. In this relativistic regime the critical density increases by a factor of $\bar{\gamma}$ (defined in Section 2.5). This enables the laser pulse to travel further into the plasma effectively pushing the critical surface into the plasma. For a given pre-plasma scale length, the position of the critical surface, z_c, can be calculated by solving Equation 2.43 for $n_e = n_c$ giving:

$$z_c = L_s \ln\left(\frac{\bar{\gamma} n_c}{n_0}\right) \tag{2.46}$$

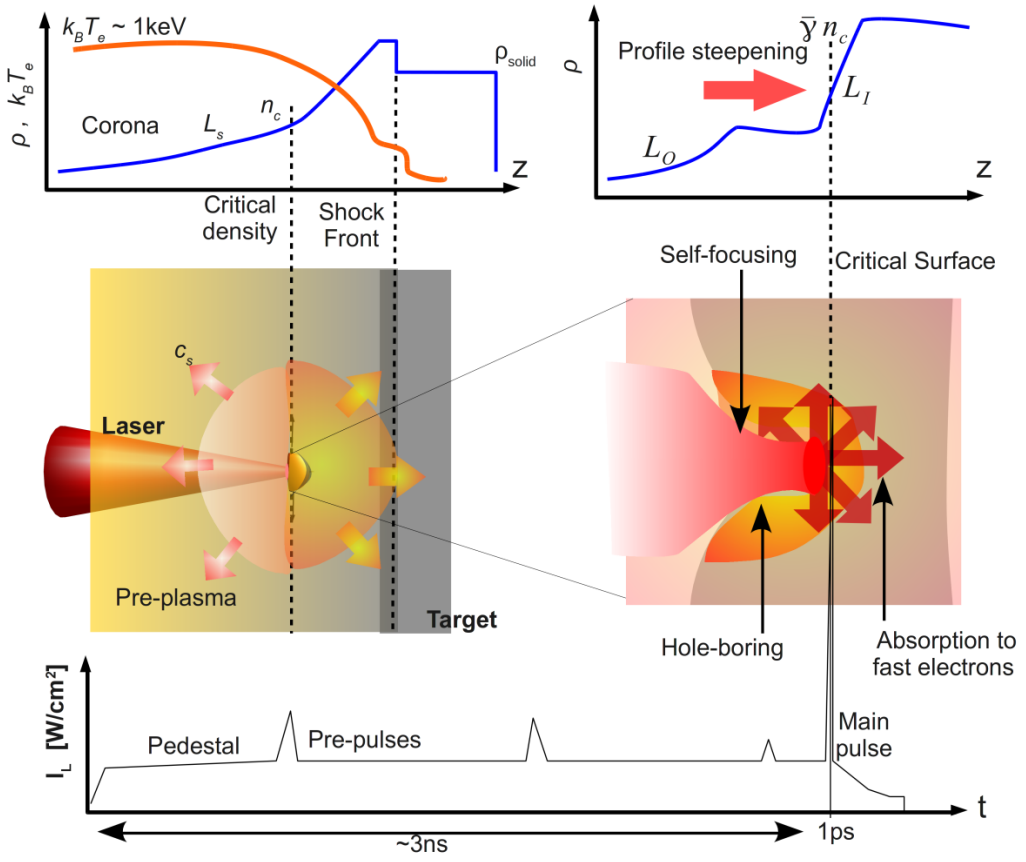

FIGURE 2.5: Schematic of laser-induced plasma at the front of target with respect to plasma density and temperature (top) laser interaction (centre) and temporal laser intensity (bottom). Two temporal regimes are depicted: the long nanosecond duration of the laser pedestal induces an expanding pre-plasma (left); the short picosecond main pulse interacts with the pre-plasma and propagates up until the critical surface (right). A number of effects including ablation, shock formation, and hole boring are discussed in the text.

Consider an example with the conditions: $\lambda_L = 1\,\mu$m, $n_c \approx 10^{27}\,/\mathrm{m}^3$, $n_0 \approx 10^{29}\,/\mathrm{m}^3$ and $L_s = 10\lambda_L$. For the non-relativistic case, z_c is located $\approx 50\,\mu$m in front of target. For a high intensity laser pulse, such that $\bar{\gamma} = 10$, the critical surface position is pushed back $\approx 25\,\mu m$ further towards the original target surface.

In the presence of a laser pedestal there are two distinct regimes of interactions: (i) a relatively long nanosecond period of front surface plasma ablation by the laser pedestal and (ii) the intense interactions of the main pulse over hundreds of femtoseconds. These two regimes are depicted in Figure 2.5. The presence of prepulses and pedestal energy creates a long scale length plasma, the ablation drives a shock front moving in the opposite direction into the target. The main laser pulse must channel through the pre-plasma which can result in self-focusing and filamentation of the laser beam. The intense ponderomotive force of the laser can push through the original critical density, steepening the pre-plasma profile and boring some microns into the target surface to

γn_c. Ultimately, a fraction of the laser energy is coupled to accelerating the fast electron population into the target beyond the critical surface.

In the case of fast electron generation which will be discussed later, the existence of the pre-plasma does complicate both the laser propagation and absorption at the critical surface. Indeed a certain amount of pre-plasma can enhance absorption dramatically [56, 57]. Plasma expansion can be imaged by probing the underdense region using a sample of the CPA beam. With the addition of interferometry, this optical probe image can be used to infer the electron density and hence the plasma scale length. However, the draw back is that the technique is diffraction limited to probing below the critical density and consequently the scale length near the absorption region is not measured. Many of the absorption processes are very sensitive to the plasma gradient at the critical surface, see Section 2.5.3. A convention introduced by McKenna *et al* [56], characterises the overdense plasma with an inner scale length L_I and the underdense plasma with an outer scale length L_O. The full density profile can be estimated using simulation codes incorporating hydrodynamic modelling for the plasma expansion.

In addition to plasma expansion, the radiation pressure from the intense main pulse can push against the pre-plasma, steepening its density gradient. This can occur if radiation pressure (P_L) is greater than the thermal pressure of the plasma (P_{th}):

$$\frac{P_L}{P_{th}} = \frac{2I_L/c}{n_e k_B T_e} > 1 \tag{2.47}$$

For the example of I_L and I_p above, profile steepening is expected with $P_L/P_{th} \approx 5$. As a tightly focused laser pulse travels through an underdense plasma, electrons will be pushed outwards from the intense laser field by the ponderomotive force, see Section 2.5.2. This inherently modifies the refractive index $\eta_L = \sqrt{1 - n_e/n_c}$ of the plasma. This can create a lensing effect leading to laser **self-focusing** [68]. Obviously, this will increase the laser intensity creating a self-focusing feedback process which can ultimately cause the beam to breakup and filament. The increase in intensity will also push back the critical surface extending the penetration depth of the laser in the plasma.

The heating and effective temperature of the pre-plasma can be estimated using analytical formulae. In a high contrast system the surface remains unperturbed until the main pulse arrives. Due to this steep gradient the intense laser pulse will be impinging on a highly overdense mirror-like wall of plasma. In the absence of absorption, the laser field will form a standing wave pattern in the front of the target, augmented by an evanescent component penetrating into the overdense region to a characteristic skin depth $l_s = c/\omega_{pe}$ where heating can occur. The bulk heating of the plasma skin depth can be estimated by calculating the energy absorbed using the heat flow expression [69]

by a method described by Gibbon [70]:

$$\frac{\partial \epsilon}{\partial t} + \nabla.(\mathbf{q} + \mathbf{\Phi_a}) = 0 \tag{2.48}$$

where ϵ is the energy density, $\mathbf{q}$ is the heat flow and $\mathbf{\Phi_a} = \eta_a I_L$ is the absorbed laser flux. Setting the energy density $\epsilon = \frac{3}{2} n_e k_B T_e$ for an ideal plasma and ignoring outward heat flow, $\mathbf{q} = 0$ and $\nabla.\mathbf{\Phi_a} \sim \mathbf{\Phi_a}/l_s$, the initial heating rate can be derived:

$$\frac{d}{dt}(k_B T_e) \simeq \frac{\mathbf{\Phi_a}}{n_e l_s} = 4 \frac{\mathbf{\Phi_a}}{\mathrm{W/cm^2}} \left(\frac{n_e}{/cm^3}\right)^{-1} \left(\frac{l_s}{cm}\right)^{-1} \mathrm{keV/fs} \tag{2.49}$$

Thus, an initial heating rate of 1 keV/fs of the skin depth can be attained for laser pulse intensity of 10^{15} W/cm^2 . Obviously after a few femtoseconds thermal transport starts carrying the heat away to cooler regions of the target creating a heat front moving at an ultra fast 10^5 m/s. After a time t the plasma temperature at the front of the target can be estimated using the Rosen [71] expression for constant absorbed laser intensity:

$$k_B T_e = 250 \left(\frac{n_e}{10^{23}/cm^3}\right)^{-2/9} Z^{2/9} \left(\frac{I_L}{10^{15}\ \mathrm{W/cm^2}}\right)^{4/9} \left(\frac{t}{100\ \mathrm{fs}}\right)^{2/9} \mathrm{eV} \tag{2.50}$$

2.5 Energy absorption and fast electron generation

The generation of a relativistic electron population, directed into the target, provides a means of coupling a significant fraction of the laser energy to heat the deeper bulk material. This is especially relevant to the use of such a beam as the Fast Ignition trigger for inertial confinement fusion. The manner in which the intense laser field interacts with the pre-plasma electrons and couples energy to produce the fast electron current is discussed in this section. Since this topic is directly relevant to the work of this thesis, a topical review relating to the key characteristics of the fast electron population is presented. This includes measurements and predictions of conversion efficiency, temperature and injection direction of the fast electron beam. The subsequent transport of this population through the overdense target is addressed in Chapter 3.

2.5.1 An electron in a laser field

The laser fields can interact and accelerate the charged particles of the plasma. By virtue of their lower mass, electrons are accelerated much more by the laser field compared to the heavier ions. Once the electron has been freed from its parent atom, its motion

within the electromagnetic field of the laser is described via the **Lorentz equation**:

$$\frac{d\mathbf{p}}{dt} = m_e \frac{d(\mathbf{v}\gamma)}{dt} = -e \cdot (\mathbf{E} + \mathbf{v} \times \mathbf{B}) \tag{2.51}$$

together with an energy equation:

$$\frac{d}{dt}(\gamma m_e c^2) = -e(\mathbf{v} \cdot \mathbf{E}) \tag{2.52}$$

To begin, consider the forces acting on the electron from the electric field **E** and the magnetic field **B**. The electric field component with amplitude E_0 will accelerate the electron transverse to the laser direction $F_\perp = eE_0 \cos(\omega_L t)$. The electric field oscillates the electron to a **quiver velocity**:

$$v_\perp = \frac{eE_0}{m_e \omega_L} \tag{2.53}$$

at the laser frequency ω_L. At the same time the electron is pushed forward and back due to the magnetic field force $F_{||} = ev_\perp B_0 = e\frac{v_\perp}{c}\frac{E_0}{2}.\sin(\omega_L t)$. Obviously the $\frac{v_\perp}{c}$ dependence for $F_{||}$ limits the $\mathbf{v} \times \mathbf{B}$ component to the relativistic regime. Under the influence of a sufficiently strong laser field, with $E_0 > 3.2 \times 10^{12}$ V/m, the electron can be accelerated so that it's quiver velocity approaches the speed of light c. This onset of the relativistic effects occurs for laser intensities:

$$I_L \lambda_L^2 > 1.37 \times 10^{18}\,\mathrm{W}\mu\mathrm{m}^2/\mathrm{cm}^2 \tag{2.54}$$

which equates to a laser intensity of $10^{18}\,\mathrm{W/cm^2}$ for a glass amplifier medium ($\lambda_L \approx 1\,\mu$m) or much lower at $10^{16}\,\mathrm{W/cm^2}$ for a longer wavelength laser ($\lambda_L \approx 10\,\mu$m) such as a gas-type medium like CO_2. One immediate consequence of the relativistic electron motion is that the magnetic field is no longer negligible - the longitudinal force $F_{||}$ exceeds the transverse force $F_\perp$. The ratio of these component forces on the electron can be used to indicate the strength of the relativistic effects and is traditionally defined using the normalised laser amplitude:

$$a_0 \equiv \frac{F_{||}}{F_\perp} = \frac{eE_0}{m_e c \omega_L} = \sqrt{\frac{I_L[\mathrm{W/cm^2}]\lambda_L^2[\mu\mathrm{m}^2]}{1.37 \times 10^{18}}} \tag{2.55}$$

A value of $a_0 \approx 20$ results in the case of a Vulcan type laser with $I_L \approx 5 \times 10^{20}\,\mathrm{W/cm^2}$ and $\lambda_L \approx 1\,\mu$m. The Lorentz factor for relativistic effects can be derived using $\gamma = 1/\sqrt{(1 - v^2/c^2)} = \sqrt{1 + a_0^2}$. Averaged over the laser cycle $\bar{\gamma} = \sqrt{1 + a_0^2/2}$ for linear polarisation and $\bar{\gamma} = \sqrt{1 + a_0^2}$ for circular polarisation. The electron mass will increase at velocities approaching c and hence modifies the plasma frequency which in turn increases the critical density thus enabling the laser field to propagate further into the plasma.

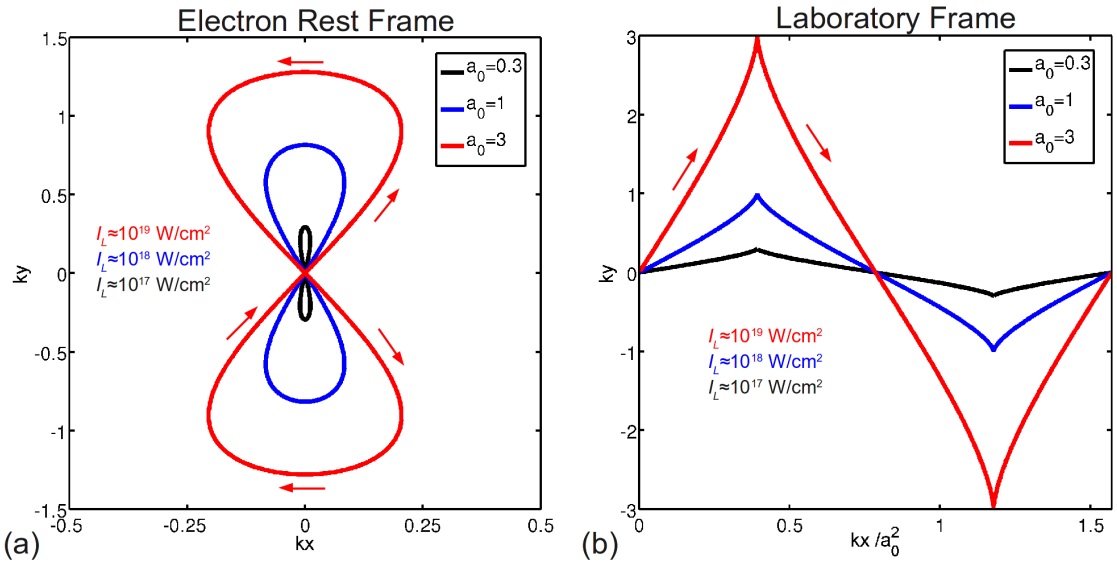

FIGURE 2.6: Electron trajectories in a linearly polarised electromagnetic field are showed for different laser intensities with 1 μm wavelength. Here the laser is propagating along the x-direction. The trajectories are the result of transverse displacement by the electric field in the y-direction and a longitudinal displacement in the x-direction by the magnetic field. (a) The combination produces a distinctive figure-of-8 as seen in the rest frame of the electron; (b) In the laboratory frame, the electron is displaced along the laser direction, increasing by a_0^2 for higher intensities. The trajectories are calculated using a method described by Gibbon [70]

For $a_0 = 20$, the laser field amplitudes are $E_0 = a_0 \frac{2\pi m_e c^2}{\lambda_L} = 64 \times 10^{12}$ V/m and $B_0 = a_0 \frac{2\pi m_e c}{e\lambda_L} = 2 \times 10^5$ T again for laser wavelength $\lambda_L = 1\,\mu$m. The magnetic force $e(\mathbf{v} \times \mathbf{B}) = eE_0$ pushes the electron to a velocity $v_{||} = \frac{a_0^2}{4+a_0^2} c = 0.99c$ and $\bar{\gamma} = 14$. Moving along at this velocity the electron would be observed to oscillate in a figure of eight due to the interplay of both forces. This trajectory is shown in Figure 2.6(a), the electron oscillates at $2\omega_L$ longitudinally and at ω_L transversely. In the laboratory frame, shown in Figure 2.6(b), the electron's motion is increasingly directed along the laser direction at higher laser intensity as indicated by the a_0^2 scaling. For circularly polarised light, the electron's rest frame trajectory is a circle with a radius $a_0/\sqrt{2}\bar{\gamma}$. However, oscillating in an homogeneous field the electron does not gain any net energy - this is known as the Lawson-Woodward theorem [72].

2.5.2 The ponderomotive force

In the case of an inhomogeneous field the situation is different. A focused laser field will not be homogeneous in reality and is typically Gaussian in space and time. The spatial variation in intensity can create strong gradients which can push the electrons out from the high intensity regions. While still oscillating at the laser frequency the position of the electron after one cycle of oscillation shifts toward the lower field-amplitude area

where the restoring force is also lower. Over many laser cycles this produces a net force that drives the charge toward the weak field area.

A force of this kind was known as electrostriction by Kelvin since 1846 and was reformulated later by Helmholtz as the **ponderomotive force** in electrostatics. Historically, the name defines any force derived from electric or magnetic fields. Starting from the Lorentz expression in Equation 2.51 the ponderomotive force on a single particle can be derived. Considering first the non-relativistic case where the electric field is dominant, the cycle averaged force is:

$$F_p = -\frac{e^2}{4m_e\omega_L^2}\nabla\mathbf{E}^2 \tag{2.56}$$

As discussed above, the force ultimately derives from a spatial gradient in the electric field and consistently pushes the electron out to lower field areas after each field cycle with velocity $\approx v_\perp$. In the relativistic regime, as $v_\perp \to c$, the ponderomotive force averaged over the laser cycle will be:

$$F_p = -mc^2\nabla\bar{\gamma} = -mc^2\nabla\sqrt{1 + a_0^2/2} \tag{2.57}$$

In the highly relativistic regime - for 1 μm laser with intensity 10^{20} W/cm^2 , the light pressure from the ponderomotive force at solid density (10^{30} /m^3) can approach the thermal pressure ($n_e k_B T_e$) of the Sun's core - i.e. 250 billion atmospheres. This enormous pressure can have serious effects on the pre-plasma scale length. The force can sweep electrons aside and clear a tunnel up to the critical density, a process called **hole-boring** [73]. Even at the critical density the pressure can be sufficient to indent the surface while pushing the critical surface further back into the solid target - **profile steepening** [74] as illustrated in Figure 2.5. Within this hole-bored surface the angle of incidence and the density scale length are modified which directly effects the absorption of laser energy [74, 75].

At relativistic intensities the magnetic field component of the ponderomotive force becomes dominant, providing an efficient means of sending fast electrons out of the restoring laser field into the overdense target by a process termed $\mathbf{j} \times \mathbf{B}$ heating. The generation of a relativistic (fast) electron beam by this and other mechanisms is presented in the next section.

2.5.3 Heating mechanisms - breaking the adiabate

It is impossible to achieve a net acceleration of an electron in a plane laser wave except when the adiabacity is broken, i.e., if the electron can escape from the laser wave before

the laser pulse finishes, propagating away with some amount of energy. There are two ways of achieving net energy :

1. Collisional transfer: the electrons undergo collisions with the plasma ions. The electrons lose their coherence in the laser wave and can leave the interaction zone with a non-zero momentum. Inverse Bremsstrahlung heating [76] is an example of collisional heating.

2. Collisionless transfer: the laser field drives electron oscillations past the critical density. With no restoring force the adiabate is broken.

The collisional heating mechanisms can be excluded for the simple reason that the electron mean free path is greater than the plasma skin depth. Even at solid densities, the electron collisional frequency is very much less than the laser frequency. According to Equation 2.27 the collisional frequency scales with plasma temperature as $\nu_{ei} \propto k_B T_e^{-3/2}$. Recall from Equation 2.50 that the plasma temperature scales with time (t) as $k_B T_e \propto I_L^{4/9} t^{2/9}$, this implies that the frequency of collisions $\nu_{ei} \propto I_L^{-2/3} t^{-1/3}$. At higher laser intensities the electron quiver velocity increases and becomes comparable to the thermal velocity $v_{te} = \sqrt{k_B T_e / m_e}$ and the effective temperature is then $k_B T_{eff} \propto \left(v_\perp^2 + v_{te}^2\right)$. The collisional scaling is now reduced further to $\nu_{ei} \propto k_B T_{eff}^{-3/2} \propto [k_B T_e.(1+v_\perp^2/v_{te}^2)]^{-3/2}$. At irradiances $I\lambda^2 \geq 10^{15}$ Wcm$^{-2}\mu$m^2 collisional absorption becomes less effective and the main means of transferring energy will depend on collisionless processes.

In the case of collisionless scenarios, the plasma electrons can absorb a sizable fraction of laser energy if pushed by the fields into the overdense plasma beyond the restoring influence of the laser thereby creating an energetic electron population directed into the target. From the previous discussion, the two driving fields are the electric and magnetic components of the incident laser. A number of distinct fast electron heating mechanisms are possible depending on the laser and pre-plasma conditions. This is illustrated in Figure 2.7 and is discussed in the following section.

Fast electron heating by electric field

An electric field with a component along the plasma density gradient incident can accelerate electrons into the target in two distinct ways depending on the scale length of the plasma.

In the case of a relatively **long scale length** plasma, $L_s > \lambda_L$, resonant waves can be induced at the critical density surface n_c if the wave can tunnel from the reflection density $n_c \cos^2 \theta_L$. If the plasma wave is driven hard enough, it can break and eject

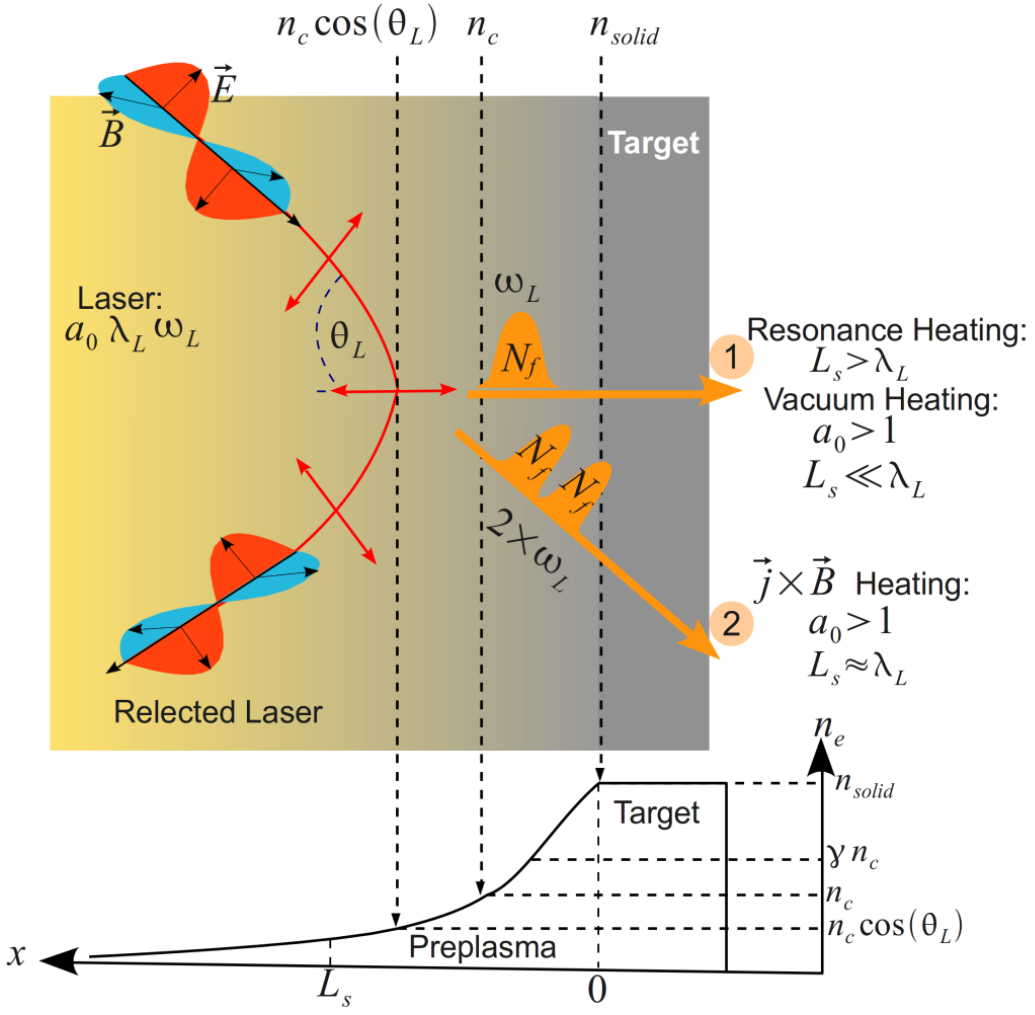

FIGURE 2.7: A summary of collisionless fast electron heating mechanisms by laser absorption. Electron oscillation waves carrying N_f fast electrons are driven through a pre-plasma across the critical density by the laser field which is p-polarised in this example. The pre-plasma scale-length, angle of incidence and laser conditions are controlling factors. See the main text for a detailed description.

fast electrons in the density gradient direction i.e. target normal. The electrons will be preferentially ejected once per laser cycle forming bunches separated by λ_L. At very steep scale length this mechanism weakens as the electron excursion length exceeds the plasma scale length. The optimal angle of incidence for **resonance absorption** is [77]:

$$\theta_R = \sin^{-1}(c/2\omega_L L_s)^{\frac{1}{3}} \tag{2.58}$$

In the case of **a short scale length** plasma, $L_s < \lambda_L$, where the amplitude of the plasma oscillation is larger than the plasma scale length a proper oscillation cannot be sustained to enable resonance absorption. In this scenario the electric field can create a fast electron population via an alternative process called **Brunel heating** [78]. In this case the laser field drags electrons out of the plasma into the vacuum and launches them

back across the sharp density gradient directed along target normal. Since the laser field only penetrates up to about the skin depth the electron escapes the laser and its quiver energy becomes kinetic energy. Corrections to the Brunel model by Gibbon [79] have shown that self-generated fields along the target surface hinder the re-entry of the electrons to the target, which are accelerated for many more laser cycles through a process termed **vacuum heating**.

The **anharmonic model** by Mulser *et al* [80] has attempted to generalise all absorption mechanisms as linear and non-linear laser-driven resonances. In the low intensity linear regime, harmonic resonance heating can be effective at shallow plasma scale lengths. For very steep scale length, the model predicts that effective fast electron heating can occur when the laser intensity is sufficient to drive non-linear anharmonic resonance of many oscillating plasma layers which then undergo disruptive chaotic wave breaking. The chaotic breaking of the electron adiabate accelerates the current through the critical density barrier. Mulser *et al* used 1D boasted collisionless PIC simulations to validate their model for a 10^{17} W/cm^2 laser intensity acting on a 80 times overcritical plasma surface. Cerchez and Mulser *et el* [81] have published measurements for absorption below this laser intensity for a sub-10fs pulse for a estimated steep scale length of $0.01\lambda_L$ where anharmonic resonance was inferred to provide the measured total absorption of 77%.

Fast electron heating by magnetic field: $\mathbf{j} \times \mathbf{B}$

At high laser intensities the longitudinal motion of electrons due to the $e(\mathbf{v} \times \mathbf{B})$ term of the Lorentz force becomes comparable to the electric field component. This effectively is the relativistic ponderomotive force, which becomes apparent as $I_L\lambda_L^2 > 10^{18}\,\mathrm{W}\mu\mathrm{m}^2/\mathrm{cm}^2$ where nonlinear effects related to the space gradients of the laser pulse begin to dominate the interaction as verified experimentally by Malka and Miquel [82]. Expressed relative to a volume of charge with density n_e, this force component is usually written as $\mathbf{j}\times\mathbf{B}$, where current density $\mathbf{j} = en_e\mathbf{v}$. For a linearly polarised electromagnetic wave propagating in z-direction, the z-component of the ponderomotive force is [83]:

$$F_p = -\frac{m_e}{4}\frac{d}{dx}v_\perp^2(1-\cos(2\omega_L t)) \tag{2.59}$$

The first term on the right hand side drives out the particles from the areas of strong field - i.e. the d.c. ponderomotive force, but acts only slightly on the ions because of their larger mass. The high frequency $2\omega_L$ term is the $\mathbf{j} \times \mathbf{B}$ component which heats the electrons via the Lorentz force $e\mathbf{v} \times \mathbf{B}$ and oscillates them along the laser direction $\mathbf{k}$ at the vacuum plasma interface depending on the non-uniformity of the laser field in the skin layer. The de-phasing of some of the electrons in this non resonant wave will be

sufficient to free them from the restoring field of the laser and kick them permanently into the overdense plasma of the target at a frequency $2\omega_L$ [83, 84]. This **injection frequency** is distinct from that of vacuum/resonance heating where the electric field accelerates the electrons bunched at the laser frequency ω_L.

The direction of acceleration is inherently different for Brunel/vacuum heating and $\mathbf{j} \times \mathbf{B}$ heating, the former is orientated along target normal and the latter along the laser direction[1]. This is illustrated in Figure 2.7. The density scale length dependence is also distinct for these heating processes. Brunel/vacuum heating requires sharp density profile and the $\mathbf{j} \times \mathbf{B}$ mechanism requires relatively longer scale length. Santala *et al* [85] inferred the fast electron direction by measuring the angular γ-ray emission from a high-Z bremsstrahlung layer at the target rear surface. The direction of the signal was observed to shift from near target normal for short scale lengths to near laser direction for intermediate scale lengths.

The plasma density and scale-length at the critical surface determine the relative importance of the various electron acceleration processes. For an obliquely incident laser pulse and long scale length plasma $L_s \gg \lambda_L$, resonance absorption accelerates electrons. For $L_s \leq \lambda_L$, there is a mixture of ponderomotive and vacuum heating depending on the laser angle of incidence and the steepness of the density profile. The $\mathbf{j} \times \mathbf{B}$ mechanism is more effective at lower laser incidence angles, while at steeper density profiles $L_s \ll \lambda_L$ or more oblique angles there is a transition to conditions where vacuum heating dominates. Ponderomotive steepening of the density profile which occurs at the laser reflection point can dynamically modify the pre-plasma conditions and the critical surface where these absorption mechanism occur. In long smooth density gradients, a process termed **volume heating** can occur in the low density foot of the profile which may provide for an effective coupling mechanism [86].

2.5.4 Laser to fast electron conversion efficiency

The total energy transferred from the laser to fast electrons is a fundamental parameter in defining the population of fast electrons injected into the target. The fraction of total laser energy imparted to the fast electrons is termed the **laser to electron conversion efficiency** and is typically written as $\eta_{L\rightarrow e}$. This term encapsulates a number of absorption processes and effects and therefore is a complex derivative. For instance, the absorption of the laser energy is subject to the heating mechanisms such as those discussed above which in turn are dependant on levels of pre-plasma and the angle of incidence of the laser pulse onto target.

[1]Since $\mathbf{v}$ is in the direction of $\mathbf{E}$ then $\mathbf{E} \times \mathbf{B}$ will be in the direction of $\mathbf{k}$.

Direct measurement of the entire fast electron energy distribution within the target is typically impossible. Electrostatic fields trap the majority of the fast electrons within the target with only a tiny fraction escaping to enable very limited direct measurements [87, 88]. Detection of secondary emissions, which provides indirect measurements of the fast electron distribution, are used in conjunction with modeling to infer a great deal of fundamental information. While these techniques can offer valuable insights, considerable uncertainly can result from the assumptions used in the modeling.

The majority of these indirect measurements are based on detecting x-ray emission which, being electrical neutral, escapes the target. Fast electrons ionising the inner shells of the target atoms can result in the emission of an x-ray photon with a characteristic energy determined by the transition. For example, a K-shell transition to an L-shell results in a K_α photon, with energy 8.05 keV in cold copper. This diagnostic is discussed in further detail in Section 4.3.2. Ultimately the yield of such photons is correlated with the number of fast electrons. In order to calculate this number the subsequent modelling must assume the (i) spectral shape, (ii) divergence $\theta_{1/2}$ (iii) temperature $k_B T_f$ (iv) and total energy, $E_L \eta_{L\to e}$, of the fast electron distribution. Hence, the value of $\eta_{L\to e}$ is not directly measured but varied within a model until the predicted photon yield matches the measurement. Consequently, a number of other unknown processes could remain hidden.

A collection of published results for $\eta_{L\to e}$ is shown in Figure 2.8. Both sets of results for Key [89] and Town [90] were performed on the Nova laser, the latter stated a scaling of $\eta_{L\to e}(I_L) = 1.2{\times}10^{-15}\, I_L^{0.74}$ denoted by the dashed line and derived using an undisclosed set of measurements. Values of $\eta_{L\to e}$ here range from $5-10\%$ at low intensity to a maximum of near 50% at high intensity [89, 90]. The assumptions used in the Monte Carlo modelling bear critical importance to the validity of these results. The key assumptions are (i) isotropic fast electron source (ii) no self generated fields and (iii) negating the influence of refluxing. The assumption of an isotropic fast electron source was found to significantly effect the calculation of $\eta_{L\to e}$. Wharton [91] found that reducing the divergence from isotropic to 30° half-angle reduced the inferred $\eta_{L\to e}$ by 30% for measurements in thick targets which prevented refluxing. Secondly, the absence of electric fields, which can inhibit transport [66, 92, 93], would lead to $\eta_{L\to e}$ being underestimated, and correspondingly over-estimated in the absence of magnetic fields which can pinch the beam [94, 95]. Thirdly, fast electrons reflected back into the target by the electrostatic sheath fields would lead to further ionisation and increasing K_α yield. Such effects of refluxing can either be negated by using thick targets (> 1 mm) or by its inclusion in the model [96]. Myatt [97] and Nilson [98] included the effects of refluxing in thin targets, and found the absorption to vary between $\eta_{L\to e} = 20 \pm 10\%$

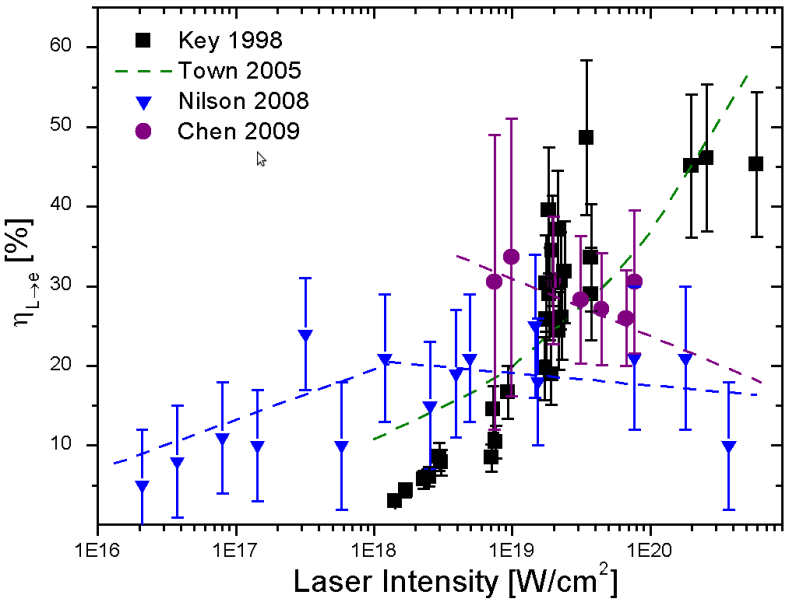

FIGURE 2.8: Values of laser to electron conversion efficiency, as a function of laser intensity, derived from measurements of K_α x-ray yield.

for $I_L = 10^{18} - 10^{20}$ W/cm^2 on the Vulcan and Omega systems. Chen [99] performed measurements using s-polarised pulses from the Titan laser and modelled conversion efficiencies in thick > 1 mm non-refluxing targets. Unlike the previous work, some attempt was also made to account for the energy losses arising from ion acceleration. The total conversion efficiencies for $I_L = 10^{18} - 10^{20}$ W/cm^2 are banded between 20% and 40% with very high error bars [99].

The pre-plasma conditions are an intrinsic variable in the published results of $\eta_{L\to e}$. Absorption can vary as a function of pre-plasma scalelength with some levels of pre-plasma been beneficial while higher levels less so [56, 57]. The Nova laser measurements were distinguished by a particularly large pre-plasma, due to contrast ratios of 10^{-3} to 10^{-4} compared to higher contrast of 10^{-6} for Titan and 10^{-8} for the Vulcan results. The effects of multiple heating mechanisms may need consideration for intense laser interactions with long scale length plasma. With sufficient amounts of pre-plasma **volume heating** can develop in the underdense region, in conjunction with $\mathbf{j} \times \mathbf{B}$ at the critical surface, resulting in increased levels of absorption [86]. At high laser intensities the variation of $\eta_{L\to e}$ between the different laser systems are consistent with a pre-plasma dependence on absorption. Further reading on laser absorption and fast electron conversion efficiency can be found in a recent review by Davies [100].

2.5.5 Fast electron temperature

The population of fast electrons are accelerated across the critical density into the overdense target with some fraction of the laser energy $\eta_{L\rightarrow e}$. As discussed in Section 2.5.6, a Maxwellian distribution of fast electron energies will be created, the mean energy of the distribution is termed the fast electron temperature k_BT_f. This is a key defining parameter and has been the subject of much work. The scaling for k_BT_f has been found to increase with the laser intensity or more precisely the laser irradiances $I_L\lambda_L^2$. An irradiance $I_L\lambda_L^2$ of 1.37×10^{18} W/cm$^2\mu$m^2 corresponds to the onset of the relativistic regime: the electron motion in the laser field gains a velocity close to the speed of light.

A number of predicted scalings are shown in Table 2.2 derived from experimental, numerical and pure theoretical calculations. The relativistic transition near $I_L\lambda_L^2 > 10^{18}$ W/cm$^2\mu$m^2 separates the scalings into two groups.

The $\mathbf{j} \times \mathbf{B}$ or Wilks [73] scaling applies to the relativistic regime for electrons accelerated by a normally incident laser pulse and results in $k_BT_f \propto [I_L\lambda_L^2]^{1/2}$. The Haines scaling is derived analytically assuming that the electrons interact with the driving fields of the laser for only a fraction of a cycle [101]. At lower laser intensities other scalings can be considered and vary with $[I_L\lambda_L^2]^{1/3}$ as is the case for resonance absorption [102] . The Gibbon scaling is derived from PIC simulations for a steep density gradient relevant to vacuum-heating [79, 103].

Direct measurements of fast electron temperature, as mentioned earlier, are limited to the escaping high energy tail of the spectrum. Indirect measurements, such as x-ray, γ-ray or optical emission, infer k_BT_f through a transport model. A single experimentally derived scaling is included in this list derived by Beg *et al* [104]. This scaling was obtained by measuring bremsstralung γ-ray emission.

Below $I_L \approx 10^{19}$ W/cm^2 the fast electron temperature was found to scale with $[I_L\lambda_L^2]^{1/3}$. Increasing the intensity into the relativistic regime appears to switch 'on' an acceleration mechanism with an accompanying shift in the acceleration acclamation direction [85]. This mechanism has been identified as the relativistic ponderomotive force resulting in a fast electron temperature defined using the Wilks scaling [84]. Brandl *et al* [105] found that the measured temperature of the laser axis population scales as $[I_L\lambda_L^2]^{1/2}$, while the fast electrons directed along target normal scales according to $[I_L\lambda_L^2]^{1/3}$. Certainly above 10^{19} W/cm^2 it is generally believed that the ponderomotive force described by the Wilks scaling [73] becomes the dominant acceleration mechanism.

Scaling	Type	$I_L\lambda_L^2$	L_s/λ_L	θ_L	k_BT_f [keV]
Resonance [102]	S	$< 10^{17}$	> 1	θ_R	$14[k_BT_eI_{16}\lambda_{\mu m}^2]^{1/3}$
Brunel [78]	T	$> 10^{17}$	< 1	73°	$3.7[I_{16}\lambda_{\mu m}^2]$
Gibbon [79]	S	$< 10^{17}$	≤ 0.1	45°	$7[I_{16}\lambda_{\mu m}^2]^{1/3}$
Beg [104]	E	$< 10^{19}$	> 1	30°	$215[I_{18}\lambda_{\mu m}^2]^{1/3}$
Haines [101]	T	$> 10^{18}$	-	-	$511[(1+(I_{18}\lambda_{\mu m}^2)^{1/2})^{1/2}-1]$
Wilks $\mathbf{j}\times\mathbf{B}$ [73]	S	$> 10^{18}$	~ 1	0°	$511[(1+0.73I_{18}\lambda_{\mu m}^2)^{1/2}-1]$

TABLE 2.2: Scaling of fast electron temperature, k_BT_f, derived using a number of approaches involving simulations (S), experiments (E) and analytical theory (T). The relevant scale length (L_s), irradiance [Wμm^2/cm^2] and laser incident angle are shown.

The scaling of k_BT_f with $I_L\lambda_L^2$ is shown in Figure 2.9, with both theoretical predictions and experimental measurements. Given that the data is shown on log-log axes, the scatter between points is relatively large. The blue-circle points are measurements which represent a large body of work reviewed by Schollmeier [106]. In general, the laser conditions here span intensities $I_L = [10^{17} - 10^{20}]$ W/cm^2, wavelengths $\lambda_L = [0.248 - 1.064]$ μm, and angles from 0° up to 45° for s- and p-polarised incidence. The contrast ratio of the prepulse level to main pulse was stated as 10^{-6} or better. A set of data from Tanimoto *et al* [107] derived from electron spectrometer measurements on the Vulcan and GXII PW laser systems, extend the $I_L\lambda_L^2$ scaling near 10^{21} Wμm^2/cm^2. Since the direct measurements are limited to the small fraction of escaping electrons, the values of k_BT_f are assumed to be similar the bulk of the fast electrons trapped within the target. The overall trend of increasing k_BT_f with increasing $I_L\lambda_L^2$ is visible, and appears to fall between the Beg and ponderomotive scalings.

While k_BT_f is typically derived using the peak laser intensity with a given scaling law, Chen *et al* [99] reported that a single intensity parameter is too simplistic - the intensity distribution across the focal spot should be taken into account. Since the ponderomotive potential is a local effect, the electron spectrum should therefore be calculated such that the focal spot intensity distribution is considered.

With low contrast lasers, the greater levels of pre-plasma can lead to self-focusing of the laser shifting its intensity to higher values, see Sprangle *et al* [108] and references therein. Higher laser intensity at the critical surface inherently effects the absorption processes and therefore the fast electron temperature. In extreme cases, self-focusing can result in a filamentation of the laser beam potentially creating many absorption zones. In most experiments the plasma scale length near the critical surface is relatively unknown. However, if the contrast of the laser system is known accurately this enables the pre-plasma scale length to be inferred from hydrodynamical simulations. However, in most cases the intensity quoted is the nominal value irrespective of pre-plasma effects.

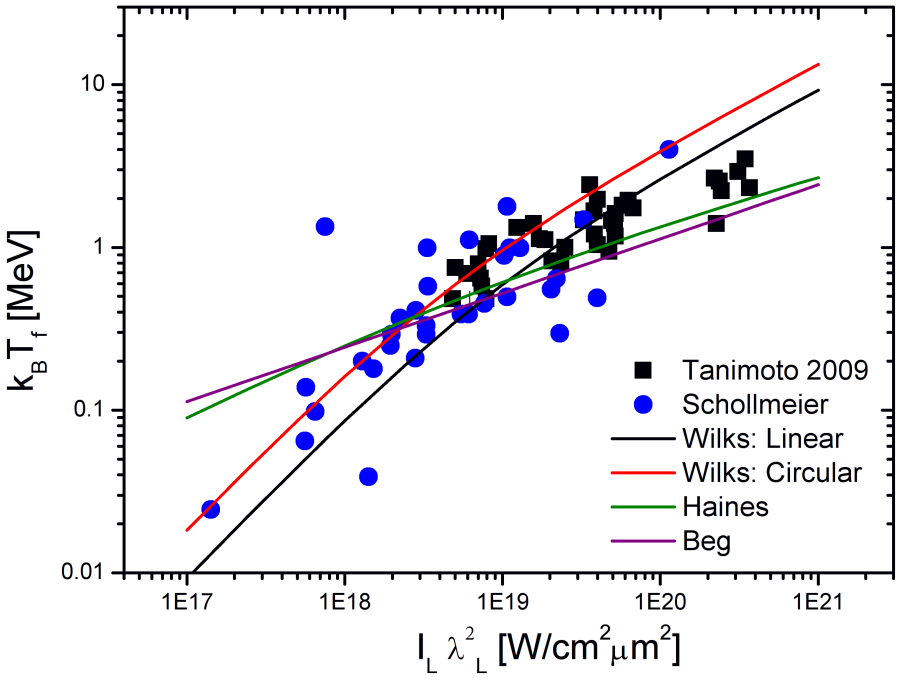

FIGURE 2.9: The scaling of fast electron temperature with irradiance, for theoretical predictions and measurements.

With higher laser intensities the ponderomotive force can push and compress the plasma to greater than critical density reducing the scale length [74]. Simulations by Chrisman *et al* [75] have shown that this profile steepening can reduce the $\mathbf{j} \times \mathbf{B}$ acceleration distance and hence the temperature of the fast electron spectrum by a factor of $\sqrt{\gamma n_c/n_s}$, where n_s is the density of the steepened shelf. This leads to a two-temperature component spectrum, a lower energy component $k_B T_f \sqrt{\gamma n_c/n_s}$ and a higher energy tail $k_B T_f$. For the conditions used by Chrisman *et al*, the modified scaling factor was $\sqrt{\gamma n_c/n_s} \approx 0.1$.

2.5.6 Fast electron spectrum

All the collisionless absorption mechanisms discussed in Section 2.5.3 will result in the coupling of a fraction of the laser energy to the super-heating of a population of plasma electrons to relativistic velocities. This population will have energies much higher than the initial bulk plasma temperature $k_B T_e$. The random or stochastic nature of the electron acceleration in the laser field results in fluctuations in their trajectories and hence their acquired energies. As pointed out by Bezzerides [109] the averaging of these single particle distributions over time evidently leads to a Maxwellian velocity distribution. A single temperature **Maxwellian** distribution can be defined as a function

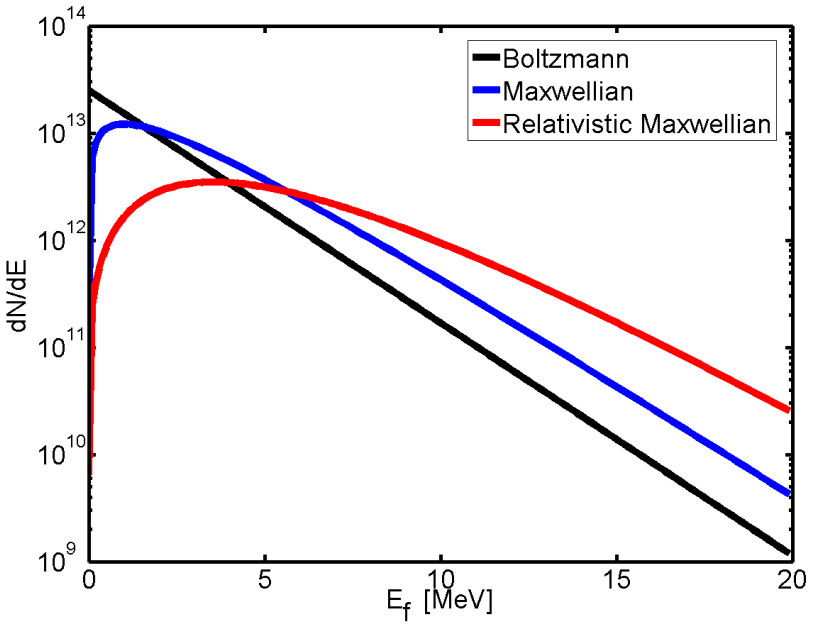

FIGURE 2.10: Initial fast electron energy spectrum calculated for $k_B T_f = 2\,\text{MeV}$ for three different distributions.

of fast electron energy, E_f, using the fast electron temperature $k_B T_f$:

$$f(E_f) = N_f \sqrt{\frac{4E_f}{\pi (k_B T_f)^3}} \exp(-\frac{E_f}{k_B T_f})$$

In reality the collective effects that influence the overall absorption can result in the departure from the pure single-temperature Maxwellian distribution. A bi-Maxwellian distributions can develop from such effects and multiple heating mechanism [79, 110]. As the plasma becomes hotter and $k_B T_f$ approaches or exceeds $m_e c^2$, the distribution in this relativistic Maxwellian regime is given by the **Maxwell-Juttner** distribution [111]:

$$f(\gamma) = N_f \frac{\gamma^2 \beta}{\frac{k_B T_f}{m_e c^2} K_2(m_e c^2 / k_B T_f)} \exp\left(-\gamma / \frac{k_B T_f}{m_e c^2}\right) \tag{2.60}$$

where $\beta = v/c$, $\gamma = \frac{1}{\sqrt{1-\beta^2}}$ and K_n is the modified Bessel function of the second kind of order n. The relative shape of both distributions is shown in Figure 2.10 in comparison with a standard Boltzmann exponential function. Both distributions integrate to N_f.

The distributions shown in Figure 2.10 are derived for $k_B T_f = 2\,\text{MeV}$ assuming $N_f = 5 \times 10^{13}$ electrons. The total number of electrons is dependant on the electron energy conversion efficiency $\eta_{L \to e}$ which is discussed in Section 2.5.4. The approximate value of N_f can be calculated using:

$$N_f = \frac{\eta_{L \to e} E_L}{k_B T_f} \tag{2.61}$$

The determination of both the number and temperature of the fast electron population poses one of the most important issues in short pulse laser interactions. The initial fast electron spectrum within the target remains relatively unknown. The distribution of fast electrons which manage to escape the target is directly measurable, typically with a magnet spectrometer sampling a small solid angle [87]. The fast electrons can escape during a brief temporal window until the electrostatic potential of the target exceeds the electron kinetic energy. Measurements by Yabuuchi [88] have inferred that the number of escaping population is also subject to the Alfven limit which is usually $\approx 1\%$ of the initial electron number, see Section 3.1. The exact relationship between the escaped and initial distribution is not presently understood. The characteristics of this population may not be representative of the larger distribution which are constrained within the target. The development of a coherent model of fast electron transport has yet to be achieved. Deriving the initial fast electron distribution may only be achievable through the combination of measurements from multiple diagnostics in order to benchmark the theoretical models.

2.5.7 Injection angle

The fast electrons, accelerated by the ponderomotive potential of the laser field, are directed into the overdense plasma at some angle relative to target normal defined as θ_e. The definition of this injection angle is distinct from the divergence angle, discussed in Section 3.4. Divergence angle, quoted as half-angle $\theta_{1/2}$, defines the lateral dispersion of the beam within the target and is a result of collective transport effects such as self generated magnetic fields in the over dense plasma.

The scattering angle of the fast electrons in the laser field determines the initial direction and dispersion of the beam into the overdense target. This can be considered for the case of a laser interaction with (i) free electrons in a vacuum and (ii) a solid target interface. Both cases are illustrated in Figure 2.11.

In the first case involving an underdense or tenuous plasma the electrons are directed by the Lorentz force, $[q(\mathbf{v} \times \mathbf{B})]$, and in the relativistic regime ($a_0 \geq 1$), they are scattered forward with an angle given by Moore *et al* [112]:

$$\theta_e(\gamma) = \tan^{-1}\left(\frac{p_\perp}{p_\parallel}\right) = \tan^{-1}\left(\sqrt{\frac{2}{\gamma - 1}}\right) \tag{2.62}$$

as shown in Figure 2.11(a). This can be a suitable approximation for short laser pulses propagating in underdense plasmas.

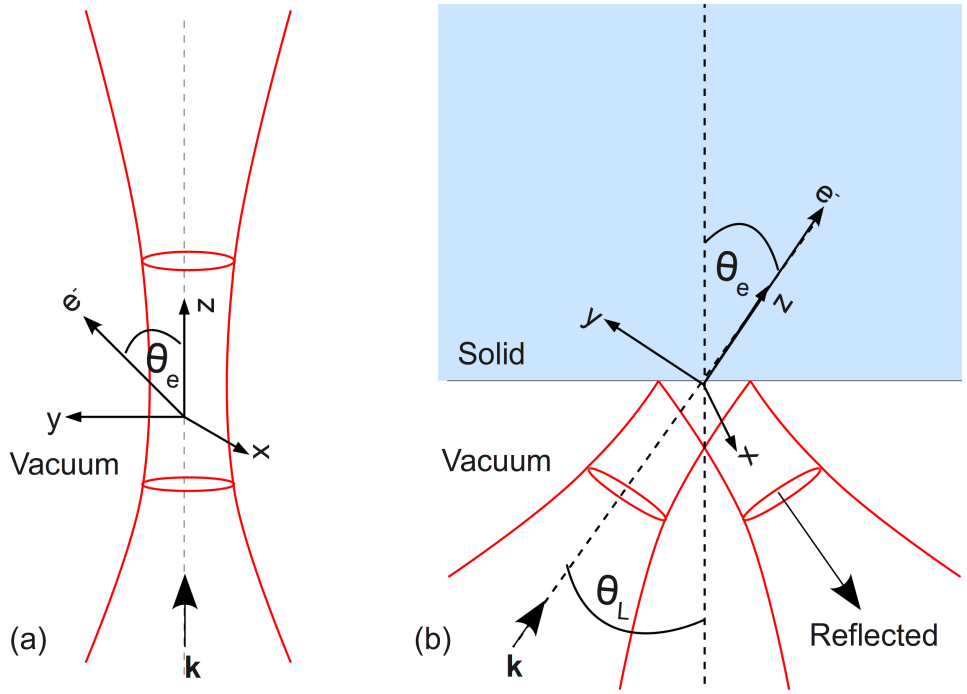

FIGURE 2.11: Injection of laser accelerated electron, e^-, in vacuum (a) and solid (b). Note the angle θ_e is defined relative to laser direction in (a) and target normal in (b).

However, the reflected laser wave is important at the interface of solid targets [113]. Sheng *et al* [114] derived a formula based on a planar laser field incident onto a solid target at angle θ_L which then specularly reflects. In this model a electrostatic field with potential Φ surrounds the target. The angular spread of individual electrons directed into the target is then related to their kinetic energy and the experienced change in the Coulomb potential $\delta\Phi$. The angular dispersion relation derived by Sheng includes momentum conservation by the reflected laser pulse. With fast electron energy in units of relativistic factor, γ, the injection angle relative to target normal is [114]:

$$\theta_e(\gamma) = \tan^{-1}\left(\pm[\frac{2(\gamma-1)(1+\delta\Phi)-\delta\Phi^2}{(\gamma-1-\delta\Phi)^2}\sin^{-2}(\theta_L)+\tan^{-2}(\theta_L)]^{-1/2}\right) \tag{2.63}$$

Note that electrons can be scattered forward into the target or back scattered away from the target surface. The Coulomb field tends to confine the injecting angles of energetic electrons close to the laser direction. Low energy electrons with $\gamma < 1+\delta\Phi$ are trapped or scattered to large angles by the Coulomb potential. Transport inhibition of low energy electrons, $E_e < 500\,\text{keV}$, can also occur due to magnetic fields at the critical surface as reported by Wei *et al* [115]. Higher energy electrons can escape at angles between $0° - \theta_L$ in the forward direction. The maximum value of $\delta\Phi$ was observed by Sheng [114] in PIC simulations to scale with laser intensity and absorption:

$$\delta\Phi_{max} \simeq \sqrt{\eta_{L\to e} a_0^2 t_0} \tag{2.64}$$

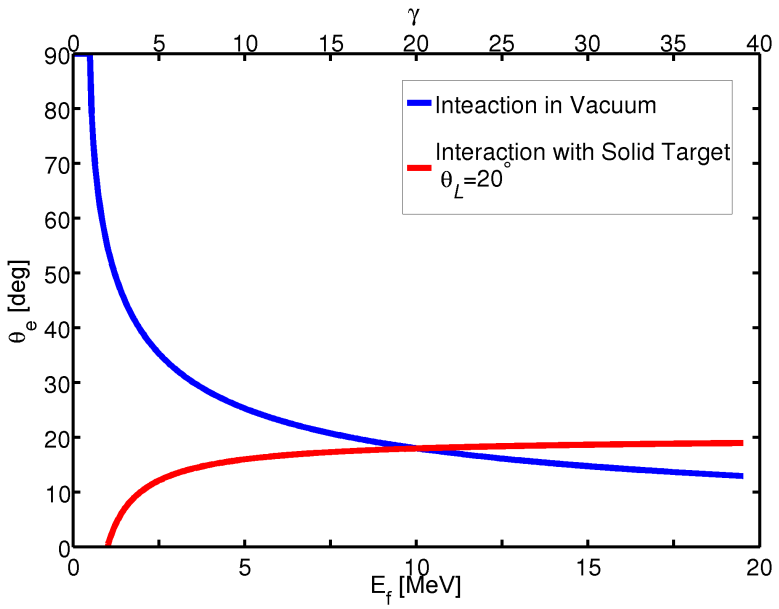

FIGURE 2.12: Predictions of injection angle of fast electrons as a function of fast electron energy calculated for a laser propagating (i) in a vacuum/tenuous plasma where θ_e is defined relative to laser direction using Equation 2.62 (ii) onto a solid target with incidence of 20° where θ_e is defined relative to target normal using Equation 2.63. In the latter case, low energy electrons are not injected due to the Coulomb potential at the target/vacuum boundary.

Here t_0 is the laser pulse length in units of 50 laser cycles. The injection angle is shown in Figure 2.11 for a laser incidence angle of $\theta_L = 20°$ and an intensity 2×10^{19} W/cm^2 where $\delta\Phi = 1$. The high energy electrons are directed along the laser axis, whereas the less energetic electrons spread out over a full hemisphere or remain trapped near the target surface by the Coulomb potential.

As shown in Figure 2.7, the injection of electrons along the laser axis direction is a key feature of ponderomotive acceleration, distinct from resonance/vacuum heating which direct along the target normal direction. Measurements providing direct experimental proof of this shift in beam directionality have been reported by both Santala [85] and Brandl [105] by $\gamma-$ray and Cerenkov radiation respectively .

The angular width of the injected beam - the divergence, is very sensitive to the electromagnetic fields at the injection region and the fast electron energy [116]. These fields are self-generated by the transport of the fast electrons over the critical surface and into the overdense target. Such collective and other collisional effects are discussed as part of a review of fast electron transport in the next chapter.

Chapter 3

Fast electron transport

The coupling of a significant fraction of the energy of an intense laser pulse ($I_L > 10^{19}\,\mathrm{W/cm^2}$) to a solid density plasma produces a pulse of electrons with kinetic energies vastly exceeding their rest mass $m_e c^2$. These relativistic or 'fast' electrons propagate into the overdense plasma and escape the influence of the laser field. Creating and transporting such a fast electron beam is currently the primary mechanism of coupling energy to spark the fusion burn in Fast Ignition. In this scenario the electrons must be transported over a few hundred microns to the compressed plasma core without much divergence of the beam. Here the energy deposition of MeV electrons will provide fast isochoric heating of the core to initiate the fusion reaction. In laser interactions with solid foils, the fast electrons can also couple energy to accelerate beams of ions from the surfaces of the target.

The transport of intense relativistic electron beams through dense plasma requires the investigation of a number of collective effects. These effects are induced by the transport of the beam which in turn act upon the beam itself, producing complex feed-back processes. Ultimately, these mechanisms can both hinder and assist the transport efficiency. These collective effects together with collisional interactions are discussed in this chapter. Acceleration of ions by the fast electron sheath fields are also discussed, this phenomena will be utilised as a diagnostic of fast electron transport in the experimental investigations discussed in the subsequent chapters.

3.1 Current Neutrality

The initial propagation of the fast electron current into the target is limited by its magnitude. To appreciate this, consider the absorption of 100 J of laser energy over a

1 ps pulse length into a distribution of fast electrons with $k_B T_f = 5\,\mathrm{MeV}$. The number of fast electrons produced can be estimated as $N_f = 100\,\mathrm{J}/5\,\mathrm{MeV} \approx 10^{14}$, which over the laser pulse length creates a fast current $I_f = 20\,\mathrm{MA}$. If such a current leaves the laser absorption region the charge separation field which develops could be sufficient to turn it back on itself.

This electric field is a function of the **current density** which in turn is a function of the density n_f and velocity $\mathbf{v}_f$ of the fast electrons:

$$\mathbf{j}_f = -e n_f \mathbf{v}_f \tag{3.1}$$

The volume containing N_f can be estimated as a cylinder of fast electrons with base and length equivalent to the laser spot and pulse length respectively: $V = \pi r_L^2 c\tau_L$. The fast electron density is then:

$$n_f = \frac{N_f}{\pi r_L^2 c\tau_L} \tag{3.2}$$

which for a laser spot diameter of $10\,\mu\mathrm{m}$ implies $n_f \approx 10^{27}\,/\mathrm{m}^3$. A relativistic electron beam travelling at velocity $\approx c$ would in this case produce $\mathbf{j}_f \approx 5 \times 10^{16}\mathrm{A/m}^2$. The ensuing **electric field** can be approximated in 1D as:

$$\partial \mathbf{E}/\partial t = -\mathbf{j}_f/\varepsilon_0 \tag{3.3}$$

which results in a magnitude of $\mathbf{E} \approx 10^{15}\,\mathrm{V/m}$. Consequently, no current would flow into the target and would instead be confined near the laser absorption region by this electric field. Another limitation is due to magnetic field effects that arises from charge separation. The **magnetic flux density** can be estimated using [92]:

$$\mathbf{B} = \frac{\mu_0 I_f}{2\pi r_L}\,[\mathrm{T}]$$

which for this example reaches a magnitude of $\mathbf{B} \approx 10^6\,\mathrm{T}$. Essentially, currents of this size cannot flow - the self-generated magnetic field is sufficiently strong to reverse the electron motion with respect to their initial propagation direction as first reasoned by Bennet [117]. This is the concept of the **Alfvén limit** [118, 119] which describes the maximum propagating current as:

$$I_A \simeq \frac{\beta\gamma m_e c^2}{e} = \beta\gamma\, 1.7 \times 10^4\,\mathrm{A} \tag{3.4}$$

The 20 MA fast electron beam greatly exceeds this limiting current ($I_A = 65\,\mathrm{kA}$) by a few orders of magnitude. To reveal how fast electron transport is indeed possible requires

the introduction of the **current balance** relation [92]:

$$\mathbf{j}_f + \mathbf{j}_r = 0 \tag{3.5}$$

This states that a **return current** ($\mathbf{j}_r$) must flow back to neutralise the fast current density and the inhibiting fields in the given volume [120]. An imbalance of 1% in **charge neutrality** would produce 10^{12} V/m electric field sufficient to halt the current within 1 μm.

The electrons which constitute the return current are sourced from the target material itself, either through the bound-electron conductivity or via ionisation. This is a key distinction of transport between insulator and conductor materials. The effectiveness of the neutralisation is limited by the resistivity of the material. For conductors, the charge neutralisation time is typically less than 1 fs, due to the large number of free electrons in metals [66]. Conversely for insulators, the free electron density is much less than the fast electron density and charge neutralisation will take much longer. In this case, the fast electron beam will need to ionise the material in order to provide the return current, a process which will dissipate the beam energy in working against the electrostatic field [66]. This results in stronger fields and a more inhibited motion, see Tikhonchuk [66] and Bell [92] for example. Significant differences in beam stability arise as a result which will be discussed as part of an investigation in Chapter 6.

The return current density needs to be **spatially localised** to balance the fast current density. This can be shown using an approach by Bell *et al* [121]. Consider the magnetic field generated by the current imbalance: a fast current moves in a cylinder of radius $r_f = 5\,\mu$m, the return current similarly flows in a slightly larger cylinder of $r_r = r_f + \Delta r$. Both carry the same current I, but in opposite directions. The magnetic field is then:

$$\mathbf{B} = \frac{\mu_0 I_f}{2\pi} \begin{cases} r(r_f^2 - r_r^2), & \text{if } r < r_f, \\ r^{-1} - r r_r^{-2}, & \text{if } r_f < r < r_r, \\ 0, & \text{if } r_f < r. \end{cases} \tag{3.6}$$

in the case of $\Delta r \ll r_f$, the peak magnetic field is:

$$B_0 = \frac{\mu_0 I_f (\Delta r / r_f)}{\pi r_f} \tag{3.7}$$

and upon integration the magnetic energy per unit length is:

$$E_B = \frac{\mu_0 I_f^2 (\Delta r / r_f)^2}{4\pi} \tag{3.8}$$

using the same values as before for $r_f = r_L = 5\,\mu$m and $I_f = 20\,$MA, the maximum magnetic field is $\approx 10^6(\Delta r/r_f)\,$T and the magnetic energy per length of cylinder is $40(\Delta r/r_f)^2\,$J/µm. The magnetic energy cannot be greater than the absorbed laser energy, so Δr must be much less than r_f for typical experimental parameters, even if all the absorbed energy is transferred to magnetic energy. This illustrates how the return current cannot follow a path much different from the fast electron current and must locally balance the fast electron current so that $\mathbf{j}_f \approx \mathbf{j}_r$.

The counter streaming nature of the forward and return currents can give rise to instabilities which can cause the beam to breakup via a number of different mechanisms. For instance, small perturbations in either current can lead to the generation of localized magnetic fields which can grow around the current perturbations and pinch them. Since counter propagating currents repel, the two sets of currents separate and filament, this process can evolve in a complex manner ultimately leading to a non uniform beam. The various guises of this phenomena are discussed in Section 3.3.

3.2 Magnetic field generation

The origin of the magnetic field is the curl[1] of the electric field, $\mathbf{E}$, required to draw the return current and hence is a function of the plasma resistivity, $\eta = \eta(x, y, z)$, [122]:

$$\mathbf{E} = \eta \mathbf{j}_r \tag{3.9}$$

$$\frac{\partial \mathbf{B}}{\partial t} = -\nabla \times \mathbf{E} = -\nabla \times (\eta \mathbf{j}_r) \tag{3.10}$$

$$\nabla \times \mathbf{B} = \mu_0(\mathbf{j}_f + \mathbf{j}_r) \tag{3.11}$$

The curl operator indicates that the $\mathbf{B}$-field will form a rotational field and will grow if perfect current neutralisation does not occur: $\mathbf{j}_f + \mathbf{j}_r \neq 0$. The resulting net current density will be $\nabla \times \mathbf{B}/\mu_0$, which is usually much smaller than both $\mathbf{j}_f$ and $\mathbf{j}_r$. The growth rate $\partial \mathbf{B}/\partial t$ can be defined in terms of $\mathbf{j}_f$ by combining the above equations:

$$\mathbf{j}_f + \mathbf{j}_r = \frac{\nabla \times \mathbf{B}}{\mu_0} \tag{3.12}$$

$$\Rightarrow \quad \mathbf{j}_r = \frac{\nabla \times \mathbf{B}}{\mu_0} - \mathbf{j}_f \tag{3.13}$$

$$\frac{\partial \mathbf{B}}{\partial t} = -\nabla \times \left(\frac{\eta}{\mu_0} \nabla \times \mathbf{B} - \eta \mathbf{j}_f \right) \tag{3.14}$$

$$\Rightarrow \quad \frac{\partial \mathbf{B}}{\partial t} = -\nabla \times \left(\frac{\eta}{\mu_0} \nabla \times \mathbf{B} \right) + \nabla \times (\eta \mathbf{j}_f) \tag{3.15}$$

[1] A non zero curl indicates the field has some rotational component.

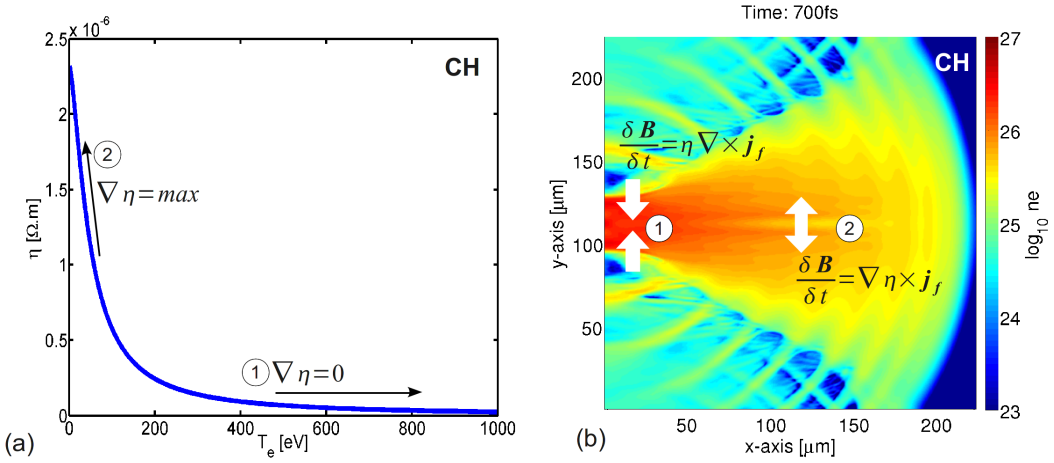

FIGURE 3.1: (a) The resistivity curve for solid plastic material CH; Spatial gradients within a plasma at high temperature tend to be uniform in terms of resistivity. This is reversed in cooler plasmas where the value of $\nabla\eta$ is greatest. (b) A simulation of fast electron transport in a plastic target; The effects of both magnetic field components on the fast electron density is shown: (1) pinching at the injection region ($\nabla\eta = 0$) and (2) beam hollowing midway through the target where the temperature is relatively cool ($\nabla\eta = \max$).

The first term on the right-hand side of Equation 3.15 represents the resistive diffusion of magnetic field through the target, defined by the diffusion coefficient η/μ_0. The second term is the source of magnetic field driven by the fast electron current. For a hot, highly ionised plasma the diffusion coefficient ≈ 1 and so the magnetic field equation reduces to:

$$\frac{\partial \mathbf{B}}{\partial t} = \nabla \times (\eta \mathbf{j}_f) \tag{3.16}$$

$$\Rightarrow \quad \frac{\partial \mathbf{B}}{\partial t} = \eta(\nabla \times \mathbf{j}_f) + \nabla\eta \times \mathbf{j}_f \tag{3.17}$$

which generates a magnetic field that acts to push the electrons towards regions of higher current density and also towards regions of higher resistivity [123].

Consider a beam of fast electrons propagating through a plasma, the beam is denser on-axis and less dense towards the edges. The magnetic field can grow out of spatial variations in either the current density or the resistivity. The strongest gradients are associated along the radial direction across the beam. Consequently the magnetic fields are predominantly **azimuthal**. The first magnetic field component, $\eta(\nabla \times \mathbf{j}_f)$, is generated by spatial gradients in the current density. A radial force is therefore exerted, $\mathbf{F} = -e\mathbf{v}_f \times \mathbf{B}$, directed towards the beam axis which can effectively **pinch the beam** reducing its divergence (also referred to as Z-pinch). This force can also act on smaller variations within the beam producing a transverse breakup of the beam. This phenomena is known as the resistive filamentation instability, see Section 3.3.

The second magnetic field source, $\nabla\eta \times \mathbf{j}_f$, arises from **resistivity gradients** in the background plasma. As before, for the electron beam travelling through the plasma, the current density is greatest along axis. This gradient in current density induces a similar temperature gradient of the background plasma which is greatest on-axis. The plasma resistivity evolves with temperature and hence a resistivity gradient develops across the beam. The direction of this gradient can be positive or negative depending on the material specific resistivity curve. For the case where higher temperature plasma is less resistive, the resistivity is minimised on-axis and increases outwards, opposite in effect to the current density gradient. The resulting magnetic field pushes the fast electrons outwards from the beam axis, effectively **hollowing the beam** [123, 124]. There is clearly a competition between the two components of Equation 3.17, both effects have roles to play over the life time of the electron beam. Usually the current gradient component is stronger. However, at the edge of the beam, where there is an appreciable temperature gradient, the current density is falling to zero and hence the pinching effect is negligible. If η changes very little over a temperature gradient than there will be no resistive component. This usually occurs at high plasma temperatures where the resistivity curve is quiet flat. This is typical at the injection region where the plasma temperature is greatest $k_B T_e \approx 1\,\mathrm{keV}$. Deeper within the target, the plasma is relatively cooler, and resistive gradients are present and beam hollowing may occur. An example of these competing effects are shown in Figure 3.1 for transport in a plastic target. In other materials, such as solid aluminium, the resistivity gradients are reversed at low temperature, which effectively provides another pinching component. Such increased levels of magnetic pinching can have significant effects relating to both beam divergence and beam filamentation, see results discussed in Chapters 5-6.

3.2.1 Magnetic pinching

Self induced collimation of the fast electron beam represents a tantalising possibility for shaping the constraints of Fast Ignition. Equation 3.17 provides in theory a self-generated magnetic field. This field is directed around the beam in a azimuthal fashion with the potential to indeed provide a **pinching force** to limit the beam's divergence. The strength of the magnetic field can be estimated from Equation 3.10,

$$\partial B \approx \frac{\eta j_f \partial t}{r_f} \tag{3.18}$$

and hence will exceed 1000 T at the injection zone where $r_f = r_L \approx 5\mu\mathrm{m}$ and $\partial t = \tau_L \approx 1\,\mathrm{ps}$. Obviously, if the beam spreads out, r_f will increase and the value of $\mathbf{j}_f$ will decrease resulting in a reduction in the strength of the pinching magnetic field. For

example, after propagating $100\,\mu$m, a beam diverging with half-angle $\theta_{1/2} = 25°$ will extend to $r_f \approx 50\,\mu$m and hence the magnetic field will drop by an order of magnitude. This is apparent in Figure 3.2 which shows a simulation exemplifying the strength of the magnetic field and its effect on the fast electron beam.

The specifics of whether self-induced collimation can occur were considered by Bell and Kingham [94], who showed that the magnetic field must be sufficiently strong to deflect fast electrons through an angle $\theta_{1/2}$ in the distance $r_f/\theta_{1/2}$ in which the beam radius doubles. For small $\theta_{1/2}$, the theory requires that the ratio of the beam radius to the gyro-radius (r_g), is:

$$\frac{r_f}{r_g} > \theta_{1/2}^2 \tag{3.19}$$

Using this condition a **collimation factor** (Γ) can be derived:

$$r_g = \frac{m_e v_f}{eB} \tag{3.20}$$

$$\Rightarrow \quad \frac{r_f}{r_g} = \frac{r_f eB}{\gamma m_e v_f} > \theta_{1/2}^2 \tag{3.21}$$

$$\Gamma = \frac{r_f eB}{\gamma m_e v_f \theta_{1/2}^2} \tag{3.22}$$

Collimation occurs for $\Gamma > 1$. As an example, for an electron beam with $k_B T_f = 5\,\text{MeV}$, with $\theta_{1/2} = 25°$, a magnetic field of $> 700\,T$ would be required for collimation. Assuming a resistivity of $2 \times 10^{-6}\,\Omega$m, the time needed to generate the field would be $r_f B/\eta j_f = 20\,$fs. Indeed these conditions are easily attainable at the injection region where the current density and hence magnetic field are greatest. The manner in which the magnetic field extends into the target interior is crucial if persistent collimation is to occur, otherwise the beam will diverge and begin spreading laterally once again. The general effect of such azimuthal magnetic fields acting upon the overall beam is termed **global pinching**, and is the subject of an investigation presented in Chapter 5.

The effect of pinching on the fast beam should be accounted for self-consistently, as any collimation will increase the fast electron current density, which will increase the rate of magnetic field generation, i.e. once initiated, collimation occurs with positive feedback. Detailed study does require sophisticated numerical simulation. An example is shown in Figure 3.2 for transport in a relatively thick aluminium target using a hybrid code called LEDA which is described in Section 4.4.2.

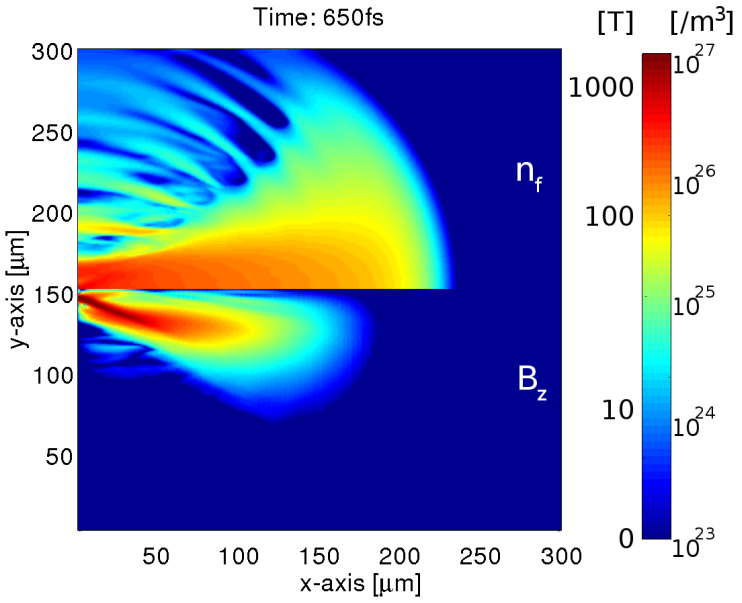

FIGURE 3.2: Simulation of fast electron transport in a aluminium target using LEDA. The fast electron density (n_f) and the self-generated azimuthal magnetic field (B_z) are shown at time 650 fs since laser incidence. The electron beam is injected from the left hand side and propagates along the x-direction. The magnetic field extends deep into the target and acts to collimate the electron beam.

3.3 Filamentation and instabilities

As discussed in Section 3.1, the propagation of the fast electron beam into the solid target is dependant on the availability of a neutralising return current. The fast electron beam cannot flow unconstrained or unperturbed. A variety of collective effects induce different instabilities. These instabilities are composed of longitudinal electrostatic and transverse electromagnetic modes that grow by extracting energy from the propagating electrons. The growth rate and spatial extent define each instability. Spatially, the development of various instabilities can be either microscopic (a scale less than the beam radius) or macroscopic (a scale of the order of the beam radius or larger).

3.3.1 Collisionless Weibel instability

This is also known as the electromagnetic filamentation instability, and is a transverse instability, which results in the radial breakup of the beam on a microscopic scale. The filamentation is produced by the magnetic repulsion between currents of opposite directions which reinforce any initial perturbation [125]. It tends to break the local current neutralisation of the incoming beam, by splitting it up in filaments. This modulation of the current density profile is accompanied by the creation of a similarly modulated electromagnetic field, accentuating the pinching of the filaments.

A representation of the instability mechanism is shown in Figure 3.3. The fast electron beam counter-propagates against the return current along the z-axis. The relatives densities are equal and initially homogeneous. The instability is **seeded** by an infinitesimal fluctuation in the magnetic field $\mathbf{B_y}(x) = B_0 \cos(\mathbf{k}x)$ which creates a force acting on the electrons $-e\mathbf{v} \times \mathbf{B_y}$ leading to inhomogeneities in the current density. The positive feedback provided by the current modulation increases the magnetic field which then results in stronger forces acting on the electrons. Ultimately, the modulations in the current density evolve into transverse filaments.

The filaments form on a time scale of the order of the plasma frequency of the beam, ω_{fe}, and on the spatial scale of the order of the plasma skin depth c/ω_{fe}. The **growth rate** of the Weibel instability depends on the beam contrast which is defined by the ratio (α) of the beam density n_f and the background plasma density n_e [126] :

$$\Gamma_w = \omega_{fe} \left(\frac{n_f}{\gamma n_e} \right)^{\frac{1}{2}} \times \frac{v_f}{c} \ [s]^{-1} \tag{3.23}$$

For typical solid density conditions, the beam density is typically $< 1\%$ of the plasma density, the growth of the Weibel instability occurs on a timescale of $\Gamma_w^{-1} \approx \omega_{fe}^{-1}$. This equates to a propagation length of the order of $10 - 100\,\mu$m. Such strong growth would significantly impair the transport of fast electron currents over long distances such as for the FI scheme

A number of numerical and theoretical studies have found that increasing the transverse beam temperature can help mitigate the instability by suppressing its growth rate and helping to stabilise the beam [127, 128]. A threshold was derived by Silva [128] using a relativistic kinetic theory. The collisionless Weibel instability will grow so long as the local pinching force is greater than the outward transverse pressure of the beam:

$$\frac{n_f}{n_e} > \gamma \left(\frac{\mathbf{p}_\perp}{\mathbf{p}_{||}} \right)^2 \tag{3.24}$$

For the range of parameters relevant for Fast Ignition, Silva concluded that the perpendicular temperature of the beam would stabilise the Weibel instability, with negligible energy loss from the beam to the magnetic field. Evans [127, 129] extended this stabilisation expression to include the effects of angular scattering such that:

$$\frac{\gamma \nu_\perp t}{\alpha \beta^2} > 1 \tag{3.25}$$

Sufficient increase in transverse beam temperature, acquired through beam plasma collisions with frequency ($\nu_\perp$) over a time ($t \approx \Gamma_w^{-1}$), can potentially stabilise Weibel induced filamentation. Here $\nu_\perp t$ is proportional to Z^2 and can be calculated using the formula

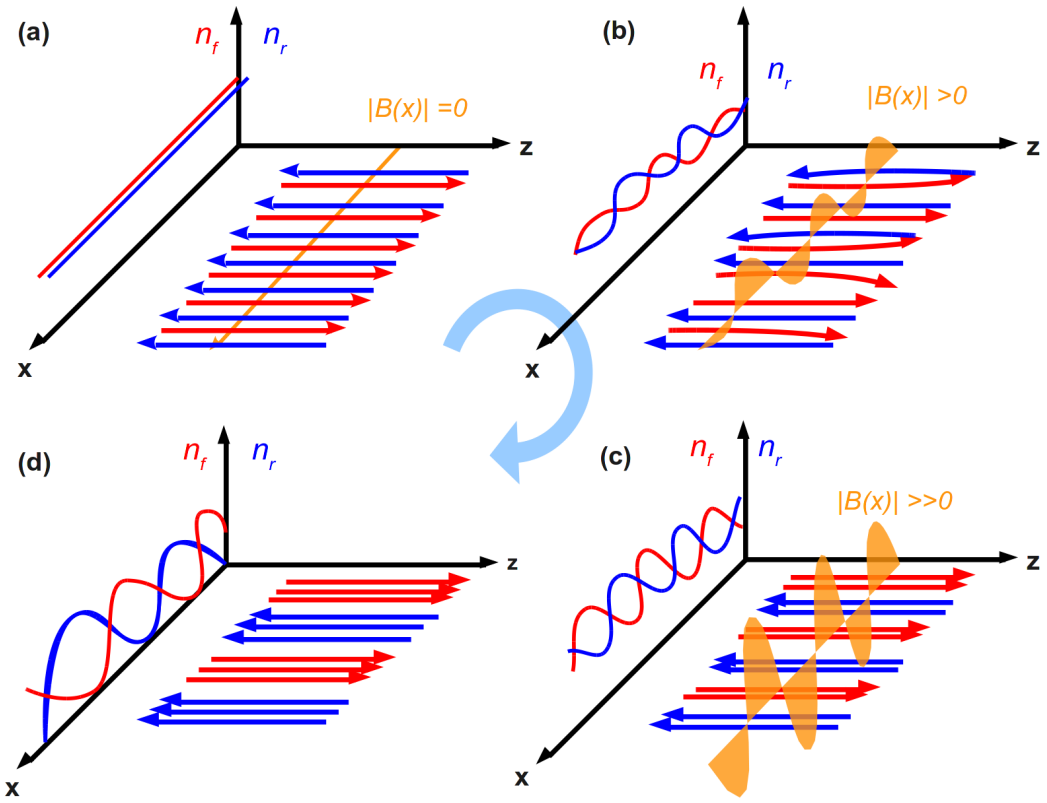

FIGURE 3.3: Illustration of the development of Weibel instability involving two counter-propagating electron beams with densities n_f and n_r (a). Small fluctuations in either density will induce a transverse magnetic field, B, which can locally pinch both currents with opposite forces (b). Once seeded the field can grow by positive feedback (c) leading to beam filamentation (d).

for angular scattering $\langle \Delta\theta^2 \rangle$ derived by Davies *et al* [52, 127]:

$$\langle \Delta\theta^2 \rangle = \left(\frac{Z^2 n_e e^4}{2\pi\varepsilon_0^2} \frac{\gamma m_e}{\mathbf{p}^3} \log \Lambda \right) t = \nu_\perp t \tag{3.26}$$

The dependence on Z^2 means that the instability is expected to be suppressed in moderate or higher Z materials such as aluminium. Conversely in low Z materials, such as plastic and lithium, which induce lower rates of scattering, the Weibel instability is predicted to be evident [127]. An investigation reported in this thesis has experimentally tested this hypothesis, see Chapter 6.

The dynamic interaction between the co-propagating currents can force the fast electron filaments to merge or coalesce [130]. This coalescence of filaments represents a major energy loss mechanism. The merging of two filaments, each carrying an Alfvén current, produces an overall filament that must itself be Alfvén current limited. At least 50% of the energy contained in the original filaments is lost during the process [130]. This abrupt loss of energy, transferred to the background plasma, is a signature of **anomalous stopping**. Filamentation and coalescence have been observed in a number of numerical

investigations using particle-in-cell codes [75, 116, 130–133].

Another consequence of the collisionless Weibel instability are its effects on the electron beam angular divergence. As the counter streaming currents separate, the magnetic neutralisation disappears and the filaments can no longer support the fast current they initially carried. Electrons are deflected from the filament by the magnetic fields, and an initially collimated beam may become more divergent [116]. This topic is discussed in Section 3.4.

3.3.2 Resistive filamentation

This is an extension of the Weibel instability in the case of a collisional return current. Similarly, the instability derives from the magnetic repulsion of counter-propagating electron currents. The magnetic fields which drive the instability derive from this resistive background plasma. The magnetic field can grow out of spatial variations in the current density $\eta(\nabla \times \mathbf{j}_f)$ see Equation 3.17. The typical time of magnetic field generation within a hot filament of radius r_F scales with the magnetic **diffusion time**:

$$\tau_d = \frac{\mu_0 r_F^2}{\eta} \tag{3.27}$$

The growth rate increases with plasma resistivity since the magnetic fields are stronger and penetrate further. This magnetic force acts on small variations within the beam producing a transverse breakup of the beam. The perturbations in the current are pinched until the inwardly directed magnetic pressure is balanced by an outward thermal pressure that is associated with the beam temperature $k_B T_f$, producing filaments within a spatial scale corresponding to the Bennett radius [117, 134]:

$$r_F = 2\sqrt{\gamma}\left(\frac{\mathbf{v}_{th}}{\mathbf{v}_f}\right)\left(\frac{c}{\omega_{fe}}\right) \tag{3.28}$$

Here, $\mathbf{v}_{th} = \sqrt{2k_B T_f / m_e}$ is the thermal velocity of the beam travelling with Lorentz factor γ and velocity $\mathbf{v}_f$, the c/ω_{fe}, factor represents the **magnetic skin depth**. The diffusion time dependence of r_F^2 indicates a sensitivity to small density perturbations across the beam. For a resistivity of $10^{-6}\,\Omega$m, a filament radius of $5\,\mu$m results in a diffusion time of $\approx 6\,$ps, whereas a smaller perturbation of $r_F = 1\,\mu$m results in faster growth time of 0.25 ps. This initial perturbation will seed the filamentation. In numerical studies this can be a transverse modulation in the background ion density [135] or the beam density [134]. The numerical study carried out by Gremillet showed resistive filamentation after propagating $10\,\mu$m in silica. The width of these resistive filaments ranged from $1-5\,\mu$m wide carrying approximately 10^5 A of fast electrons, comparable to

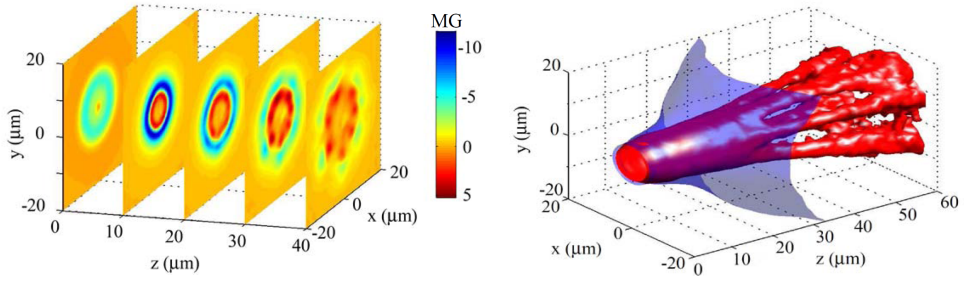

FIGURE 3.4: 3D simulations of the resistive filamentation instability from Storm *et al* [136]; (a) Cross sections through the azimuthal magnetic field for a 60 μm target, 350 fs after the peak of the laser pulse. (b) Fast-electron-density iso-surface at 50% of the peak density in each transverse plane, 350 fs after the peak of the laser pulse (red) and the iso-surface with the magnetic field artificially suppressed (blue).

the Alfvén limit. Other work by Storm *et al* [136] using the hybrid code LSP, shown in Figure 3.4, indicated simultaneous effects of resistively driven collimation and filamentation acting across the beam. Here the simulation results show that global pinching, acting transversely across the beam, can potentially suppress the local resistive filamentation. The effects of magnetic collimation and resistive filamentation is discussed as part of the investigation reported in Chapter 6.

3.3.3 The ionisation instability

In metal targets, the neutralisation current is provided by the free electrons in a time $\tau_n = \varepsilon_0 \eta < 0.1$ fs. In insulator targets, ionisation is required to provide the electrons for the return current. Perturbations in the ionisation rate along the front of the beam have been shown to develop as an instability which induces a rippling or corrugation of the beam, see the work of Krasheninnikov [137] and Debayle *et al* [138].

The charge separation at the head of the propagating electron beam produces a strong electrostatic field, which very rapidly ionises the material. This liberated cold current travels in the opposite direction, and continues the ionisation process by electron-atom collisions. The velocity along the **ionisation front** increases with the electron beam local density. This enhances small corrugations of the ionisation front which grow in time creating an instability [137]. The growth rate is relatively weak, $10^{12} - 10^{13}$ /s and depends strongly on the target ionisation potential. The front corrugation can be amplified by magnetic pinching effects along the front, creating positive feedback for the instability, increasing the instability growth rate to 10^{14} /s, which is comparable to the resistive and Weibel instabilities. A analytical study carried out by Debayle, characterised its dependence on the fast beam density and energy [138]. For a beam with a current density of $\approx 10^{15}$ A/m^2 and an electron energy of 5 MeV, the model predicted a breakup of the beam front into 5 μm wide filaments after 100 μm of propagation [138].

3.3.4 Measurements of beam filamentation

The calculation of ionisation and material break down is computational intensive and as such is not implicit in most numerical codes [139]. Simulations are performed with materials which are in pre-ionised state and hence the majority of electron transport modeling does not yet include ionisation instabilities. Distinguishing the dominant instability mechanism remains an open question.

Experimental measurements of beam instabilities can provide some clarity on their relative development. A number of indirect diagnostic approaches have been employed: optical [136] and proton emission [140] from the rear surface and K_α imaging from buried layers [141]. A sample of such measurements is shown in Figure 3.5 for conductor and insulator materials. In general, materials such as glass or plastic produce the most prominent features characteristic of beam filamentation.

The transverse spatial scale of the instability has been inferred from such images. It is apparent that in relatively thin targets, as shown in Figure 3.5(a), there are indications of filamentation for both conductor and insulator materials. Filamentation over such short spatial scales is indicative of the Weibel instability. Moreover, refluxing is especially pronounced in thin targets and could fragment the on-coming beam. This would not influence transition radiation measurements, which in theory diagnoses those initial escaping electrons before the onset of refluxing. Such is the case for Figure 3.5(a) indicating the occurrence of both filamentation and hollowing of the beam in thin conductor foils reported by Storm *et al* [136]. The transverse size of the filaments are within the micron range predicted by theoretical modelling.

Jung *et al* [126] reported on measurements of electron transport through thick albeit low density foam targets. In this case the material was pre-ionised by a radiation wave thus minimising possible ionisation instability growth. A ring-like beam comprising of many $10\,\mu$m size filaments were measured surrounded by a cloud of finer μm scale structure. The onset of filamentation was observed in PIC simulations after $10-20\,\mu$m coinciding with strong $3\,$kT magnetic fields. Imaging K_α emission measurements from buried layers have provided distinct signs of transport variations in conductors and insulator materials. In Figure 3.5(b) the spatial profile of transport in plastic is clearly filamented contrasting with that of aluminium [141]. The lateral extent of the respective beams also differ. This correlation between the collimation of the beam by magnetic pinching is examined as part of the investigation in Chapter 6 where instabilities were diagnosed using ion emission. The spatial profile of ion beams are directly sensitive to the rear surface electron sheath, and hence can diagnose the effects of instabilities for the bulk MeV electron population which can disrupt the sheath uniformity. This method

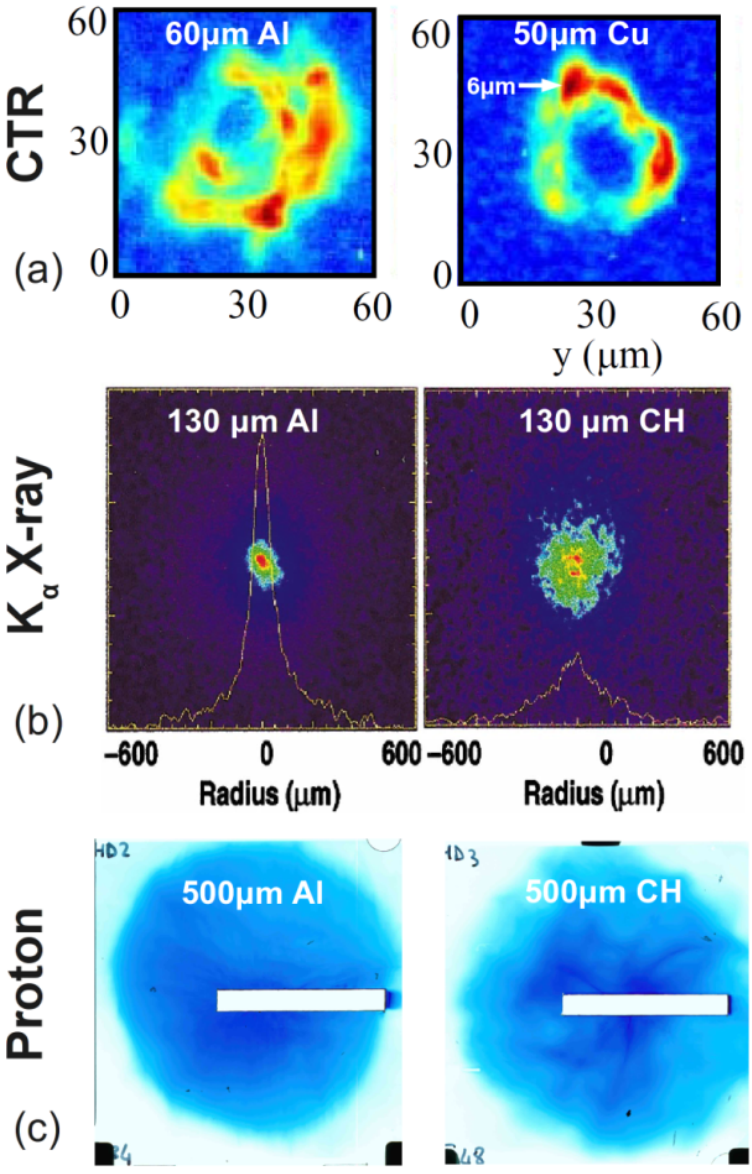

FIGURE 3.5: Diagnostic approaches of measuring transverse beam instabilities; (a) Coherent transition radiation [136] (b) K_α imaging [141] (c) Rear surface proton emission.

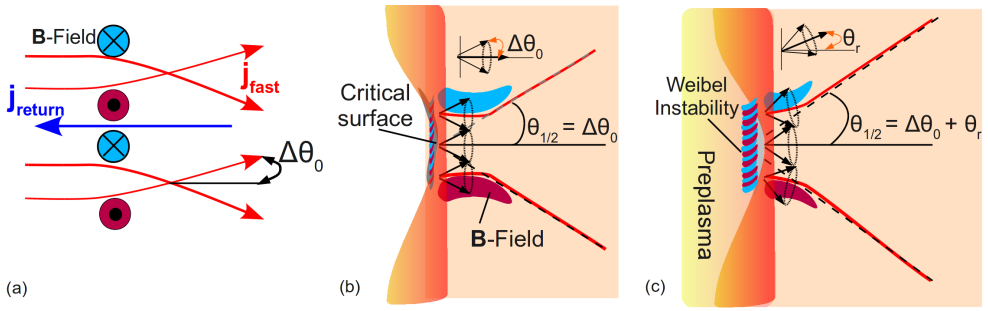

FIGURE 3.6: The initial divergence of the electron beam is a result of the scattering of electrons in magnetic fields of the Weibel instability near the critical surface; (a) This field deflects the electrons transversely. After leaving this area, the trajectories become stable, keeping the electrons at an angle of deviation. This angle depends on the energy of the electron. (b) After entering the overdense plasma, self induced collimation can mitigate the beam spread. (c) The presence of preplasma enhances the Weibel instability and also increases the plasma volume where electron acceleration occurs. These two effects combine to weaken the collimation magnetic field resulting a higher beam divergence.

remains effective even in very thick targets. In such conditions the instabilities appear to dominate for insulator materials, see Figure 3.5(c). The intense caustic structures for the case of CH material are nonuniform features of the electron sheath and are described further in Chapter 6.

3.4 Electron beam divergence

The fast electrons are injected with an initial angular distribution into the over dense target. As discussed in Section 2.5.7, the acceleration direction is predominately along the laser axis. Once the electrons are injected into the overdense target, they are then subject to a number of collective effects which dominate the angular spread of the beam. This angular spread defines the divergence of the beam.

Adam *et al* [116] correlated the initial divergence of the beam with the angular deflection of fast electrons in the magnetic fields generated by the Weibel instability in the under dense plasma. This was observed using 2D PIC simulations and occurs in a thin layer just behind the critical surface. The fast electrons are scattered in the fields with a **dispersion angle** $\Delta\theta_0$, see Figure 3.6(a). For a laser intensity $I_L = 10^{20}\,\mathrm{W/cm^2}$, it was shown that the fast electrons propagate into the overdense plasma without any further change of direction and are emitted in a cone with a half angle $\theta_{1/2} = \Delta\theta_0 \approx 20°$. Debayle et el [142] have recently published work which establishes a second component to the divergence angle: the **local mean propagation angle** θ_r. This depends on the transverse component of the laser ponderomotive force and therefore on the radial position. In a short density profile $\Delta\theta_0$ dominates the injection. After the critical surface,

the spread of the beam is constrained by the self-generated magnetic field which is strongest at the injection zone, see Figure 3.6(b). The presence of preplasma significantly changes the divergence of the beam. In this case the fast electrons can also be accelerated in the volume of the preplasma where the background density is lower than at the critical surface [116]. This condition increases the strength of the magnetic fields induced by an enhanced Weibel instability in the underdense region and as a result the fast electrons are scattered to larger angles as they transit across the critical surface. This can increase the total beam divergence when compared with a sharp density profile as illustrated in Figure 3.6(c). Debayle *et al* [142] make the point that such details are usually missing from electron transport modeling which may under-estimate the injection divergence and correspondingly the driver energy required for Fast Ignition.

3.4.1 Measurements of beam divergence

As a consequence of collective influences, it very likely that the divergence of the fast electron beam is not a fixed quantity either spatially or temporally. Theoretical models suggest that the beam divergence is governed by the interplay of magnetic collimation and the beam-plasma instabilities. The characteristics of the target material and the laser absorption conditions are primarily responsible for these collective effects. Consequently, the laser interaction with preplasma, transport field effects involving material resistivity and plasma heating need to be considered in appraising experimental investigations.

Measurements regarding beam divergence over the past decade are discussed in order of diagnostic to review the experimental tests of global magnetic pinching. The diagnostic methods include shadowgraphy, K_α and optical transition radiation imaging.

Shadowgraphic measurement

This method involves siphoning a fraction of the incident CPA laser beam to probe the target along the transverse direction. An edge-on shadow of plasma expansion, front and rear, is imaged providing both spatial and density data. The delay, relative to the laser incidence, can be varied to probe at different temporal points.

Tatarakis et al [143] imaged plasma expansion at both the front and rear surfaces of solid targets. At the front, a cone of plasma was observed with $\theta_{1/2} = 16^\circ$. At the rear, the size of the plasma sheath was measured after 22 ps relative to the laser incidence. Based on the lateral extent of the plasma sheath an argument was made suggesting magnetic collimation. For the conditions of this experiment the fast electrons would

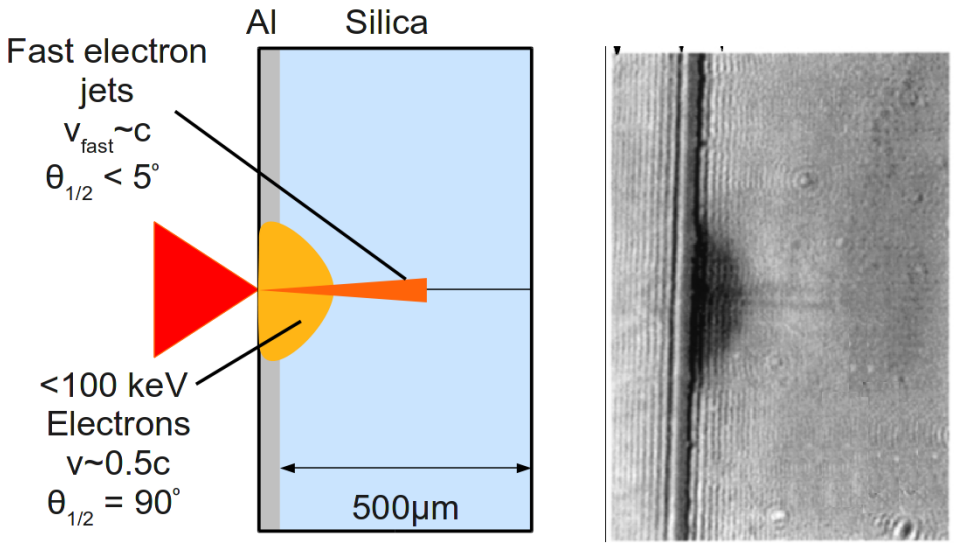

FIGURE 3.7: Fast electron transport inferred form shadowgraphic measurement of ionisation channels in transparent glass, 1.2 ps after laser incidence, from Gremillet *et al* [144]. The low energy keV component of the fast electron distribution spread over a 2π half-angle. The jets correspond to the hottest electrons which propagate along the direction of the laser at a velocity close to 3×10^8 m/s.

transverse the target in 0.5 ps. When the plasma expansion is measured at 22 ps the fast electrons will have transversed the target over 10 times due to refluxing. In this case the shadowgraphy imagery does not offer a definite measure of the initial beam divergence before refluxing and plasma expansion began occurring.

The work of Gremillet *et al* [144] differs in two respects: 1) The shadowgraphy probed at a much finer picosecond resolution; 2) The transport inside the target was probed. Observations of collimated jet-like ionisation tracks extending over 400 μm in transparent glass at picosecond intervals over multiple shots enabled a time sequence to be constructed and a relativistic propagation velocity was measured ($\approx c$). A slower spherical cloud extending from the focal spot into the target was also detected and identified as an ionisation front created from collisional interactions of slow electrons ($k_B T_f < 100\,\text{keV}$) with the bulk material. An example shadowgraphy image from this investigation is shown in Figure 3.7. Similar observations, albeit at lower laser intensity, have also been reported by Teng *et al* [145].

The work reported by Green *et al* [146] and Lancaster *et al* [147] also employed shadowgraphy and measured the expansion at the rear surface of thin targets (< 75 μm) after 200 ps from laser incidence. Over the sequence of targets a divergence of $\theta_{1/2} = 56°$ was measured. Since the plasma had been expanding for 200 ps and given the pronounced degree of refluxing occurring, very little can be concluded relating to the initial electron beam divergence and to testing magnetic collimation.

K_α measurements

A propagating beam of relativistic electrons can undergo collisions with the bound atomic electrons. Subsequent electron transitions between the atomic shells fluoresce emitting characteristic photons, e.g. for copper K_α emission, a 8.05 keV photon results from an L to K shell transition. This emission escapes the target and is imaged providing a magnified spot-like signal indicative of the time integrated emitting region. Careful interpretation of such spatial data is required since fast electrons can transit a typical target multiple times. As pointed out by Ovchinnikov *et al [148],* the K_α imaging measurements can often over-estimate the fast electron divergence.

Wharton *et al* [91] measured K_α emission from targets with a fluorescence layer at successive depths, $100-750\,\mu$m, to diagnose the beam divergence. This work was carried out using the NOVA laser. Consideration was given to removing the effects of refluxing on the fluorescence using 1 mm backing of CH. While not evident in thinner targets, tentative evidence for beaming, or collimation in thick targets was reported. However, the sizable error-bars prevented firm conclusions.

Similar methods were later employed by Stephans *et al* [141] with improved spatial resolution carried out using both Vulcan and LULI. This work provided measurements of K_α source size from a buried fluor layer at depths extending to $500\,\mu$m with Al and CH targets, some of which included a thick backing layer to remove refluxing effects. For aluminium, after a depth of $\approx 100\,\mu$m, the low energy fast electrons, $k_B T_f < 100$ keV, are stopped. The source size below $100\,\mu m$ was found to be relatively constant, which may indicate that the low energy electrons spread out in a hemispherical cloud as observed by Gremillet *et al* [144]. For the bulk population of electrons with energy > 100 keV a divergence half-angle of 27° was measured. Stephans *et al* quoted a value of 20° at thickness $> 200\,\mu$m, this corresponds to $k_B T_f > 200$ keV.

Divergence measurements, carried out using the Vulcan system, from both pure fluorescence targets and embedded layers were reported by Green *et al* [146] and Lancaster *et al* [147]. Laser conditions were distinct, with a longer pulse duration of $\tau_L = 5$ ps employed in Green *et al* resulting in $I_L \approx 4 \times 10^{19}\,\mathrm{W/cm^2}$, compared to $\tau_L = 0.5$ ps and an order of magnitude higher intensity used in Lancaster *et al.* The targets were relatively thin, $< 75\,\mu$m, metal foils and the results indicated a ballistic transport with constant divergence of $\theta_{1/2} \approx 17°$ and $\theta_{1/2} \approx 27°$ for Green and Lancaster respectively. However, there was no mitigation of the effects of refluxing on the data, which may be especially pronounced in the case of the longer pulse duration used in Green *et al* [146]. As the targets were limited to a thin range of thickness's, these results may not be effective

as a test of self-generated magnetic pinching. As discussed in Chapter 5, high levels of refluxing can potentially fragment and inhibit the fields responsible for global pinching.

Coherent transition radiation (CTR) measurements

This approach images the transition radiation created by the fastest electrons which manage to escape the target at the initial breakout at the rear surface. Hence, the effects of refluxing on the spatial distribution are avoided. The coherent bunching of the electrons must be preserved as they propagate to the rear surface resulting to a geometrical signature of fast-electrons crossing the target-vacuum boundary.

Santos *et al* [149] helped to pioneer this method, reporting measurements from Al targets up to 400 μm in thickness carried out using the LULI laser. The spread of the fast electron beam inside the target was constant at $\theta_{1/2} = 17°$. Jung *et al* [150], observed smaller divergence albeit for low density foam targets with $\rho = 0.1 - 0.2\,\mathrm{g/cm^3}$ and at higher laser intensity using the Vulcan laser. This is surprising since much weaker fields are generated in low density materials and a larger beam divergence would therefore be expected [151]. Differences in laser and pre-plasma conditions may also be a significant influence here. The filamented beam profiles were characterised with an inner and outer divergence of 5° and 10° respectively. Storm *et al* [136] reported on measurements that indicated both electron-beam filamentation and annular propagation with a constant 16° divergence half-angle. An additional step taken involved deriving an initial (injected) beam divergence from hybrid code simulations equal to 56° half-angle. The simulations reproduced the measured annular pattern and divergence. Magnetic collimation was inferred to explain the difference between the simulated initial and measured divergence.

Conclusions:

To summarise this body of work, the following conclusions can be drawn. The highest energy electrons have a characteristically low divergence $\theta_{1/2} < 20°$ [126, 136, 149]. The bulk distribution of electrons were shown to have slightly higher divergence $\theta_{1/2} \approx 20° - 27°$ [141]. These measurements are shown in Figure 3.8. In the case of low energy population, $k_B T_f < 100\,\mathrm{keV}$, there is evidence of large degree of scattering [141, 144] possible due to collisional effects and also via the magnetic fields associated with critical surface instabilities [116]. The argument for global magnetic pinching is somewhat tentative. An investigation using ion emission diagnostics, presented in Chapter 5 provides more conclusive evidence for global magnetic pinching.

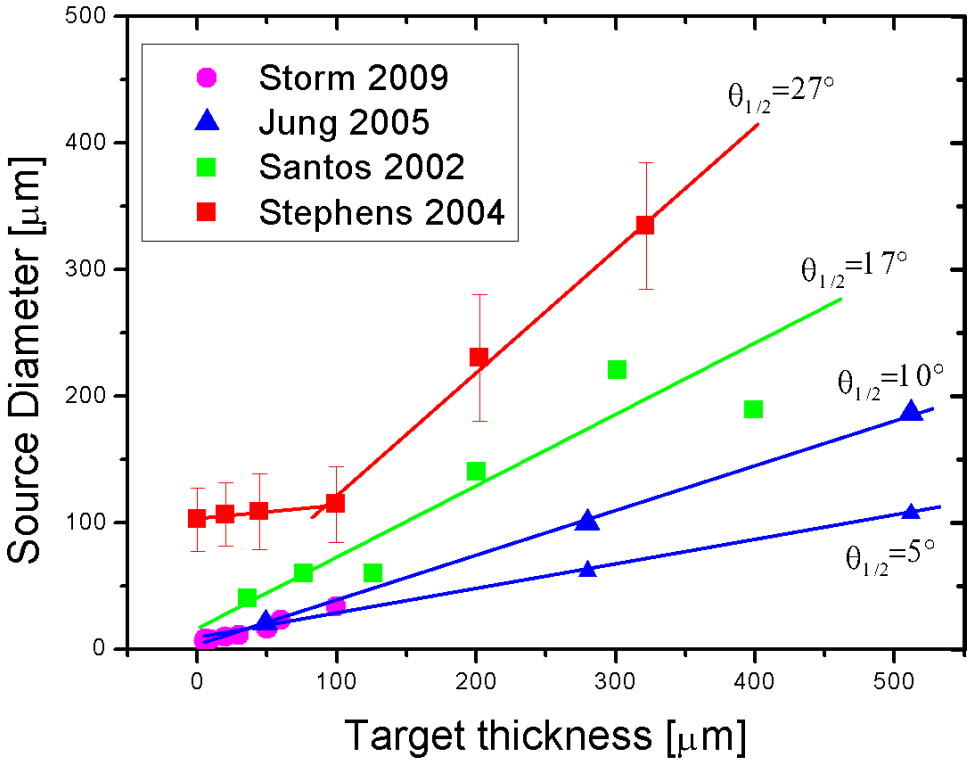

FIGURE 3.8: Measurements of source size FWHM for CTR emission from Santos [149], Jung [126], Storm [136] and x-ray K_α emission from buried copper layers in aluminium from Stephens [141]. The inferred electron beam divergence is shown for each set of measurements.

3.5 Collisions & Stopping

The propagation of the fast electron beam occurs in an initial cold target medium and hence is affected by collisions with the ions and electrons which constitute the background material. These interactions can be elastic or inelastic, leading to an angular deflection and a loss of energy of the electron beam. Inelastic interactions with atomic electrons are the principal mechanism responsible for collisional energy losses. The energy lost by fast electrons is transferred to the material in the form of excitation, ionisation or radiation emission via atomic transitions. Elastic collisions, on the other hand, take place with the ions where a small part of the primary electron energy is yielded to the atom as recoil energy without its state being affected. Due to the large difference in mass between electrons and ions, elastic collisions play a minor part in energy transfer and is several orders of magnitude lower than that in electron-electron collisions. However, elastic collisions contribute more to the angular diffusion of the electron beam.

To quantify this energy loss the concept of a stopping power dE/ds is used. This is a function of the incident electron energy and of the material characteristics, and takes into account the various mechanisms of energy exchange during collisions. In a

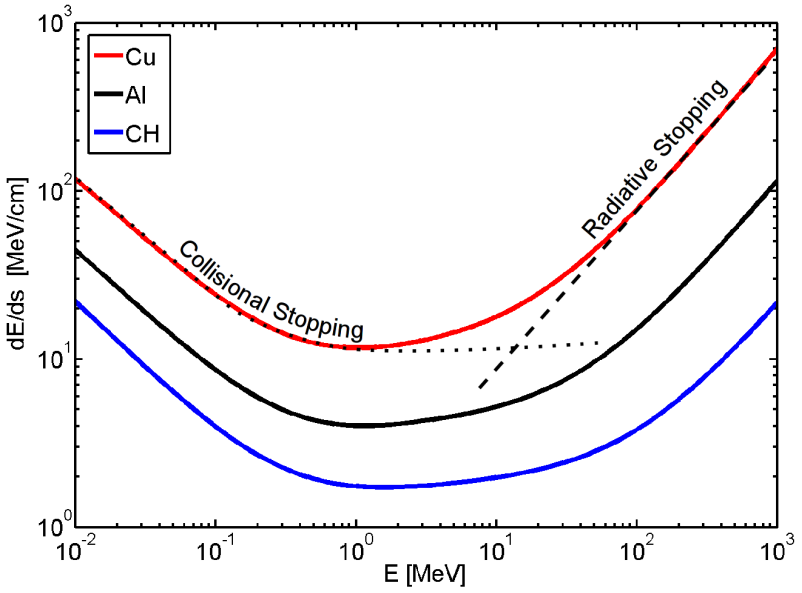

FIGURE 3.9: Stopping power for Cu, Al, and CH as a function of fast electron energy [152]. The collisional (dotted line) and radiative (dashed line) components are shown for the case of stopping power in Cu.

cold material, the total stopping power is the sum of the individual effects involving collisional/ionisation and radiative losses:

$$\left(\frac{dE}{ds}\right)_{total} = \left(\frac{dE}{ds}\right)_{coll} + \left(\frac{dE}{ds}\right)_{rad} \tag{3.29}$$

The radiation loss relates to bremsstrahlung emission due to the interaction with the nuclear electric field. This is important at high electron energies and for heavy or high Z elements such as gold or lead. For hot plasmas, the stopping also includes the effects of free electrons and plasmons or plasma wave excitation. The excess of free electrons and the increase in ionisation potential with higher temperatures means that ionisation stopping is reduced.

The stopping power for some example materials is shown in Figure 3.9. In these U-shaped curves, collisional losses dominate until the radiative component becomes apparent at higher energies $\gtrsim 10\,\text{MeV}$. The data is sourced from the estar stopping tables which are available from the NIST database online [152]. Here, the collisional component is calculated using the theory of Bethe [153, 154] with a density effect correction [155] involving the measured mean excitation energy of the material. The radiative component is derived using a combination of theoretical bremsstrahlung cross section [156], together with analytical formulas and accurate numerical results [157].

The total stopping can also be used to calculate the range using the continuous-slowing-down approximation (CSDA). This is a very close approximation to the average path

length travelled by a charged particle as it slows down to rest. The rate of energy loss at every point along the track is assumed to be equal to the total stopping power. Energy-loss fluctuations are neglected. The CSDA range is obtained by integrating the reciprocal of the total stopping power with respect to energy.

As an example, a 1 MeV electron will slow down with $dE/ds \approx 4\,\mathrm{MeV/cm}$ in Al, which translates to a range of around 2 mm. This is over an order of magnitude longer than the typical target thickness used in many electron transport experiments with solid targets. The fast electrons do propagate their full range; they are confined to reflux through the target until absorbed, this is investigated in Chapter 7.

3.6 Target Heating

The energy contained within the fast electron beam can dissipate and heat the background material via both direct collisions and by field generation losses which induces resistive heating via the return current.

As the background plasma temperature $k_B T_e$ increases, there will be a corresponding increase in the degree of ionisation, Z^*, and the plasma density $n_e = n_i Z^*$, of the respective material. An analytical model used to calculate Z^* was devised by More [158] based on the Thomas-Fermi theory of atomic electrons. The model formulae, which can be found in Appendix B, defines Z^* as a function of all densities and temperatures:

$$Z^* = Z\, f\left(\frac{k_B T_e}{Z^{4/3}}, \frac{\rho}{ZA}\right) \tag{3.30}$$

The solution for aluminium, $\rho = 2.7\,\mathrm{g/cm^3}$ and A=27, with an ion density of $n_i \approx 6\times10^{28}/\mathrm{m^3}$ is shown in Figure 3.10. The value of Z^* increases significantly after $\approx 10\,\mathrm{eV}$, and is almost fully ionised at 1 keV. At a few hundred eV, the plasma electron density would be expected to be $n_e \approx 5 \times 10^{29}\,/\mathrm{m^3}$.

Heating of the plasma modifies its resistivity, η, and hence the effects of electromagnetic fields will also change. The diffusion of the magnetic fields through the plasma defines the time scale of field induced heating:

$$\tau_d = \frac{r_f^2}{\eta \varepsilon_0 c^2} \tag{3.31}$$

In the case of aluminium, the resistivity varies as shown in Figure 2.3. Over the first few hundred eV, the mean value of η is $2 \times 10^{-6}\,\Omega\mathrm{m}$ and hence the diffusion time is $\approx 4\,\mathrm{ps}$. In the examples given below regarding plasma heating, the fast electron beam

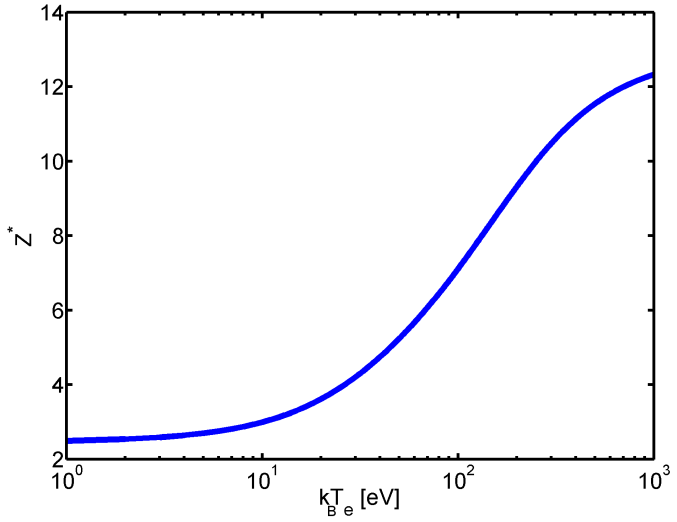

FIGURE 3.10: The degree of ionisation for solid density aluminium as a function of temperature calculated using the More model [158].

propagates as a cylinder with radius $r_f = 2.5\,\mu$m and with density $n_f = 10^{26}\,/\mathrm{m}^3$ at velocity $c\beta_f$ where $\beta_f = \mathbf{v}_f/c$.

Energy is deposited from the electron beam to the target material via a number of mechanisms. Direct energy loss can occur via collisions of fast electrons with the material atoms. The collisional stopping power, dE/ds, for a cold solid can be determined using the curves in Section 3.5. The energy lost, per unit length, to the plasma by collisions is [159]:

$$W_C = \pi r_f^2 n_f \beta_f c t \left(\frac{dE}{ds}\right) \tag{3.32}$$

The drawing of the return current, for current neutralisation, is the other main loss mechanism. First, energy is transferred to the electromotive magnetic field which slows down the beam. The fields then draw the return current, which is highly collisional and couples the field energy to the plasma by ohmic/resistive-heating. This can be estimated using the method employed by Gremillet [160] based on the Lovelace-Sudan model [161]. The energy lost by the fast electron beam $\mathbf{j}_f$ to the background plasma via the return current $\mathbf{j}_r$, is first coupled to the magnetic field. The power per unit length lost by a Gaussian beam to the field is [159]:

$$\frac{\partial W_f}{\partial t} = \int \mathbf{j}_f \cdot \mathbf{E} dA = \int \eta \mathbf{j}_f \mathbf{j}_r dA \tag{3.33}$$

Integrating further, to time t, gives the energy loss per unit length [160]:

$$W_f = \left(\frac{I_f}{c}\right)^2 \ln\left(1 + \frac{2t}{\tau_d}\right) \tag{3.34}$$

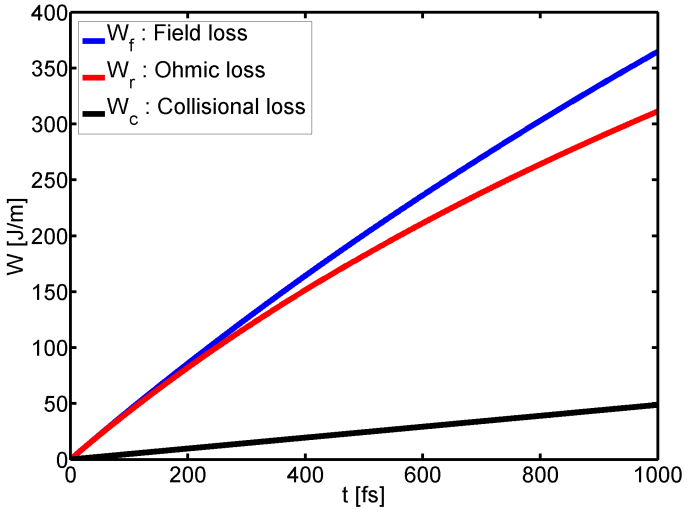

FIGURE 3.11: The energy loss mechanisms calculated for a 10 MeV electron beam in aluminium with $\eta = 2 \times 10^6\,\Omega$.m.

where the ratio of total beam current, $I_f/c = e\pi r_f^2 n_f \beta_f$, is calculated using cgs units. The energy transferred from the fields to the return current can be calculated by the integration of $\mathbf{j}_r \cdot \mathbf{E} = \eta \mathbf{j}_r^2$, and is given by [160]:

$$W_r = \frac{1}{2}\left(\frac{I_f}{c}\right)^2 \ln\left(1 + \frac{4t}{\tau_d}\right) < W_f \tag{3.35}$$

The energy loss for a 10 MeV electron beam in aluminium is shown in Figure 3.11 as a function of time. Compared to the resistive effects, the losses to collisions are minimum.

The transfer of this energy to the plasma will induce heating. This can be estimated by assuming the plasma is an ideal gas of free electrons $n_e = Z^* n_i$, and calculating the heating in a volume defined by the beam $V_f = \pi r_f^2 l_f$ [159, 160]:

$$\frac{3}{2} n_e k_B T_e V_f = W_{c,r} l_f \tag{3.36}$$

Solving for temperature $k_B T_e$, the heating of the background plasma can be estimated for both collisional ($k_B T_e^c$) and resistive ($k_B T_e^r$) effects:

$$k_B T_e^c = \frac{2 n_f \beta_f c t\ (dE/ds)}{3 n_e}\ \text{[eV]} \tag{3.37}$$

$$k_B T_e^r = \frac{2 W r}{3 n_e \pi r_L^2}\ \text{[eV]} \tag{3.38}$$

An example of collisional and ohmic heating for an aluminium target is shown in Figure 3.12. The ionisation state is calculated using the curve in Figure 3.10, and the heating effects are calculated using Equations 3.39 and 3.38 for a monoenergetic fast electron

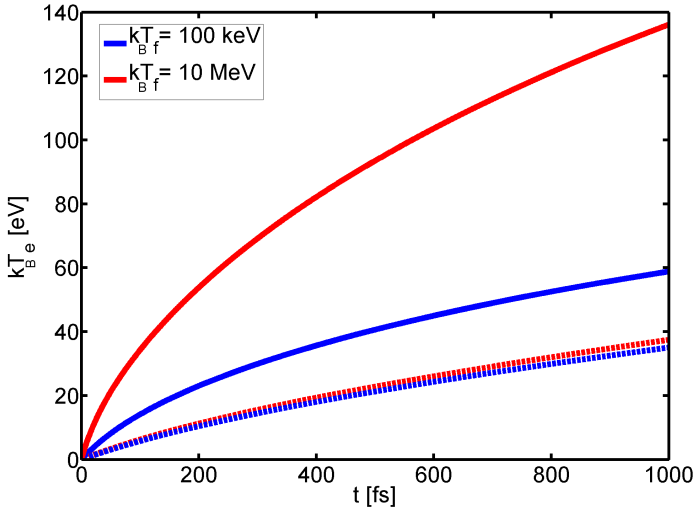

FIGURE 3.12: The heating of the background plasma by a monoenergetic fast electron beam with temperature $k_B T_f$ and density $10^{26}\,/\mathrm{m}^3$. The effects of two processes are shown: collisional heating (dashed lines) and ohmic or resistive heating (solid lines). [51]

beam for two different fast electron temperatures. Even though this simple model neglects other collective dynamics, such as instabilities, significant heating of up to a few hundred eV is achieved for petawatt laser conditions. The heating by resistive effects are considerable for relativistic electron beams ($k_B T_f > 0.5\,\mathrm{MeV}$) and exceed the collisional contribution. A more practical expression for resistive heating derived by Gremillet [160] states the relevant dependencies:

$$k_B T_e^r\,[\mathrm{eV}] \approx 400\beta_f^2 \left(\frac{Z^* n_i}{6\times 10^{22}/\mathrm{cm}^3}\right)^{-1} \left(\frac{n_f}{10^{20}/\mathrm{cm}^3}\right)^{2} \left(\frac{\eta}{10^{-6}\,\Omega\mathrm{m}}\right) \left(\frac{t}{500\,\mathrm{fs}}\right) \qquad (3.39)$$

Numerical simulations can provide a more sophisticated treatment. This is shown in Figure 3.13 using the LEDA code for an electron beam with a Maxwellian spectrum and mean temperature $k_B T_f = 10\,\mathrm{MeV}$. Here the heating is calculated self-consistently for the local density $\mathbf{j}_f$, electric fields and resistivity η for both aluminium and plastic materials. The background temperature ranges from $20 - 200\,\mathrm{eV}$ for the bulk of the target occupied by the beam and up to $\approx 1\,\mathrm{keV}$ at the injection region. In the case of CH, a transverse instability is evident. This contributes to higher localised heating as the filaments contain higher current density.

The confinement of fast electrons to the target will ultimately result in the full deposition of the beam energy into the plasma. If this occurs in a limited mass target, the resulting high energy densities can provide very high bulk temperature. Experimental measurements usually infer the bulk temperature through x-ray spectroscopy. Nilson *et al* [98] have reported peak temperatures of $\approx 200\,\mathrm{eV}$ determined using the ratio of the K_α/K_β

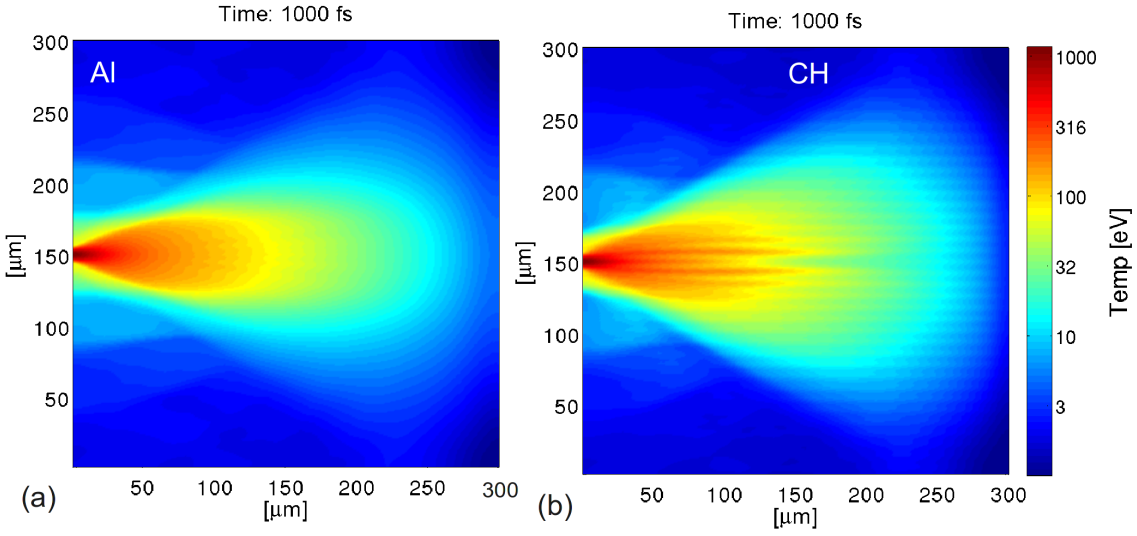

FIGURE 3.13: Simulation of fast electron transport in aluminium and plastic targets using the hybrid code LEDA. The heating of the background material is shown as a $\log_{10}$ color map at a time equal to 1 ps. The laser intensity is 5×10^{20} W/cm^2 with a 5 μm spot size.

line intensity. The maximum bulk temperatures measured to date are ≈ 1 keV [43] and are maintained for ≈ 20 ps. This measurement was performed by temporally imaging optical emission from the rear of 10 μm targets.

The interplay of plasma heating, resistivity and field generation on the fast electron beam is a significant and complex phenomena. The response of resistivity to plasma heating can in turn modify magnetic pinching and also transverse filamentation of the electron beam, as reported in Chapter 6. Other recent studies have shown that the pressure gradients induced by ohmic heating can cause cavitation of the background plasma [162]. A dynamic treatment of the plasma is therefore required [163] which is typically static in hybrid numerical models [164] such as LEDA [135]. Over timescales > 5 ps, Kingham *et al* [163] found that the dynamic motion of the heated background plasma by pressure gradients can effectively suppress the beam hollowing force, $\nabla\eta \times \mathbf{j}_f$, discussed in Section 3.2. This in turn permits the pinching force, $\eta(\nabla \times \mathbf{j}_f)$, to dominate which can greatly enhance the overall collimation of the fast electron beam.

3.7 Sheath fields & refluxing

After propagating through the target, the fast electron beam arrives at the rear surface with some angular spread that is energy dependant. A fraction of the overall population, those with the highest energy, can escape the target. This population is typically $\approx 1\%$ of the original fast electron population. On the escape of these fastest electrons the

target becomes electrically charged. The ensuing electric field is sufficiently strong to pull back the oncoming beam and reflect it back into the target. A similar reflection occurs at the front surface. Reflection at both surfaces confine the fast electrons to transit the target multiple times. This process is termed **refluxing**, and is discussed further as part of an experimental investigation in Chapter 7.

The 'fountain' effect created by the fast electrons crossing the target surfaces generates a large-scale azimuthal magnetic field [165]. This toroidal magnetic field induced at the target/vacuum boundary can spread the electrons over large transverse distances by a purely kinematic $\mathbf{E} \times \mathbf{B}_\theta$ force [166]. This surface spreading of fast electrons is termed **lateral transport** and has been measured experimentally by McKenna *et al* [167].

The sheath field at the target rear is quasi-static over the life-time of the fast electrons. An important implication of these sheath field effects is that the energy spectrum measured outside of the target maybe significantly altered from the original spectrum. For many experimental measurements, it is these escaping fastest electrons whose features are quoted to characterise the initial population created within the target. Hybrid PIC model analysis for a 30 fs laser pulse by Cottrill *et al* [168] have shown that the electrostatic field structure is strongly dependent on target geometry. As a result, the escaping distribution that is measured will largely depend on the shape and size of the targets being used.

The number of fast electrons that escape can be estimated by an analytical approach used by Myatt *et al* [97]. Here, the fraction of the electrons trapped by the electrostatic potential can be approximated by estimating the capacitance of the target. The target is assumed to be a perfectly conducting thin disk in vacuum. The capacitance of the target is:

$$C = 8\varepsilon_0 r \approx 70.8 \times 10^{-15}\, r_{\mathrm{mm}} \text{ [Farads]} \tag{3.40}$$

where r_{mm} is the radius of the disk in milli-meters. This is equivalent to the escape of a number of electrons from the target:

$$N_{escape} = 4.42 \times 10^{11} \cdot r_{\mathrm{mm}} \cdot V_{\mathrm{MV}} \tag{3.41}$$

that is required to produce a potential drop V [MV] in a target of radius r_{mm}. The required potential V is determined self-consistently, for a Boltzmann distribution of electrons with temperature $k_B T_f$, so that the potential satisfies:

$$N_{escape} = N_f \exp\left(-\frac{V}{k_B T_f}\right) \tag{3.42}$$

The fast electron temperature, $k_B T_f$, can be estimated using the ponderomotive scaling

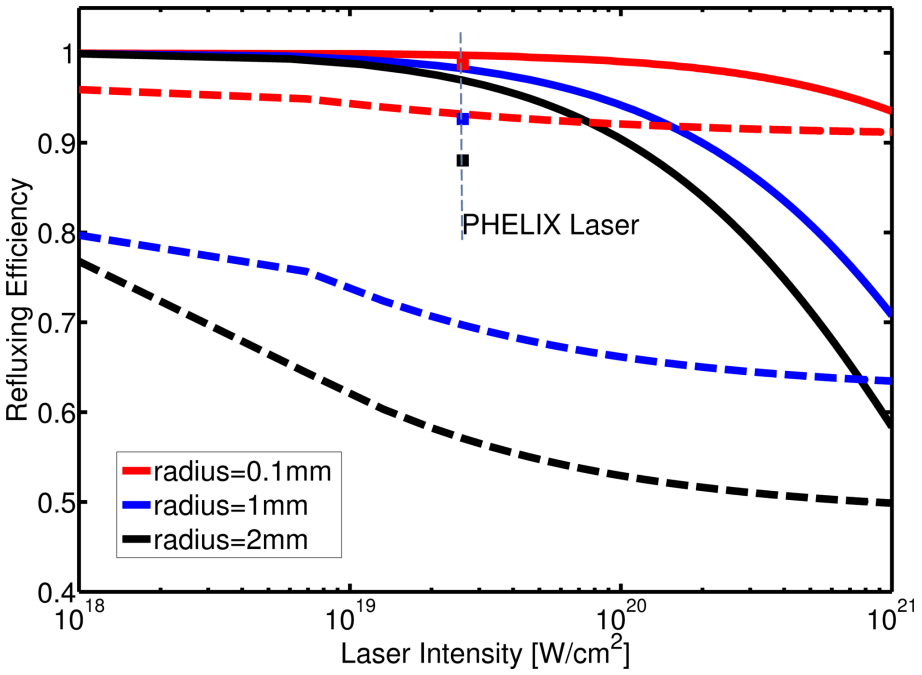

FIGURE 3.14: Refluxing efficiency versus laser intensity for different target sizes obtained from the capacitance model. The intensity is scaled with (i) constant $E_L = 300\,\mathrm{J}$ denoted by solid lines and (ii) variable E_L denoted by the dashed lines, both for a picosecond pulse length. The refluxing efficiency is sensitive to the total number of electrons produced which is proportional to E_L. An example for the PHELIX laser is shown as squares.

which is dependant on the laser irradiance. The laser energy, E_L, determines the number of fast electrons produced $N_f = \eta_{L\to e} E_L / k_B T_f$. Substituting the values for N_{escape} as defined previous in the capacitance Equation 3.41 and N_f into Equation 3.42 gives an expression involving the quantity κ:

$$N_{escape} = N_f \exp\left(-\frac{V}{k_B T_f}\right) = N_f \kappa \left(\frac{V}{k_B T_f}\right) \tag{3.43}$$

$$\kappa = 7.08 \times 10^{-2} \left(\frac{r_{\mathrm{mm}} k_B {T_f}^2}{\eta_{L\to e} E_L}\right) \tag{3.44}$$

$$\Phi = \frac{V}{k_B T_f} \tag{3.45}$$

$$\text{Solve for V}: \frac{\exp(-\Phi)}{\Phi} = \kappa \tag{3.46}$$

The value for κ is derived for units of MeV, J, and mm for $k_B T_f$, E_L and r_{mm} respectively. The laser-electron conversion efficiency used here is $\eta_{L\to e} = 20\%$. Solving for V gives the refluxing efficiency:

$$\eta_r = 1 - \exp\left(-\frac{V}{k_B T_f}\right) \tag{3.47}$$

The number of fast electrons trapped by the target potential is sensitive to the total number N_f and the target size r_{mm}. Examples values for η_r are shown in Figure 3.14, and are calculated for a number of target sizes. For the investigation discussed in Chapter 7, involving the PHELIX laser system, the model predicts that $\approx 95\%$ of the fast electrons

are constrained from escaping the target.

3.8 Target Normal Sheath Acceleration (TNSA)

The escape of the fastest electrons from the rear side of the target induces a strong electrostatic potential due to the charge separation in the vicinity of the target-vacuum boundary. As soon as the other fast electrons pass this boundary they are decelerated and pulled back into the target. This process creates an electron sheath which forms at the rear surface of the target. The thickness is defined by the typical excursion distance of fast electrons into vacuum before returning to the foil which is $\approx \lambda_D$, i.e. the fast electron Debye length $\propto (k_B T_f / n_f)^{1/2}$ (see Equation 2.4). The strength of the electric field associated with the sheath can first ionise and then accelerate ions from the rear surface to multiple MeV energies. A schematic of this acceleration mechanism is shown in Figure 3.15.

3.8.1 The Mora-Fuchs model

A number of sheath and ion beam properties can be estimated using an analytical model involving simple ballistic transport of fast electrons from the front to the rear target surface. This approach, devised by Fuchs *et al* [169], estimates the sheath density and ion acceleration time and then uses Mora's [25] formulae to calculate the maximum ion energy and spectrum.

The lateral size of the sheath can be estimated assuming a constant divergence, $\theta_{1/2}$, of the electron beam through the target of thickness d:

$$r_{sheath} = \phi_L/2 + d \tan\theta_{1/2} \tag{3.48}$$

$$S_A = \pi r_{sheath}^2 \tag{3.49}$$

An estimate of the fast electron density at the rear surface (neglecting refluxing) can be made using:

$$n_{f0} = \frac{\eta_{L\rightarrow e} E_L}{S_A c \tau_L k_B T_f} \tag{3.50}$$

To calculate the electric-field strength and hence the ion acceleration potential, the analytical model devised by Mora [25] can be used. This model begins with a 1-D space, with a target/vacuum boundary located in the centre where $x = 0$. The cold ions are initially at rest with density n_{i0} with a sharp cutoff to zero at the vacuum boundary. The fast electrons have density n_{f0} at the boundary and expand into the vacuum with

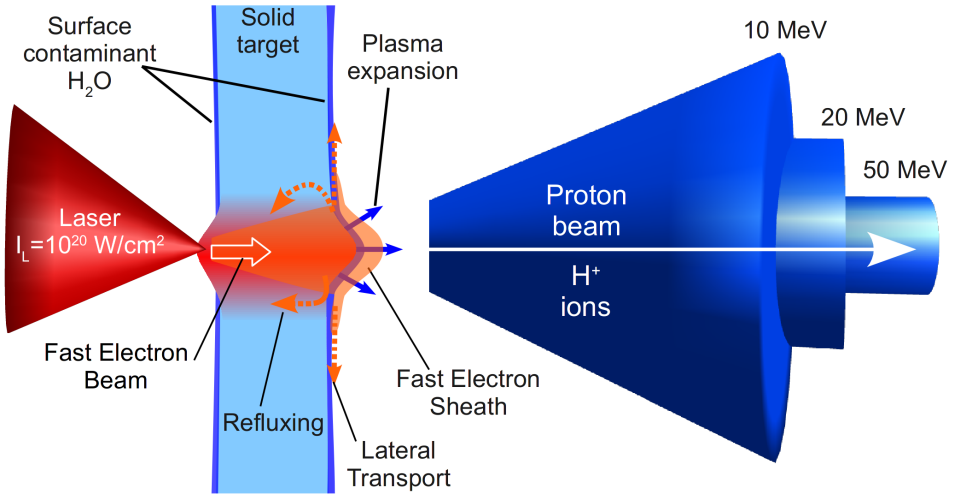

FIGURE 3.15: Acceleration of ions from the rear surface by a fast electron sheath field. The TV/m field and hence the ion acceleration is directed along target normal. The lighter hydrogen ions (H^+) are accelerated to multi-MeV energies. The ion beam divergence is energy dependant and is greater for lower energy ions.

a Boltzmann distribution assumed to be in LTE with its potential:

$$n_f(x) = n_{f0} \exp\left(\frac{e\Phi(x)}{k_B T_f}\right) \tag{3.51}$$

The electrostatic potential $\mathbf{\Phi}$ is generated as the electrons exit the target. This satisfies the Poisson equation, where $\rho(x)$ is the total charge density distribution:

$$\frac{\partial^2 \mathbf{\Phi}}{\partial x^2} = -\frac{\rho(x)}{\varepsilon_0} = \frac{e n_{f0}}{\varepsilon_0} \times \begin{cases} \exp\left(\frac{e\mathbf{\Phi}(x)}{k_B T_f}\right) - 1, & \text{for } x \leq 0, \\ \exp\left(\frac{e\mathbf{\Phi}(x)}{k_B T_f}\right), & \text{if } x > 0, \end{cases} \tag{3.52}$$

The initial conditions, at $t = 0$, before any expansion of the rear surface, describe a target with ion density equal to the initial electron density, $Z n_i = n_{f0}$. This implies the target is charge neutral as $x \to -\infty$ and therefore $\Phi(\infty) = 0$. The potential equation can be solved analytically for $x > 0$:

$$\frac{e\mathbf{\Phi}(x)}{k_B T_f} = -2 \ln\left(1 + \frac{x}{\sqrt{2\exp(1)}\lambda_D}\right) - 1 \tag{3.53}$$

and the electric field is simply the gradient of the potential. The peak electric field, E_0, which occurs at the vacuum boundary can be derived by:

$$E_0 = -\frac{\partial \mathbf{\Phi}}{\partial x}\Big|_{x=0} = \sqrt{\frac{2}{\exp(1)}} \cdot \frac{k_B T_f}{e\lambda_D} = \sqrt{\frac{2}{\exp(1)} \cdot \frac{k_B T_f n_{f0}}{\varepsilon_0}} \approx \sqrt{\frac{k_B T_f n_{f0}}{\varepsilon_0}} \tag{3.54}$$

For a fast electron temperature $k_B T_f = 1\,\text{MeV}$ and an electron density of $n_f = 10^{26}\,/\text{m}^3$

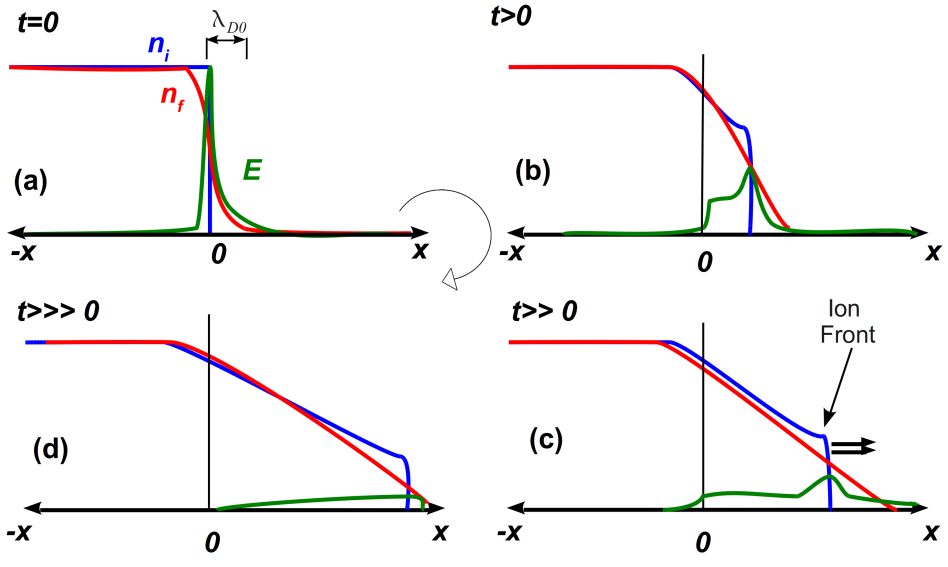

front.

FIGURE 3.16: Temporal evolution of rear surface plasma expansion driven by fast electrons exiting the target rear surface. (a) Initially at time $t = 0$, the ions, n_i, are at rest and the fast electrons, n_f, form a sheath with thickness λ_{D0}. (b) The ions are subsequently accelerated out into vacuum by the electric field, E, forming a well-defined front. (c) The electrons begin to slow down as energy is coupled to the ions. (d) At later times, this results in the accelerating field reducing to zero.

the initial field is $E_0 \approx 5 \times 10^{12}$ V/m. This is well above the threshold for field-ionisation of atomic hydrogen, 3.2×10^{10} V/m.

This estimate for the initial electric-field strength shows that the fields at the target rear are by far strong enough to ionise atoms. These ions can subsequently be accelerated in the same fields. The protons, which have the highest charge-to-mass ratio, are preferentially accelerated. The presence of hydrogen derives from contaminants of water or oil vapor which form a thin layer of ≈ 10 nm on the target surfaces, see Figure 3.15.

The ions gain energy coupled from the fast electrons via the Coulomb force between them as both species propagate in a **quasi-neutral** plasma cloud. As energy is gradually transferred from the fast electrons to the ions the accelerating field generated by the charge-separation gradually decreases to zero. Some recombination between electrons and ions can occur, typically a few percent [170]. A schematic of the plasma expansion model is shown in Figure 3.16.

After the initial time $t = 0$, the ion plasma of the target expands into vacuum. A series of measurements [171] imaging the ion front expanding over time is shown in Figure 3.17. In the Mora model, this ion expansion can be described via the continuity equation and the

momentum equation using the local velocity $v_i(x,t)$ and number $n_i(x,t)$ distributions:

$$\frac{\partial n_i}{\partial t} + v_i \frac{\partial n_i}{\partial x} = -n_i \frac{\partial v_i}{\partial x} \tag{3.55}$$

$$\frac{\partial v_i}{\partial t} + v_i \frac{\partial v_i}{\partial x} = -\frac{e}{m_i} \frac{\partial \mathbf{\Phi}}{\partial x} \tag{3.56}$$

As the plasma expands into vacuum the ions form a well defined front. This expansion has a self-similar solution, valid for $x + c_s t > 0$, where the velocity and density of the ions can then be solved using:

$$v_i(x,t) = c_s + \frac{x}{t} \tag{3.57}$$

$$n_f(x,t) = Z n_i(x,t) = n_{f0} \exp\left[-\frac{x}{c_s t} - 1\right] \tag{3.58}$$

Substituting Equation 3.58 into Equation 3.51 yields a constant electric field between $x = -c_s t$ and the plasma edge. This field can be calculated using the self similar solution to the fluid equations of continuity and motion, assuming that the expanding plasma is quasi-neutral ($n_f = Z n_i$) [25]:

$$E_{ss} = \sqrt{\frac{n_f k_B T_f}{\varepsilon_0}} \frac{1}{\omega_{pi} t} \tag{3.59}$$

where c_s is the hot ion sound speed, $c_s = \sqrt{Z k_B T_f + k_B T_i / m_p} \approx \sqrt{k_B T_f / m_p}$, with $k_B T_i \ll k_B T_f$, and ω_{pi} is the ion plasma frequency, $\omega_{pi} = \sqrt{Z n_{f0} e^2 / \varepsilon_0 m_i}$. The self-similar electric field scales with fast electron temperatures and decreases in time and with the rear plasma scale length. The self similar condition breaks when the initial Debye length λ_{D0} is greater than the plasma scale length $L_s = c_s t$.

The position of the ion front over time can be estimated by using the condition when the self similar solution becomes invalid. This occurs when the local Debye length $\lambda_D > ct$. At the ion-front $\lambda_D = \lambda_{D0} \left(n_{f0}/n_f\right)^{1/2} = \lambda_{D0} \exp\left[\left(1 + x/c_s t\right)/2\right]$. This occurs at position $1 + x/c_s t = 2 \ln\left(\omega_{pi} t\right)$, where the self similar solution predicts a velocity $v_{front} = 2 c_s \ln\left(\omega_{pi} t\right)$, implying that the electric field at the front is twice the self-similar field [25]:

$$E_{front} = 2E_{ss} = \frac{k_B T_f}{e c_s t} = \frac{2E_0}{\omega_{pi} t} \simeq \left(\sqrt{\frac{2 n_{f0} k_B T_f}{\exp(1) \varepsilon_0}} \frac{1}{1 + \tau_p^2}\right) \tag{3.60}$$

where time is now normalised to the ion plasma frequency, $\tau_p = \omega_{pi} t / 2\exp(1)$. The ion front position and velocity are then:

$$x_{front} \simeq 2\sqrt{2 e \lambda_{D0}} \left[\tau_p \ln\left(\tau_p + \sqrt{\tau_p^2 + 1}\right) - \sqrt{\tau_p^2 + 1} + 1\right] \tag{3.61}$$

$$v_{front} \simeq 2 c_s \ln\left[\tau_p + \sqrt{\tau_p^2 + 1}\right] \tag{3.62}$$

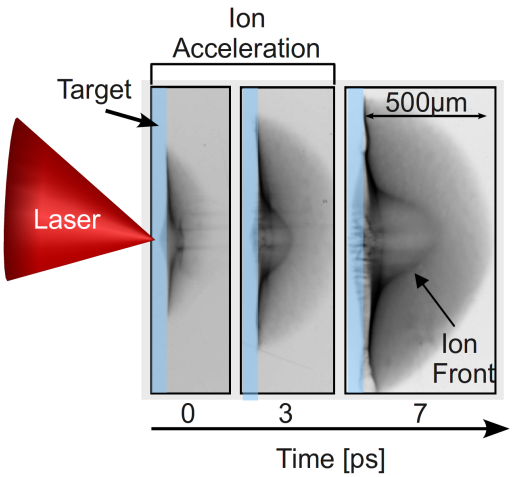

FIGURE 3.17: Measurements of the expanding ion front at different times probed by proton deflection [171].

The maximum energy, E_{max}, gained by the ions can be calculated using the final Mora formula [25]:

$$E_{max} = 2Zk_BT_f \left[\ln\left(\tau_p + \sqrt{\tau_p^2 + 1}\right)\right]^2 \tag{3.63}$$

Obviously, a longer acceleration time will accelerate the ions to greater maximum energy. A logical limit for t is the laser pulse length τ_L. However, simulations have shown that for incident laser intensities greater than $3 \times 10^{19}\,\mathrm{W/cm^2}$, the ion acceleration time is $t = t_a \approx 1.3\tau_L$ [169]. The acceleration time increases at lower intensities due to the slower expansion. In general, t_a can be approximated using [106]:

$$t_a = \begin{cases} 1.3 \times (\tau_L + 60\,\mathrm{fs}), & \text{for } I_L \geq 3 \times 10^{19}\,\mathrm{W/cm^2}, \\ (\text{-}6.07{\times}10^{-20} \times (I_L{-}2{\times}10^{18}) + 3) \times (\tau_L + 60\,\mathrm{fs}), & \text{for } I_L \in 2 \times 10^{18}, 3 \times 10^{19}\,\mathrm{W/cm^2}, \end{cases}$$

Due to the $\ln(\sqrt{n_f})$ dependence, the maximum ion energy only weakly depends on the hot electron density, the fast electron temperature is the dominating influence [106].

The proton **energy spectrum** predicted by the self-similar solution extends up to the peak energy of the protons situated at the front. The integrated beam energy is typically $< 6\%$ of the laser driver [172]. According to this simple fluid model the numbers of ions (N) per energy (E) can be estimated up to E_{max} using [25]:

$$\frac{dN}{dE} = \left[\frac{n_{f0}c_s t_a S_A}{\sqrt{2EZk_BT_f}}\right] \exp\left[-\sqrt{\frac{2E}{Zk_BT_f}}\right] \tag{3.64}$$

The Mora plasma expansion model is very much idealised, since it is one-dimensional and isothermal, and it neglects the laser interaction and electron transport. In reality the fast electron temperature will fall as the electrons impart energy to the ions which will 'catch

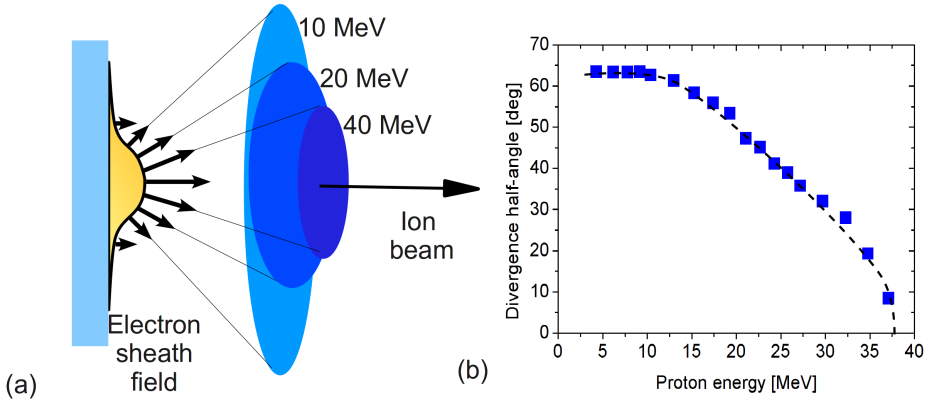

FIGURE 3.18: (a) The energy-dependant ion beam divergence originates due to the electric field profile; (b) An example of a measured distribution is shown for protons from a Vulcan Petawatt experiment.

up' with the electrons, ending the acceleration. This is not taken into account when an isothermal expansion is assumed. The rate at which the fast electron temperature decreases is inversely proportional to the square of the expansion time and results in electron co-propagating with the ions for a few hundred microns.

The ablating plasma of the front surface has a much longer scale-length, compared to the rear. Although the potential difference is equal for both target surfaces, the electric fields at the front are much lower due to the larger Debye length. As the potential difference and the electric fields are only kept up as long as the electron temperature remains high, ions accelerated at the target-front side gain much lower energies by the TNSA-mechanism.

3.8.2 Proton beam divergence, source size and emittance

The electron sheath is fully developed before significant expansion of the protons occurs. The protons with the highest energy are accelerated by the strongest part of the electric field that has its maximum in the center. The accelerating electric field amplitude decays like a Gaussian in the transverse direction, therefore lower energy protons originate from larger radii, see Figure 3.18(a). The proton beam source size derives from the early stages of the acceleration process, when the electric field of the sheath is governed by the Poisson equation as $\mathbf{E} \propto \sqrt{k_B T_f n_f}$. The energy of the proton beam is directly correlated with this accelerating field. The strength of the local electric field at the rear surface determines the energy and source size of the ions accelerated from this region. The divergence of the proton beam is thus energy dependant, an example is shown in Figure 3.18(b).

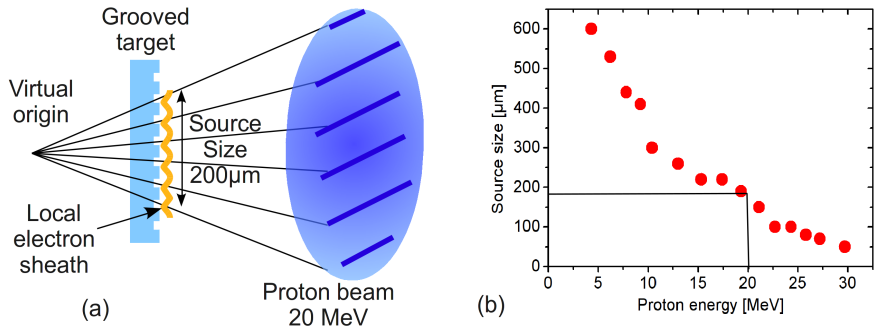

FIGURE 3.19: (a) A schematic of the proton emission from grooved target. The grooves are reproduced in the proton data at the detector plane. The proton source size can be extrapolated from the grooved data. A virtual source position can also be defined. (b) The energy resolved, real source size for a laser-accelerated proton beam.

The source size of the proton emission is also energy dependant. This has being demonstrated by measurements using grooved targets [173, 174]. A schematic is shown in Figure 3.19(a). The modulations of the rear surface are mapped onto the electron sheath and hence the sheath field is also modulated. The grooves are imprinted onto the proton beam, and due to the large opening angle of the beam, the grooves are magnified by a few orders of magnitude at the detector plane. The spatial images at distinct proton energies are recorded by the detector. By counting the lines and by multiplying the number with the known grooves separation, the source size at the target rear side can be determined. Using this method, the source size is obtained for each energy component of the overall proton beam.

A measurement of source size as a function of proton energy, performed using the Vulcan laser, is shown in Figure 3.19(b). The source size decreases with increasing energy, from about 50 μm diameter for high energy protons to over 600 μm diameter for low energy protons. A virtual source can be defined as the location from where the protons appear to originate. The location of the virtual source can be determined by extrapolation of the proton trajectories to a region typically in front of the target. The size of the virtual source provides quantitative information regarding the beam quality and is a useful parameter for comparison between different proton beams.

The fast electron sheath at the rear surface laterally extends to hundreds of microns [167, 175]. The density and temperature of the fast electron sheath determines the electric field and hence the energy of the accelerated ions. The latter correlates with intensity of the laser [84]. An example is shown in Figure 3.20 for a comparison of data for two different lasers. The higher laser intensity induces a stronger sheath field at the rear surface and hence the initially stationary ions are accelerated to higher energies. The pulse length of the laser determines the length of the electron beam and hence the

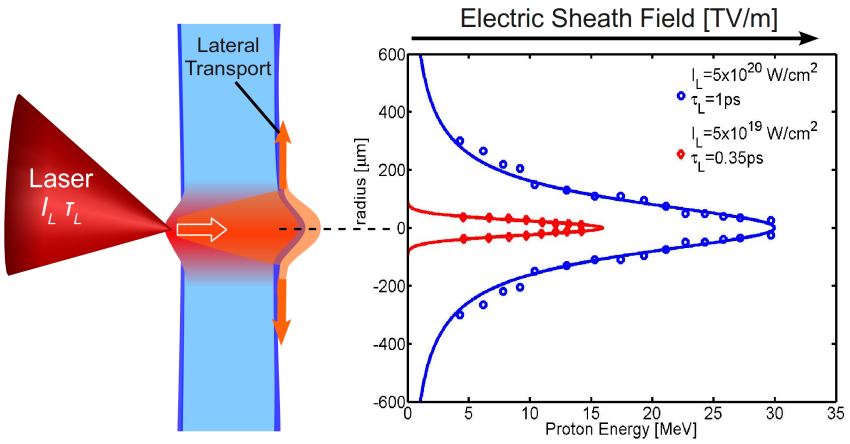

FIGURE 3.20: Proton source size is shown in for two examples using: the 100 TW LULI laser (red) [176] and the Vulcan Petawatt laser (blue) [174]. The electric field distribution expands laterally along the rear surface by the expansion of the fast electron sheath. The proton source size is shown to be larger in the case of the more intense/longer pulse length Vulcan laser.

acceleration time and final energy of the ions. Also, if the fast electron population is heated by the laser for a longer duration, the lateral expansion of the rear surface sheath field will be greater. This can be responsible for the greater measured size of the ion source width for the case of the longer pulse duration. If the electrons spread along the rear surface at the speed of light [175], then after 1 ps the sheath would extend to over 600 μm in diameter compared to 200 μm for a pulse length of 0.35 ps. While this is a simple approximation, the examples shown in Figure 3.20 are consistent that the lateral transport along the surface strongly influences the maximum ion source size.

The efficient mapping of the rear surface groove structure onto the beam suggests a very high degree of **laminarity**. A good laminarity means that the different proton trajectories do not cross and overlap. This can be formally characterised by measuring the transverse **emittance** which is defined using the angle of emission, x' [mrad] at position x [mm]. Using grooved target data, the source size and angle can be plotted for the different proton energies. This tends to form an ellipse as shown in Figure 3.21, the area of the ellipse then provides a measure of emittance. Typically laser-driven proton beams have a very low emittance < 0.004 mm.mrad [173]. This translates to very high beam quality making it possible to treat the proton beam as a virtual point source $< 10\,\mu$m [177].

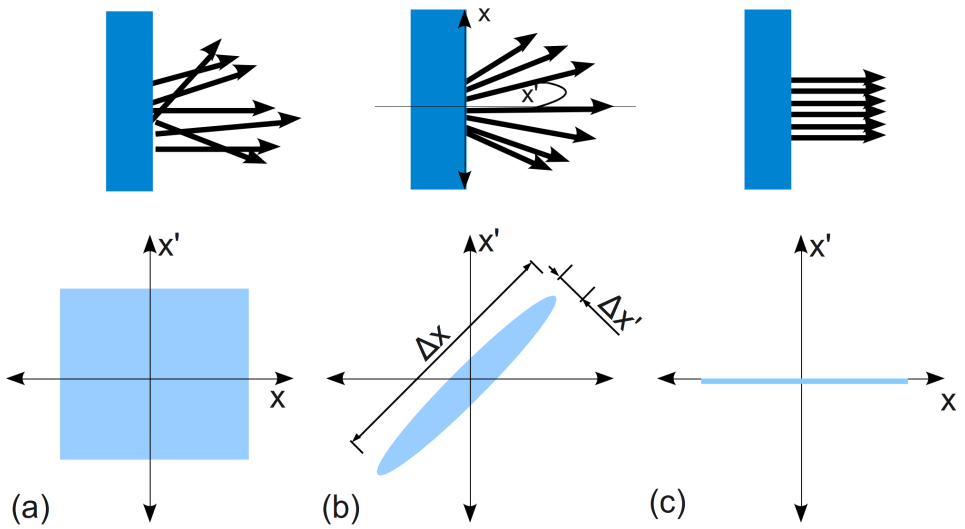

FIGURE 3.21: The concept of emittance is illustrated in terms of spatial direction (top) and phase-space (bottom) for (a) turbulent (b) diverging and (c) collimated beam respectively. Emittance is calculated using the surface area of the phase space boundary $\approx \Delta x.\Delta x'/\pi$

Chapter 4

Methods: Experiments & Modelling

The investigations of fast electron transport in dense plasma, such as those discussed in Chapters 5−7, involve a number of challenging stages. These experimental investigations were carried out at national research facilities both in the UK and abroad. Facility-based campaigns offer a short concentrated period to conduct experimental measurements and hence require a good deal of fore-planning to meet the objectives of the experiment. This chapter begins with an overview of the general process from the experiment stages to the analysis and interpretation of results. The following sections then describes the laser systems, diagnostics and numerical computer codes relevant to the results presented in Chapters 5-7.

4.1 Overview

World class laser facilities are required to achieve the laser-plasma conditions relevant to Fast Ignition and more generally fast electron transport in dense plasma. The allocation of 'beam-time' at such facilities is competitively sought-after by the global community of research groups. Access is allocated on the merits of the proposal and is typically 3-6 weeks in duration. The acceptance of an experimental proposal instigates the planning stages usually several months before the experiment commences. The involvement of facility personnel including engineers and scientists together with the primary research group and the collaborating groups is necessary in the planning stages to collectively ensure that the experimental objectives can be best achieved. Each experiment brings new challenges in design and implementation and is fundamentally a collaborative effort.

At larger national facilities the setup and running of the experiment is performed by a group of 6-10 individuals. As an example, at the Vulcan facility the team hierarchy consists of the Principle Investigator (PI), the Target Area Operator (TAO), and a number of scientists or graduate students. The experiment is set up in and around the vacuum chamber within the target area which is a controlled clean environment separated from the control room by safety interlocks. The TAO manages the activities within the target area while the PI is responsible for overseeing the general objectives and other externalities of the campaign from the control room. A dedicated team of facility scientists and technicians are responsible for the performance and delivery of the laser pulses into the target area.

The location of the laser-target interaction point is typically termed Target-Chamber-Centre (TCC) and corresponds to the focus of the parabola. Best focus provides the smallest laser spot-size at the front of target and thus maximum intensity. The quality of the laser spot is dependant on the particular parabola and whether it has been suitably optimised. This process involves fine adjustments to the roll and tilt axis to create the best achievable focal spot distribution ideally free of any astigmatism. Optimal results are usually achieved using a microscope with CCD camera placed at TCC under vacuum. The position of this TCC point within the target chamber can be shifted according to the translation axes of the parabola. The tip of a fine wire target is placed to within a few microns of this point, again using a microscope camera under vacuum. Once this point has been established it is referenced by two or more helium-neon diode lasers with magnified imaging lines. Next the suite of diagnostics are setup and aligned to this TCC point.

A host of diagnostics are typically employed and are optimised for each laser shot to record a collective snapshot of the interaction and the ensuing emissions. An assortment of measurements of photon and particle radiation by temporal, spatial and spectral methods endeavor to provide a complete physical study. In reality the space for optics and diagnostics becomes very limited in the environs of the target. This means that a core suite of primary diagnostics are responsible to provide data to meet the experimental objectives. Typical facilities such as Vulcan Petawatt and PHELIX have a laser shot cycle of $\approx$ 1 hour, to allow flash-lamp cooling, resulting in 6-10 shots per day. The initial scanning and analysis of the diagnostic data during the campaign means that new unanticipated directions can be pursued.

The subsequent months after a typical experiment involve the necessary task of detailed data analysis. Together with analytical and numerical modelling a coherent physical picture can emerge finalising with an eventual journal publication.

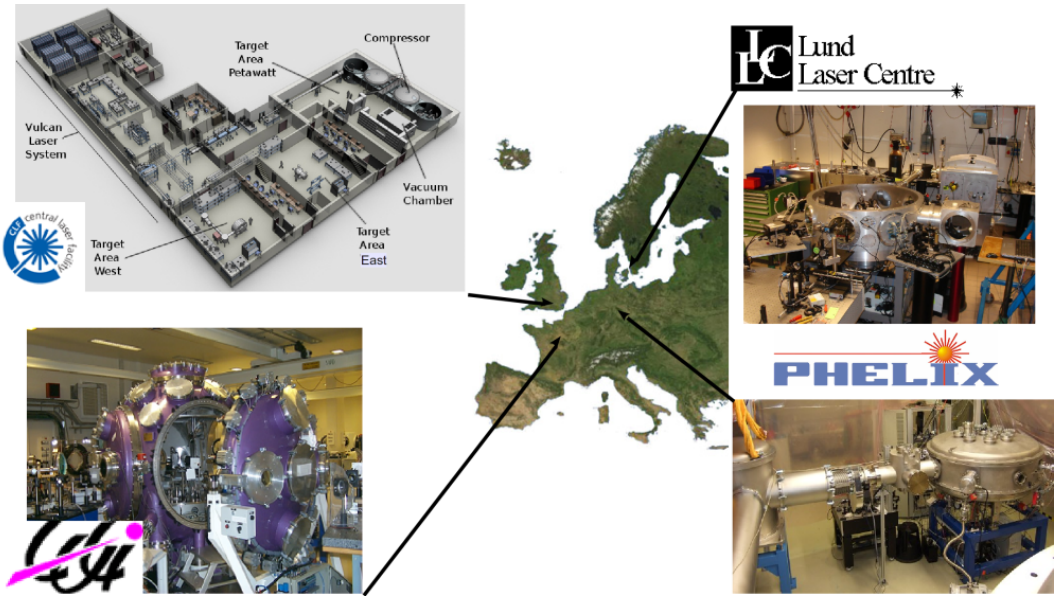

FIGURE 4.1: A selection of high energy short pulse laser facilities located in Europe. The author was involved in a number of experimental campaigns at these facilities,. The results reported in this thesis concern the Vulcan and PHELIX systems.

4.2 Experimental facilities

The author was involved in campaigns at a number of experiential facilities within Europe as shown in Figure 4.1. The experimental investigations, discussed in Chapters 5−7, were carried out using the Vulcan laser at the Rutherford Appleton Laboratory in the UK and the multi-TW PHELIX laser system at the GSI facility in Germany. In both cases the operation of the short pulse CPA systems was carried out by dedicated laser engineers. This section introduces these two laser systems in-terms of the specifics of the laser-chain and the target area.

4.2.1 Vulcan Petawatt

The system draws on over 3 MJ of total electrical energy to deliver ≈ 600 J of coherent short-pulse laser radiation into the target area petawatt (TAP). A separate long pulse is capable of delivering up to 300 J over nanosecond pulse lengths. The layout of the Vulcan[1] Petawatt short-pulse beam-line is shown in Figure 4.2 illustrating the major components which are described in the following sections.

[1]The name Vulcan was chosen from the roman god of fire. A Latin acronym was devised by R G Evans: “Versicolor Ultima Lux Cohaerens pro Academica Nostra”

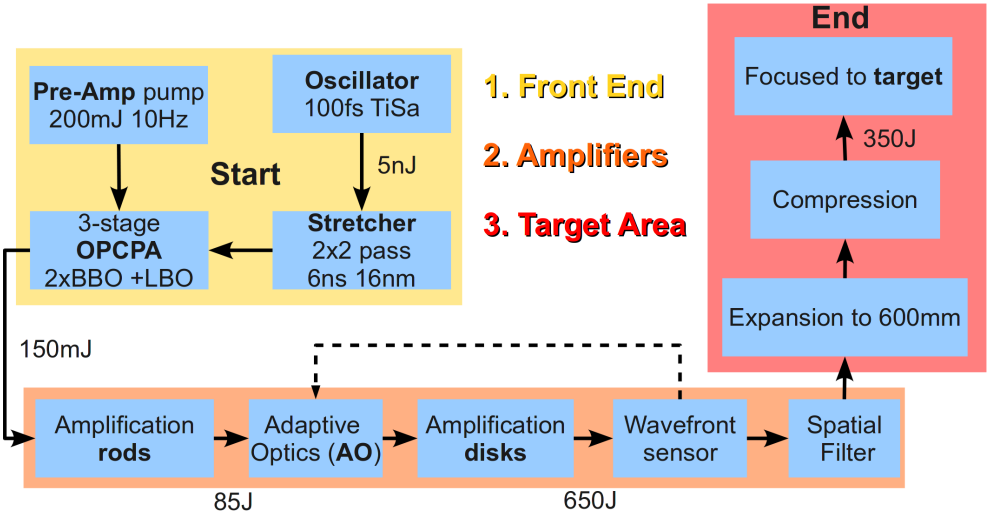

FIGURE 4.2: A flow chart description of the VULCAN Petawatt laser chain.

4.2.1.1 Frontend

The initial seed laser pulse is produced from a Ti:Sapphire oscillator. The seed is selected from a train of pulses and is typically 200 fs in duration with a few nJ of energy and a wavelength centered at 1053 nm. Next, the pulse length is stretched to nano-seconds. This reduces the intensity of the pulse before being amplified and prevents non-linear processes which can cause the pulse to break up. The different frequencies of the pulse will travel different path lengths in the stretcher so that the longer wavelength (red) components of the pulse travel a shorter distance through the system and arrive ahead of the shorter wavelength (blue) components. See Section 2.2 for a detailed description.

The first stage amplification occurs in the **OPCPA** preamplifier in the front-end room, prior to its injection to the rod and disc chain. Optical Parametric Amplification uses a nonlinear crystal pumped by a shorter wavelength laser [178]. Here the seed pulse is amplified to a few milli-joules. The pre-amp pump laser energises the three stage optical parametric amplifier. The nonlinear crystals used for the three amplification stages are each maintained at a temperature of 40° C. The signal beam passes through each crystal which is separately pumped by the higher frequency pump beam. Photons from the pump beam are down converted to photons of the signal beam, with an idler beam carrying away the leftover energy. OPCPA provides higher gain per unit volume than a standard laser medium. More importantly, however, the pulse length of the pump laser can be matched to the pulse length of the signal beam such that the gain medium is only 'on' when the signal beam is being amplified, thus reducing spontaneous emission and increasing the intensity contrast of the laser relative to the prepulse.

4.2.1.2 The mixed glass amplifiers

The laser main amplifier chain is formed by a set of rod amplifiers and disc amplifiers which are flash-lamp pumped. The amplifiers have been manufactured using neodymium (Nd) glass as the gain medium mixed with either phosphate or silicate. The beam at the input of the chain is a few millimetres in diameter and is gradually expanded up to one hundred or two hundred millimetres by the time it reaches the output of the disc chains. The mixed glass is used to reduce the effect of bandwidth narrowing and results in a central laser wavelength of $\lambda_L = 1.055\,\mu$m. The high gain is provided by the Nd:silicate rod amplifiers. A sliding mirror can re-direct the beam through three more disc amplifiers. After this final stage the pulse energy is $\approx 600\,$J. While normal laser runs employ both silicate and phosphate lines, there are occasions where a single line is used. This changes the inherent bandwidth and hence the duration of the pulse. In this case the amplifiers can be driven harder to compensate and maintain overall energy.

An **adaptive-optics** (AO) system is used to improve the quality of the laser wavefront [179]. This is essential for achieving the best possible laser spot on target and for re-compression of the stretched pulse. The AO consists of a deformable mirror comprising an array of separate elements. The system adapts to slowly varying aberrations using a feedback loop mechanism based on wave front measurements made at the end of the amplification chain. The aberrations are due to thermal gradients set up in the amplifiers during the course of firing laser shots throughout the day.

4.2.1.3 Target area

Target Area Petawatt (TAP) is separated from the laser area by a shutter controlling laser access. The target area contains the compressor, which is under ultra high vacuum and the target chamber which are separated by a gate valve. When the target chamber is at atmospheric pressure, the gate valve window allows alignment beams to enter form the laser area. The large dimensions of the target chamber provide a walk-in environment with standing room for users who must wear full body suits, gloves and face masks to maintain the clean-room standards. Chamber inter-lock keys are also worn to ensure vacuum safety. A number of chamber ports and windows provide access to optical beam lines and diagnostics. In practice the chamber is 'pumped down' to a vacuum level of $10^{-4}\,$mbar before the gate valve is opened to the compressor ($10^{-6}\,$mbar). The 'pump down' and 'let up' procedures normally take 40 and 20 minutes respectively. A continuous wave (CW) alignment laser is available for parabola optimisation and target alignment. This CW laser is an infared beam and is injected from the laser area along the path of the actual high power laser.

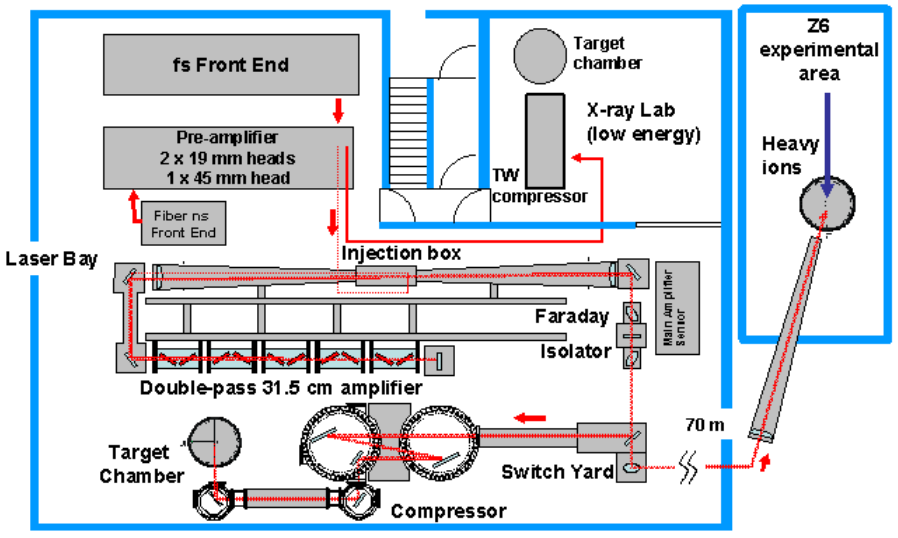

FIGURE 4.3: A schematic of the PHELIX laser and target area (`http://www.gsi.de/forschung/pp/phelix/`). The system begins at the ns or fs frontend and can typically delivers a few hundred Terawatts of laser energy to the target chamber.

In shot-mode, the high power laser pulse which enters the area is nominally $\approx 600\,\mathrm{J}$ and is spread over 5 ns. The action of the compressor shortens the pulse length to $\approx 1\,\mathrm{ps}$ using a pair of gold coated gratings with an energy transmission efficiency of 60%. The diameter of the gratings is 940 mm, which enables the beam to be expanded to a large diameter so that the energy per area is below the damage threshold of the gratings. The beam is then passed into the target chamber with a final diameter of 600 mm and is focused onto target with an $f/3$ off-axis parabola. The spot size of the focused beam at FWHM is $\approx 5\,\mu\mathrm{m}$ which contains 50% of the laser energy. The energy incident on target is therefore: $0.6 \times 0.5 \times 600\,\mathrm{J} = 180\,\mathrm{J}$ which for a pulse length of 700 fs delivers a peak intensity of $\approx 10^{21}\,\mathrm{W/cm^2}$ within the focal spot.

4.2.2 PHELIX

The PHELIX[2] laser facility is based at the GSI[3] laboratory near Darmstadt, Germany. A novel feature of PHELIX is the possibility of coupling the intense laser plasma facility to the established heavy ion linear accelerator at GSI [180]. The laser system comprises of flash-lamp-pumped Nd:glass amplifiers employing two frontends (ns and fs), a pre-amplifier and a main amplifier delivering intense laser beams with powers > 100 TW [181, 182]. A schematic of the laser and target area is shown in Figure 4.3.

[2] Petawatt High-Energy Laser for Heavy Ion EXperiments
[3] **G**esellschaft für **S**chwer**i**onenforschung

4.2.2.1 Frontends and pre-amplifier

PHELIX provides a choice of either a short or long pulse frontend. The short femtosecond frontend generates seed pulses with a duration of 100 fs and energies around 4 nJ. The initial seed pulse is then stretched with a ratio of 190 ps/nm. This ensures that the pulse at peak power is below the laser damage threshold of the optical components in the amplification chain. The stretched pulse enters a pair of Ti:Sapphire regenerative amplifiers and the typical output energy is 30 mJ. The nanosecond frontend can deliver arbitrary pulse shapes and pulse durations between 1 and 15 ns. Since the long pulse frontend did not feature in this work the following description of gain and compression will only concern the femtosecond seed pulse.

Before the main amplification takes place, the pulse enters into a sequence of three three flash-lamp pumped Nd:glass pre-amplifiers. The pulse is now amplified to ≈ 5 J. Afterwards the beam diameter is increased to a maximum exit beam diameter of 70 mm in order to keep the fluence within safe limits, below the damage threshold. Spatial aberrations introduced in main/pre-amplifiers are corrected by a deformable adaptive optics mirror coupled with a sensor located at the end of the laser chain.

4.2.2.2 Main-amplification and compression

The pulse takes a double pass through the main-amplifiers. The gain media consists of five flashlamp-pumped Nd:glass cassettes. The pulse can in principle be amplified to ≈ 250 J. This energy is only limited by the laser damage threshold of the Faraday isolator protecting the laser against possible back reflections. In practice the energy is of the short-pulse if limited to ≈ 120 J to comply with the current permitted radiation safety levels.

After leaving the main-amplifier the stretched pulse enters the compressor. The pulse can typically be compressed to < 1 ps and can exit with a power of up to a few hundred terawatt. The compressor consists of two 48-cm-wide optical gratings used in single-pass configuration with results in an 80% throughput. While the compressor grating configuration remains fixed, the resulting re-compressed pulse duration can be changed by adjustment of the pulse stretcher of the femtosecond front-end.

After the pulse compressor, a 90° off-axis parabola focuses the laser beam into the target chamber. The parabola is a copper coated $f/6.7$ optic with diameter of 300 mm, focal length of 2 m and reflectivity of 80% [183]. A focal spot of 15 μm FWHM containing 50% of the laser energy was measured during the experiment reported in Chapter 7. PHELIX delivers typical laser energy of ≈ 120 J to the compressor of which approximately 50 J

is delivered within the FWHM of the laser focus. Sub-picosecond pulse lengths are achievable with nominally a few hundred terrawatts of power delivered onto target with peak intensity of $5 \times 10^{19}\,\mathrm{W/cm^2}$.

4.3 Diagnostic methods

A typical electron transport experiment is studied using the collective data from a number of diagnostics. A schematic of such a setup is depicted in Figure 4.4. This can vary for different experimental campaigns depending on limitations of space and objectives. The various diagnostics enable measurements of many physical phenomena related to fast electron generation and transport. Most of the diagnostics are time integrated with the exception of the 'HIgh-Speed Sampling Camera' (HISAC) and transverse probing. An exhaustive description of all the diagnostics is not possible here. Only those diagnostics associated with the results of Chapter $5-7$ will be discussed in the following sections.

4.3.1 Proton emission

The acceleration of MeV proton beams by the TNSA mechanism is a primary diagnostic of electron transport for the work of this thesis. As discussed in Section 3.8, the electric field responsible for ion acceleration is induced by the fast electrons. Key measurements of proton and ion beams involve their energy, spatial and angular properties.

A fundamental feature of proton beams is their concise energy-dependent penetration depths in material. This contrasts with photons and electrons which deposit significantly more energy continuously over their range. The stopping curve for ions show a characteristic peak release of energy at a given depth as described by the 'Bragg curve'. This is a major avenue of development for ion beams as an oncology source. Additionally, this property is very useful for diagnostic design using a stack of detectors at successive depths. A stack of dosimetry film can provide high resolution spatial images of the beam at successive energies. This is described in Section 4.3.1.1. The deflection of ions in a Thomson spectrometer offers an additional approach to measurement. In this case the energy spectra of the beam can be finely resolved to include multiple species of ions, see Section 4.3.1.2.

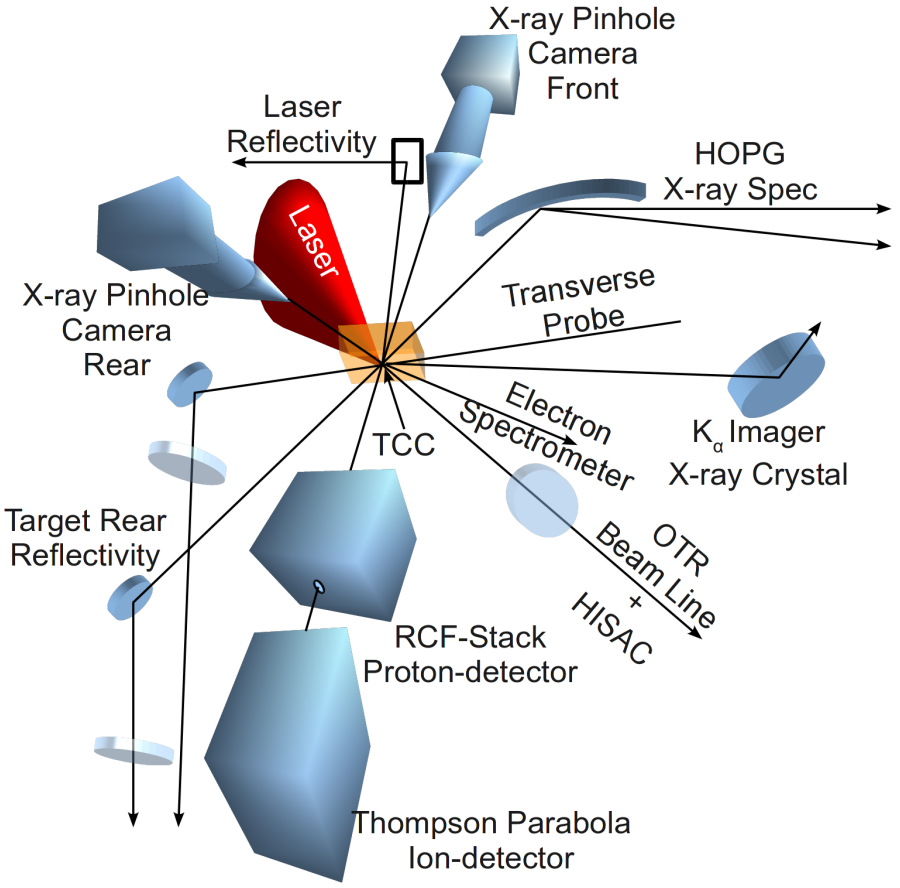

FIGURE 4.4: A schematic of the diagnostic arrangement within the target chamber for a typical electron transport experiment. The laser is incident onto the target at Target-Chamber-Centre (TCC). This is the initial alignment point for the collection of diagnostics. The beam-line arrows point to the detectors where the data is recorded.

4.3.1.1 RCF-stack

Ions deposit the majority of their kinetic energy just before they are stopped at a given penetration depth. This abrupt stopping is characterised by a distinctive Bragg peak in the stopping curve of the ions with a given energy. The Bragg peak of more energetic ions is located deeper in the material. Protons, having the lightest ion mass, can propagate through millimetres of low-Z material. Placing layers of proton sensitive material at successive depths provides a simple basis for an energy and spatially resolved proton diagnostic.

The measurement of energy deposition in each layer is performed using stacks of dosimeter film. Radio-chromic film (RCF) can be purchased[4] in sheets and then sub-divided and assembled as successive layers in a stack. While initially clear, when exposed to ionising radiation an organic dye in the film turns blue. RCF is thus self-developing, with higher doses of radiation resulting in deeper shades of blue. This change in the

[4]See GAFCHROMIC at `http://online1.ispcorp.com/_layouts/Gafchromic/index.html`

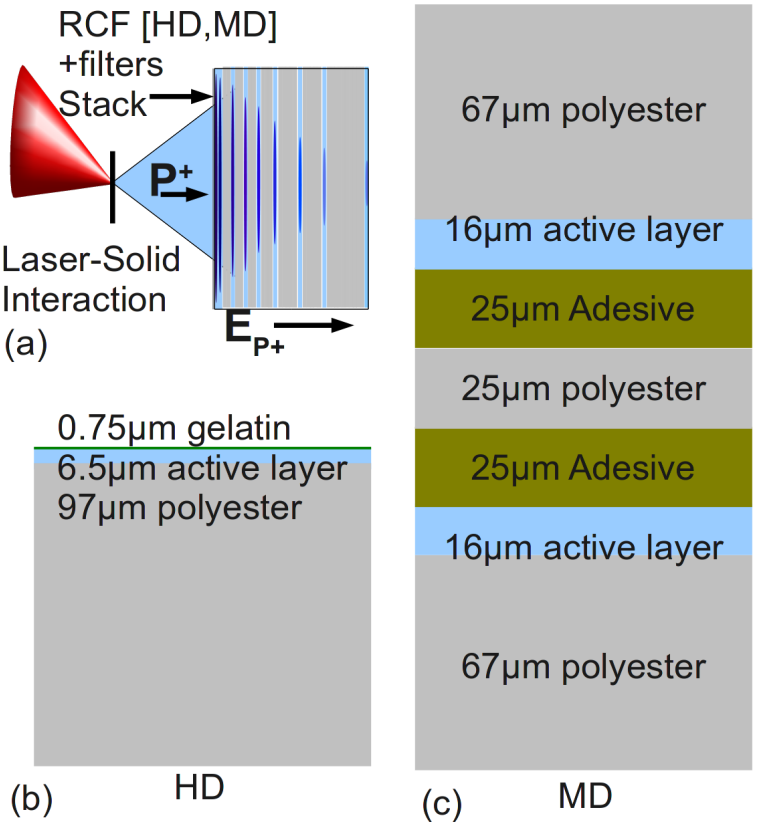

FIGURE 4.5: The proton stack diagnostic is assembled with sequential layers of dosimetry film and filters. (a) The stack is placed parallel to the rear of the target for measurements of TNSA proton emission. Analysis of RCF stack data can provide the measured proton energy-spatial distribution. Each type of RCF is the combination of active and plastic layers. Two types of RCF used in stack configurations are shown: (b) HD and (c) MD.

opacity of the film is quantified as optical density and is calibrated to provide dose and proton number conversion. A good deal of information regarding RCF characterisation can be found in the literature [184–186]. A key characteristic of this film is its high spatial resolution of $\approx 1\,\mu$m due to the small grain size of the active medium. It's low density ($\rho \approx 1.4\,\mathrm{g/cm^3}$) ensures that scattering effects are minimised as particles propagate through multiple layers. Most of the coloration ($\approx 90\%$) occurs within the first milliseconds after exposure to the radiation, and is complete within 24 hours. Obviously, care must be taken to store the film away from the influence of background light. In a typical stack configuration, RCF is preferentially sensitive to protons. This has been confirmed by placing CR39 within the stack and comparing the measured signals [187].

Two varieties of RCF were employed in the experiments presented in Chapters $5-7$. The primary type of RCF was HD-810' with a small number of 'MD-55' layers. As the names suggest, MD is used for moderate doses, whereas HD is suitable for high doses. These two films differ in the thickness of the active dye layer with the thicker MD layer having greater sensitivity. This results from a greater dose being deposited

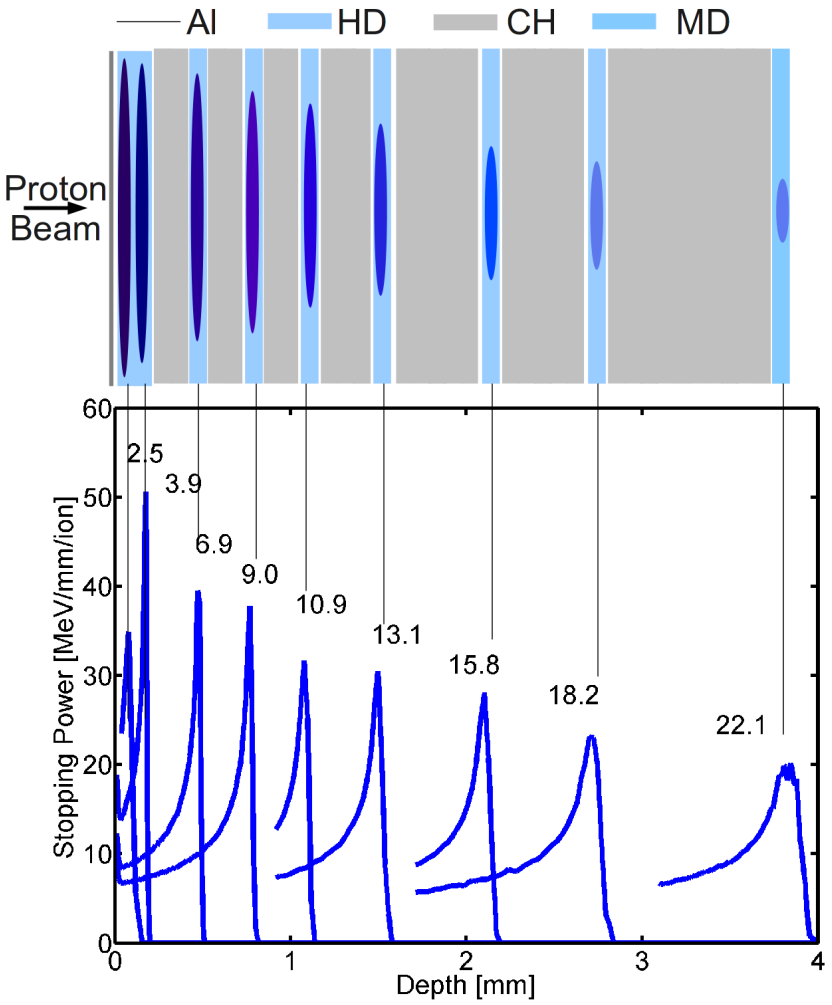

FIGURE 4.6: An example of an RCF stack design with 9 HD layers and 1 MD layer (top). The filter materials are Al and CH. The Bragg curves calculated using SRIM are shown for each layer with the corresponding proton energy in MeV (bottom).

by ionising radiation as it passes through the active. An example proton stack is shown in Figure 4.6, which begins with a thin aluminium layer to remove ions and low energy protons. The layers of HD are placed at successive depths separated by filters. A final layer consists of a more sensitive MD-type RCF to detect lower particle numbers. The thickness of each RCF layer corresponds to a narrow range of proton energies. While a pure RCF stack offers the best energy resolution, an economic compromise of using relative larger energy steps is usually sufficient.

The proton Bragg (stopping) curves are calculated using a Monte-Carlo simulation software package called **SRIM** (Stopping and Range of Ions in Matter[5]). Here a stack is defined comprised of successive layers of material, the paths of particles propagating with a defined initial energy is then characterised.

[5]Available from `www.srim.org`

Ideally, the stack is wide enough to accommodate the full beam and sufficiency deep to record its maximum energy. In reality, a continuous stack of RCF is expensive, so instead filters of low-Z material can be used to space out the energy interval between layers. Thin layers of Al or CH are the usual choice of filters. A single layer of Al at the front prevents optical exposure of the RCF and stops the majority of ions heavier than protons. Electrons escaping the target can propagate straight through the stack. For the TAP campaigns a sequence of 4 shots would usually be taken under vacuum. The 4 stacks would be housed on a wheel with each in turn been rotated to the shooting position defined as a gap in a plate of lead shielding. The passive nature of the RCF stack provides a most reliable diagnostic insensitive to electronic effects and giving instant information on proton beam quality, which itself can affirm the success of a shot.

The data provided by the RCF stack is multifaceted. Primarily, it provides spatial imaging of the beam at successive energies. This in itself provides several pieces of information: 1) proton beam divergence with respect to proton energy, 2) the spatial intensity distribution/uniformity of the beam and 3) the proton beam energy spectrum which can provide 4) the laser-proton energy conversion efficiency.

The proton beam divergence, dose profile and uniformity as a function of energy are easily determined. The proton beam divergence is calculated from the subtended half-cone angle of the radius of a circular fit to the proton beam. The circularity of the proton beam dose profile is calculated as the ratio of the circumference of the proton beam to the circumference of the circular fit. The uniformity of the proton beam is characterised by the variation parameter $\sigma_{N_p}/\bar{N_p}$ by calculating the standard deviation σ_{N_p} and mean $\bar{N_p}$ of the proton signal across a sample of the beam profile.

The energy spectrum can be approximated by determining the number of protons N_p detected at each layer, with a central Bragg peak energy E_{Bpk}. The value of N_P is essentially proportional to the total energy E_{Total} deposited within the layer. The total energy deposited in a layer, with thickness d_l and density ρ_l, can be determined by summing up the measured dose (D) and area (A) for each pixel i:

$$E_{Total} = d_l \rho_l \sum_{i=1}^{N} (D_i A_i) \tag{4.1}$$

$$N_p = \frac{E_{Total}}{E_{Bpk} dE} \tag{4.2}$$

The energy width, dE, is the difference in energy between protons stopped at the front and protons stopped at the back of the RCF active layer.

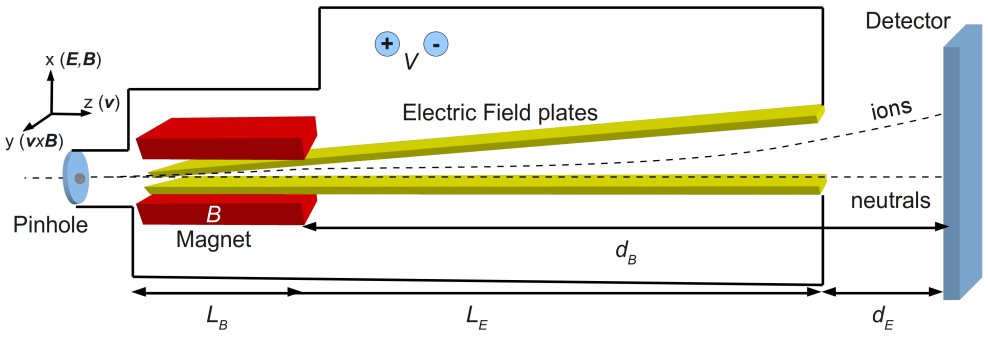

FIGURE 4.7: Schematic of the modified Thomson ion spectrometer. Ions are incident from the left and are dispersed by charge and energy via electric/magnetic fields.

4.3.1.2 Thomson parabola spectrometer (TP-Spec)

The emission of ions from laser solid interactions can involve a number of different species with distinct charge states. The electromagnetic fields of a Thomson spectrometer can separate and resolve the number and energy of the ion species and charge states into parabolic tracks onto a suitable detector. A high voltage ($V = 5\,\mathrm{kV}$) power supply generates the electric field between two copper plates with length along the x-axis of $L_E = 200\,\mathrm{mm}$ for the specific spectrometers used in this work. The magnetic field is produced by two permanent square NdFeB magnets with $B = 0.6\,\mathrm{T}$ and length $L_B = 50\,\mathrm{mm}$. After exiting the fields the ions continue to propagate until absorbed by a detector creating a spatial image of the dispersed ions and neutrals. The distances between the end of the electric and magnetic fields and the detector plane are d_E and d_B, respectively. A schematic of the instrument is shown Figure 4.7. The arrangement of the electric field plate is a novel feature of this particular design [188]. At the entrance of the spectrometer the plates are separated by $d_0 = 2\,mm$ which increases linearly to a value of $d_{max} = 22.5\,\mathrm{mm}$ at the exit. The angle between the plates is defined using $\theta_E = \tan^{-1}(d_{max}/L_E) \approx 6°$. The electric field ($\boldsymbol{E}$) can be described using the co-ordinate system shown in Figure 4.7 where its magnitude at a given point between the electric plates is calculated using the vector form [189]:

$$\boldsymbol{E}\,(x, y, z > z_0) = \begin{bmatrix} E_x \\ E_y \\ E_z \end{bmatrix} = \begin{bmatrix} \frac{z\boldsymbol{E}}{(x^2+z^2)\theta_E} \\ 0 \\ \frac{-x\boldsymbol{E}}{(x^2+z^2)\theta_E} \end{bmatrix}$$

Both electron and magnetic fields are directed along the x-axis, although the respective forces are orthogonal. The ions with velocity v_i along the z-axis are deflected by a $v_i \times \mathbf{B}$ force in the y-axis and by the electric field in the x-axis. The charge-to-mass ratio (q/m_i)

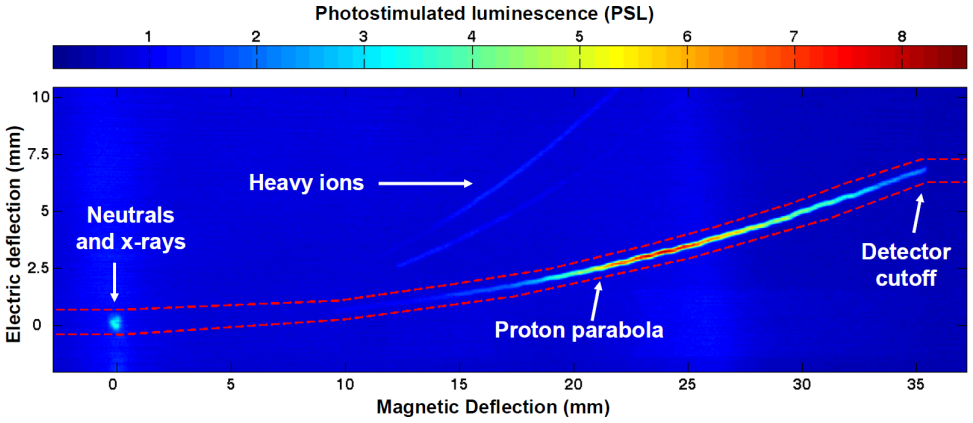

FIGURE 4.8: Example TP-Spec data scanned from image plate with pixel values converted from quantum level to PSL [190]. The proton spectrum is measured within a sample region, defined using dashed red lines. The deflection along the magnetic axis can be used to generate the energy spectrum.

of the ions determines the relative displacement for both fields [188]:

$$D_E = \frac{q_i \mathbf{E} L_E}{m_i v_i^2} \left(\frac{1}{2} L_E + d_E \right) \tag{4.3}$$

$$D_B = \frac{q_i \boldsymbol{B} L_B}{m_i v_i} \left(\frac{1}{2} L_B + d_B \right) \tag{4.4}$$

At the detector plane, each ion will create a point with dispersion coordinates D_B and D_E. The neutral particles are not deflected ($D_{\mathbf{B}} = D_{\mathbf{E}} = 0$) and thus propagate along the beam axis and create a distinct reference point on the detector. Since the strength of the fields are known, a set of analytical formulae can be used to fit ion charge states to the detected tracks. The fact that the copper plates are tilted results in the ability to separate the different charge states of an ion at higher energies. Once an ion species is identified, the velocity and therefore the energy must be solved for each point along the parabola. This is done by solving the magnetic field deflection equation for v_i and then the ion kinetic energy is simply $KE_i = 0.5 m_i v_i^2$, for non-relativistic velocities. Obviously, higher energy ions will have less magnetic field deflection. Hence the parabola defines an energy scale with higher energies located towards the neutral point.

The choice of detector medium is usually between image plate and CR39[6], although multi-channel plate (MCP) with scintillator technology can also be used. The image plate is sensitive to all ionising radiation such as x-rays and electrons, and so must be adequately shielded. The photo-simulated luminescence (PSL) values of the image plate can be converted to proton number via the calibration for the TR-type image plate given by Mancic *et al* [191]. CR39 is a transparent plastic material which is unresponsive to electrons and photons and can capture 100% of the ions with stopping distance less than

[6] **C**alifornia **R**esin 39

its thickness. The impact of an ion creates a pit within the CR39 with the number of pits representing the number of ions. Since the pit is located at some depth into the material, etching of the surface material is required. This is achieved within a bath of heated sodium hydroxide solution (NaOH, e.g. 6.25 molar solution at 86°C for ≈ 0.5 hr), where the etching occurs until the pits are revealed. The pits can be individually identified with a microscope and counted as a function of D_B. The pit density limits the dynamic range of the CR39 to ions. If too high, the ion pits start to overlap and become difficult to identify individually. If too low, then distinguishing the signal from background can be an issue and statistical fluctuations are observable. Multiple etches and scans of the CR39 are typically required. While heavy ions are deposited near the front surface of the CR39, the protons are stopped throughout its thickness, with higher energy protons stopping towards the rear surface.

4.3.2 The K_α imager

This is a electron transport diagnostic which involves the collection and imaging of x-ray emission from collisions by fast electrons with the atoms or ions of the target. The K_α emission results from a specific transition of an electron in the inner-shell of the atom. An electron, bound to the K-shell of an atom, interacts or collides with a passing fast electron and is ejected from its atom. A K_α photon is radiated as an L-shell electron transits to the K-shell, with an energy characteristic for each material. A schematic for the atomic transition is shown in Figure 4.9. This radiative decay of an exited atomic state competes with Auger decay, and increasingly dominates for higher Z materials. The fraction of radiative decays for such K-shell vacancies is termed the **fluorescence yield** ω_K. The likelihood of a fast electron ionising a K-shell electron is given by the K-shell ionisation **cross-section**, which is again unique for each material. This cross-section is a function of incoming-electron energy and typically peaks at a few times the ionisation energy. After dropping from this peak, the cross-section begins to rise again for relativistic energies, as $E_f > m_e c^2$, due to the Lorentz contraction of the electron's field. An analytical model to calculate the cross-section with relativistic effects devised by Quarles can be found in Appendix B. The copper K_α cross section is shown in Figure 4.9. For this example the ionisation potential is 8.979 keV and the fluorescence photons have energy 8.048 keV. This corresponds to the K-shell potential in cold material. In hot plasmas, where $k_B T_e > 100\, eV$, the effects of bulk material heating should be considered as the ionisation potentials are modified [192].

The multitude of such K-shell interactions induced by the fast electron beam moving through the target induce the emission of a large number of K_α photons. The total

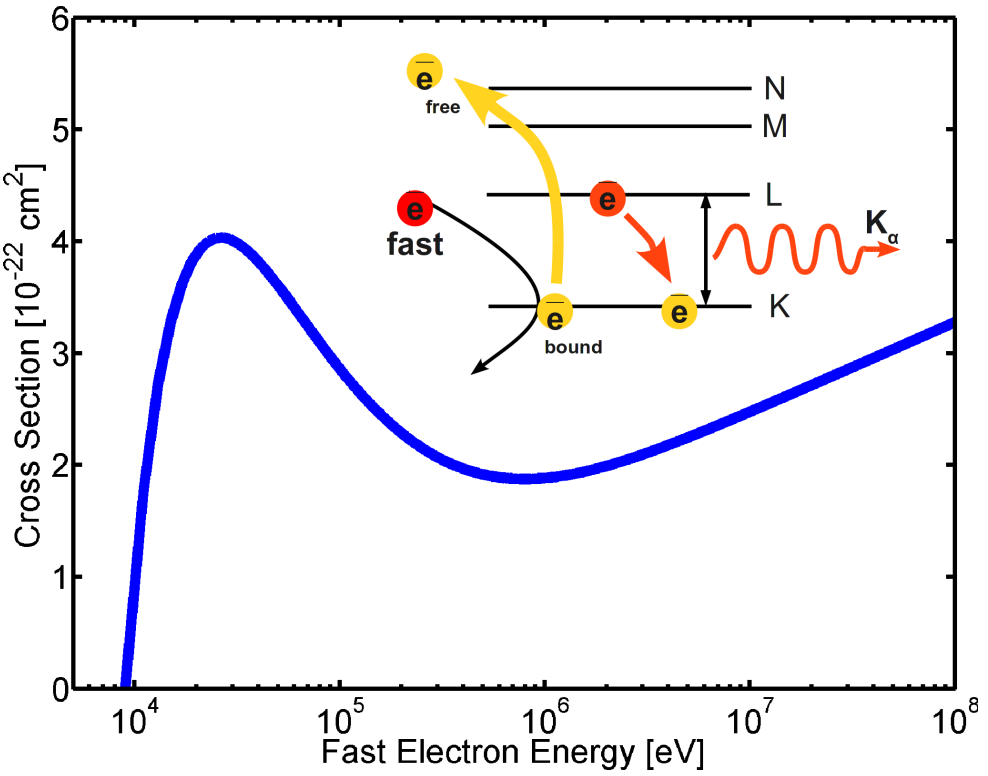

FIGURE 4.9: The interaction of a fast electron with a bound atomic K-shell electron is shown (inset). The specific atomic transition is for K_α emission. The cross-section for the K-shell interaction is shown for copper where $E_{K\alpha} = 8.048\,\text{keV}$.

number can be calculated by integrating the cross section for a distribution of fast electrons over the thickness of the fluorescence layer. Obviously, as the beam losses energy and slows down the cross-sections change, so the integration should involve intervals of distance. This will continue over thousands of microns until the energy of the beam of electrons is fully absorbed by the plasma. The random emission direction of the fluorescence results in a 4π (spherical) spread of x-ray photons with energy equal to $E_{\text{K}\alpha}$. A model to calculate the yield of photons is outlined in Chapter 7. The conditions of this investigation with $I_L = 2 \times 10^{19}\,\text{W/cm}^2$ resulted in a total yield of 10^{13} copper K_α photons per laser shot.

Besides K_α photons, a number of other emission lines would be produced as well a continuum of bremsstralung radiation. The other emission lines correspond to other atomic transitions, such as K_β for M→K-shell transitions. As the material is heated to hot plasma temperatures, the relative spectral position and intensity of the lines will change. This is the result of outer-shell ionisation and provides a useful diagnoses of the bulk plasma temperature. An atomic spectra code called FLYCHK [193] can be used to predict the effects of plasma temperature on the intensity and wavelength of the emission lines.

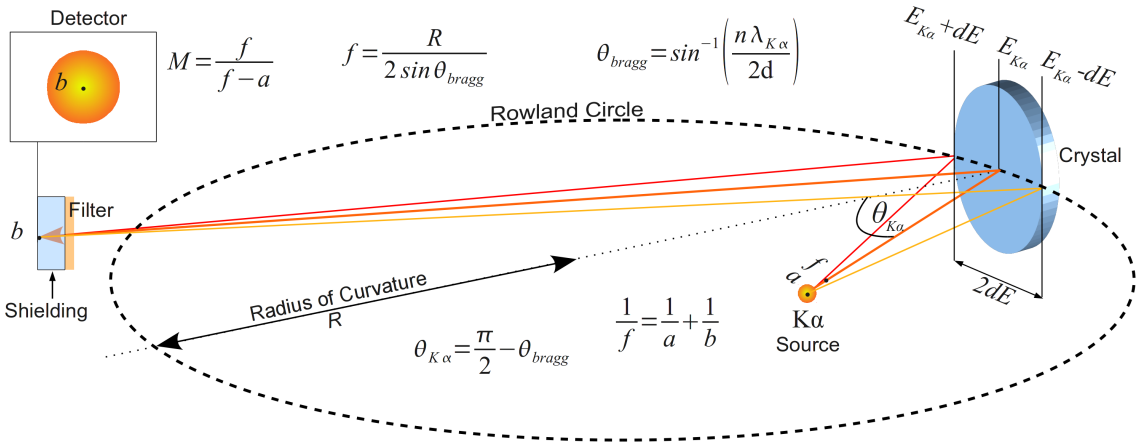

FIGURE 4.10: A schematic of the K_α imaging diagnostic with a spherical bent crystal with lattice spacing d, radius of curvature R and focal length f. The angle of incidence for a source with energy E_{K_α} relative to the crystal normal is θ_{K_α}. This is defined using the Bragg x-ray diffraction formula for a source wavelength λ_{K_α} The bandwidth of the crystal is limited by its aperture to $2dE$. The positions of source and detector relative to the crystal are defined using the lens-makers formula. The image formed at the detector has magnification M.

The purpose of the K_α imager is to collect and focus the monochromatic photons to a detector. The spatial distribution of the emission region gives information on the fast electron beam size. The collector is usually a spherically bent Bragg crystal which can reflect and focus x-rays to a detector. The photon energy collected is set by the angle of incidence from the source onto the crystal to satisfy the Bragg condition $\theta_{\text{bragg}} = \sin^{-1}(n\lambda_{K_\alpha}/2d)$ with a wavelength $\lambda_{K_\alpha} = hc/E_{K_\alpha}$. An arrangement of source, crystal and detector is shown in Figure 4.10. In the case of second order diffraction of copper K_α photons ($E_{K_\alpha} = 8.048\,\text{keV}$ and $\lambda_{K_\alpha} = 1.541\,\text{Å}$) from a crystal with spacing of $2d = 3.082\,\text{Å}$, the Bragg angle is 88.697°. The angle of incidence at the centre of the crystal should be set to $\pi/2 - \theta_{\text{bragg}} = 1.31°$. The radius of curvature (R) of the crystal determines the focal length $f = R/2\sin\theta_{\text{bragg}}$. The relative distances to the source (a) and the detector (b) distance can be calculated for a magnification $M = f/(f-a)$ using the lens formula: $\frac{1}{f} = \frac{1}{a} + \frac{1}{b}$.

The detector can be either x-ray image plate, CCD camera or x-ray film. Since the target chamber is flooded with ionising radiation a suitable shielding material such as lead is required. Also, to narrow the bandwidth of the Bremsstralung radiation reaching the detector a thin filter can be placed in front of the detector. For the case of Cu K_α, a 25 μm Cu filter will reduce the number of photons with energies above the Cu K-shell photo absorption edge. Furthermore, a separate x-ray spectrometer can provide an accurate measure of the Bremsstralung intensity at the energy of the K_α line. Background correction techniques are therefore required when evaluating the K_α imager data.

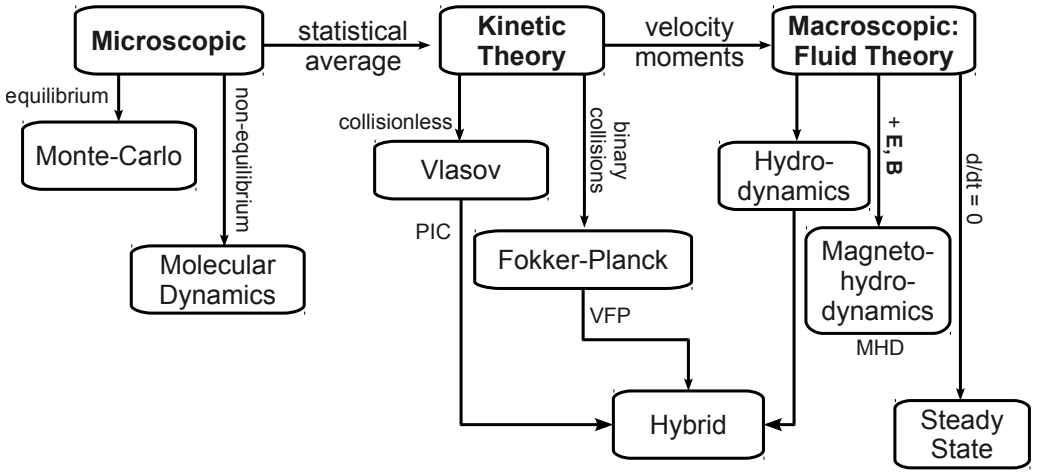

FIGURE 4.11: The physical models are shown along the top row and the common numerical approaches underneath, after Gibbon [70].

4.4 Numerical modelling

Experimentally, most of the physical electron transport parameters can only be measured indirectly, via x-ray and proton emission for example. Creating a theoretical model that includes the essential physics can provide a powerful tool for interpreting these experimental measurements. Simple analytical models can include a relatively small number of phenomena that can offer a good deal of insight to certain problems. A more complete physical picture must incorporate a large number of parameters and collective effects.

The need for increasingly accurate calculations for particle numbers, momenta and the electromagnetic fields as a function of time and space has consistently pushed the limits of numerical modelling. Indeed the limits of computational physics have co-evolved with the processing power of computers. This has been particularly significant in terms of spreading the computational load over a number of parallel processors. Clusters of hundreds of computers can effectively break down large spatial-array calculations over individual cores or processors.

The variety of interactions and plasma conditions encompass a wide range of temperatures and densities. Thus, in choosing a numerical approach, it makes sense to decide on the level of detail required to address the specific conditions of the system. Increased detail typically demands more computation requirements. For instance, the number of spatial dimensions required, the number of velocity components, the density of the plasma and the spatial and temporal extent of the simulation are all limiting factors. A generalised hierarchy of modelling techniques is shown in Figure 4.11.

The propagation of individual particles in a given material can be simulated using a particle tracking code such as GEANT4 [194]. Here Monte-Carlo algorithms calculate the collisional trajectories of a few million particles such as fast electrons through some target material. However, the transport of fast electrons, which number $\approx 10^{14}$, is governed by collective effects rather than collisions.

A simulation of the collective effects of particles in realistic numbers is presently impossible. The implementation of statistical treatments fall into two main categories: kinetic and fluid. **Kinetic simulations** follow the plasma evolution in phase space using distribution functions. This is achieved by either numerically solving the plasma kinetic equations or by simulating collective particles and their interaction via electromagnetic fields. **Fluid simulations**, in contrast, integrate over velocity phase space to maintain only very basic information about distribution functions such as the mean particle velocity (fluid velocity) and temperature (mean square velocity spread). For both treatments, the continuum of space and time are replaced with a finite set of values. This discretisation results in a grid or mesh of points in space and time. The grid can either be fixed relative to the material (**Eulerian**) or alternatively be non-fixed and travel and change with the material (**Lagrangian**). The grid points are the locations where the variables such as momentum, density and mass or fields are evaluated. The change in these physical quantities are calculated over fixed time-steps along the temporal grid. Advancing the variables to the next time step can be performed using only the previous values (**explicit**) or indeed using the new and old values (**implicit**). The latter case requires solving the matrix equations reiteratively and so is more demanding although more robust numerically. A number of kinetic approaches solve the grid-based quantities using **finite-difference** methods. Here the difference between adjacent grid points are used to solve the differentials.

While not all-inclusive, the various simulation methods can be classified as (i) Particle in Cell (PIC), (ii) Vlasov, (iii) Vlasov-Fokker-Planck (VFP), hydrodynamics and (iv) hybrid approaches.

Particle in Cell (PIC) **code**: This approach divides the simulation into a population of **macro-particles** interacting via grid-based fields. Each such particle represents some large number of electrons or ions to reduce the computational load. The number of real-particles represented by one macro-particle is scalable since the Lorentz force depends only on the charge to mass ratio, so a macro-particle will follow the same trajectory as a real particle would. These macro-particles are moved individually in Lagrangian fashion at each time step according to the Lorentz equation with field generation by Maxwell equations. The fields are solved by first mapping the particle variables onto the grid where the current and charge densities ($\mathbf{J}$ and ρ) are calculated. The fields are then

interpolated back to the positions of the particles using the same weighting process used to transfer the particle charges and currents onto the grid. The fields then provide the 'particle push'. This cycle repeats for each time step.

PIC codes are the closest to a 'numerical experiment' and make fewer approximations than any of the other methods. Compared to the Vlasov approach, a distinct advantage is that the phase space is only sampled where the macro-particles exist rather than than the entire grid space. The disadvantages of PIC methods are that (i) material properties, collisions and ionisation are not easily included, (ii) the number of particles required for solid density targets is prohibitively high, (iii) the spatial grid size and particle density should be sufficient to resolve the Debye length, while the temporal interval should be less than the plasma frequency. Changing to an implicit model can help relax the time and spatial constraints.

Vlasov code: This method numerically solves the Vlasov partial differential equations on a Eulerian grid in phase space. The Vlasov equation calculates the changes to the velocity distribution which can be solved by time integration over a temporal grid by finite differencing. With three spatial and three velocity components the Vlasov method tackles a six-dimension phase-space and hence is more demanding than the PIC approach. However, in the case of modelling electron transport, the fast electrons represent a relative small fraction of the total electrons in the simulation. In this scenario a Vlasov code can be more efficient than a PIC code. Unlike a PIC code, the Vlasov approach applies equal computational effort to the part of phase space occupied by fast electrons and to the part of phase space occupied by the majority of the plasma electrons. This attention to the entire grid is also a disadvantage, the equations are also solved in unoccupied areas of the grid. Also, unlike PIC methods, Vlasov codes do not have to spatially resolve a Debye length in all problems.

The main difficulty with a standard Vlasov code is the number of phase space grid-points needed in two spatial dimensions. A reasonable number of Cartesian grid-points in space (x, y, z) and momentum (p_x, p_y, p_z) are required. This is resource-intensive in memory and computational time. Also, a Cartesian grid in momentum space is poorly adapted to accurately model some relevant processes such as collisions and gyration in a magnetic field, which naturally move electrons diagonally across the momentum grid. The addition of collisions using the Fokker-Planck terms can enable a transform of the Cartesian phase space into spherical phase space. Characterising this angular phase space by a sequence of spherical harmonics reduces the number of velocity dimensions from three to one .

Vlasov-Fokker-Planck (VFP): The inclusion of collisions to the Vlasov equation (see

Equation 2.6) is necessary to model high density plasmas. The collisions determine how the particles propagate relative to each other, this essentially defines a number of transport effects such as resistivity. The collisional Fokker-Planck term represents the cumulative effect of many small angle collisions using a probability function. The probability can be calculated by summing over all possible binary collisions. The effects of collisions manifests in the velocity phase space of the electrons specifically by diffusion and advection effects. Advection tends to draw particles towards zero velocity by energy loss to other particles, while diffusion tends to spread the particles out in velocity space. The latter is more evident for electron beam transport in hot plasma. This diffusion smooths out the electron distribution in velocity space and hence reduces the amount of information needed for an adequate description. For a 1D example, the velocity distribution can be described with just $|\mathbf{v}|$ and an angle θ relative to the x direction, $v_x = v\cos\theta$. Bell *et al* [195] showed that this velocity distribution $f\,(x, v)$ can be reduced to a sum of Legendre polynomials $P_n(x)$ with degree n:

$$f = \sum_{n=0}^{\infty} f^{(n)}\,(x, v)\,P_n(\cos\theta) \tag{4.5}$$

For three velocity components the distribution function is described with the additional angle ϕ so that $f = f\,(p, \theta, \phi)$ using a spherical polar 3-momentum. The terms of the expansion define **spherical harmonics** with order n. The number of spherical harmonics are reduced or truncated to a small value of n as isotropisation by angular scattering damps successive $f^{(n)}$ at a rate proportional to $n(n+1)$ so the large n terms in the series are close to zero. In many cases it is sufficient to keep only the first two terms in the series, in which case the distribution can easily be generalised into two or three dimensions.

$$f(\mathbf{r}, \mathbf{v}) = f^{(0)}(\mathbf{r}, v) + \mathbf{f}^{(1)}(\mathbf{r}, v) \cdot \frac{\mathbf{v}}{v} \tag{4.6}$$

where the vector $\mathbf{f}^{(1)}$ has components in the x, y and z directions. At any spatial point, the electron density in the whole of the velocity space is represented by the four functions $f^{(0)}$, $f_x^{(1)}$, $f_y^{(1)}$, $f_z^{(1)}$ which are functions of the one-dimension magnitude v of the velocity instead of the 3D velocity vector $\mathbf{v}$, thus reducing the number of velocity dimensions from three to one. This represents a large reduction in information content and a large saving in computing effort. For this reason, a finite difference VFP code is much faster than a PIC code with collisions for most problems of relevance to fast electron transport.

Hydrodynamic codes treat the plasma as a fluid, usually as a single fluid, using the hydrodynamic equations mapped over a grid which can be Eulerian or Lagrangian. The hydrodynamic treatment is discussed in Section 2.3.1 and includes equations of state (relating pressure to the internal energy of the plasma) and mass/momentum

conservation. Hydrodynamic codes generally do not directly include Maxwell's equations of electromagnetism (the laser is generally treated as a heating term). The inclusion of magnetic field generation via magnetic induction (dB/dt) enables the determination of the electric field via Ohm's law. With this addition the model is referred as a MHD code for **Magnetic-HydroDynamics**. The parameters that hydrodynamic codes solve for are flow velocity, mass density, pressure, temperature and the magnetic field.

Hybrid: The kinetic and fluid models can be effectively combined to address distinct populations of plasma particles. Such hybrid codes can provide very efficient simulation of solid targets dominated by fast electron transport. Here the bulk background plasma is treated as a fluid while the relativistic fast electrons are described via a kinetic model [164]. The latter can be either PIC or VFP. The role of the background plasma is to model the material properties of the target material, such as resistivity and ion density. The transport of fast electrons through the target induces a response from the background plasma involving heating and field generation. While the background fluid is typically static, the development of a dynamic treatment of the plasma is desirable. Recent results from a hybrid-VFP code called FIDO have demonstrated distinct differences in beam transport over multi-picosecond timescales using a dynamic rather than a static fluid background [163].

4.4.1 Hydrodynamic simulations: POLLUX

POLLUX [196] is a hydrodynamic code, written in Fortran, and is a 'stripped down' version of the magnetic-hydro code MAGT [197]. POLLUX performs 2D hydrodynamic simulations within a defined simulation box subdivided into a Eulerian spatial mesh. A target material is defined with a given thickness and position within the simulation box. The parameters of the material are density, mass number and Z-number. The equation of state utilised is the perfect-gas equation of state. The electrons are heated by inverse bremsstrahlung from the laser heat flux close to critical density. The main physical effects not included in the code are a real equation of state and the transport of thermally produced x-rays.

For the work of this thesis, POLLUX is predominantly used to predict the plasma expansion induced by the laser pedestal and pre-pulse. The effects of which are characterised by extracting the electron density on-axis after a few nano-seconds and calculating the scale length parameter. POLLUX requires modest computation resources, using a single CPU, and thus can run effectively on a personal computer.

4.4.2 Electron transport simulations: LEDA

LEDA is 2D hybrid code, written by A. P. L. Robinson [198] and is used to model field generation, filamentation and other collective effects regarding electron transport within a range of target materials. The code requires a cluster of processors to share the computational load using Message Passing Interface (MPI). Two such clusters, HIPPO at the University of Strathclyde and SCARF at RAL, facilitated the LEDA runs. Both clusters were accessed remotely, HIPPO via 'secure-shell' (ssh) protocol and SCARF requiring connection via the national grid. In the latter case up to a hundred nodes or CPU's were used per job with a typical duration of $10 - 24$ hrs.

The hybrid approach employed in LEDA treats the background plasma as a static fluid and the fast electrons are described using the VFP equation, as discussed above. The simulation space is filled with target material which acts as the transport medium. The material is predefined by Z-number, ion density and an initial temperature. The material resistivity is an important feature in the generation of electric and magnetic fields in response to the fast electrons. A resistivity curve is defined for each material. This characterises the value of resistivity at any temperature. The specific heat capacity determines how the material heats up in response to the heating $\Delta Q = W.dt$ from energy deposition by Ohmic heating and collisions over each time-step dt. The heat capacity at constant volume is calculated using the Thomas-Fermi model as used by Davies [164]:

$$C = 0.3 + 1.2 k_B T_e' \frac{2.2 + k_B T_e'}{(1.1 + k_B T_e')^2} \tag{4.7}$$

The temperature at the previous time step $k_B T_e$ is used to calculate C where $k_B T_e' = Z^{-4/3} k_B T_e$ [eV]. The change in material temperature is therefore $\Delta k_B T_e = \Delta Q / C$. Measurements of resistivity exist for some materials, such as Al [51] and Cu [199], for temperatures below ≈ 100 eV. The value of η beyond this limit can be estimated by the Spitzer resistivity. Thermal conduction is included in LEDA.

The fast electrons are described by a separate set of algorithms, specifically a KALOS[7] algorithm [121]. Here the Vlasov-Fokker-Planck equation is solved by representing the electron distribution function in momentum space by an expansion in spherical harmonics. The distribution function is solved using a finite difference method which discretises the continuous distribution function onto a grid. The fast electrons are injected into the target over the pulse length of the laser assuming a Maxwellian distribution:

$$f_{injected} \propto \cos^M \theta p^2 \exp\left[-\frac{\sqrt{p^2 + m_e c^2}}{k_B T_f} \right] \tag{4.8}$$

[7] KALOS: Kinetic Laser-plasma Simulation

The temperature of the distribution, $k_B T_f$, is determined by the ponderomotive scaling [73] if $I_L > 10^{19}\,\mathrm{W/cm^2}$, otherwise the Beg [104] scaling is used. The fast electrons are injected with a divergence half-angle of $\theta_{1/2} \approx 67^\circ/\sqrt{M} \approx 25^\circ$ for $M = 8$. The transport of the fast electrons is governed by field generation, collisions and heating. Upon reaching the boundaries of the simulation space the fast electrons are reflected which is similar to the physical mechanism of refluxing investigated in Chapter 7.

Chapter 5

Effect of self-generated magnetic fields on fast electron beam divergence in solid targets

5.1 Introduction

The divergence of a relativistic electron beam propagating inside a solid density target is of fundamental significance to the understanding of fast electron transport in over-dense plasma. This is particularly relevant to the design parameters of electron based Fast Ignition. Here, the beam divergence defines the maximum electron source size (hence the laser spot size) and the maximum distance between the electron source and the fuel assembly [200]. Accurate knowledge and control of the fast-electron beam divergence is crucial for a successful demonstration of the electron-based Fast Ignition scheme and for the enhancement of laser-driven ion sources.

As described in Section 3.2, the azimuthal magnetic field produced by the return current can in principle be responsible for fast electron collimation as described theoretically by Davies *et al* [52], Bell and Kingham [94] and Honrubia *et al* [200]. An order of magnitude estimate of expected collimation can be made using the Bell-Kingham expression [94]:

$$\Gamma = 0.022 \left[\frac{n_e}{10^{29}\,/\mathrm{m}^3}\right] \times \left[\frac{P_f}{10^{12}\,\mathrm{W}}\right]^{-1} \times \left[\frac{r_f}{10^{-6}\,\mathrm{m}}\right]^{2} \times \left[\frac{k_B T_f}{0.511\,\mathrm{MeV}}\right]^{1/2} \times \left[2 + \frac{k_B T_f}{0.511\,\mathrm{MeV}}\right]^{-1/2} \times \left[\frac{k_B T_e}{1\,\mathrm{keV}} - \frac{k_B T_{e0}}{1\,\mathrm{keV}}\right] \left[\frac{\theta_{1/2}}{\mathrm{rad}}\right]^{-2} \tag{5.1}$$

which predicts collimation when the factor $\Gamma > 1$. In the above expression, P_f, $k_B T_{e0}$ are the fast electron beam power and the initial plasma temperature, the other variables

have been defined in previous chapters. The collimation effectiveness, Γ, is strongly coupled to the fast electron beam radius and divergence. There is a clear competition between the transverse spread of the electrons imparted by the injection process and the azimuthal magnetic field which evolves with current density and resistivity. Beyond this simple picture it is apparent there are complex inter-dependencies which create both positive and negative feedback which drive or dampen the pinching effect.

Numerical studies indicate that the initial divergence of the beam is attributed to the scattering of fast electrons in the fields generated by the collisionless Weibel instability region near the critical surface [116]. After injection into the material, strong localised self-generated magnetic fields can counteract this scattering, reducing the initial beam divergence. As discussed in Section 3.2.1, the collimating fields are expected to be strongest at the injection zone where the current density is greatest. These injection fields are expected to be limited to depths of tens of microns within the target [142]. Hence, to provide a constraint of beam divergence over depths of hundreds of microns, necessary for Fast Ignition, global (whole beam) magnetic pinching is required. A review of the experimental attempts to measure beam divergence and magnetic pinching is presented in Section 3.4. Measurements up to now have indicated tentative [144] or indeed no evidence [146, 147] for global magnetic pinching in a homogeneous plasma [201].

The work presented in this chapter employs a different experimental approach for measuring the effect of magnetic collimation on fast-electron beam transport. This is based on measurements of multi-MeV proton emission from the rear of Al targets over a large range of thickness ($25\,\mu\text{m} - 1400\,\mu\text{m}$). The effects of global magnetic pinching are examined as follows: Firstly, the measurements are compared to analytical predictions where the fast electron transport is ballistic i.e. no magnetic collimation. Secondly, the initial transverse size of the electron sheath at the rear surface is inferred from the experimental measurements. Finally, numerical simulations are carried out to provide a comparison to the experimental measurements. These results have been published in *New Journal of Physics*, **12** (2010), 6, 063018.

5.2 Experimental method

The experiment was carried out using the Vulcan Petawatt laser at the Rutherford Appleton Laboratory which is described in Section 4.2.1. During this campaign, the laser energy on target, E_L, was $280 \pm 20\,\text{J}$, with duration, τ_L, equal to 1 ps (full width at half maximum, FWHM) and wavelength equal to $1.053\,\mu\text{m}$. The p-polarized pulses were focused with an $f/3$ off-axis parabolic mirror onto target at an incident angle equal

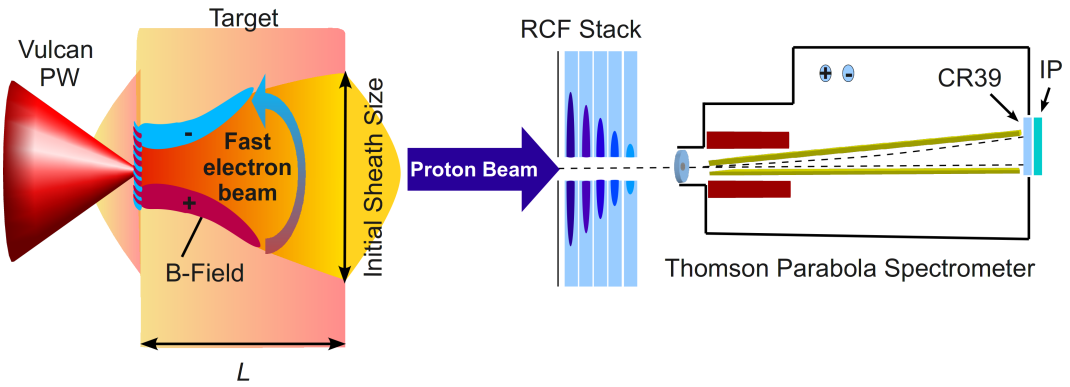

FIGURE 5.1: Schematic of experimental setup investigating magnetic collimation of electron transport through the target. Self-generated magnetic fields surround the electron beam and can in theory reduce beam divergence. The initial electron sheath size is diagnosed using proton emission as a function of target thickness.

to 13° with respect to the target normal axis, and to a calculated peak intensity of $5 \times 10^{20}\,\mathrm{Wcm^{-2}}$. The laser pulse parameters were fixed throughout the experiment.

Fast electron transport in aluminium foil targets was investigated. These targets measured 3 mm × 7 mm with thickness, L, varied in the range 25 μm to 1.4 mm. The primary diagnostic was a passive stack of 5 cm × 5 cm dosimetry film (RCF: Gafchromic film, HD-810 and MD-V2-55) positioned 6 cm from the rear of the target and centred on the normal axis to the target. The RCF stack measures the spatial intensity distribution of the beam of accelerated protons at energies given by the Bragg peak deposition in each piece of film, see Section 4.3.1.1. A Thomson parabola ion spectrometer (TP-Spec) was positioned behind the stack pointing along the target normal axis through a 3 mm wide slot machined in the RCF stack. A schematic of the experimental setup is shown in Figure 5.1.

5.2.1 Experimental measurements

The maximum proton energy (E_{max}) as a function of target thickness (L) is shown in Figure 5.2. Both RCF and TP-Spec measurements are in close agreement. The measured trend of E_{max} with L is the most salient result of this investigation. This differs sharply from what is expected on the basis of simple ballistic transport (i.e. constant divergence) of fast electrons through the target. Previous measurements have indicated ballistic transport in Al targets ($L < 200\,\mu$m) for lower laser pulse duration, energy and intensity [169, 202].

The expected E_{max} as a function of L calculated using a ballistic transport model are also shown in Figure 5.2. The ballistic model predicts E_{max} using a 1-D isothermal plasma expansion formulae derived by Mora [25], which has been successfully applied previously

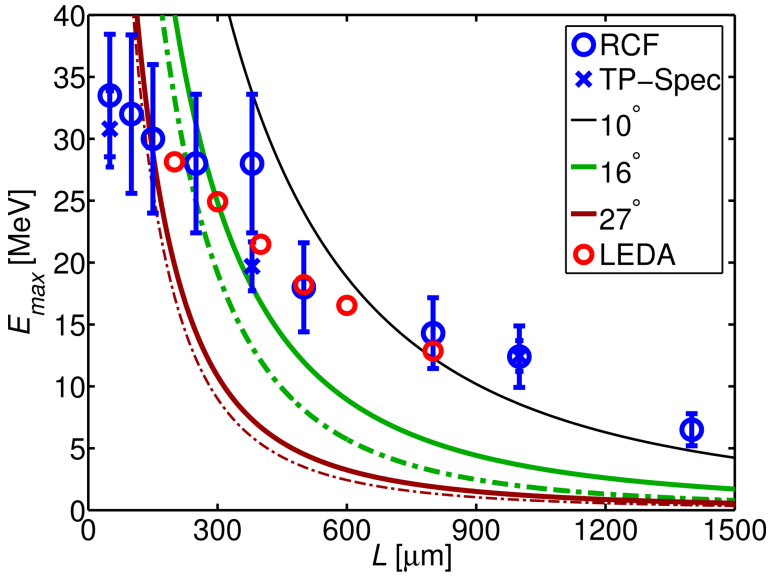

FIGURE 5.2: Maximum proton energy as a function of target thickness is shown for Al foils. Measurements made using RCF and a Thomson parabola spectrometer (TP-Spec) are shown as blue symbols. Error bars represent the variation over multiple shots and the energy resolution. The solid lines correspond to calculations using a ballistic electron transport model at given fixed divergence angles. The dashed lines include a correction due to scattering within the target. The red symbols are the result of plasma expansion calculations using electron densities determined from electron transport simulations using the LEDA code.

for similar laser and target parameters [169, 172, 202]. Further details are discussed in Section 5.3. Here the fast electron density at the target rear is determined assuming a given constant half-angle of divergence, $\theta_{1/2}$. From previous work, the value of $\theta_{1/2}$ for relatively thin targets was measured to be $\approx 27°$, see Green *et al* [146]. Predictions using other values of $\theta_{1/2}$ are also shown for comparison, Storm *et al* [136] inferred half-angle divergence of 10° and 16°. These ballistic predictions share a consistent trend of a more rapid decrease in E_{max} with L compared with the more linear dependence of the experimental measurements.

5.3 Ballistic model predictions

A schematic of the ballistic model used previously by Fuchs *et al* [169] is shown in Figure 5.3. This illustrates the steps involved in calculating the proton E_{max} with the assumption of a constant electron beam divergence. Details regarding these steps are listed here:

1. Generate fast electrons: it is assumed that 25% of the laser pulse energy is converted into fast electrons ($E_{L\rightarrow e} = 0.25$). This is within the range of measured values discussed in Section 2.5.4. The mean electron energy $k_B T_f = 7.4$ MeV,

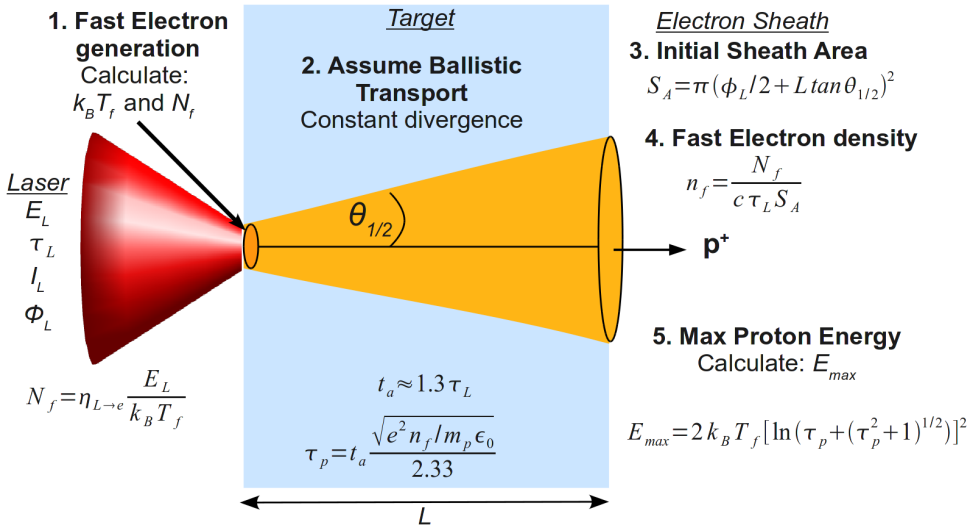

FIGURE 5.3: Schematic of ballistic model to calculate proton max energy.

as given by ponderomotive scaling [84]. This is assumed to remain constant with increasing L, which is justified on the basis of electron transport simulation results discussed in Section 5.5. The number of fast electrons generated is determined as $N_f = \eta_{L\Rightarrow e} E_L / k_B T_f = 6 \times 10^{13}$.

2. Assume ballistic transport: This number of fast electrons are assumed to propagate through the target with constant divergence $\theta_{1/2}$

3. Electron sheath: The electrons form a uniform layer at the rear surface defining the sheath area (S_A) which is a function of L, $\theta_{1/2}$ and ϕ_L.

4. Sheath density: The fast electron density within this sheath (n_f) is determined.

5. Maximum proton energy: The value of E_{max} is calculated using the Mora formula, see Equation 3.63. The proton acceleration time t_a is $1.3\tau_L$, as used previously by Fuchs *et al* [169].

The calculated E_{max} as a function of L from this model is shown in Figure 5.2 for $\theta_{1/2} = 10°$, 16°, and 27°. While variation of the parameters $\eta_{L\to e}$ and t_a changes the predicted maximum proton energies this does not significantly change the overall shape of the predicted E_{max} as a function of L curve and thus cannot reproduce the measurements.

The ballistic model has been adjusted to include the effects of electron scattering from target atoms, these results are also shown in Figure 5.2 (dashed lines). The scattering effect is estimated using the Monte Carlo code GEANT4 [194] to simulate a group of 8 MeV electrons propagating through a 2 mm aluminium target with a given divergence. The lateral extent of the scattered electrons is calculated at the rear surface as a function of target thickness. A slight increase in the sheath size is measured which has the effect

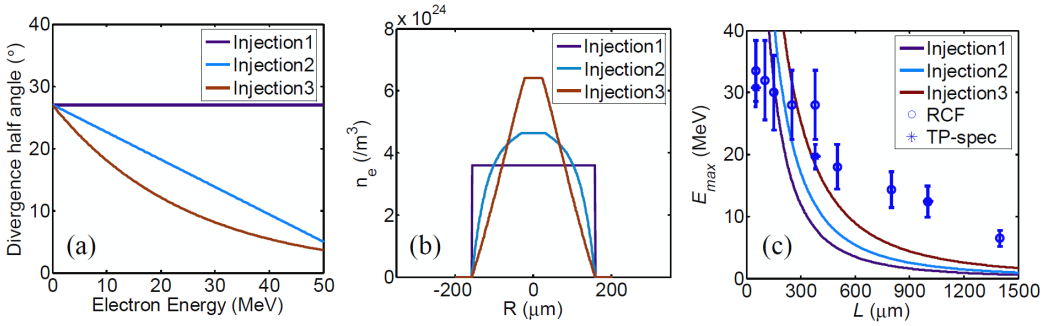

FIGURE 5.4: Ballistic model results for three different fast electron injection angle configurations. (a) Example distributions of fast electron beam injection half-angle with energy; (b) The corresponding electron density distribution at the rear surface of a 300 μm-thick target; (c) The resulting maximum proton energies as a function of target thickness as calculated using the Mora plasma expansion formulae. The calculations include the effects of electron stopping in the target.

of reducing the sheath density n_f, and therefore E_{max}. However, the effective trend is unchanged.

Also considered is the interplay between the fast electron injected angular distribution as a function of energy and electron stopping within the target. If the electron beam injection angle decreases with increasing energy, the increased stopping of low energy electrons within the target may reduce the overall transverse extent of the fast electron distribution as the target thickness is increased. To investigate whether this effect could account for the measured distribution, the expected E_{max} is calculated as a function of L assuming different distributions of electron divergence angle with energy and incorporating electron stopping. Three different injection functions are modelled as shown in Figure 5.4(a). 'Injection 1' corresponds to a constant injection angle, resulting in a uniform electron density at the target rear as shown in Figure 5.4(b). This is the distribution used in the calculations shown in Figure 5.2. The divergence angle decreases linearly with energy for 'Injection 2', which results in a parabolic sheath profile, and 'injection 3' corresponds to an exponential decrease in divergence angle with energy and results in an approximately trapezoidal sheath profile, as shown in Figure 5.4(b). The effects of fast electron stopping within the target are included in the calculations. An electron with a kinetic energy of 1 MeV has a stopping distance of about 2 mm [152] and hence the bulk of the fast electrons pass through the target with little energy loss. Furthermore, because the target is a metal, the effects of resistive inhibition [203] are far less than a insulator material [66]. The results of applying the Mora plasma expansion formula for the densities determined with the three different injected electron distributions (assuming $k_B T_f = 7.4$ MeV and $t_a = 1.3\tau_L$, as discussed above) are shown in Figure 5.4(c). The electron divergence distribution clearly affects the maximum proton energy, but does not account for the nearly linear decrease in E_{max} with L measured.

The fact that the model over estimates E_{max} for thin targets maybe attributed to the initial transverse extent of the fast electron source. The model assumes this to be on the same order as the laser spot size, $\approx 5\,\mu$m, whereas there are measurements suggesting a larger initial source size may be applicable $\approx 20 - 40\mu m$ [141, 147, 204]. Such an extended initial front surface source diameter would effectively reduce the rear surface sheath density therefore reducing $E_{max}(L)$ without changing the shape of the ballistic prediction curves.

As demonstrated above, the measured dependence of E_{max} on L cannot be explained by ballistic transport of fast electrons through the target at a constant angle of divergence. In order to reproduce the results the electron beam divergence must reduce with increasing L. The implication is that self-generated fields in the target must be reducing the transverse spreading of the beam (particularly in thicker targets). Magnetic pinching is the obvious candidate for this effect.

5.4 Initial sheath size model

The initial arrival of the fast electron beam at the rear of the target defines the initial transverse size of the electron sheath before it expands along the surface [167]. The evolution of the sheath from this initial transverse size is subsequently responsible for the measured characteristics of the proton beam. The initial sheath size and therefore the effective divergence of the fast electron beam can in principle be determined by reverse engineering the measured proton beam. In order to quantify the change in the transverse size of the initial electron sheath with target thickness, the evolution of the sheath and ion front in space and time are modelled using an approach discussed below.

A schematic of the sheath evolution model is shown in Figure 5.5(a). The key input parameters are the initial electron sheath size, D_e and the maximum electric field strength E_0. The model result is a distribution of proton beam divergence with energy $\theta(E_p)$ - this is compared to the experimental measurements. The values of D_e and E_0 are varied until the distributions match. The value of E_0 controls the cut off energy of the distribution, it can be easily set in the model to match the measured value of E_{max}. The shape of the divergence distribution is sensitive to D_e, this value is adjusted so that a best fit in $\theta(E_p)$ results with experiment. The process is repeated for each target thickness yielding a value of $D_e(L)$. The strength of the sheath field $E(y,t)$ evolves in time (t) and space (y) while inducing ionisation and then acceleration of protons from the rear surface. The plane of the target rear surface is taken as the y-axis. .

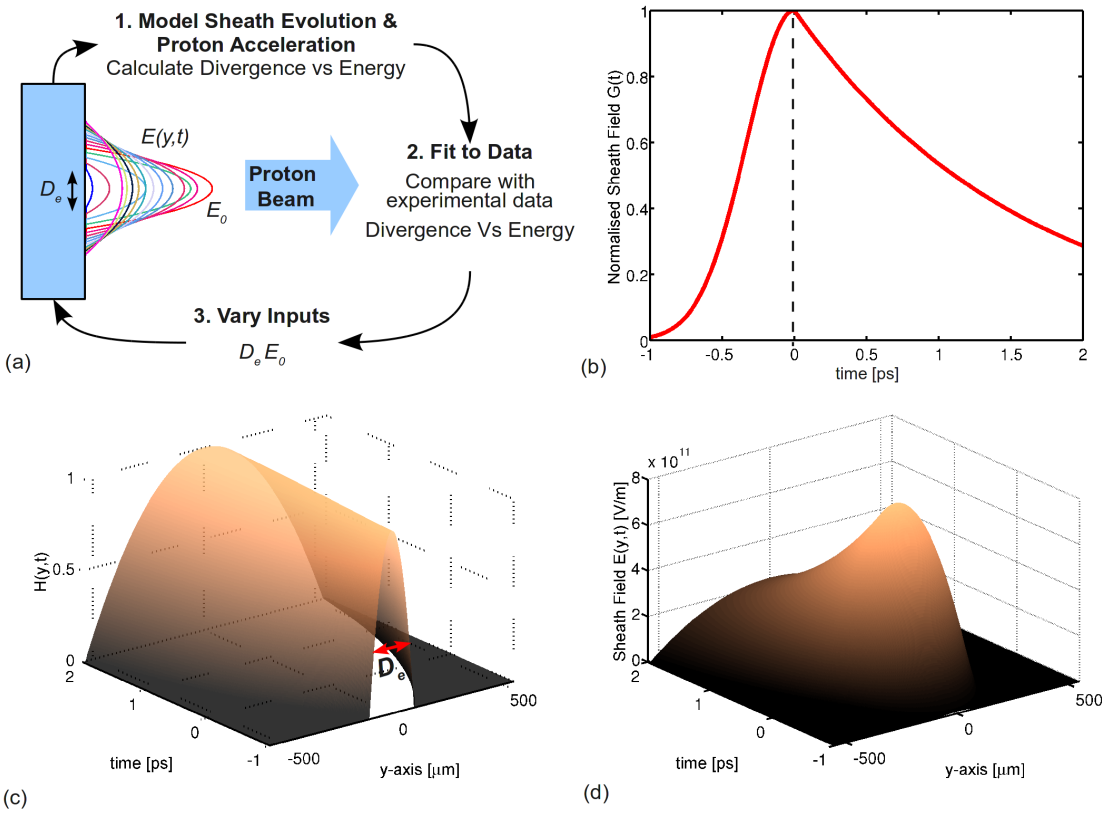

FIGURE 5.5: (a) A schematic of the sheath evolution model is shown. (b) The temporal evolution of the sheath field, referred to as $G(t)$ in the text, increases up to the peak field at time = 0 and decreases exponentially afterwards. (c) The sheath shape is parabolic and spreads along the rear surface defining $H(y,t)$. (d) The spatial and temporal sheath field $E(y,t)$ is shown with peak field of $E_0 = 0.8\,\mathrm{TV/m}$.

The model of the sheath evolution involves three considerations regarding (i) the shape of the sheath; (ii) the transverse expansion velocity of the sheath as a function of time; and (iii) the temporal evolution of the magnitude of the sheath electric field. The sheath field shape is assumed to be parabolic, based on the conclusions of Brambrink *et al* [205]. Other sheath shapes were also considered including Gaussian and hyperbolic profiles, but did not reproduce the measured proton beam divergence as a function of energy. The parabolic sheath field peaks on axis and spreads along the rear surface over time. The initial transverse sheath expansion velocity is set equal to c, as reported in previous work for very similar laser parameters [167, 175], and decreases exponentially with time, with $1/e = 1.6$ ps, consistent with optical probe reflectometry measurements by Antici *et al* [206]. The field strength increases with the rising edge of the laser pulse with a Gaussian profile to a maximum value, E_0, set by the measured E_{max} and follows an exponential decrease thereafter (with $1/e = 1.6$ ps), as also inferred from previous work [167, 207].

The sheath expansion begins at time $t = t_i$. The normalised sheath field strength, $G(t)$,

increases and reaches peak strength at $t = 0$, afterwards the field strength decreases. The temporal profile of the sheath field is shown in Figure 5.5(b) and is calculated using the Gaussian and exponential terms. The shape of the parabolic sheath is defined in one spatial dimension as $H(y,t)$ using $p(t)$ defined using the FWHM width $W(t)$. The rear surface sheath field evolves in strength and spreads transversely along the rear surface over time. The evolution of this field, $E(y,t)$, is calculated by the product of $G(t)$, $H(t)$, E_0 as shown and also in Figure 5.5(b-d).

$$G(t) = exp\left(\frac{-4\ln(2)t^2}{\tau_L^2}\right) \quad [\mathrm{t} < 0] \tag{5.2}$$

$$G(t) = exp\left(\frac{-t}{1.6 \times 10^{-12}}\right) \quad [\mathrm{t} > 0] \tag{5.3}$$

$$H(y,t) = 1 - \frac{y^2}{4\,p(t)} \tag{5.4}$$

$$p(t) = \frac{W(t)^2}{8} \tag{5.5}$$

$$E(y,t) = E_0 G(t) \cdot H(y,t) \tag{5.6}$$

Field ionisation of hydrogen along the target surface provides a population of protons which are then accelerated away from the target under the influence of the sheath field and define an ion front [67]. The spatial extent and profile of the expanding ion front, and thus the emitted angle of protons produced along the front, are calculated as a function of time. The energy resolved divergence of the final proton beam is compared with the equivalent experimental measurements. The reiteration ends when a close fit of model and measurement is achieved, this fixes the value for initial electron sheath size D_e and is repeated for each experimental measurement.

5.4.1 Bench-marking the model

Two methods involving calibrated measurements of proton source size are used to bench-mark the sheath evolution model. As discussed above, the model fits to the measured proton beam divergence versus energy to arrive at the initial electron sheath size D_e. The resulting proton source size D_p is compared with the equivalent calibrated source size measurement to test the validity of the model.

In the first case, the model predictions are compared to measured proton beam data from a 'grooved' target. This is a 25 μm-thick Au target with lines (grooves with separation equal to 10 μm and depth equal to 1 μm) manufactured into the rear surface [174]. The line structure is mapped into the measured proton spatial intensity profile and the proton source size as a function of energy is determined by counting the lines in each RCF layer [174]. The fit of model to measured beam divergence is shown in Figure 5.6(a).

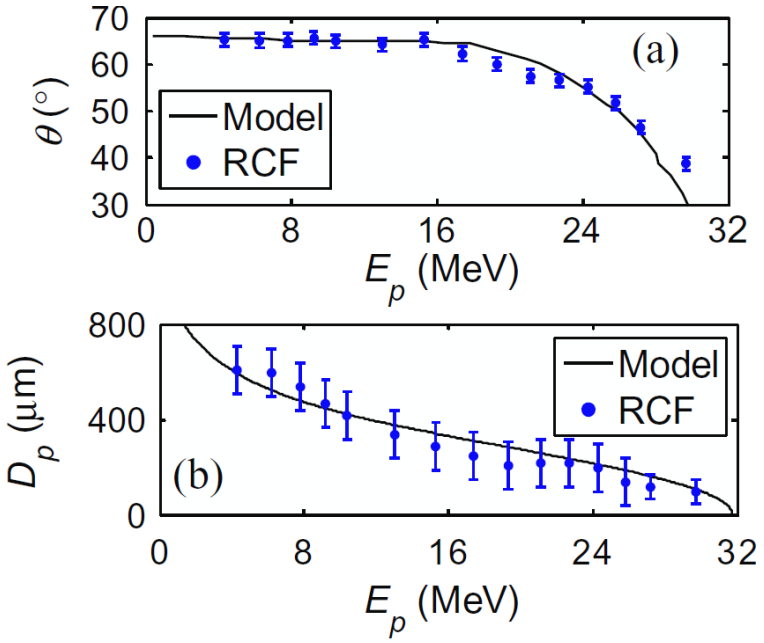

FIGURE 5.6: Bench marking of sheath size model using RCF data from a 25 μm grooved target irradiated by the Vulcan PW laser. Comparison of (a) proton beam divergence and (b) proton source size as calculated using the sheath expansion model with measurements made by irradiation of a target with linear grooves machined into the rear surface.

The predicted proton source size matches very closely to the actual measured values as a function of energy.

In the second method involving a regular foil target, the energy resolved proton source size is provided by TP-Spec measurements. Here, the lateral extent of the spectrally dispersed track provides $D_p(E)$. This is shown in Figure 5.7(a-b). The beam divergence is provided by RCF stack measurements for this same shot. The resulting prediction for $D_p(E)$ once again is in close agreement with the known size as shown in Figure 5.7(c).

5.4.2 Model results

This initial sheath size model is applied to the proton beam measurements used in Figure 5.2, the resulting initial sheath size (full-width) as a function of L are shown in Figure 5.8. For relatively thin targets ($L < 300$ μm) the increase in D_e with increasing L is consistent with an approximately constant divergence angle of $\approx 27°$. A transition is observed at around $300 - 400\,\mu$m, above which the growth in D_e with L is much lower than expected from ballistic transport. Indeed the beam divergence is shown to decrease to $\leq 16°$.

This reduction in the effective beam divergence in thick targets is likely to result from the pinching effect of the azimuthal magnetic field resistively self-generated by the fast

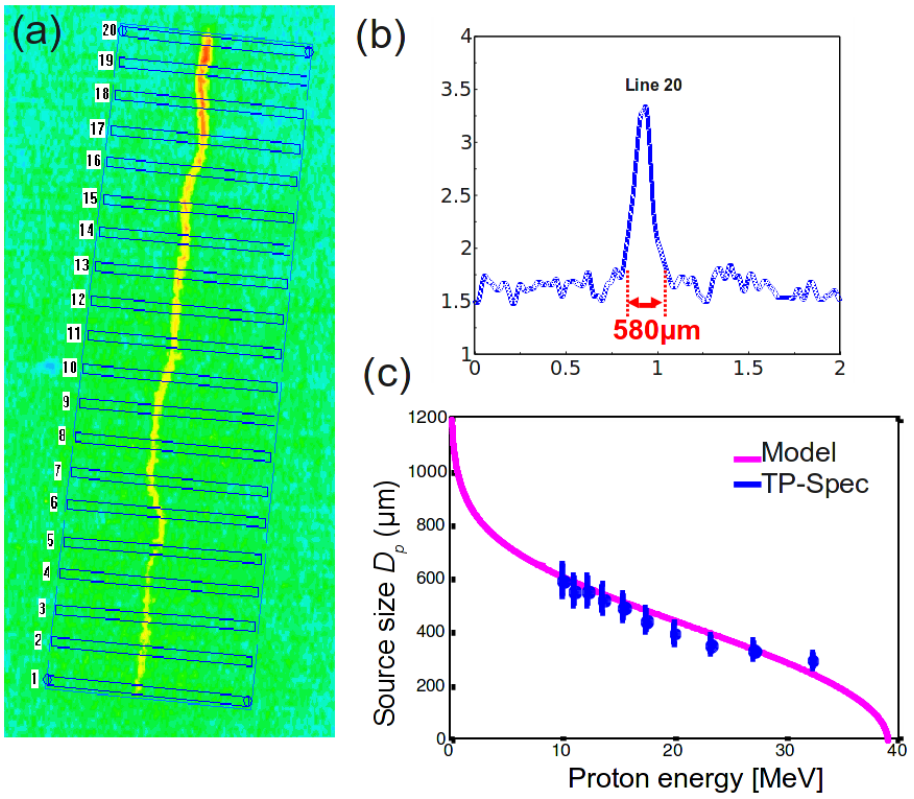

FIGURE 5.7: Bench-marking sheath size model with TP-Spec data. (a) Measured TNSA proton spectrum from Vulcan PW laser interaction with 250 μm Al target. The lateral extent of the proton track provides a measure of the proton source size at a given energy. An example profile is shown in (b). The results of the sheath size model is compared with the proton source size measurements in (c).

electron beam [94]. For the conditions of the experiment the Bell-Kingham expression (Equation 5.1) gives $\Gamma \approx 14$ and predicts some collimation to occur. From the values used here, ($r_f = 25\,\mu$m, $\theta_{1/2} = 20°$, $P_f = 100\,$TW assuming $\eta_{L\to e} = 0.25$, $n_e = 6 \times 10^{29}\,/\mathrm{m}^3$ for $k_B T_e = 500\,$eV), the Bell-Kingham prediction for collimation exhibits a significant sensitivity on both the initial electron source radius r_f and divergence $\theta_{1/2}$. The growth of the self-generated magnetic field is also governed by the target material properties [94] particularly resistivity which varies with bulk heating. The apparent lack of beam pinching for $L < 300$ μm may be related to electron refluxing within the target during the laser pulse duration [96, 208]. Counter streaming fast electrons may act to disrupt the growth and therefore the pinching effect of the magnetic field.

5.5 Hybrid simulations

Beyond the analytical predictions of the Bell-Kingham expression it is evident that a self-consistent numerical treatment is required to determine if 'global' pinching of the fast electron beam via self-generated magnetic fields is responsible for the reduction in

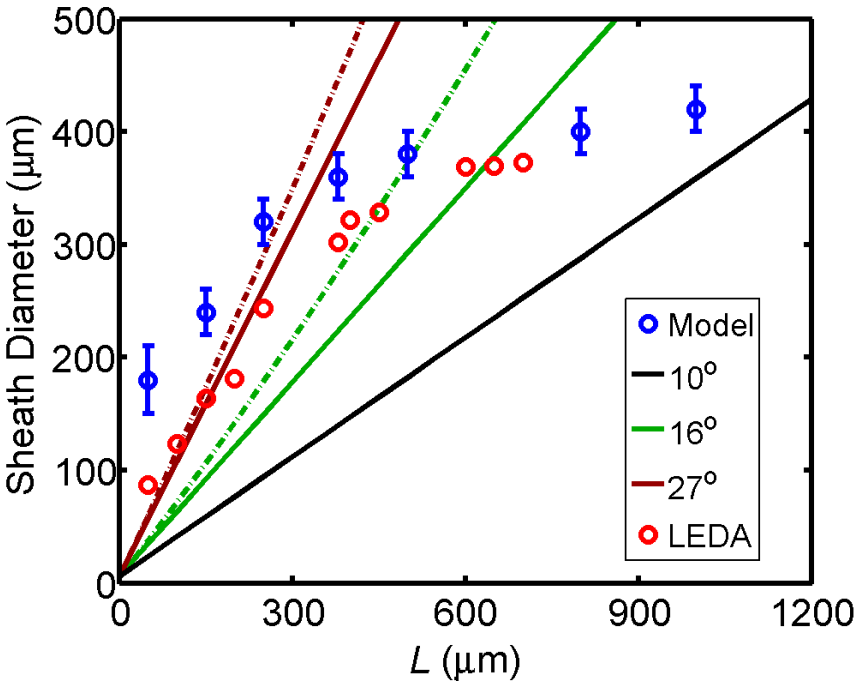

FIGURE 5.8: The initial electron sheath size (full-width) as a function of target thickness is shown. Blue symbols result from the application of the sheath evolution model to the experiment data. The error bars include the variation over multiple shots and the energy resolution of each piece of RCF film. The solid lines correspond to ballistic electron transport at given fixed divergence angles. The dashed lines include a correction due to scattering within the target. The red symbols correspond to the lateral extent of the fast electron beam (at the point in time when the electrons reach the rear surface) in 2D LEDA hybrid simulations.

the transverse extent of the fast electron population in thick targets. The numerical investigation was carried out using the 2D hybrid-Vlasov-Fokker-Planck code LEDA.

The code is described in detail in Section 4.4.2. The fast electrons are injected at the left-hand side of the 2D spatial grid, in a pulse with duration equal to 0.7 ps. A relativistic Maxwellian of the form $(cos^8\theta)p^2 \exp(-(p^2+m_e^2c^2)^{1/2}/k_BT_f)$ defines the fast electron distribution with laser conversion efficiency $E_{L\rightarrow e} = 0.25$ and $k_BT_f = 9\,\mathrm{MeV}$. While this temperature is slightly higher than the value expected in the experiment, a set of comparative example simulation runs with $k_BT_f = 7.4\,\mathrm{MeV}$ show that this small temperature difference does not significantly affect the simulation results or the conclusions of this work. The initial fast electron divergence half-angle is $\theta_{in} \approx 24°$ and the initial background temperature is set to 1 eV. A uniform spatial grid is used for all the simulation runs, with a cell size equal to 1 μm. The number of cells in x is varied between 80 and 800, to simulate the variation in L, and the cell number in y is typically 480. Besides the variation in target thickness all other initial parameters are fixed.

An example of fast electron transport in 300 μm Al target is shown in Figure 5.9. Here

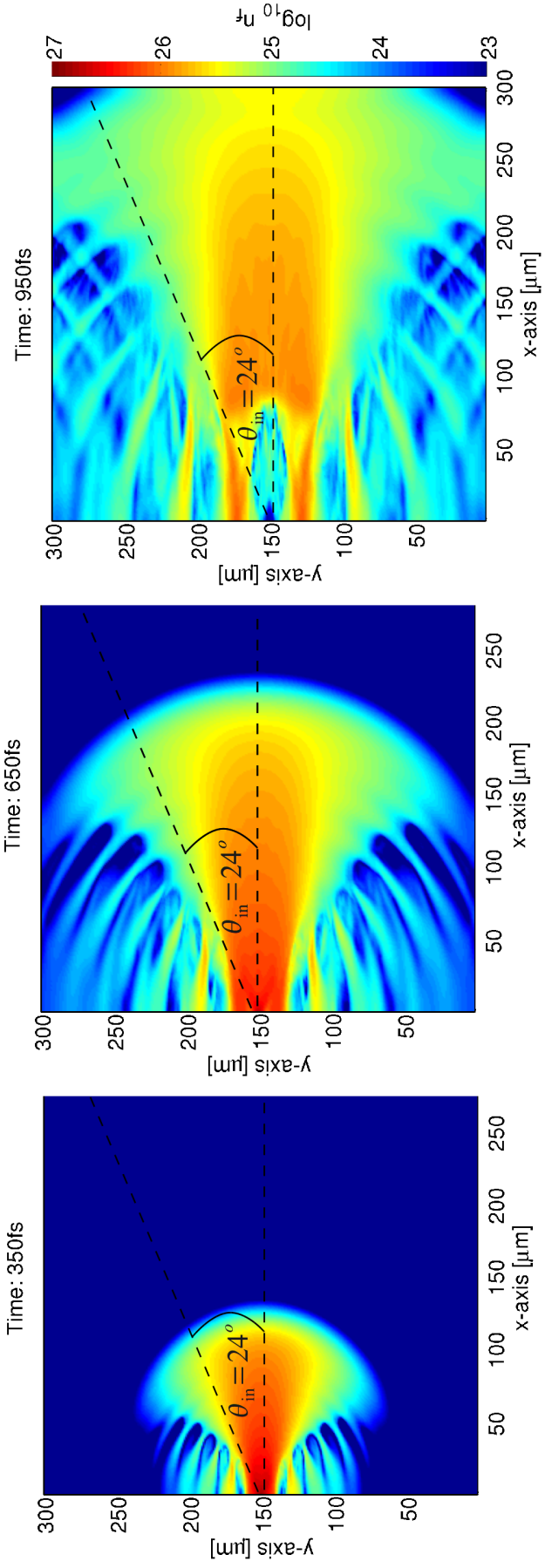

FIGURE 5.9: The divergence of a fast electron beam relative to the injection angle is shown at successive depths in a aluminium target. At 100 μm the beam fills the injection cone. At later stages, deeper in the target, the beam divergence is reduced by global magnetic pinching.

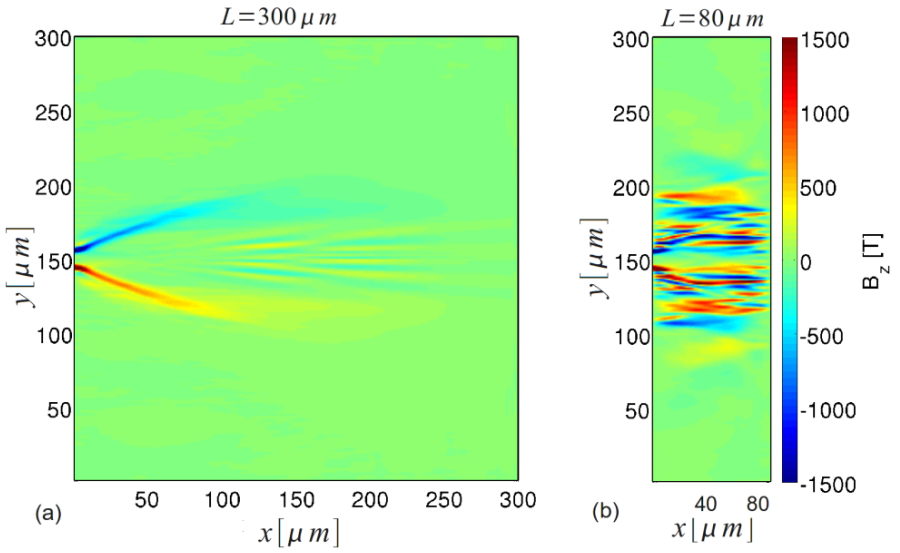

FIGURE 5.10: Fast electron transport simulation results using the LEDA code: The magnetic flux density (in tesla) for example target thickness equal to (a) 300 μm and (b) 80 μm, at 1.4 ps after the laser pulse interaction (at $x = 0$, $y = 150$).

the spread of the beam is compared to the injection angle, indicated by a fixed 24° half-angle cone, at successive depths in the target. The magnetic fields at the injection region are sufficient to collimate the beam for the first 20 μm into the target. The beam subsequently spreads out to fill the injection cone as shown in Figure 5.9(a) at 350 fs. Over time the azimuthal magnetic field extends into the target and grows in strength. After 650 fs, the field is sufficient to restrain the fast electron beam's angular spread resulting in a comparatively lower divergence relative to the injection angle, see Figure 5.9(b). This effect is sustained at longer times and at 950 fs, as shown in Figure 5.9(c), the beam arrives at the rear surface with a diameter of 220 μm resulting in a final effective divergence of $\approx 20°$.

A map of the magnetic flux density at 1.4 ps for the same 300 μm target is shown in Figure 5.10 (a). This illustrates the azimuthal profile of the self-generated field, which exceeds 10^3 T and extends over 100 μm from the electron source. Figure 5.10 (b) shows the simulation result for an 80 μm Al target for otherwise identical conditions. After 1.4 ps the refluxing electrons, which are reflected in the sheaths formed on both sides of the target, have made multiple passes through the thinner target and the resulting magnetic field is considerably fragmented, reducing its effectiveness in collimating electrons.

Two main parameters of the fast electron beam are extracted from the LEDA simulation results. The first parameter is the average fast-electron density on-axis ($y = 150$) at the rear surface of the target, which is plotted in Figure 5.11(a) as a function of L. A change in the rate of decrease is observed at $L \approx 400\,\mu$m. These values of n_f are used with the

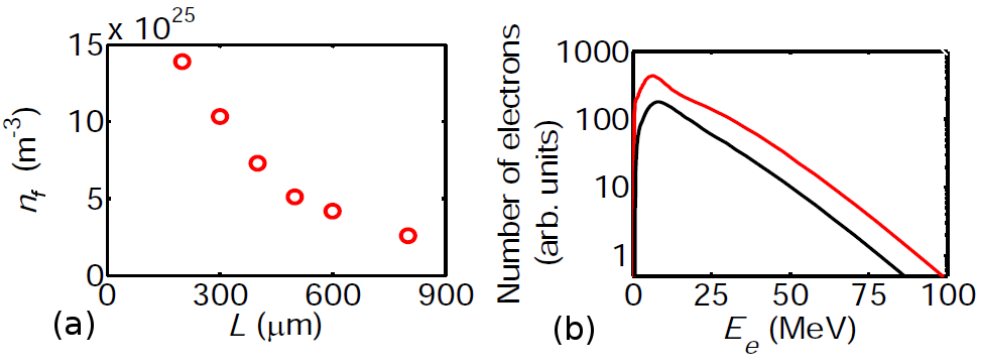

FIGURE 5.11: (a) Temporally averaged fast electron density at the rear surface of the target as a function of target thickness. (b) Electron spectrum on axis at the rear surface for example $L = 400$ μm and $L = 800$ μm

Mora [25] plasma expansion formulae (with the same assumptions and input parameters discussed above) to calculate E_{max}. The resulting trend is found to be in excellent agreement with the experimental results, as shown in Figure 5.2. The second parameter extracted is the lateral extent (full-width) of the beam of fast electrons as they reach the target rear surface and before any reflection has occurred (the simulation output time at which the distribution is sampled increases with L accordingly). As shown in Figure 5.8, although smaller than the initial sheath size extracted from sheath evolution model fit to the experimental data, a similar overall increase in sheath size with L is observed, including the differences between thinner and thicker targets.

The numerical simulation results obtained using LEDA are, in both cases, in good agreement with the experimental results. This is particularly so in the case of the maximum energies (see Figure 5.2). On examining the LEDA simulations it is clear that the magnetic field is reducing the transverse extent of the fast electron beam in thick targets which enhances the beam density. As a result, the value of n_f and therefore E_{max} decreases less rapidly with target thickness when compared to the simple ballistic model.

A fundamental assumption implicit in this work is that the fast electron temperature at the target rear surface does not change significantly with L. Two example electron spectra extracted from the LEDA runs are shown in Figure 5.11(b). Here the spectrum is sampled on-axis at the target rear surface for $L = 400$ μm and $L = 800$ μm. The fast electron density is reduced for the thicker target, but a significant change in $k_B T_f$ is not observed. Thus, these results from the LEDA simulations runs confirm that the constant $k_B T_f$ assumption is valid.

5.6 Conclusion

Results from an experimental investigation of the effects of magnetic pinching on fast-electron transport are presented in this chapter. The investigation used measurements of multi-MeV proton emission which are directly sensitive to the density of fast-electrons at the target rear surface.

The experimental measurements indicate that some magnetic pinching of the fast-electron beam occurs in thick metallic targets. Furthermore, an analytical model of electron sheath evolution has determined that the measured proton beam properties are consistent with a reduction on fast electron beam divergence. The results are found to be in good agreement with fast-electron transport simulations, which show that self-generated kilo-tesla magnetic fields are responsible for the observed decrease in beam divergence. The simulations also indicate that increased levels of fast electron refluxing disrupts the field growth in thin targets.

A self-induced collimation of the electron beam is most desirable for Fast Ignition. The implications of these results for parameters of Fast Ignition are as follows. Firstly, Fast Ignition is likely to require laser pulses with duration between 10 and 20 ps and intensity $\approx 3 \times 10^{19}\,\mathrm{W/cm^2}$ to produce electrons with $k_B T_f \approx 1.2\,\mathrm{MeV}$ [200]. According to the Bell–Kingham criteria [94] the degree of self-collimation increases both for longer pulse duration and lower electron temperature. Secondly, the Fast Ignition fuel target has a low effective Z, which may reduce the magnitude of the self-generated magnetic [94]. Finally, the significant density gradients of the compressed fuel extend over 3 orders of magnitude above the experimental conditions reported here. Further investigations will be required to measure the effects of fast electron collimation in such conditions.

Chapter 6

The effects of scattering and low temperature resistivity on electron transport instabilities

6.1 Introduction

The presence of transport instabilities in dense plasma can significantly disrupt the propagation of the fast electron beam. The development of electron beam instabilities is important for Fast Ignition as it could critically affect the efficient delivery of energy from the ignitor laser pulse to the compressed fuel core. A thorough understanding of the sensitivity of the instabilities to the beam and plasma parameters is also therefore essential in the assessment of Fast Ignition.

Previous work in intense laser-solid experiments has shown that there are circumstances in which fast electron beam filamentation occurs, and in which it does not occur (see for example [140, 209]). As discussed in Section 3.3, there are a number of plasma instabilities which could cause filamentation, including the Weibel [125, 130, 208], two-stream [210], and resistive (collisional-Weibel) filamentation instability [134]. Another potential cause of filamentation is the development of an ionisation instability via the breakdown of insulating targets by the fast electrons [137]. Similarly, a number of mechanisms of filamentation suppression have been identified theoretically. For example, the collisionless Weibel instability can be suppressed by a high transverse beam temperature [127–129]. In this scenario, increased transverse beam temperature can be acquired via fast electron scattering with the background plasma which scales with Z^2.

Other numerical results show that even when beam scattering suppresses the collisionless Weibel instability the resistive form can still be induced by the collisional return current [211, 212]. Experimental data on instability growth is available for only a small range of laser and target parameters. Hitherto, it has not been possible to ascertain conclusively via experiment either the main causal agents of electron beam filamentation or any mechanisms that can effectively suppress filamentation.

Presented in this chapter are the first direct experimental investigations of the effects of beam scattering and resistivity on the growth of transverse filamentation instabilities in fast electron beam transport in solid targets irradiated by ultrahigh intensity laser pulses. The approach uses high resolution measurements of multi-MeV proton emission to measure electron transport patterns (introduced by Fuchs *et al* [140]) in a range of metallic and insulator targets over a thickness range of $50\,\mu\text{m} - 1200\,\mu\text{m}$. Correlations between the measured proton data and the electron beam uniformity are made using a 3D sheath evolution to proton beam model. Numerical simulations are performed using a 3D hybrid code to determine the sensitivity of electron beam filamentation to the temperature dependant resistivity of the materials.

6.2 Experimental Investigation

The experimental measurements were carried out using the Vulcan laser at the Rutherford Appleton Laboratory. Each laser shot delivered a 1 ps pulse of light with wavelength equal to 1.053 μm and energy $280 \pm 20\,\text{J}$ on to target. The p-polarized beam was incident at 13° with respect to the target normal axis. The laser pulse intensity contrast was $\approx 10^8$ at 1 ns and $\approx 10^6$ at 60 ps prior to the peak of the pulse. The pulses were focused with an f/3 off-axis parabolic mirror onto the front surface of the targets to a $5\,\mu m$ FWHM spot size containing 50% of the incident energy. The resulting peak laser intensity is calculated as $5 \times 10^{20}\,\text{W/cm}^2$.

The development of plasma instabilities effectively disrupt the transverse uniformity of the fast electron beam. The experimental challenge to diagnose the electron beam uniformity was met using high resolution measurements of multi-MeV proton emission. This approach has previously been shown to be a sensitive diagnostic of instabilities in fast electron transport. Fuchs *et al* [140] have shown, using modelling and PIC simulations, how complicated electron sheath distributions including filaments are mapped into the proton beam spatial-intensity distribution. Similarly, Schollmeier *et al* [176] have also shown that the proton beam profile matches the profile of the fast electron beam transported through the target. Further studies of the sensitivity of proton beams

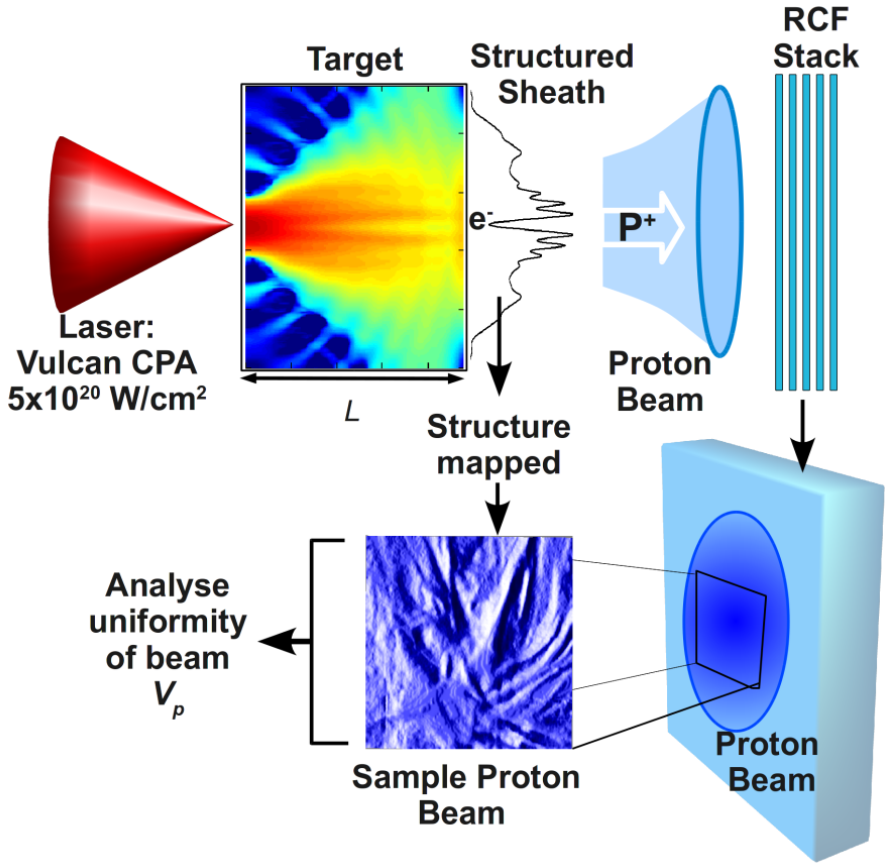

FIGURE 6.1: Schematic of the experiment illustrating the diagnostic technique of utilising proton beam emission to probe the uniformity of the rear surface electron sheath. Fast electron transport instabilities induce nonuniformities in the electron sheath which can be mapped to the measured spatial profile of the proton beam.

to electron beam uniformity is reported in Section 6.3. Filamentation of fast electron beam can thus be effectively diagnosed using TNSA proton emission.

A number of distinct target materials are tested for signatures of electron transport instabilities. These include a selection of conductors and insulators with varying Z number. The targets are summarised in Table 6.1 and include C_3H_6 (polypropylene, hereafter referred to as CH) plastic, SiO_2 and BK7 (silica with 10% boron oxide) glass, and Li, Al and Au metals. The effects of oxidation on Li was minimised by storing the targets in an inert environment prior to use. The targets all measured 3 mm $\times$7 mm and the thickness, L, was varied in the range 50 μm to 1.2 mm. The rear surfaces of the targets (except Li, due to its susceptibility to oxidation) were prepared to a surface roughness of less than 1 μm by employing a lapping technique. This was done to remove surface structure which can be mapped into the proton beam spatial intensity profile [213]. A limited set of Al and CH foils with a 50 nm-thick coating of Au on both surfaces were also tested.

Target	L [μm]	Z^2	η_{cold}
Al	50-1000	169	C
Li	50-380	9	C
Au	100-250	6241	C
CH	50-550	5	I
SiO_2	550-1200	100	I
BK7	145	94	I

TABLE 6.1: List of target materials used for the investigation of beam filamentation. The target thickness range (L), scattering rate $\propto Z^2$, cold resistivity (C: conductor, I: insulator) are specified.

The spatial intensity distribution of the beam of accelerated protons was measured using passive stacks of dosimetry film (RCF: Gafchromic film, HD-810 and MD-V2-55). The film is preferentially sensitive to protons and Bragg peak deposition enables the beam distribution to be sampled in coarse energy steps. Modulations in the electron sheath due to filamented transport of the fast electrons in the target are mapped into the expanding ion front and measured as nonuniformities in the proton dose distribution in the RCF. Figure 6.1 shows a schematic of the arrangement.

6.2.1 Experimental measurements

A primary finding of this investigation is that irrespective of target Z, the different metal materials tested produce highly uniform proton beams. Significantly, it is found that the low-Z metal, Li, targets produce a smooth proton beam. Conversely, significant structure is observed in the proton beam profiles measured with all insulating targets again regardless of Z-number. This is shown in the representative example RCF images of Figure 6.2. Generally the modulations observed with the insulator targets take the form of caustic-like structures which are typically in a radial pattern from the centre of the beam. This is a signature of the filamentation of the fast electron beam within the target [140].

The spatial homogeneity of the proton beam is compared for the complete set of data shots to determine the sensitivity of filamentation to target material and thickness. This is carried out at proton beam energies for which the beam intensity is similar for each target. Multiple regions, corresponding to a total of 10% of the beam area, were sampled around the centre of the beam where the proton beam laminarity is highest [174]. The parameter of variation, V_p, quantifies the percentage variation of the beam above the mean value of proton number. This is calculated using the standard deviation, σ_{N_p} and

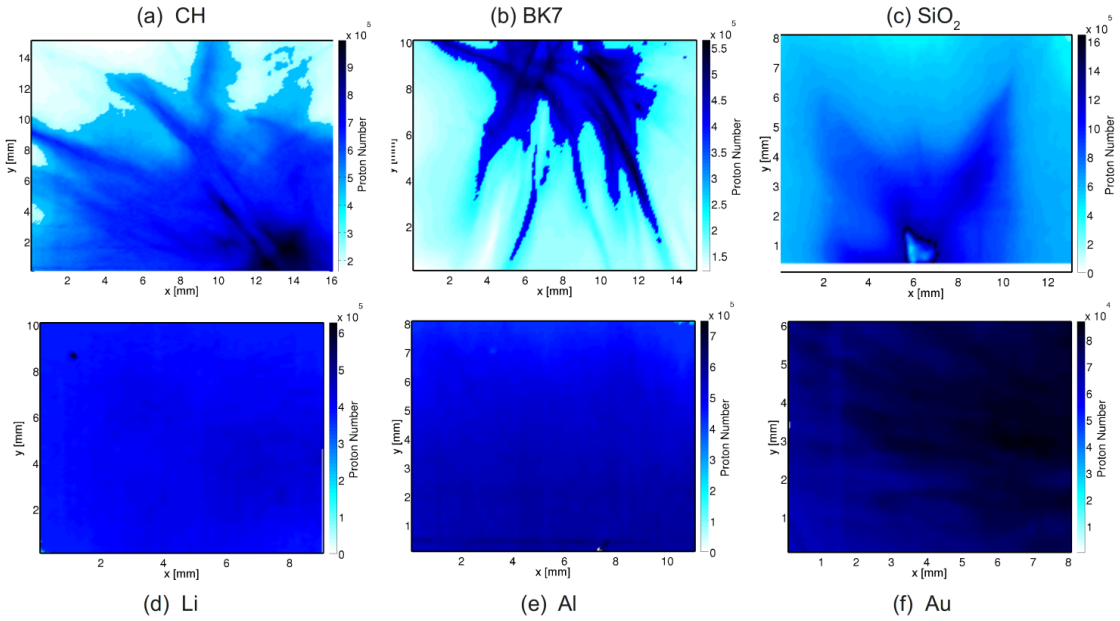

FIGURE 6.2: Representative proton beam spatial profiles near the centre of the proton beam for: (b) 270 μm CH plastic, (c) 520 μm SiO_2 glass, (d) 150 μm BK7 glass, (e) 250 μm Li, (f)380 μm Al and (g) 250 μm Au targets.

mean $\bar{N}_p$ of the proton number distribution over the sampled area of the beam:

$$V_p = \frac{\sigma_{N_p}}{\bar{N}_p} \times 100\% \tag{6.1}$$

As shown in Figure 6.3, a similar beam variation is measured for all metal targets despite the large differences in Z and the wide range of target thicknesses explored. By contrast, the degree of electron beam filamentation in the insulator targets is higher and increases considerably with target thickness. The proton beam variation for plastic (CH) targets increases with L from a value similar to that produced by metal targets for $L = 50$ μm to a heavily filamented beam for $L = 550$ μm. The variation values for the glass targets (SiO_2 and BK7) are high for all L sampled. Importantly, when comparing the results for CH, with average $Z = 2.7$, with SiO_2 and BK7, with average $Z = 10$ and 9.7, respectively, it is clear that despite the increased fast electron scattering for the latter cases there is no reduction in beam filamentation.

The trend of proton beam spatial uniformity for the insulator materials suggests a correlation with target thickness. The increase from a low variation for relatively thin targets to high variation in thick targets maybe the result of several effects. Firstly, the growth rate of the instabilities may result in a higher degree of filamentation over larger propagation lengths. Secondly, resistive filamentation growth is expected to be enhanced in colder material due to a higher resistivity as in the case of thicker targets [134]. Thirdly, increased rates of fast electron refluxing [96] in thinner targets may also act to smooth

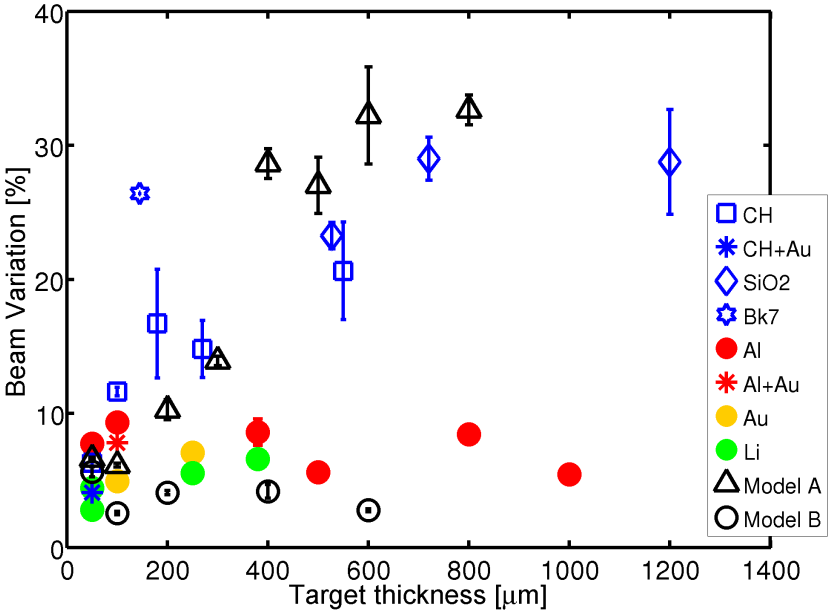

FIGURE 6.3: The proton beam intensity variation is shown as a function of target thickness for the collective materials. The spatial variation is measured relative to mean proton number near the centre of the proton beam, sampled at an energy equal to 50% of the maximum proton energy. Error bars correspond to statistical variations over the multiple samples.

the filamented beam. However, as discussed in the next section, any change in beam filamentation may be masked by differences in the sheath evolution in thick and thin targets. Specifically, if the fast electron beam propagates with a fixed angular distribution and filaments into a given number of filaments, the separation of these filaments at the rear surface will increase with target thickness. Considering that radial expansion of the filaments will occur at the rear surface, in thin targets for which the filaments are more closely spaced the modulations in the sheath field may be quickly smoothed out. Thus the measured differences in proton beam uniformity with target thickness may be accounted for by the spacing of the filaments forming the sheath and how quickly they merge. This implies a threshold target thickness such that the sheath size is sufficiently small to enable the inhomogeneities to merge before the spatial shape of the ion front has developed. Results from a sheath expansion model are shown in Figure 6.3 and suggest that the measured trend in the proton beam spatial variation with target thickness is the result of this process. The model and results are discussed in the next section.

6.3 Filamented sheath/proton beam modelling

The correlation of the proton beam uniformity at the detector to that of the electron sheath is investigated using an analytical model of the evolution of both smooth and

filamented electron sheath fields and the resulting proton beam acceleration. A 2D spatial grid of 1000×1000 cells of $1\,\mu$m size is defined as the target rear surface centred at $x = y = 0$. In temporal steps of $\Delta t = 50\,$fs the electron sheath field distribution evolves and spreads over the spatial grid for a duration of 3 ps.

The magnitude of the field, $E_0.G(t)$, increases with the rising edge of the laser pulse with a Gaussian temporal profile to a maximum value, E_0 at $t_{peak} \approx \tau_L$, and follows an exponential decrease thereafter (with $1/e = 1.6\,$ps), as inferred from previous work [167, 207]:

$$G(t) = \exp\left(-\frac{4\ln(2)(t - t_{peak})^2}{\tau_L^2}\right) \quad [\mathrm{t} \leq \mathrm{t_{peak}}] \tag{6.2}$$

$$G(t) = \exp\left(-\frac{(t - t_{peak})}{1.6\,\mathrm{ps}}\right) \quad [\mathrm{t} > \mathrm{t_{peak}}] \tag{6.3}$$

The initial fast electron beam diameter (FWHM), D_e, at the rear surface is set as a function of target thickness assuming ballistic transport through the target with a divergence half-angle, $\theta_{1/2}$, equal to 27° [146], using $D_e = 2L\tan\theta_{1/2}$. This ballistic approximation holds in the absence of significant self-induced collimating magnetic fields [94, 95] and scattering in low-Z insulating materials. The sheath area, centred at $x = y = 0$, is seeded with $n = 100$ individual filament sub-sheaths with random position (x_i, y_i) to represent filaments of the electron beam. The relative strength of the quasi-electrostatic field arising from each filament, A_i, is also random and is normalised as $0 < A_i \leq 1$. A Gaussian distribution of initial filament sizes is used with mean equal to $5\,\mu$m (FWHM).

The transverse expansion velocity, $v_\perp$, of the individual sub-sheaths along the rear surface is initially set $\approx c$, as determined in previous studies of sheath expansion for very similar laser conditions [167, 175]. The value of $v_\perp$ decreases exponentially with time, with $1/e = 1.6\,$ps, consistent with optical probe reflectometry measurements of sheath expansion by Antici [206]:

$$v_\perp(t) = c\left(0.94\,\exp\left[-\frac{t}{1.6\,\mathrm{ps}}\right] + 0.06\right) \tag{6.4}$$

An inverse parabolic function is used to describe the shape of each filament defined using $p_i(x, y, t)$ with relative amplitude A_i, using the expanding half-width $W_i(t)$, where $i = 1, 2, 3, ...n$:

$$W_i(t > 0) = W_i(t - \Delta t) + v_\perp(t)\Delta t \tag{6.5}$$

$$p_i(x, y, t) = A_i\left[1 - \frac{(x - x_i)^2}{W_i(t)^2} - \frac{(y - y_i)^2}{W_i(t)^2}\right] \geq 0 \tag{6.6}$$

This collection of filaments evolve as individual sub-sheaths which spread radially along the rear surface with velocity $v_\perp$ and merge defining a total fast electron sheath $P(x, y, t)$, which is again scaled to $0 - 1$:

$$P(x, y, t) = \sum_{i=1}^{n} p_i(x, y, t) \tag{6.7}$$

The spatial and temporal evolution of the sheath field magnitude, $E(x, y, t)$, is then calculated using:

$$E(x, y, t) = E_0 \cdot G(t) \cdot P(x, y, t) \tag{6.8}$$

Ionisation of the surface (defined as a uniform layer of hydrogen) is calculated using the ADK field rate [64] at each time step. The resulting protons are accelerated by the evolving sheath field over successive time intervals reaching a maximum energy at the final time step. The local gradients of the ion front surface provides the angular mapping of protons from the target to detector plane using polar co-ordinates. A 6 cm $\times$ 6 cm spatial grid defines the detector which is comprised of 600 $\times$ 600 cells. After a 3 ps simulation time the energy resolved proton beam spatial profiles are calculated at the detector plane set 5 cm away from target, matching the experimental setup. A 10 $\times$ 10 pixel averaging window is applied across the detector plane profile in order to filter pixel noise. The spatial variation of the proton beam is calculated in the same manner as the experiment using the spatial profile at half the maximum energy.

6.3.1 Model results

The filamented sheath model is applied to a range of target thickness to determine the sensitivity of rear surface proton emission to the spatial uniformity of the fast electron sheath. These results are shown in Figure 6.3 as 'Model A'. For comparison, a smooth unfilamented sheath is also shown as 'Model B'. For relatively thin targets the proton beams are uniform in both cases. The nonuniformities in the initial electron sheath are effectively smoothed out as individual filaments spread laterally and overlap forming a uniform central peak. In the case of thicker targets, after $\approx 200\,\mu$m, nonuniformities in the electron sheath persist to later times and consequently the nonuniformity of the proton beams become more apparent resulting in an increase in spatial variation.

An example detailing this comparison in the case of 100 μm and 400 μm target thickness is shown in Figure 6.4. The uniformity of the sheath field near the time of peak strength, at 1 ps, strongly influences the proton beam uniformity. For the thinner target in this example, the initial filamentation is completely smoothed well before the time of peak field strength. This is not the case for the thicker target, at 1 ps the sheath field is

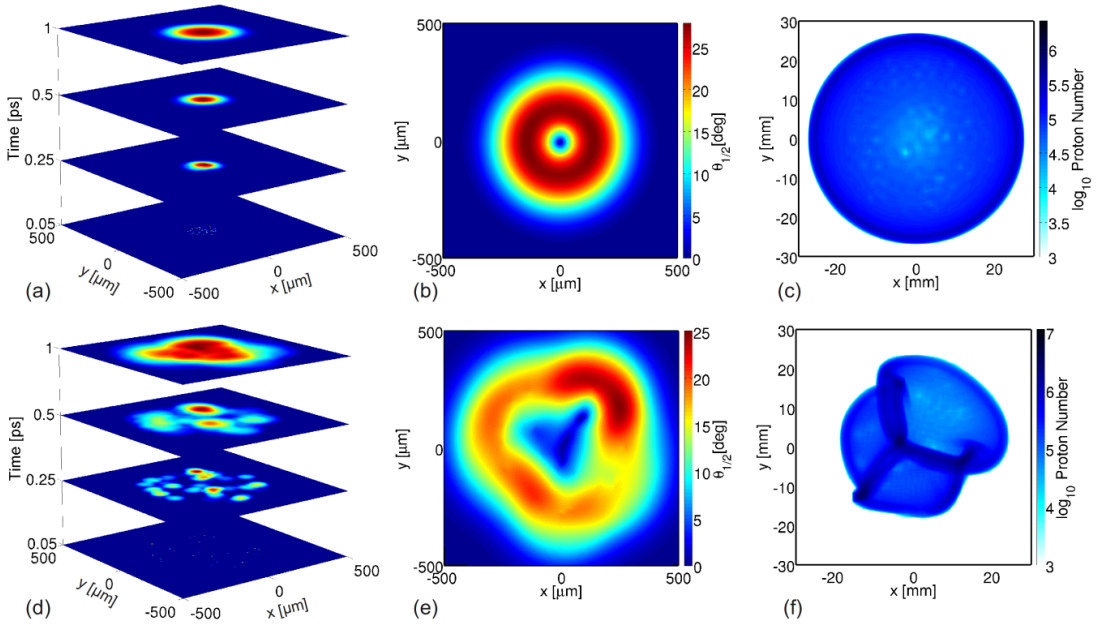

FIGURE 6.4: Sheath evolution and proton beam generation for target thickness of 100 μm (top row) and 400 μm (bottom row). In each example the temporal evolution of the electron sheath field is shown up until the peak field time at 1 ps (a & d). The proton beam divergence from the target surface (b & e) and the final overall proton beam spatial intensity distribution at the detector (c & f) show the respective effects of filamentation at the rear surface for both examples.

clearly non-uniform, see Figure 6.4(d). The spatial map of proton beam divergence from the target surface, which reflects the local uniformity of the ion front, illustrates the translation of protons from target to detector. The intense caustic features present in the final proton beam in Figure 6.4(f) are a result of low divergence from the relatively flat ion-front regions existing between neighbouring sheath inhomogeneities.

Filamented sheath structure must persist until near peak field time ($t \approx \tau_L$) for such features to transfer effectively to the proton beam. This is determined by the radial expansion velocity and the size of the initial sheath diameter. Consider the extreme case of filaments located at opposite ends of the sheath, radial expansion will result in overlap and superimposition of their respective fields ultimately resulting in a uniform sheath. Assuming an average expansion velocity of $\bar{v}_\perp \approx 0.5c$ over a time $\approx \tau_L$, complete overlap will occur if the initial sheath diameter $D_e \approx \bar{v}_\perp \tau_L \lesssim 150\,\mu$m. For ballistic electron divergence of $\theta_{1/2} = 27°$, this condition is met for targets thinner than $\approx 150\,\mu$m. Above this thickness threshold the distance across the initial sheath diameter is sufficient to prevent complete smoothing and the global inhomogeneity of the sheath will become more pronounced with increasing target thickness. As shown in Figure 6.3, the spatial profiles of the calculated proton beams reflect this inhomogeneity and follow a similar trend with increasing target thickness to the experimental measurements. It is therefore

likely that the measured dependence of proton beam uniformity with target thickness results from the diagnostic approach.

6.4 Hybrid simulations

The presence of a disrupted electron sheath indicates a filamentation of the fast electron beam during its transport through the target. The effects of beam instabilities, measured within the sensitivity of the proton emission diagnostic, appear to only manifest in a subset of targets investigated, namely the insulator materials. It had previously been suggested that increased scattering in high-Z materials prevents beam filamentation by constraining the collisionless Weibel instability through an increased transverse beam temperature [127]. This is investigated in Section 6.4.1 using the LEDA code to test instability growth with increasing rates of scattering. The origin of the beam instabilities which induce the measured sheath field modulations is investigated in Section 6.4.2 using the ZEPHYROS code. Here the effects of material resistivity on the growth of the collisional Weibel/resistive instability is tested.

6.4.1 The effects of scattering on filamentation

The effect of fast electron scattering from target ions was studied by carrying out a series of LEDA simulations, for an aluminum target, in which the fast electron-ion collision frequency was varied. The collision frequency is given by [214]:

$$\nu_{ei}(p) = \frac{Z^2 n_i e^4}{v_e p_e^2} \frac{\ln \Lambda}{4\pi\varepsilon_0^2} \tag{6.9}$$

where p_e and v_e are the electron momentum and velocity respectively and n_i is the ion density. The Coulomb Logarithm $\ln \Lambda$ was used as an arbitrary control parameter to increase the rate of scattering. Effectively, a series of simulations with $\ln \Lambda$ set to increasingly larger values are performed until the scattering rate is sufficient to produce a measurable change to the smoothness of the electron density distribution at the target rear surface.

It is found that increasing the scattering rate by a factor of 5 ($\ln \Lambda = 2 - 10$) produces only a marginal smoothing of the fast electron density distribution. The scattering rate must be increased far beyond what is physically justifiable, by a factor of ≈ 50 ($\ln \Lambda$=100) to produce a significant smoothing effect, as shown in Figure 6.5. Such high levels of scattering are unrealistic. Therefore these simulations support the conclusion derived from the experimental results that fast electron scattering from target ions does not

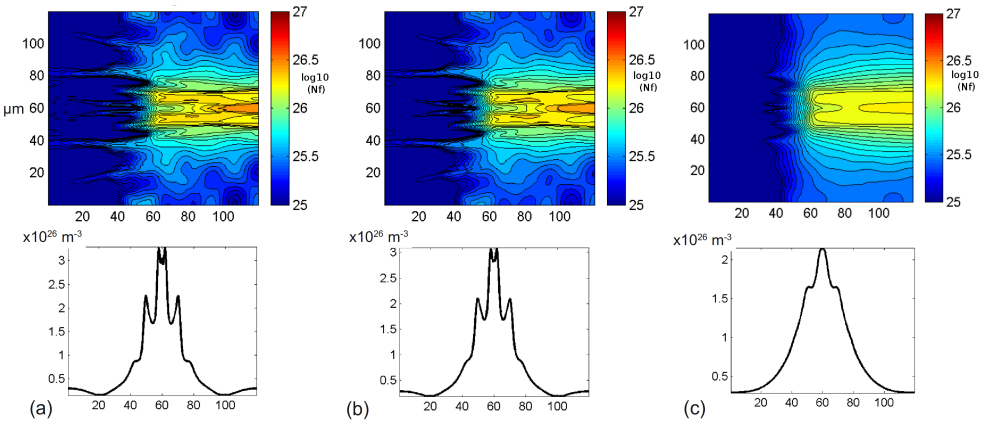

FIGURE 6.5: LEDA simulation output showing the effect of increasing the electron-ion collisional operator. The fast-electron density at 700 fs for (a) $\ln\Lambda$=2, (b) $\ln\Lambda$=10 and (c) $\ln\Lambda$=100 is shown in a $\log_{10}$ scale. Corresponding fast electron density profiles at the target rear surface

play a significant role in suppressing filamentation of the fast electron beam produced by near-petawatt, picosecond laser pulses.

As discussed in Chapter 3, specifically regarding Equation 3.25, significant differences in electron beam uniformity are predicted for low and medium Z materials based on the inherent degree of beam plasma scattering. The fact that independent of Z, relatively uniform proton beams are obtained with all three metallic targets leads to the conclusion that, for the parameter range investigated, scattering is not a key factor in instability growth. Significantly more structured beams are obtained with all three (initially) insulating targets irrespective of Z. This leads to the conclusion that other factors, such as target resistivity or material breakdown, are more important in the development of electron beam filamentation. Whether the resistivity curve or material breakdown is more important can be determined by comparing the whole set of measured results to a series of hybrid simulations where only the resistivity curve effects are included, and this is pursued in the next section.

6.4.2 The effects of resistivity on filamentation

The sensitivity of filamentation by the collisional Weibel instability to plasma resistivity was investigated using simulations which were carried out by A. P. L Robinson using the 3D PIC/fluid hybrid code ZEPHYROS [201]. Here the fast electrons are treated using a PIC approach with a static fluid describing the background plasma. These simulations modelled the transport for Al, CH, and Li to determine the influence of resistivity on the collisional Weibel instability, but not the effect of material breakdown.

The simulation space was defined as a $200 \times 200 \times 200$ μm box with cell size equal to $1 \times 1 \times 1$ μm. The fast electrons population was injected from the $y = 0$ plane and centred on $x = z = 100$ μm. The transverse absorption profile from laser to fast electrons is calculated along the radial distance (r) using:

$$I = \eta_{L \to e} I_L \cos^2 \left(\frac{\pi r}{2 r_L} \right) \tag{6.10}$$

where r_L is the FWHM of laser focal spot. In these simulations, the value of $\eta_{L \to e}$ was set to 0.1, I_L was set to 3×10^{20} W/cm^2, and r_L was set to 5 μm to closely match the experimental parameters. The laser pulse duration was set at 600 fs. An exponential probability distribution of electron energies was employed, with fast electron temperature equal to 7 MeV. The fast electrons were injected with a $\cos^8 \theta$ angular distribution ($\approx 24^\circ$ half angle) with 60000 quasi-particles injected per time step. The simulations were run up to 1.5 ps and reflective spatial boundaries were employed throughout. The initial simulation background temperature was 1 eV.

Critical to these investigations are the material specific resistivity-temperature curves. For Al and CH, the resistivity curves and the Thomas-Fermi model for specific heat capacity are the same as used in the simulations by Davies [164]. The Al resistivity is based on a fit to the Milchberg *et al* measurements [51]:

$$\eta_{Al} = \frac{k_B T_e}{5 \times 10^6 + 170\, k_B T_e^{2.5} + 3 \times 10^5 k_B T_e} \ \Omega.\text{m} \tag{6.11}$$

and Davies' heuristic curve is used for CH [164]:

$$\eta_{CH} = \frac{k_B T_e}{1.3 \times 10^3\, k_B T_e^{2.5} + 4.3 \times 10^5 k_B T_e} \ \Omega.\text{m} \tag{6.12}$$

Both resistivity curves are shown as a function of the background plasma temperature $k_B T_e$ in Figure 6.6.

The resistivity curve for Li was calculated by M. P. Desjarlais for the purpose of this investigation. For low temperatures, up to 10 eV, the resistivity was derived using quantum molecular dynamics (QMD) calculations based on density-functional theory. This was followed by a Kubo-Greenwood calculation of the electrical conductivity [215] using a code called VASP[216, 217]. A wide-range model for the resistivity was derived by tuning generalised Lee-More algorithms [218] to the QMD results.

Two resistivity curves were generated for Li based on the ions being ordered or disordered. These are shown, as solid and dashed red curves respectively, in Figure 6.6. The solid curve is generated assuming that the Li ions retain the ambient lattice structure.

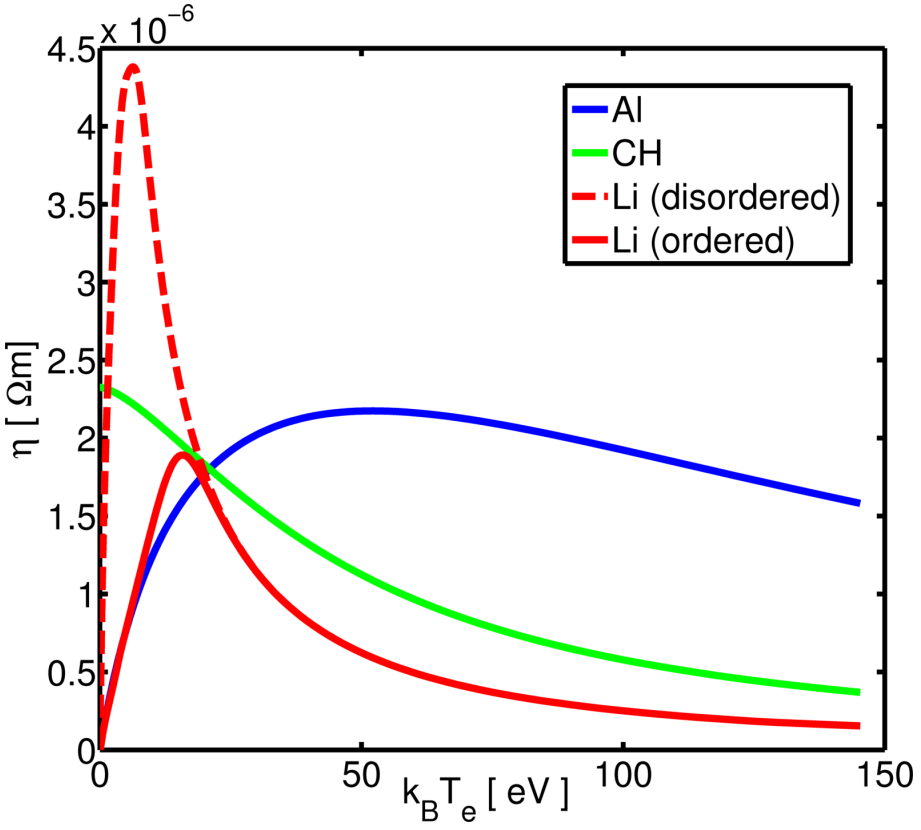

FIGURE 6.6: Resistivity as a function of plasma temperature is shown for Al, CH and Li. The curve for Li is calculated for two different ion conditions: a disordered molten structure (dashed curve) and an ordered crystalline structure (solid curve). The latter is relevant here for the picosecond conditions of the experiment.

The resistivity for this ordered Li can be expressed as:

$$\eta_{Li} = \frac{k_B T_e}{7.2 \times 10^6 + 5.8 \times 10^3\, k_B T_e^{2.5} - 2.2 \times 10^5 k_B T_e} \ \Omega.\mathrm{m} \tag{6.13}$$

The dashed curve is generated assuming the ions are in the molten state, in thermal equilibrium with the background electrons. This disordered state of Li results in a higher resistivity at low plasma temperatures, and can be fitted by:

$$\eta_{Li*} = \frac{k_B T_e}{4.4 \times 10^5 + 2.9 \times 10^3\, k_B T_e^{2.6} + 1.1 \times 10^5 k_B T_e} \ \Omega.\mathrm{m} \tag{6.14}$$

From the simulations, the resulting fast electron density distributions were extracted at the rear surface of the targets and are shown in Figure 6.7. The fast electron density profile for Al is relatively smooth and centre-peaked. The corresponding profile for CH is larger and contains significant filamentary structure. These simulation results qualitatively agree with the experimental observations that the rear surface electron sheath is much more structured for CH than for Al targets.

The specific resistivity curve for each material is critical in order to achieve good agreement with experiment. This correlation with electron beam filamentation is clearly demonstrated by the theoretical analysis of resistivity in the case of lithium. Both representations for the lithium resistivity in Figure 6.6 are valid but for dramatically different conditions of material structure. Over the short picosecond time scales of the experiment, the ions have too little time to move and equilibrate. The simulation of transport in Li with this ordered ionic configuration agrees with the experimental results, see Figure 6.7(c). In this case the ordered arrangement provides a relatively lower plasma resistivity which results in more uniform electron transport patterns. For the alternative case, the disordered ion lattice predicts a higher plasma resistivity and accordingly a high degree of filamentation is observed in the transport simulations, see Figure 6.7(d). The differences between the two curves are entirely in the low temperature region ($k_B T_e < 20\,\mathrm{eV}$).

The interpretation of the results from the Li targets therefore indicates that invoking material breakdown alone to distinguish between metallic and insulating targets is insufficient. Correct treatment of the target resistivity even when it is a nominally good conductor or metal is also critical, particularly at low temperatures. Furthermore it is interesting that it is not necessary to include material breakdown in the numerical model to explain the filamentation observed in CH.

The hybrid simulation results also show a correlation between the transverse extent of the fast electron beam and the beam uniformity. Where a simulation results in filamentation, the beam is always wide, and where a simulation results in no filamentation, the beam is always more collimated, as observed in Figure 6.7. This increase in collimation is a result of the azimuthal magnetic field around the fast electron beam. This effect was measured experimentally for aluminium in the investigation reported in Chapter 5. The strength of this magnetic field is seen here to be sensitive to the shape of the resistivity curve. In the case of 'ordered' Li, for example, a peak magnetic flux density of 680 T is obtained, compared to 396 T for the 'disordered' Li for otherwise same simulation parameters. This 'globally pinching' [94] magnetic-field is generated according to Equation 3.17 and shows a dependence on resistivity. Assuming the plasma is hottest along the beam axis, the specific direction of the $\nabla\eta \times j_f$ component can enhance or reduce the transverse pinching force acting globally across the beam. In the Spitzer treatment of resistivity, where $\eta \propto k_B T_e^{-1/3}$, a hollowing force results from $\nabla\eta \times j_f$ that is opposing the pinching component, $\eta\nabla \times j_f$. However, for low temperature plasma, $k_B T_e \leq 20\,\mathrm{eV}$, the resistivity curves suggest that for ordered Li, the transverse gradient, $\nabla\eta$, will instead be pointing radially inwards - re-enforcing the global pinching component. Conversely, for disordered Li the gradient points outwards form the beam axis which reduces the pinching component.

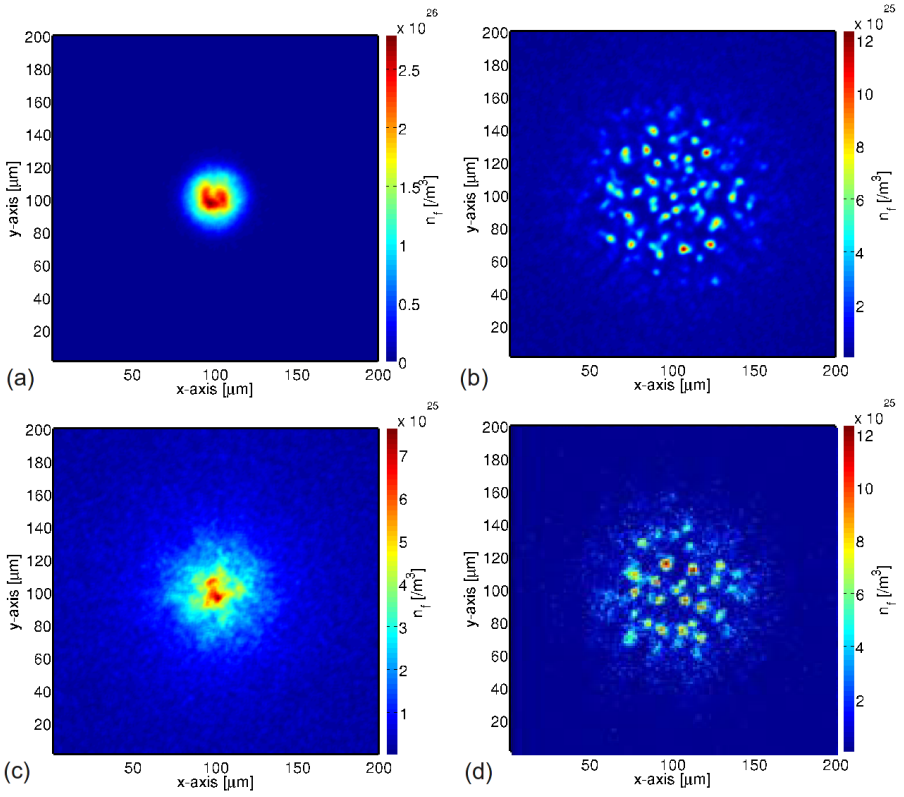

FIGURE 6.7: ZEPHYROS simulation output showing the fast electron density distribution in the plane at the rear of a 200 μm-thick target all at 1.5 ps after the start of the simulation (a) Al, (b) CH, (c) 'ordered' Li and (d) 'disordered' Li .

Thus it can be seen how the details of the relatively low-temperature resistivity curve must effect the growth of the magnetic field.

Significant global beam pinching can can also give rise to an increase in the transverse temperature of the beam. Gremillet [134] has shown that there is a transverse beam temperature dependence of the filamentation growth rate. If the transverse temperature is raised high enough it can suppress filamentation. However, early theoretical work by Molvig [219] predicted that this can only occur for collisionless plasma and that increased transverse beam temperature alone cannot stabilise resistive instability growth. In this case a sufficiently strong magnetic field is required, where stabilisation occurs when [219]:

$$\frac{\Omega^2}{\omega_b^2 \beta^2 \gamma} > 1 \ \ [\text{cgs}] \tag{6.15}$$

Here $\Omega = eB/m_e c$ is the cyclotron resonance frequency for an electron in a magnetic field, B, and ω_b is the fast electron beam plasma frequency. In the case of Al which produces the smoothest beam, the LEDA simulations predict a magnetic field $B \approx 4 \times 10^3$ T and the Molvig expression is ≈ 2. Conversely, filamentation is greatest in the case of CH, where $B \approx 400$ T, and here the stabilisation expression is ≈ 0.01, which is two orders of

magnitude lower than Al. For similar beam conditions, the magnetic suppression of the resistive instability scales as B^2. As the growth of the magnetic field is a response to the material resistivity, the details of the resistivity curve play a significant role in the suppression of resistive filamentation.

6.5 Conclusion

In this investigation, the spatial uniformity of multi-MeV proton beams was used to diagnose the filamentation of fast electron transport in a range of solid targets with thickness $50 - 1200\mu$m. The spatial uniformity of the proton beams was shown to be sensitive to that of the fast electron sheath as previously inferred by Fuchs *et al* [140]. Furthermore, analytical modelling of the sheath evolution indicates an greater sensitivity of proton emission to electron beam filamentation in thicker targets. An increasing trend of beam variation with target thickness is also evident in the experimental measurements. For the ultra-intense laser pulse parameters used in this experiment, it is found that electron-ion scattering has no measurable effect in suppressing fast electron propagation instabilities in solid targets. Instead, the transport patterns for different materials are consistent with resistivity.

More specifically, numerical simulations show the variation of resistivity to temperature in the non-Spitzer regime has a significant role in defining the fast electron transport pattern. The simulations results suggest that ion order strongly influences the resistivity over the low temperature range, $k_B T_e < 20\,\text{eV}$. A disordered ion lattice induces higher resistivity. The simulations show an enhanced growth of the collisional-Weibel (resistive) instability with a higher resistivity in this temperature regime. Other factors such as anomalous resistivity and ionisation may not need to be invoked to account for filamentation. Further experimentation is required to test this new hypothesis. The simulation results also indicate that global pinching of the fast electron beam by the self-generated azimuthal magnetic field acts to suppress filamentation.

Chapter 7

Refluxing of fast electrons in solid targets irradiated by intense, picosecond laser pulses

7.1 Introduction

As discussed in Chapter 3, the irradiation of a solid target by an intense laser pulse injects a multi-mega-ampere current of fast electrons into the cold target material. Upon reaching the rear surface of the target some of the hottest electrons escape, establishing a space-charge sheath potential which reflects the majority of the electrons back into the target [168]. A similar sheath potential forms at the front of the target and can reflect the fast electrons returning to the front surface, giving rise to refluxing (or recirculating) fast electrons within the target.

Although refluxing is thought to be intrinsic to the transport of fast electrons in thin solid targets, there has been little direct investigation of the extent to which it occurs and the effect it has on the interpretation of experimental results. It has been inferred in previous experimental studies of fast electron transport and heating of solid targets (see for example [18, 192, 220, 221]) and in particular in volumetric heating of thin or small mass targets involving K-shell spectroscopy from tracer layers [97, 98, 222–224]. For these studies a single pass of the fast electron population would be insufficient to produce the measured degree of heating. Recirculation of fast electrons has also been used to explain measured enhancements in the maximum energy of protons accelerated from thin (< 10 μm) foil targets [208, 225]. However, fast electron transport and heating

physics are often inferred without consideration of the influence that circulating electrons have in relatively thin targets.

The work reported in this chapter investigates the effects of refluxing on electron transport measurements from solid density targets. The target is composed of two layers: a diagnostic layer and a propagation layer. The thickness of the latter is increased to vary the number of transits in the diagnostic layer which has a fixed thickness. The fast electron transport in the diagnostic layer is studied using K_α x-ray emission. Proton emission from the rear of the target is also measured, enabling a comparison to be made regarding the diagnostical sensitivity to refluxing. Both analytical and numerical modelling are used to interpret the measurements. Results from this investigation have been published in *Plasma Physics and Controlled Fusion*, **53** (2011), 025007.

7.2 Experiment

The experiment was performed using the PHELIX laser at GSI in Darmstadt, Germany. This facility is described in Section 4.2.2. For this campaign, the laser delivered 1 ps pulses with energies, E_L, on target of ≈ 90 J. The s-polarised pulses were focused onto target at an angle $\theta_i = 45^\circ$ with respect to target normal, to a focal spot diameter of $\phi_L = 15$ μm FWHM. The calculated peak intensity is $I_L = 2 \times 10^{19}$ W/cm^2. The intensity contrast of peak to ASE pedestal was measured at 3 ns prior to the laser peak to be 10^7. A schematic of the experimental setup is shown in Figure 7.1.

The laser pulse was incident onto planar foil targets, measuring 2 mm $\times$ 2 mm, and which consisted of two layers. A front layer of copper with thickness $L_{Cu} = 20$ μm was backed by a plastic layer with thickness (L_{CH}) varied in the range $0 - 300$ μm. The specific plastic was polypropylene, C_3H_6, which is referred to hereafter as CH. The transport of fast electrons within the Cu layer was diagnosed by measuring Cu K_α emission. As discussed in Section 4.3.2, the ejection of a K-shell electron from a Cu atom by a fast electron creates a valence state which when filled by an L-shell electron produces a photon of K_α x-ray radiation with energy equal to 8.05 keV at room temperature. The K_α photons are assumed to be emitted over the full 4π solid angle. The choice of CH as the variable thickness fast electron propagation layer ensures minimal scattering and transmission losses of the Cu fluorescence emission. Varying the thickness of the CH propagation layer while the Cu layer thickness remained constant provided an effective method of controlling the number of transits of the refluxing fast electrons across the fluorescence layer.

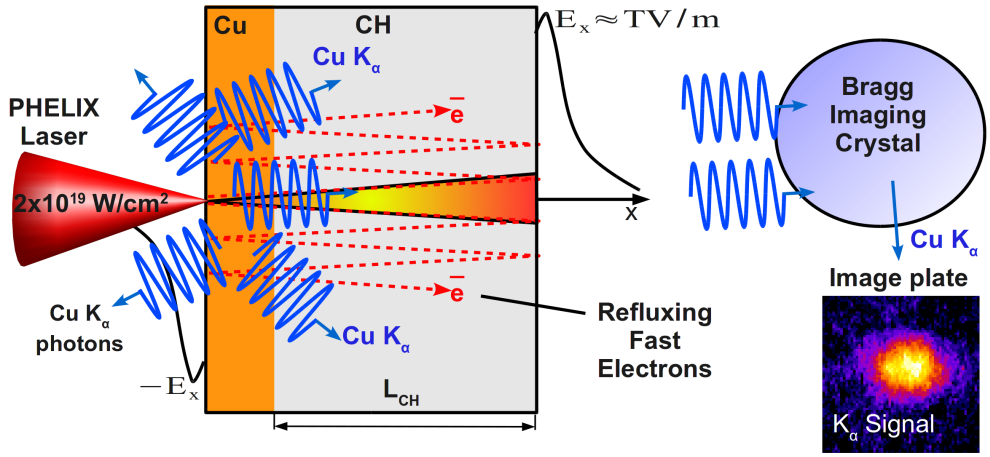

FIGURE 7.1: Schematic of experimental setup investigating fast electron refluxing. Fast electrons generated at the front (Cu layer) are transported through the layered Cu-CH target and can be reflected by the sheath potential, E_x, formed on both surfaces, thereby giving rise to refluxing inside the target. This effect is investigated by measuring the yield and spatial extent of the K_α emission, using a Bragg spherical imaging crystal and image plate detector, as the thickness of the CH propagation layer is varied.

The K_α emission from the rear of the target was imaged by a spherically-bent Quartz Bragg crystal onto Fujifilm Imaging Plate (IP). The film was subsequently scanned and the photo-stimulated luminescence (PSL) quantified. The Bragg crystal images x-rays within a narrow 6 eV bandwidth (centred at 8.05 keV) emitted in a solid angle equal to 10 msr. The viewing angle, at the rear of the target, was $\approx 75°$ relative to the laser axis. The crystal reflectivity was equal to 6×10^{-4} with $2d = 3\,\text{Å}$. The crystal and detector were positioned to produce an x-ray image with $\times 3$ magnification and spatial resolution equal to 20 μm.

The K_α x-ray emission from the Cu fluorescence layer is subject to attenuation in the CH propagation layer. This absorption was accounted for by correcting the recorded signal intensity using known x-ray mass attenuation values for cold plastic [226]. The yield of K-shell emission from the Cu layer was determined by integrating the signal contained within the image after background subtraction. The scanned image plate PSL values was converted to number of K_α photons using the calibration reported in [227]. The loss of signal due to the fade-time before scanning was accounted for using the calibration reported in [228]. A correction to the K_α signal was also made to account for the partial occlusion of the imaging cone by another diagnostic. The lateral extent of the source was calculated by fitting the measured distribution with a Gaussian profile and determining the full width at half maximum (FWHM). The results are shown in Figure 7.2.

Proton emission from the rear surface of the target was also diagnosed on the same laser shots. The properties of the proton beam were measured using a passive stack of 5 cm $\times$ 5 cm dosimetry film (RCF: Gafchromic® film, HD-810 and MD-V2-55)

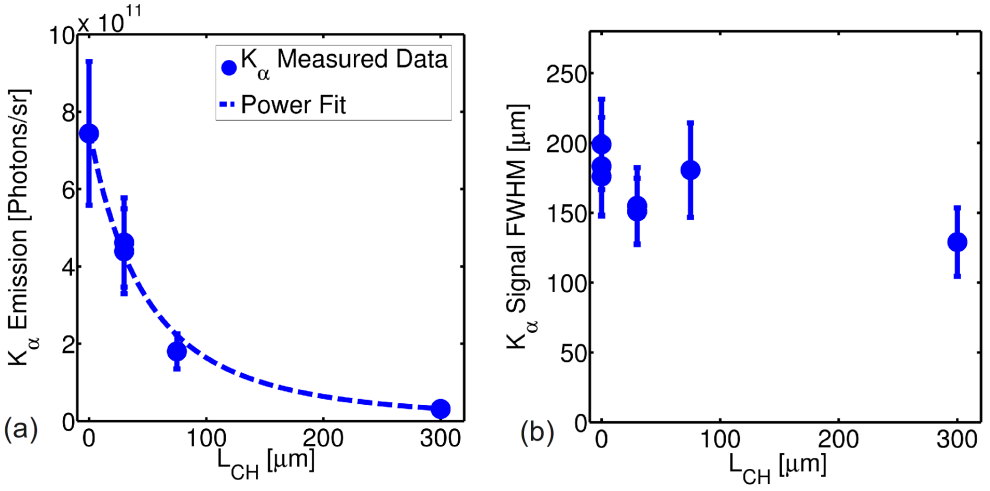

FIGURE 7.2: Experimental measurements of: (a) Total yield of Cu K_α emission adjusted for absorption in CH; the dashed line is a power fit; (b) Lateral extent (FWHM) of the K_α source, as a function of the thickness of the CH propagation layer.

positioned at the rear of the target. This diagnostic enables measurement of the spatial intensity distribution of the proton beam at energies given by the Bragg peak deposition in each film as discussed in Section 4.3.1.1.

The yield of K_α emission from the Cu layer is measured to increase significantly as the thickness of the CH propagation layer, L_{CH}, is decreased, as shown in Figure 7.2(a). In the absence of fast electron refluxing the Cu K_α signal should remain approximately constant (when corrected for absorption and scattering) since the fast electron population would pass through the Cu layer only once. The significant enhancement in the signal as the target thickness is decreased demonstrates that the fast electron beam is refluxing between the front and rear boundaries of the target, with the number of refluxes increasing with decreasing target thickness.

The measured lateral extent of the K_α source as a function of L_{CH} is shown in Figure 7.2(b), and is observed to increase only slightly as L_{CH} is decreased from 300 μm to 0 μm. Scattering of the K_α emission within the CH layer can be discounted as simulations using GEANT4 [194] indicate negligible effects. The size of the K_α source depends not only on the lateral expansion of the fast electron population within the target, but also any spreading of fast electrons along the front surface [167]. The contribution from surface spreading of electrons was determined by coating the surface of a 20 μm Cu foil with a 2 μm layer of CH. The K_α source size measured 155 μm for this test case, similar to the main result involving uncoated targets. This indicates that front surface spreading of electron current is unlikely to define the measured K_α distribution size.

These measurements of the lateral size of the K_α emission with L_{CH} indicate that the fluorescence source size is relatively independent of refluxing and is mainly produced

by electrons on their first pass through the Cu layer. After each successive reflux the electron beam density decreases and contributes little to increasing the lateral extent of the K_α emission in the Cu layer. The large lateral extent suggests a relatively large spatial distribution of electrons in the front Cu layer. The fact that the refluxing current enhances the overall yield within the large K_α distribution at the front of the target without significantly increasing the lateral source size may indicate that a highly divergent low energy electron population is responsible for defining the lateral extent of the K_α emission region on the first pass through the Cu. These low energy electrons are absorbed or scattered and do not contribute to the refluxing current. The higher energy electrons which can reflux multiple times may have a smaller divergence angle to travel back into the Cu layer giving rise to a relatively small increase in the size of the K_α emission region with decreasing target thickness.

7.3 Refluxing model for K_α emission

In order to calculate the expected yield of K_α emission from a Cu layer as a function of L_{CH}, an analytical model was developed. This model calculates the fluorescence yields for a distribution of fast electrons as a function of their initial energy.

The population of fast electrons is assumed to propagate within a layered target, with reflection at the front and rear surfaces, until they lose all their energy. The initial fast electron spectrum $f(E_{f0})$ is assumed to have the following Maxwellian distribution:

$$f(E_{f0}) = 2\sqrt{\frac{E_{f0}}{\pi(k_B T_f)^3}}\,\exp\left(-\frac{E_{f0}}{k_B T_f}\right) \tag{7.1}$$

with the temperature $k_B T_f$ given by the ponderomotive scaling $k_B T_f = m_e c^2(\sqrt{1+a_0^2/2}-1) = 1.2$ MeV where the dimensionless laser intensity $a_0 = 4.6$ for the conditions of the experiment. The constants c and m_e are the speed of light in vacuum and the electron rest mass, respectively. In the model calculations, the initial fast electron spectrum is separated into 0.05 MeV energy bins with central energy E_{f0}. As the electrons travel through the Cu layer the cross sections for K_α production are integrated over the layer thickness (i.e. 20 μm). Using a similar approach to that used by Myatt *et al* [97], the total K_α photon yield is calculated as:

$$N_k = \eta_r N_f \int_0^\infty f(E_{f0})dE_{f0} \int_{E_{f0}}^0 \omega_k n_{Cu}\sigma_k \left(\frac{dE}{ds}\right)^{-1} dE \tag{7.2}$$

$$= \eta_r N_f \omega_k n_{Cu} \int_0^\infty f(E_{f0})dE_{f0} \int_0^{s(E_{f0})} \sigma_k[E(E_{f0}, s)]ds \tag{7.3}$$

where the total number of fast electrons is calculated using $N_f = \eta_{L\to e} E_L/(k_B T_f)$ assuming a laser-to-electron energy conversion efficiency $\eta_{L\to e} = 20\%$ [224]. The fraction of electrons which reflux $\eta_r = N_{f(reflux)}/N_f$ is assumed to be 0.95 as calculated in Section 3.7 using the capacitance model [97]. The atomic density of Cu is $n_{Cu} = 8 \times 10^{22}/\text{cm}^3$ and $\omega_k = 0.44$ is the fraction of ionised K-shell states which decay through K_α emission as opposed to Auger decay [229]. Opacity effects which define the expected absorption for 8.05 keV photons in Cu are included using:

$$N_{trans} = \exp(-\mu L_{Cu}) \tag{7.4}$$

where $\mu = 463\ \text{cm}^{-1}$ is the attenuation coefficient for 8.05 keV photons in cold solid Cu. The relativistic K-shell ionisation cross section in Cu, σ_k, is calculated using the Quarles method [230] (Figure 7.3(d)) for a potential of 8.979 keV. The formulae for this calculation can be found in Appendix B. Collisional and radiative losses for electrons in Cu and CH are incorporated, as calculated using the ESTAR stopping tables [152]. The effects of material bulk temperature on K-shell ionisation rates are included and are discussed in Section 7.4.

Electric field inhibition in CH

In addition to collisional and radiative losses, electric field inhibition in the propagation of fast electrons in the plastic layer provides an additional mechanism of energy loss (also known as anomalous stopping). As discussed in Section 3.1, the principle of current neutrality requires that the forward going fast electron ($\mathbf{j}_f$) current is balanced by a return current ($\mathbf{j}_r$) such that $\mathbf{j}_f + \mathbf{j}_r \approx 0$ [92]. In the case of a metal, the return current is readily available in the form of the valence electron population. However for materials that are initially insulators, a return current population of thermal electrons must be made available through ionisation of the background material. With increased ionisation at high plasma temperatures, insulators such as CH become conductors. In the absence of a sufficient return current an electrical charge separation field is induced and acts to inhibit the forward propagation of the fast electron beam. Since it is a function of the material conductivity κ, the **electric field** can grow significantly large in insulators:

$$\mathbf{E} \approx \frac{e n_f v_f}{\kappa} > \text{GV/m} \tag{7.5}$$

where e, n_f and v_f are the electron charge, fast electron beam density and velocity, respectively. The fast electrons lose energy in working against the inhibiting electric field. This energy loss mechanism is accounted for in this model of fast electron refluxing.

Fast electron energy loss in dielectric materials has been studied by Tikhonchuk [66] who derived the following expression for the effective frictional force acting on the electrons due to the field ionisation:

$$F_i = \frac{9}{2}\pi\Lambda^2 m_e \nu_{ep} v_f n_f a_B^3 (\frac{J_H}{J_{CH}})^2 \tag{7.6}$$

where J_{CH} and J_H are the ionisation potentials for plastic and hydrogen, ν_{ep} is the collision frequency and a_B is the Bohr radius. The Λ term is a large logarithmic factor arising due to the exponential dependence of the ionisation rate on the electric field amplitude, and is defined as:

$$\Lambda = \log[\frac{2\omega_a r_e n_a c^2}{3\pi\nu_{ep} n_f^2 a_B^4 v_f^2} (\frac{J_{CH}}{J_H})^4] \tag{7.7}$$

where ω_a, r_e, n_a are the atomic frequency, classical electron radius, and the atomic density respectively. For transport in CH, where $J_{CH} = 78$ eV, $n_f = 1 \times 10^{25}$ m^{-3} and $\nu_{ep} = 1 \times 10^{15}$ s^{-1}, $\Lambda \approx 20$ and an energy loss of $F_i \approx 1$ keV/μm is calculated. As the material is

Refluxing Model results

Total yield of Cu K$_\alpha$ emission, calculated as a function of L_{CH} is shown in Figure 7.3(a). These results are labelled 'cold' and 'hot' and are fluorescence predictions for cold material at room temperature and for a heated plasma respectively, as discussed in Section 7.4. The cold material prediction over-estimates the fluorescence yield by a factor of 3.5. Including the influence of material heating brings the model into agreement with the experimental measurements. As discussed above, in the absence of refluxing the K$_\alpha$ signal produced by the passage of the fast electron population through the Cu layer should remain constant, independent of L_{CH} (when corrected for absorption in the CH layer). The significant increase in K$_\alpha$ yield with decreasing L_{CH} is explained by refluxing, which increases the number of passes of the electrons through the Cu layer, see Figure 7.3(b). The model fits particularly well with the experiment data when the electric field inhibition in CH is included. The results in Figure 7.3(c) show that this effect plays a significant role, the number of refluxes, and hence the K$_\alpha$ emission, is very sensitive to the electron energy losses caused by electric field inhibition. Without it the fast electrons reflux a larger number of times before stopping. Indeed, it is apparent that collisional losses alone would not bring the model predictions into agreement with the measured data.

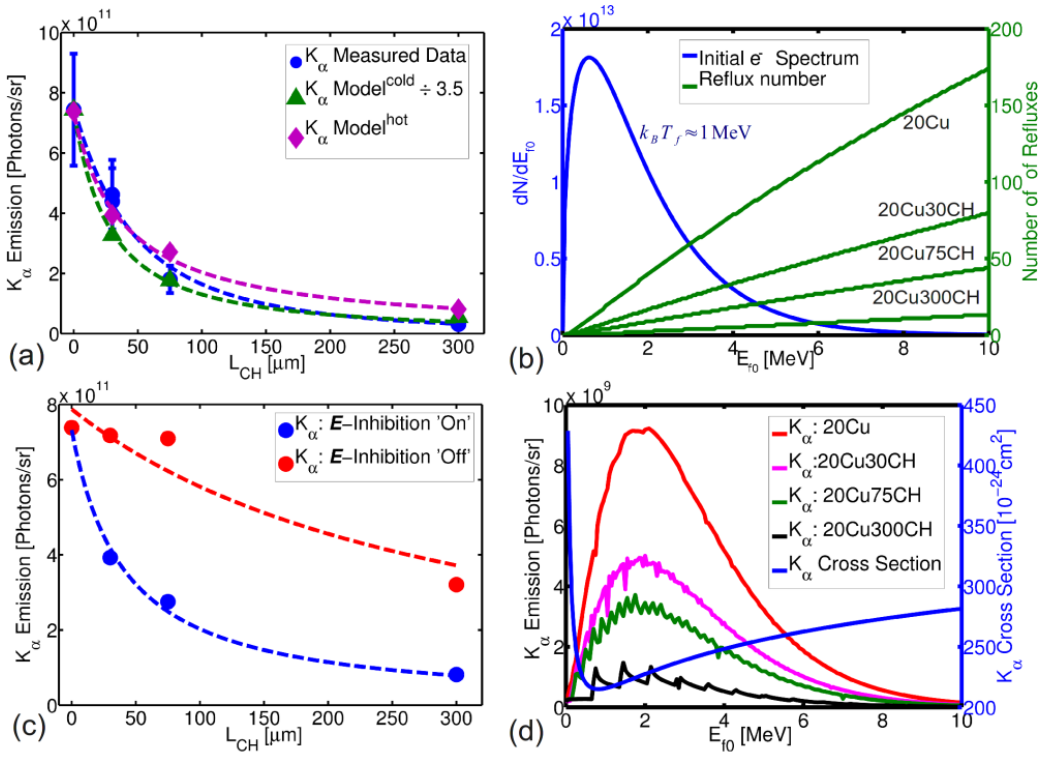

FIGURE 7.3: The results from the analytical model of fast electron refluxing in Cu-CH targets. Dashed lines are power fits; (a) Total number of Cu K_α photons produced as a function of L_{CH} from the refluxing model for both cold and hot material. These predictions are shown with the experimental measurements for comparison; (b) The initial fast electron spectrum and the resulting energy-dependant number of electron refluxes for each target thickness inclusive of E-field inhibition effects; (c) The effect of inclusion of E-field inhibition in CH in the model; (d) The total number of Cu K_α photons as a function of initial fast electron energy, E_{f0}, for each specific target. The energy dependant cross-section for Cu K-shell ionisation is also shown.

The contribution to the overall K_α yield as a function of the initial fast electron spectrum is shown in Figure 7.3(d) for each target. The largest contribution is made by the population of fast electrons with initial energy $E_{f0} \approx 2$ MeV. Either side of this maximum there is a trade-off between the number of fast electrons and their maximum number of refluxes. The step-like features within the curves (specifically the peaks) correspond to fast electrons which start with sufficient energy to complete a whole number of refluxes back into the Cu fluorescence layer. The step-width relates to the total energy loss per reflux in the respective target. This is most obvious for the thickest target, 20Cu+300CH, where there is a loss of ≈ 0.8 MeV per reflux. The calculated cross section for Cu K_α production is also shown in Figure 7.3(d). The cross section is maximum for tens of keV electrons, but this population is absorbed in the Cu layer and does not reflux. The model shows that the measured increase in the K_α emission with decreasing target thickness is explained by the refluxing of MeV electrons, with anomalous stopping due to electric field effects in the CH propagation layer.

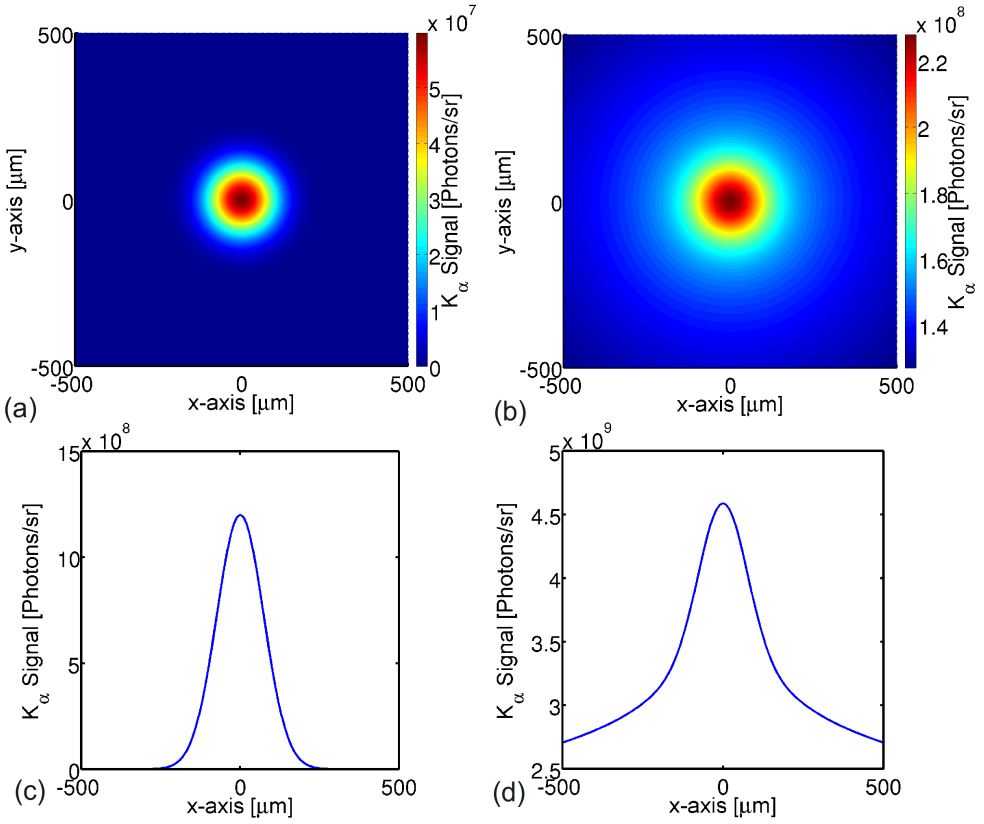

FIGURE 7.4: Spatial distribution of K_α emission for 20 μm Cu without refluxing (left) and with refluxing (right).

The spatial distribution of the K_α emission can be approximated by assuming the beam of fast electrons propagates ballistically through a Cu foil with divergence $\theta_{1/2}$. A 2D Gaussian distribution is assumed here to describe the transverse profile of the beam. For a single pass, the distribution of fluorescence emission is calculated after a depth of 20 μm. In the case of refluxing, the fluorescence distributions for multiple transits are summed producing an integrated image. The results for both cases are shown in Figure 7.4. The 2D K_α distributions are similar in shape but differ in signal intensity. Refluxing adds over an order of magnitude in K_α intensity compared to the case of single pass, see Figure 7.4(a-b). It is clear that the first pass transit of fast electrons produces the effective source size distribution. The effect of refluxing is to enhance this distribution, especially in the wings, see Figure 7.4(c-d). In the first pass scenario, the bulk of the K_α yield is produced by fast electrons with energy < 500 keV. This is a consequence of the increased K_α cross-section for lower energy electrons. In the case of refluxing, the higher energy electrons in the MeV range are responsible for the higher fluorescence yields. For the low energy component, $E_{f0} < 500$ keV, a high divergence of $\theta_{1/2} = 77°$ is required to recreate the measured source size of ≈ 180 μm. Measurements of proton acceleration, discussed in Section 7.5, are consistent with the higher energy fast electrons, $E_{f0} > 1$ MeV, having a lower divergence of $\approx 15°$ half-angle.

7.4 Fast electron transport simulations

The effects of fast electron refluxing was investigated further using the numerical electron transport code LEDA [231]. As discussed in Section 4.4.2, this is a 2D hybrid code which treats fast and thermal electrons as two distinct populations. The latter is approximated by a fluid while the fast component is modelled using a Vlasov-Fokker-Planck algorithm similar to that of KALOS [121].

The simulations were performed using a 2D spatial grid of target material without vacuum boundaries and with 1 μm cell size. The target material consisted of two layers matching the experiment: a front 20 μm Cu layer backed with a variable thickness of CH. The total target size was 800 μm in the y-axis and L_{CH+Cu} in the x-axis. The fast electrons were injected into the target with a $\cos^8\theta$ angular distribution with $\theta_{1/2} = 25^\circ$ over the nominal duration of the laser pulse, set to 1 ps, with an initial beam size of 15 μm FWHM. A relativistic Maxwellian with temperature $k_B T_f = 1$ MeV defined the initial fast electron spectrum. A laser-to-electron energy conversion efficiency of $\eta_{L\to\bar{e}} = 20\%$ was assumed. The material temperature and hence resistivity is calculated self consistently over the course of the simulation in response to the fast electron propagation. The resistivity of Cu with temperature was defined using measurements carried out by Sandhu [199] and extended beyond 50 eV assuming a Spitzer scaling. The resistivity response of CH with temperature is the simple heuristic model derived by Davies [164]. The resistive electric field which acts to inhibit the fast electrons is also included as per the standard hybrid model [164]. Fully reflective boundaries surround the simulation space and the full fast electron population is refluxed within the target. The hybrid simulations were performed for the range of targets used in the experiment.

An example of refluxing electron transport is shown in Figure 7.5 for 20 μm Cu + 75 μm CH target. Both electron density and current density, j_x, are shown. The latter clearly distinguishes the current direction: forward going current is negative. The transport through the target is dominated by collective effects. The injection zone is marked by strong localised pinching from the strong azimuthal B-field. Instabilities form as opposing currents drive resistive filamentation. The beam traverses the target in $\approx$ 300 fs, after which the fast electrons reflect from the rear surface.

The main parameter extracted from over the duration of the simulations is the mean fast electron beam density within the 20 μm Cu layer as a function of L_{CH}. The density was averaged within a 20 μm $\times$ 200 μm box. The results are shown in Figure 7.6(a). The electron density increases significantly as the target thickness is decreased due to refluxing. The peak electron density for each target thickness is shown in Figure 7.6(b) and is observed to follow a similar trend to the K_α measurements.

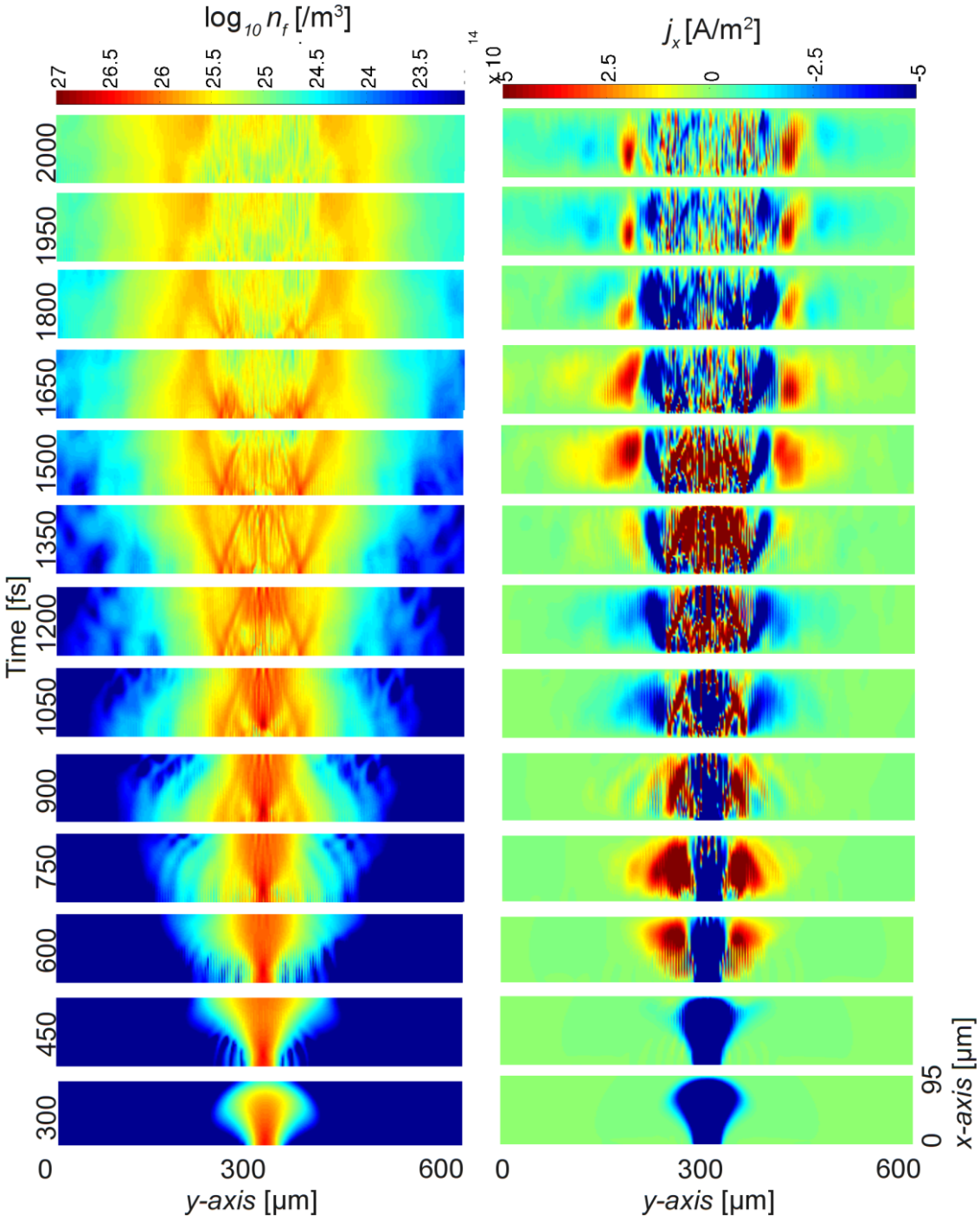

FIGURE 7.5: Simulation of electron transport in layered target 20Cu+75CH over 2 ps duration. The propagation of the electron beam is shown using both electron density (left) and current density in the x-direction j_x (right). The refluxing of fast electrons begins to occur after 500 fs.

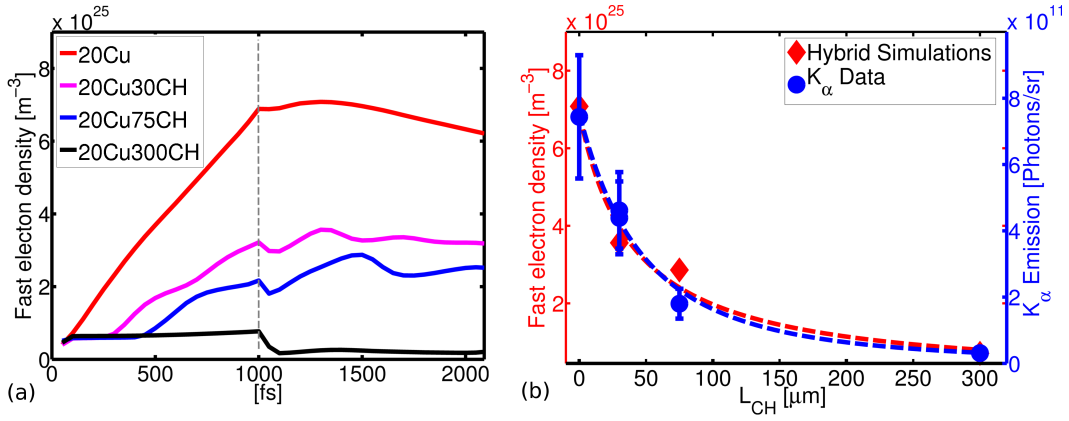

FIGURE 7.6: Hybrid simulation results showing: (a) the fast electron density (in the Cu layer) as a function of time, for given targets. The laser pulse switches off at 1 ps as indicated by the dashed line; (b) The peak fast electron density as a function of L_{CH} is compared with the integrated K_α measurements. The dashed lines are power fits.

Temperature effects

The propagation of relativistic electrons in a solid target induces heating of the initially cold background material via the highly collisional cold return current. This is discussed in detail in Section 3.6. The refluxing of fast electrons should give rise to enhanced heating as the target thickness is decreased. Although a measurement of the Cu target temperature could not be made, the LEDA simulation results were used to estimate $k_B T_{\mathrm{Cu}}$ for each target thickness investigated.

The on-axis plasma temperature in the Cu layer is shown in Figure 7.7(a) for each target over a 2 ps duration. The temperature of the target is found to increase with the number of transits of the fast electron population across the target. An increasing temperature of the Cu layer and the corresponding change in ionisation state directly affects the K_α fluorescence, and results in a broadening and shifting of the emission line to shorter wavelengths. Due to the narrow band width of the imaging crystal (6 eV) the measured

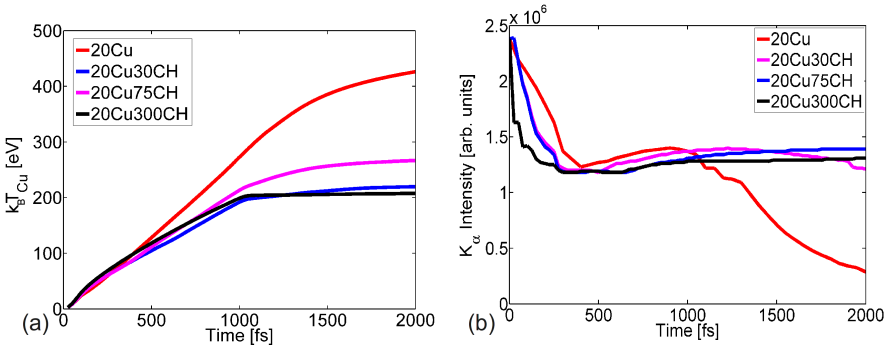

FIGURE 7.7: (a) The on-axis plasma temperature in the Cu layer is shown as calculated from the hybrid simulations; (b) The effects of material heating on the intensity of the K_α emission as calculated using the FLYCH atomic code.

K_α signal is sensitive to such temperature shifts [192]. The intensity of the detected K_α signal is expected to decrease with increasing plasma temperatures. As a correction to the refluxing model, the reduction in K_α signal due to heating of the Cu is estimated using the FLYCHK atomic spectroscopy code suite [193]. The emission spectrum for Cu is calculated using the temporal evolution of the target temperature determined from the hybrid simulation results as an input parameter. The intensity of the Cu K_α line within the window of the Bragg crystal is shown in Figure 7.7(b). Target heating has an effect, particularly for the thinnest (20 μm) target where the maximum temperature approaches 500 eV. Including this effect improves the correlation between experiment and the refluxing model, as shown in Figure 7.3(a).

7.5 Proton acceleration results

The measured proton beam properties for the same laser shots are shown in Figure 7.8. The protons are accelerated by target normal sheath acceleration at the rear surface of the targets, see Section 3.8 for a description of this mechanism.

The maximum proton energy, E_{max}, shown in Figure 7.8(a) is sensitive to both the temperature and density of the fast electrons giving rise to the sheath field at the rear of the target. The overall coupling of energy from laser to protons via the fast electrons, as described by the conversion efficiency, shown in Figure 7.8(b), is obtained by integrating the proton energy spectra. This measurement is sensitive to the total numbers and energy of the accelerated protons. The maximum proton energy is greatest in the case of the thinnest target as is the conversion efficiency. The influence of refluxing on these measurements are investigated using both numerical and analytical models.

As discussed in Section 3.8, the maximum proton energy can be predicted as a function of n_f and $k_B T_f$ using Mora's 1-D isothermal plasma expansion formula [25]:

$$E_{max} = 2k_B T_f \left[\ln\left(\tau_p + \sqrt{\tau_p^2 + 1}\right)\right]^2 \tag{7.8}$$

where t_a and $\tau_p = t_a\sqrt{e^2 n_f / m_p \varepsilon_0}/2.33$ are the acceleration time and normalised acceleration time, respectively [169].

The fast electron density on-axis at the rear surface of each target is extracted from the hybrid simulation results as a function of time. The temporal on-axis profile of n_f is shown in Figure 7.9 for each target. A temporally averaged value electron density is used, over an acceleration time $t_a = 1$ ps, beginning from the arrival time of the fast electrons at the rear surface. Figure 7.8(a) shows the resulting calculation of E_{max} for

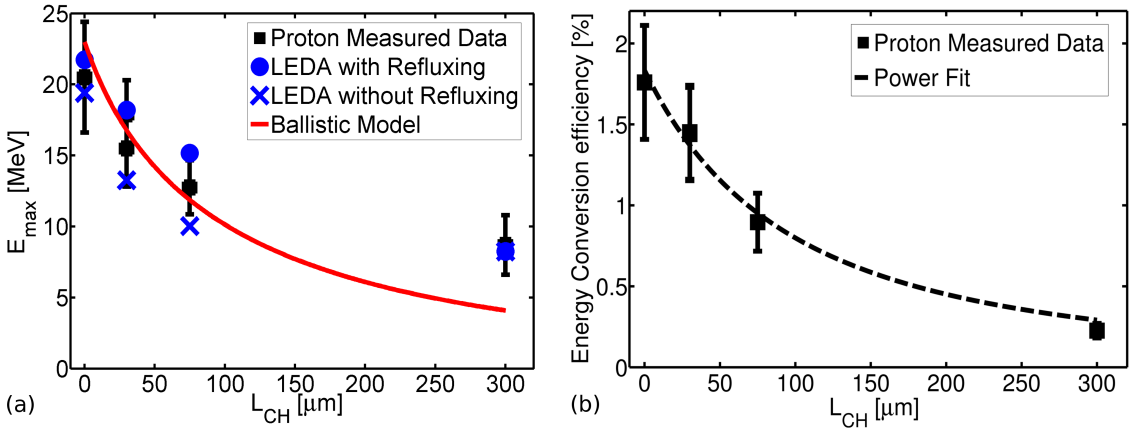

FIGURE 7.8: (a) Measurements of maximum proton energy as a function of target thickness. Also shown are predictions using fast electron densities determined from LEDA hybrid simulations and the Moral model. This is calculated with and without refluxing. The solid red line i and a calculation based on simple ballistic transport of fast electrons into a cone with divergence half angle equal to 15° are also shown; (b) laser-to-proton energy conversion efficiency as a function of L_{CH}. The dashed line is a power fit.

each target using the Mora plasma expansion formulae. This calculation is repeated for the case without refluxing. This is achieved by extracting the on-axis fast electron density at depths x = 20, 50, 95 and 320 μm in the simulation results for the thickest target, for which refluxing does not occur within the time window sampled (1 ps from the arrival of the fast electrons). The predicted values of E_{max} in the absence of refluxing is also shown in Figure 7.8(a).

Predictions using a ballistic transport model are also shown in Figure 7.8(a). This analytic model of proton acceleration is similar to that used in a number of previous

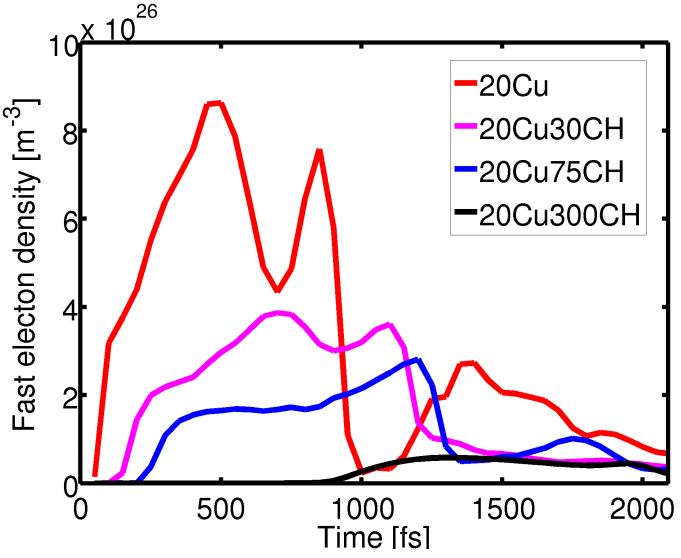

FIGURE 7.9: The fast electron density on-axis at the target rear surface as calculated using hybrid simulations is shown.

works [95, 169, 172] including the investigation of Chapter 5. This approach involves calculating the average rear surface electron density as a function of target thickness using $n_f = N_f/(c\tau_L S_A)$, assuming simple ballistic transport of the fast electrons through the target at a fixed beam divergence angle. The sheath area is calculated as $S_A = \pi(\phi_L/2 + L\tan\theta_{1/2})^2$ for a target with thickness L. The maximum proton energy is then calculated using the Mora plasma expansion formulae. The result shown in Figure 7.8(a) was calculated for half angle $\theta_{1/2} = 15°$. This simple analytical model, which does not include refluxing effects is also in broad agreement with the experimental data. Refluxing can in principle increase the fast electron density at the rear surface of thin targets (thickness less than $c\tau_L/3 = 100$ μm) and therefore the maximum proton energy. Analytical predictions by Huang *et al* [232] suggest that refluxing effects can enhance proton max energy for these experimental conditions. However, the Huang model does not account for angular spreading of fast electrons with L. In the Mora model [25], any relative enhancements to the electron density at the rear surface by refluxing are lessened by the log dependence of E_{max} with n_f. The limits of uncertainty in the measured maximum proton energy do not enable a conclusion of whether refluxing has enhanced E_{max} experimentally. Compared to K_α emission, maximum proton energy is a much less sensitive diagnostic to fast electron refluxing.

Shown in Figure 7.8(b) are measurements of energy conversion efficiency from laser to protons (above 2 MeV) as a function of target thickness. The total energy content of the proton beam is sensitive to a large number of factors, including the transverse extent of the fast electron sheath (proton source size) and the time for which fast electrons are present at the target rear surface to transfer energy to the protons. Ridgers *et al* [233] have suggested that the increased number of fast electrons provided by refluxing can enhance the ion flux. A detailed examination of the effects of refluxing electrons on proton acceleration is beyond the scope of this work and will require further investigation.

7.6 Conclusion and discussion

The results reported in this chapter regards an investigation of fast electron refluxing in layered targets with thickness in the range 20 μm $-$ 320 μm irradiated by intense, picosecond laser pulses. Measurements of the intensity of K_α emission from a Cu fluorescence layer at the front surface of the target is found to increase significantly with decreasing target thickness. The results are explained by multiple transits of the fast electron population through the florescence layer due to reflection in the sheath fields which are formed on both the front and rear surfaces of the target.

An analytical model of fast electron refluxing within the target predicts a scaling of K_α emission with target thickness which is in good agreement with the experimental data when the effects of target heating and E-field inhibition in a CH propagation layer are included. This model predicts that the population of electrons with initial energies of the order of 2 MeV contribute most to the enhancement of the K_α yield. Furthermore, hybrid simulations of fast electron transport, which include electron refluxing via reflective boundaries, predict fast electron density scaling consistent with the experimental K_α emission results.

Measurements of the spatial extent of the K_α emission as a function of target thickness suggest that low energy (tens of keV) electrons injected into the target with a large divergence angle define the overall K_α source size and that the population of higher energy (MeV) refluxing electrons are contained within a smaller divergence half-angle, of the order of 15° as inferred from measured proton emission. The combined results of K_α yield and source size are therefore consistent with an energy dependant angular distribution of fast electrons. Measurement of the maximum energy of protons as a function of target thickness is shown to be a much less sensitive diagnostic of fast electron refluxing than K_α fluorescence.

An understanding of the extent to which refluxing influences experimental results is necessary if such results are subsequently applied in bench-marking fast electron transport models and codes. In addition to the direct effects on energy deposition and beam divergence, refluxing electrons can strongly affect other aspects of laser-solid interaction physics, such as field generation. In the investigation reported in Chapter 5, regarding the influence of self-generated azimuthal magnetic fields on fast electron beam divergence, refluxing in thin foil targets is shown to destroy the structure of the collimating field.

There are a number of techniques for minimising the effects of refluxing. The simplest is increasing the target thickness by the addition of thick propagation layers as used in the present work. Alternatively, the sheath fields formed on the target surfaces can be perturbed which enable the fast electrons to escape. For example, this can be achieved by applying a separate nanosecond pulse to the rear surface creating a long density gradient as used in an investigation involving the author [221, 234]. Although somewhat more difficult to implement, time-resolved measurements can also be used to negate refluxing effects.

Chapter 8

Summary and Conclusions

The investigations presented in this thesis have resulted in a number of fundamental results on the transport of Mega-Ampere relativistic electron beams in solid density plasmas. In this final chapter these results and their contribution to the field will be summarised.

8.1 Summary of results

A core feature of the experimental investigations presented in this thesis is the implementation of rear surface proton emission to diagnose the electron transport occurring over picosecond timescales within the solid density plasma of the target. The measurements have been complemented by a combination of numerical and analytical calculations. The outstanding questions introduced in Chapter 1 regarding the effects of magnetic fields, filamentation and refluxing have been investigated. The results make clear that there is an interdependence of these collective phenomena which together define the primary physics of fast electron transport. A summary of these results is presented here for each investigation.

8.1.1 Effect of self-generated magnetic fields:

Prior to this work there had been a lack of strong or indeed no evidence for global magnetic pinching as predicted by Bell & Kingham [94]. Many previous measurements of electron beam divergence have been limited to thin targets, below 100 μm, by the opacity range of x-ray fluorescence measurements [146, 147] or the electron bunch coherence required for transition radiation [136]. In all such cases, the electron beam width was

found to increase linearly with target thickness. The ensuing physical picture of beam divergence has been one of simple ballistic spreading through the target.

The investigation reported in Chapter 5 differed in methodology to previous work in two regards. Firstly, the rear surface electron beam width is inferred from proton beam properties. Secondly, proton emission remains effective past the previous limits of target thickness.

The measurements are interpreted as a transition to non-ballistic transport in thick solid density aluminium targets. A decrease in lateral size of the sheath in thick targets indicates an effective reduction in beam divergence in thick ($> 300\,\mu$m) aluminium targets. Numerical modelling using a hybrid code shows that this reduction in divergence may result from an increased effectiveness of magnetic collimation in thicker targets. Higher rates of fast electron refluxing in relatively thin targets is shown to fragment the magnetic field. Refluxing inhibits the formation of the azimuthal magnetic field and therefore reduces its effectiveness in pinching the fast electron beam.

8.1.2 The effects of scattering and low temperature resistivity on electron transport instabilities:

A myriad number of phenomena involving different instabilities and material properties are potential influences in the development of filamentation in fast electron beams. In previous experimental work, filamentation had been observed in low Z insulators while medium and high Z metals exhibited no such evidence of filamentation [140]. A prediction correlating the degree of filamentation with low rates of fast electron scattering had been proposed [127]. The investigation reported in Chapter 6 sought to distinguish whether scattering or material resistivity were the dominant influence.

The presence of filamentation was investigated for a wide selection of materials with different Z-number and initial resistivity over a target thickness range spanning hundreds of microns. Crucially, the low-Z metal lithium was studied for the first time. Measurements of the electron transport instabilities were performed by inferring the spatial homogeneity of the rear surface electron sheath via measurements of the proton beam spatial intensity profile.

Transport through the lithium target results in a smooth electron sheath. This evidently shows that the role of angular scattering is minimal in suppressing the growth of beam filamentation. Resistivity is proposed to be the dominating material characteristic concerning the growth of beam filamentation. The resistivity curve for lithium was derived in order to test resistive filamentation growth. Numerical studies suggest that the ionic

order of the material greatly effect its low temperature resistivity and hence the growth of beam instabilities. Global magnetic pinching can effectively suppress the breakup of the beam by stabilising the resistive filamentation.

A sheath evolution model is created to study the development of the proton beam from the filamented fast electron sheath. The expansion of the sheath along the rear surface is found to recreate the trend of measured proton beam intensity variation with target thickness. This trend arises due to the smoothing effects that are predominant over smaller initial sheaths sizes in thinner targets. The initial sheath diameter determines whether the sheath expansion smooths out the initial filamented structure. This expansion at the rear surface limits the sensitivity of proton emission for measuring electron beam filamentation to targets that are relatively thick. This is the case when the initial sheath diameter D_e is greater than the spread of the sheath within the laser pulse time such that $D_e > \tau_L \bar{v}_s$ which is equivalent to a thickness $L \gtrsim 150\,\mu$m for Vulcan-like laser conditions. Also, for relatively thin targets the sheath field homogeneity is affected by refluxing electrons which can disrupt the proton beam spatial distribution regardless of material.

8.1.3 Refluxing of fast electrons in solid density plasma:

Motivation for this work was provided by the lack of dedicated direct investigations of fast electron refluxing. This phenomena is frequently ignored in the interpretation of K_α spatial data for determining electron beam source size. Presented in Chapter 7 is experimental proof that a large fraction of fast electron population do not escape the target but are constrained to propagate between the front and rear sheath fields. This is determined by measuring the yield of x-ray photons from a front fluorescence layer while increasing the thickness of a rear plastic transport layer.

An analytical model shows that the bulk of the fluorescence yield derives from the MeV fast electron population. The lateral size of the fluorescence emission from the front layer changes very little as the backing layer thickness is increased. This large size of the distribution is consistent with an almost spherical spread of electrons with energies above $\approx 9\,$keV. In order to reflux, the electrons require MeV energies to transverse the target multiple times. The angular divergence of these refluxing electrons must be distinct with the high energy electrons having a more confined spread. Measurements of proton emission, specifically maximum energy, indicate a relatively low divergence for MeV electrons. Compared to the K_α fluorescence yield, proton emission exhibits less sensitivity to refluxing.

8.1.4 Probing electron transport with proton emission

The development of proton emission as an electron transport diagnostic has been proven most effective and versatile in these investigations. The maximum proton energy provides a measure of the maximum fast electron density and sheath field potential at the rear surface for a given fast electron temperature $k_B T_f$. The spatial profile of the proton beam, measured over many energy steps, can be reverse engineered to calculate the initial transverse diameter and hence effective divergence of the electron beam. Spatial uniformity of the proton beam is also correlated with that of the electron sheath and is sensitive to electron beam filamentation. Unlike many other diagnostic approaches to electron transport, proton beam measurements are effective from microns to millimeters of target thickness for a petawatt laser driver. Also, many of the characteristics of the proton beam can be predicted analytically with relative simplicity by modelling the electron sheath geometry and evolution in time and space. In other work, picosecond resolved proton probing has provided detailed images of electron transport in the interior of the target, albeit limited to low density foam material [235]. In this case both filamentation and divergence of the beam were measured. Together, these various measurements of proton emission from solid density targets have provided significant insight to the collective phenomena of fast electron transport.

8.2 Implications for an electron transport driver for Fast Ignition

The on-going development of the HiPER project, coupled with the recent completion of both the OMEGA EP laser and the National Ignition Facility makes this an exciting time for ICF research. Full scale experiments at NIF [236], OMEGA [237, 238] and FIREX [239, 240] are in progress, building towards the prospect of achieving Ignition. A number of approaches to ICF are being pursued including Central Ignition [241], Shock Ignition [242] and Fast Ignition [7]. In this section, the results of this thesis are discussed with respect to the development of electron based Fast-Ignition.

As discussed in Section 1.2.1, the realisation of fusion energy by inertial confinement using the Fast Ignition scheme is dependant on a set of relatively stringent criteria. Two efficient energy conversions are required (i) the absorption of laser energy to fast electrons (ii) the deposition of this energy to the dense plasma core by fast electron stopping. Measurements of laser conversion efficiency, discussed in Section 2.5.4, confine $\eta_{L\rightarrow e} = 20 \pm 10\,\%$ [243]. The efficient deposition of this energy to the dense core is dependant on the initial beam divergence, the final divergence and the stopping/heating

at the core. Once the beam arrives at the core the ignition heating is provided by mainly Coulomb stopping of the fast electrons [200]. The values of the initial and final divergence are ultimately correlated with the role of magnetic fields.

As discussed in Section 3.4 the initial dispersion of fast electrons is a consequence of stochastic deflection during injection across the boundary of the critical surface [116]. The deflection fields here are a result of the Weibel instability in the underdense region. This is subsequently compensated by the magnetic pinching at the injection region after the critical surface which reduces the measured divergence to $20^\circ \pm 10^\circ$ half-angle as shown in Figure 3.8. A distance of some $100 - 300\,\mu$m must be traversed before the fast electrons reach the dense core. Further magnetic pinching extending over this range is highly desirable. The results presented in Chapter 5 indicate that global magnetic pinching can indeed occur over such distances for solid density aluminium reducing the divergence by $\approx 10^\circ$ half-angle. This is the case in the absence of refluxing currents which can fragment the collimating fields. At conditions relevant to fast ignition, average plasma densities are over 10^3 times greater than the experiment in Chapter 5. Numerical modelling of these conditions by Honorubia *et al* [200] indicate that magnetic pinching enhances the energy deposition at the core by a factor of 2.

The pinching magnetic field can also potentially act to stabilise the beam by suppressing filamentation. This feature is again very desirable as filamentation can extract an inordinate amount of energy from the beam [130]. As shown by the results of Chapter 6, the resistivity, specifically at low temperature, plays a large role in determining the likely-hood of filamentation in a given material by resistive or collisional-Weibel instability. Conductors, which have low resistivity at room temperature, exhibit much smoother beams than insulators. With regards the transport medium in Fast-Ignition, the overdense plasma has already been highly compressed and hence will be heated well into the Spitzer regime. Therefore, the collisional form of the Weibel instability will no longer be the primary instigator of filamentation. This is also the case for the ionisation instability. In this high-temperature regime the collisionless Weibel instability may be the dominating instability. The hot transport medium of the compressed fuel spans 4 orders of magnitude in density from the coronal plasma to the core. Such conditions have yet to be tested in relation to fast electron propagation.

8.3 Summary of fast electron transport

A model of electron transport in solid density material can be summarised with the addition of the novel results from the investigations of this thesis. The key features of are shown in Figure 8.1 and are discussed in the following section.

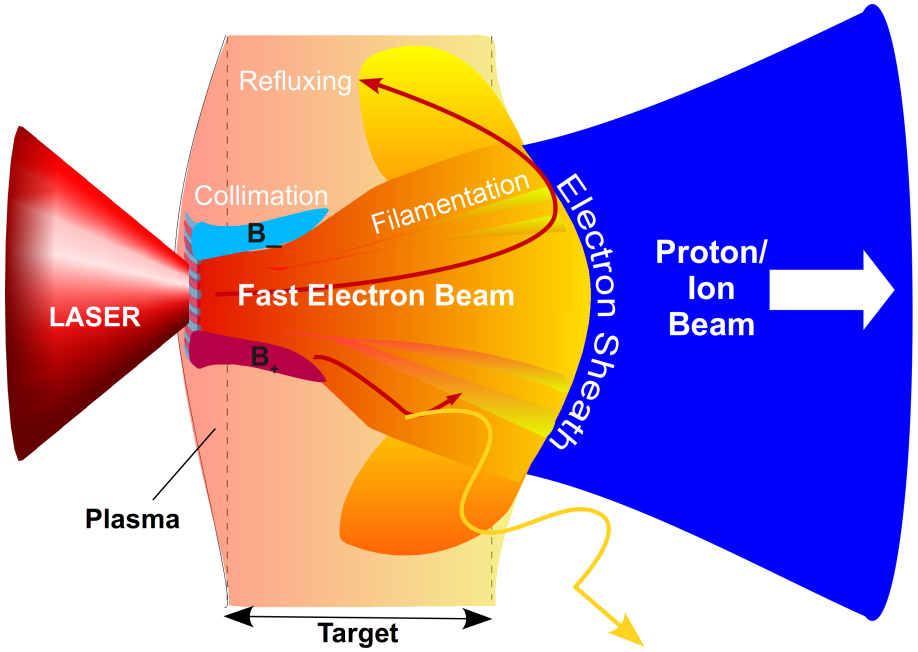

FIGURE 8.1: A generalised illustration of the key phenomena investigated in this thesis.

Fast electron transport is fundamentally dependant on the slow moving electrons which constitute the surrounding plasma. Without these 'cold electrons' the fast current is essentially brought to a halt by the electric fields induced by charge separation. Equal current densities of fast and cold electrons neutralise this field enabling transport to occur. The current density is such that kilo-tesla magnetic fields are induced which surround and help **pinch** the beam.

The effect of these fields have been measured to reduce the fast electron beam divergence in aluminium, albeit in thick targets. Similar self-generated fields induced by the counter streaming fast and cold currents can act on a smaller scale causing **filamentation** to occur. In initially cold solid targets the low temperature resistivity has been shown to be a possible mechanism in influencing the growth of the collisional Weibel instability induced by the collisionality of the return current. Increased levels of scattering have no measurable effect in mitigating this instability. Rather it is global magnetic pinching acting across the beam that can provide some form of suppression.

Once the fast electron beam reaches the rear surface of the target its forward motion is halted. Here at the interface to vacuum there are no plasma electrons to provide a return current and the charge separation fields pulls the fast electrons back into the target. This is termed **refluxing** and is a key transport phenomena where the bulk of the fast electrons are prevented from escaping and as a result recirculate within the target. Direct evidence of refluxing was measured in this work and is dominated by

energetic MeV electrons. In thin targets, refluxing can disrupt the formation of the azimuthal magnetic fields responsible for collimating the beam.

The refluxing fast electrons have millimeter ranges in solid density material and consequently transfer their kinetic energy to a number of phenomena such as x-rays, $\gamma-$rays and thermal heating of the target. The sheath fields which constrain the fast electrons can exceed 10^{12} V/m and are also responsible for accelerating **ion beams** from the target surface. In this manner, the initial energy of the laser is coupled to a sequence of processes involving particles, fields and radiation.

8.4 Future work

Over the past 15 years, since the advent of the first petawatt laser facilities, the experimental field of relativistic electron transport has evolved from investigating the early theoretical considerations of the 1970's [161, 219, 244, 245] to providing new unexpected discoveries regarding ion acceleration, x-ray generation as well as developments in laser-fusion. Equally has the limits of computer based simulations provided great leaps forward in the theoretical field with modelling solid density conditions in two and three spatial dimensions. Both experimental and theoretical investigations have evolved in a complimentary fashion since the mid 1990's, ultimately paced by their respective technological limits. The outlook to the future will see these limits proceed to new horizons. Considering the experimental progression, increases in laser intensity will push into new regimes of fast electron energies and hotter/denser plasmas probed by novel diagnostic methods.

Further investigation of magnetic collimation and filamentation phenomena will be necessary at higher laser intensities and to provide a better understanding of material influences. The effect of the ion lattice structure on resistivity and filamentation proposed in Chapter 6 will be tested in future work. Some materials such as carbon exist in multiple forms with either ordered or disordered ion lattice states. A study of transport in such materials can provide a direct test of the relevance of ion ordering to resistivity and filamentation. An alternative arrangement could involve preheating the target material by a few eV to modify the initial target resistivity. For the work on collimation, further investigations are needed to expand the measurements reported in Chapter 5. This can involve different materials such as insulators where the simulation results predict lower magnetic fields and a correlation with a higher degree of filamentation. The scaling of the Bell-Kingham collimation formula also indicates a sensitivity to laser intensity and spot size. Engineering structured targets to enhance magnetic collimation is another avenue that has been shown to be effective [201] and may be developed further. The

investigation of refluxing has indicated a very large source size of K_α emission indicating a highly divergent electron beam. The corresponding proton emission measurements are consistent with a more compact fast electron source size. A recent numerical study [148] has shown that because of refluxing the time integrated K_α signal will always overestimate the first-pass fast electron source size. Further experimental work is clearly needed to resolve the relationship between fast electron energy and divergence and also the correlation between different diagnostics.

Such experimental measurements are critical in bench-marking numerical codes. These codes are often used in modelling the exotic physics of warm dense matter and in the development of large projects such as Fast Ignition. In the latter case, experimental investigations will necessarily involve studies of electron transport in shock compressed targets. An investigation of transport through 1D compressed material, which involved the author, found signs of modified transport in compressed aluminium and plastic targets [221]. Other recent investigations of transport in cylindrically compressed (0.1-5 g/cm^3) foam indicate signs of increased fast electron collimation [246**?**]. In this case the implosion is believed to induce collimating magnetic fields by driving the formation of resistivity gradients in the plasma. Further development of transport in compressed material and in low Z material such as DT are evidently required for Fast Ignition.

Over the next decade, the combined developments of laser and target technology can be expected to provide novel regimes of electron transport physics. The drive for development in this field is intrinsically tied to key applications. In this regard, it is the versatility of fast electron transport in coupling the laser energy to numerous other phenomena that will provide the continual motivation for its development as a field of science.

Bibliography

[1] Maiman, T. H. 'Stimulated Optical Radiation in Ruby'. *Nature*, **vol. 187**(4736), 493, 1960, URL http://www.nature.com/doifinder/10.1038/187493a0. 1

[2] Kapetanakos, C. 'Filamentation of intense relativistic electron beams propagating in dense plasmas'. *Applied Physics Letters*, **vol. 25**(9), 484, 1974, URL http://link.aip.org/link/?APPLAB/25/484/1. 2

[3] Prono, D., Ecker, B., Bergstrom, N. *et al.* 'Plasma-Return-Current Heating by Relativistic Electron Beams with $\nu/\gamma\sim10$'. *Physical Review Letters*, **vol. 35**(7), 438, 1975, URL http://link.aps.org/doi/10.1103/PhysRevLett.35.438.

[4] Okamura, R., Nakamura, Y., and Kawashima, N. 'Interaction of a high intensity short pulse-width relativistic electron beam with plasma'. *Plasma Physics*, **vol. 19**(11), 997, 1977, URL http://stacks.iop.org/0032-1028/19/i=11/a=001?key=crossref.fd9c51b97d1543c3ac74a5df7317e25f. 2

[5] Hares, J., Kilkenny, J., Key, M. H. *et al.* 'Measurement of Fast-Electron Energy Spectra and Preheating in Laser-Irradiated Targets'. *Physical Review Letters*, **vol. 42**(18), 1216, 1979, URL http://link.aps.org/doi/10.1103/PhysRevLett.42.1216. 3

[6] Wilks, S. C., Langdon, A. B., Cowan, T. E. *et al.* 'Energetic proton generation in ultra-intense laser-solid interactions'. *Physics of Plasmas*, **vol. 8**(2), 542, 2001, URL http://link.aip.org/link/PHPAEN/v8/i2/p542/s1&Agg=doi. 3

[7] Tabak, M., Hammer, J., Glinsky, M. E. *et al.* 'Ignition and high gain with ultrapowerful lasers'. *Physics of Plasmas*, **vol. 1**(5), 1626, 1994, URL http://link.aip.org/link/PHPAEN/v1/i5/p1626/s1&Agg=doi. 3, 4, 6, 160, 198

[8] Ledingham, K. W. D. and Galster, W. 'Laser-driven particle and photon beams and some applications'. *New Journal of Physics*, **vol. 12**(4), 045005, 2010, URL http://stacks.iop.org/1367-2630/12/i=4/a=045005?key=crossref.dae3ff13d55e1d3a56697d1dd2930135. 3, 9

[9] Patel, P., Mackinnon, A. J., Key, M. *et al.* 'Isochoric Heating of Solid-Density Matter with an Ultrafast Proton Beam'. *Physical Review Letters*, **vol. 91**(12), 125004, 2003, URL `http://link.aps.org/doi/10.1103/PhysRevLett.91.125004`. 3, 9

[10] Koenig, M., Benuzzi-Mounaix, A., Ravasio, A. *et al.* 'Progress in the study of warm dense matter'. *Plasma Physics and Controlled Fusion*, **vol. 47**(12B), B441, 2005, URL `http://stacks.iop.org/0741-3335/47/i=12B/a=S31?key=crossref.60cd5d6fe3e344e34b0a45bdb0790b17`. 3

[11] Remington, B. A. 'Modeling Astrophysical Phenomena in the Laboratory with Intense Lasers'. *Science*, **vol. 284**(5419), 1488, 1999, URL `http://www.sciencemag.org/content/284/5419/1488.abstract`. 3

[12] Roth, M., Cowan, T., Key, M. H. *et al.* 'Fast Ignition by Intense Laser-Accelerated Proton Beams'. *Physical Review Letters*, **vol. 86**(3), 436, 2001, URL `http://link.aps.org/doi/10.1103/PhysRevLett.86.436`. 6, 9

[13] Naumova, N., Schlegel, T., Tikhonchuk, V. T. *et al.* 'Hole Boring in a DT Pellet and Fast-Ion Ignition with Ultraintense Laser Pulses'. *Physical Review Letters*, **vol. 102**(2), 025002, 2009, URL `http://link.aps.org/doi/10.1103/PhysRevLett.102.025002`. 6

[14] MacPhee, a. G., Divol, L., Kemp, A. J. *et al.* 'Limitation on Prepulse Level for Cone-Guided Fast-Ignition Inertial Confinement Fusion'. *Physical Review Letters*, **vol. 104**(5), 055002, 2010, URL `http://link.aps.org/doi/10.1103/PhysRevLett.104.055002`. 6

[15] Mulser, P. and Schneider, R. 'On the inefficiency of hole boring in fast ignition'. *Laser and Particle Beams*, **vol. 22**(02), 157, 2004, URL `http://www.journals.cambridge.org/abstract_S0263034604222108`. 6

[16] Sarri, G., Lancaster, K. L., Trines, R. *et al.* 'Creation of persistent, straight, 2 mm long laser driven channels in underdense plasmas'. *Physics of Plasmas*, **vol. 17**(11), 113303, 2010, URL `http://link.aip.org/link/PHPAEN/v17/i11/p113303/s1&Agg=doi`.

[17] Hain, S. and Mulser, P. 'Fast Ignition without Hole Boring'. *Physical Review Letters*, **vol. 86**(6), 1015, 2001, URL `http://link.aps.org/doi/10.1103/PhysRevLett.86.1015`.

[18] Lancaster, K. L., Sherlock, M., Green, J. S. *et al.* 'Effect of reentrant cone geometry on energy transport in intense laser-plasma interactions'. *Physical Review E*, **vol. 80**(4), 045401, 2009, URL `http://link.aps.org/doi/10.1103/PhysRevE.80.045401`. 141

[19] Pasley, J. and Stephens, R. 'Simulations investigating the effect of a deuterium-tritium-ice coating on the motion of the gold cone surface in a re-entrant cone-guided fast ignition inertial confinement fusion capsule'. *Physics of Plasmas*, **vol. 14**(5), 054501, 2007, URL `http://link.aip.org/link/PHPAEN/v14/i5/p054501/s1&Agg=doi`. 6

[20] Kodama, R., Norreys, P. A., Mima, K. *et al.* 'Fast heating of ultrahigh-density plasma as a step towards laser fusion ignition.' *Nature*, **vol. 412**(6849), 798, 2001, URL `http://www.ncbi.nlm.nih.gov/pubmed/11518960`. 7

[21] Key, M. H. 'Status of and prospects for the fast ignition inertial fusion concept'. *Physics of Plasmas*, **vol. 14**(5), 055502, 2007, URL `http://link.aip.org/link/PHPAEN/v14/i5/p055502/s1&Agg=doi`. 7

[22] Dunne, M., Alexander, N., Amiranoff, F. *et al.* 'HIPER: Technical Background and Conceptual Design Report 2007'. Tech. rep., 2007. URL `http://www.hiper-laser.org/overview/TDR/tdr.aspj`. 7

[23] Blanchot, N., Behar, G., Berthier, T. *et al.* 'Overview of PETAL, the multi-Petawatt project on the LIL facility'. *Plasma Physics and Controlled Fusion*, **vol. 50**(12), 124045, 2008, URL `http://stacks.iop.org/0741-3335/50/i=12/a=124045?key=crossref.784e7472541623f57b7d0a9e604f796a`. 8

[24] Backe, H., Bernard, D., Canova, F. *et al.* 'PROPOSAL FOR A EUROPEAN EXTREME LIGHT INFRASTRUCTURE (ELI)'. URL `http://www.extreme-light-infrastructure.eu/pictures/ELI-scientific-case-id17.pdf`. 8

[25] Mora, P. 'Plasma Expansion into a Vacuum'. *Physical Review Letters*, **vol. 90**, 185002, 2003, URL `http://link.aps.org/doi/10.1103/PhysRevLett.90.185002`. 8, 76, 79, 80, 111, 123, 153, 155

[26] Snavely, R., Key, M., Hatchett, S. P. *et al.* 'Intense High-Energy Proton Beams from Petawatt-Laser Irradiation of Solids'. *Physical Review Letters*, **vol. 85**(14), 2945, 2000, URL `http://link.aps.org/doi/10.1103/PhysRevLett.85.2945`. 8

[27] Gaillard, S. A., Flippo, K. A., Lowenstern, M. E. *et al.* 'Proton acceleration from ultrahigh-intensity short-pulse laser-matter interactions with Cu micro-cone targets at an intrinsic 10^{-8} contrast'. *Journal of Physics: Conference Series*, **vol. 244**(2), 022034, 2010, URL `http://stacks.iop.org/1742-6596/244/i=2/a=022034?key=crossref.850f9d2e625c98c89eb83556514e70de`. 8

[28] Tajima, T., Habs, D., and Yan, X. 'Laser Acceleration of Ions for Radiation Therapy'. *Reviews of Accelerator Science and Technology*, **vol. 2**, 201, 2009. 9

[29] Tikhonchuk, V. T., Schlegel, T., Regan, C. *et al.* 'Fast ion ignition with ultra-intense laser pulses'. *Nuclear Fusion*, **vol. 50**(4), 045003, 2010, URL http://stacks.iop.org/0029-5515/50/i=4/a=045003?key=crossref.dc174af8ef4a11cb99ea9fe3c937dd9e. 9

[30] Snavely, R. A., Zhang, B., Akli, K. *et al.* 'Laser generated proton beam focusing and high temperature isochoric heating of solid matter'. *Physics of Plasmas*, **vol. 14**(9), 092703, 2007, URL http://link.aip.org/link/PHPAEN/v14/i9/p092703/s1&Agg=doi. 9

[31] Borghesi, M., Schiavi, A., Campbell, D. H. *et al.* 'Proton imaging: a diagnostic for inertial confinement fusion/fast ignitor studies'. *Plasma Physics and Controlled Fusion*, **vol. 43**(12A), A267, 2001, URL http://stacks.iop.org/0741-3335/43/i=12A/a=320. 9

[32] Ledingham, K. W. D., McKenna, P., McCanny, T. *et al.* 'High power laser production of short-lived isotopes for positron emission tomography'. *Journal of Physics D: Applied Physics*, **vol. 37**(16), 2341, 2004, URL http://stacks.iop.org/0022-3727/37/i=16/a=019?key=crossref.dce227d283ba648d90e9e2adcbede670. 9

[33] Linz, U. 'Comment on 'High-power laser production of short-lived isotopes for positron emission tomography''. *Journal of Physics D: Applied Physics*, **vol. 38**(23), 4256, 2005, URL http://stacks.iop.org/0022-3727/38/i=23/a=N01?key=crossref.a8610b6c4d092457c9b1e576fa049dd4. 9

[34] Feurer, T., Morak, A., Uschmann, I. *et al.* 'Femtosecond silicon Kα pulses from laser-produced plasmas'. *Physical Review E*, **vol. 65**(1), 016412, 2001, URL http://link.aps.org/doi/10.1103/PhysRevE.65.016412. 9

[35] Reich, C., Gibbon, P., Uschmann, I. *et al.* 'Yield Optimization and Time Structure of Femtosecond Laser Plasma Kα Sources'. *Physical Review Letters*, **vol. 84**(21), 4846, 2000, URL http://link.aps.org/doi/10.1103/PhysRevLett.84.4846.

[36] Sokolowski-Tinten, K., Blome, C., Blums, J. *et al.* 'Femtosecond X-ray measurement of coherent lattice vibrations near the Lindemann stability limit.' *Nature*, **vol. 422**(6929), 287, 2003, URL http://www.ncbi.nlm.nih.gov/pubmed/12646915.

[37] Bargheer, M., Zhavoronkov, N., Gritsai, Y. *et al.* 'Coherent atomic motions in a nanostructure studied by femtosecond X-ray diffraction.' *Science*, **vol. 306**(5702), 1771, 2004, URL http://www.ncbi.nlm.nih.gov/pubmed/15576618.

[38] Zhavoronkov, N., Gritsai, Y., Bargheer, M. *et al.* 'Microfocus Cu K_α source for femtosecond x-ray science'. *Optics Letters*, **vol. 30**(13), 1737, 2005, URL `http://www.opticsinfobase.org/abstract.cfm?URI=OL-30-13-1737`. 9

[39] Svanberg, S. 'Some applications of ultrashort laser'. *Measurement Science and Technology*, **vol. 12**, 1777, 2001, URL `http://iopscience.iop.org/0957-0233/12/11/304`. 9

[40] Kieffer, J., Krol, a., Jiang, Z. *et al.* 'Future of laser-based X-ray sources for medical imaging'. *Applied Physics B: Lasers and Optics*, **vol. 74**(9), s75, 2002, URL `http://www.springerlink.com/openurl.asp?genre=article&id=doi:10.1007/s00340-002-0870-3`. 9

[41] Giulietti, D. and Gizzi, L. A. 'X-ray emission from laser-produced plasmas'. *La Rivista del Nuovo Cimento*, **vol. 21**(10), 1, 1998, URL `http://www.springerlink.com/index/10.1007/BF02874624`. 9

[42] Lee, R. W., Kalantar, D., and Molitoris, J. 'Warm Dense Matter : An Overview'. Tech. rep., LLNL, 2004. URL `https://e-reports-ext.llnl.gov/pdf/307164.pdf`. 10

[43] Nakatsutsumi, M., Davies, J. R., Kodama, R. *et al.* 'Space and time resolved measurements of the heating of solids to ten million kelvin by a petawatt laser'. *New Journal of Physics*, **vol. 10**(4), 043046, 2008, URL `http://stacks.iop.org/1367-2630/10/i=4/a=043046?key=crossref.79b543e804fe3535437f4c4c00806c98`. 10, 73

[44] Strickland, D. and Mourou, G. 'Compression of amplified chirped optical pulses'. *Optics Communications*, **vol. 56**(3), 219, 1985, URL `http://linkinghub.elsevier.com/retrieve/pii/0030401885901208`. 12

[45] Maine, P., Strickland, D., Bado, P. *et al.* 'Generation of ultrahigh peak power pulses by chirped pulse amplification'. *IEEE Journal of Quantum Electronics*, **vol. 24**(2), 398, 1988, URL `http://ieeexplore.ieee.org/lpdocs/epic03/wrapper.htm?arnumber=137`.

[46] Pessot, M., Maine, P., and Mourou, G. '1000 times expansion/compression of optical pulses for chirped pulse amplification'. *Optics Communications*, **vol. 62**(6), 419, 1987, URL `http://linkinghub.elsevier.com/retrieve/pii/0030401887900113`. 12

[47] Chen, F. F. *Introduction to Plasma Physics and Controlled Fusion*, vol. 1. Plenum Press, New York, 2nd ed., 1984. URL `http://stacks.iop.org/0741-3335/38/i=1/a=004?key=crossref.c83f75c37bf9374ed7cab1618ae7d31b`. 15, 16, 21

[48] Boyd, T. and Sanderson, J. *The Physics of Plasmas*, vol. 74. Cambridge University Press, 2003. URL http://www.cambridge.org/catalogue/catalogue.asp?isbn=9780521452908. 22

[49] Lee, Y. T. and More, R. M. 'An electron conductivity model for dense plasmas'. *Physics of Fluids*, **vol. 27**(5), 1273, 1984, URL http://link.aip.org/link/PFLDAS/v27/i5/p1273/s1&Agg=doi. 22

[50] Spitzer, L. and Härm, R. 'Transport Phenomena in a Completely Ionized Gas'. *Physical Review*, **vol. 89**(5), 977, 1953, URL http://link.aps.org/doi/10.1103/PhysRev.89.977. 22, 23

[51] Milchberg, H., Freeman, R. R., Davey, S. *et al.* 'Resistivity of a Simple Metal from Room Temperature to 10^6 K'. *Physical Review Letters*, **vol. 61**(20), 2364, 1988, URL http://link.aps.org/doi/10.1103/PhysRevLett.61.2364. 22, 23, 72, 107, 136

[52] Davies, J. R., Bell, A. R., Haines, M. *et al.* 'Short-pulse high-intensity laser-generated fast electron transport into thick solid targets'. *Physical Review E*, **vol. 56**(6), 7193, 1997, URL http://link.aps.org/doi/10.1103/PhysRevE.56.7193. 23, 57, 109

[53] Ziener, C., Foster, P. S., Divall, E. J. *et al.* 'Specular reflectivity of plasma mirrors as a function of intensity, pulse duration, and angle of incidence'. *Journal of Applied Physics*, **vol. 93**(1), 768, 2003, URL http://link.aip.org/link/JAPIAU/v93/i1/p768/s1&Agg=doi. 24

[54] Doumy, G., Quéré, F., Gobert, O. *et al.* 'Complete characterization of a plasma mirror for the production of high-contrast ultraintense laser pulses'. *Physical Review E*, **vol. 69**(2), 026402, 2004, URL http://link.aps.org/doi/10.1103/PhysRevE.69.026402.

[55] Dromey, B., Kar, S., Zepf, M. *et al.* 'The plasma mirror-A subpicosecond optical switch for ultrahigh power lasers'. *Review of Scientific Instruments*, **vol. 75**(3), 645, 2004, URL http://link.aip.org/link/RSINAK/v75/i3/p645/s1&Agg=doi. 24

[56] McKenna, P., Carroll, D., Lundh, O. *et al.* 'Effects of front surface plasma expansion on proton acceleration in ultraintense laser irradiation of foil targets'. *Laser and Particle Beams*, **vol. 26**(04), 591, 2008, URL http://www.journals.cambridge.org/abstract_S0263034608000657. 24, 30, 40

[57] Paradkar, B., Wei, M., Yabuuchi, T. *et al.* 'Numerical modeling of fast electron generation in the presence of preformed plasma in laser-matter interaction

at relativistic intensities'. *Physical Review E*, **vol. 83**(4), 046401, 2011, URL http://link.aps.org/doi/10.1103/PhysRevE.83.046401. 24, 30, 40

[58] Keldysh, L. V. 'Ionization in the field of a strong electromagnetic wave'. *Soviet Physics JETP*, **vol. 20**, 1307, 1965, URL http://www.csa.com/partners/viewrecord.php?requester=gs&collection=TRD&recid=A6524948AH. 25

[59] Perelomov, A. M., Popov, V. S., and Terent'ev, M. V. 'Ionization of atoms in an alternating electric field'. *Soviet Physics - JETP*, **vol. 23**(5), 1966. 25

[60] Perelomov, A. M., Popov, V. S., and Terent'ev, M. V. 'Ionization of atoms in an alternating electrical field'. *JETP*, **vol. 23**(2), 336, 1967. 25

[61] Reiss, H. R. 'Unsuitability of the Keldysh parameter for laser fields'. *Physical Review A*, **vol. 82**(2), 023418, 2010, URL http://link.aps.org/doi/10.1103/PhysRevA.82.023418. 25

[62] Burnett, K., Reed, V. C., and Knight, P. L. 'Atoms in ultra-intense laser fields'. *Journal of Physics B: Atomic, Molecular and Optical Physics*, **vol. 26**(4), 561, 1993, URL http://stacks.iop.org/0953-4075/26/i=4/a=003?key=crossref.9b3829517e363989102e2f8c204f0ce7. 25

[63] Freeman, R. R. and Bucksbaum, P. H. 'Investigations of above-threshold ionization using subpicosecond laser pulses'. *Journal of Physics B: Atomic, Molecular and Optical Physics*, **vol. 24**, 325, 1991. 25

[64] Ammosov, M. V., Delone, N. B., and Krainov, V. P. 'Tunnel ionization of complex atoms and of atomic ions in an alternating electromagnetic field'. *Soviet Physics - JETP*, **vol. 64**(6), 1191, 1986, URL http://link.aip.org/link/?SPJ/64/1191/1. 27, 132

[65] Auguste, T., Monot, P., Lompre, L. A. *et al.* 'Multiply charged ions produced in noble gases by a 1 ps laser pulse at lambda =1053 nm'. *Journal of Physics B: Atomic, Molecular and Optical Physics*, **vol. 25**(20), 4181, 1992, URL http://stacks.iop.org/0953-4075/25/i=20/a=015. 27

[66] Tikhonchuk, V. T. 'Interaction of a beam of fast electrons with solids'. *Physics of Plasmas*, **vol. 9**(4), 1416, 2002, URL http://link.aip.org/link/PHPAEN/v9/i4/p1416/s1&Agg=doi. 27, 39, 50, 114, 147

[67] Hegelich, M., Karsch, S., Pretzler, G. *et al.* 'MeV Ion Jets from Short-Pulse-Laser Interaction with Thin Foils'. *Physical Review Letters*, **vol. 89**(8), 085002, 2002, URL http://link.aps.org/doi/10.1103/PhysRevLett.89.085002. 27, 117

[68] Mora, P. and Antonsen, T. 'Electron cavitation and acceleration in the wake of an ultraintense, self-focused laser pulse'. *Physical Review E*, **vol. 53**(3), R2068, 1996, URL http://link.aps.org/doi/10.1103/PhysRevE.53.R2068. 30

[69] Nicholas, D. J. *The development of fluid codes for the laser compression of plasma.* RAL, Chilton, 1982. 30

[70] Gibbon, P. *Short Pulse Laser Interactions with Matter: An Introduction.* Imperial Coll., London, 2005. 31, 33, 102

[71] Rosen, M. D. 'Scaling laws for femtosecond laser-plasma interactions'. vol. 1229, pp. 160–169. SPIE, 1990. URL http://link.aip.org/link/?PSI/1229/160/1. 31

[72] Lawson, J. D. 'Lasers and accelerators'. *Nuclear Science, IEEE Transactions on*, **vol. 26**(3), 4217 , 1979. 33

[73] Wilks, S. C., Kruer, W., Tabak, M. *et al.* 'Absorption of ultra-intense laser pulses'. *Physical Review Letters*, **vol. 69**(9), 1383, 1992, URL http://link.aps.org/doi/10.1103/PhysRevLett.69.1383. 34, 41, 42, 108

[74] Kemp, A. J., Sentoku, Y., and Tabak, M. 'Hot-Electron Energy Coupling in Ultraintense Laser-Matter Interaction'. *Physical Review Letters*, **vol. 101**(7), 075004, 2008, URL http://link.aps.org/doi/10.1103/PhysRevLett.101.075004. 34, 43

[75] Chrisman, B., Sentoku, Y., and Kemp, A. J. 'Intensity scaling of hot electron energy coupling in cone-guided fast ignition'. *Physics of Plasmas*, **vol. 15**(5), 056309, 2008, URL http://link.aip.org/link/PHPAEN/v15/i5/p056309/s1&Agg=doi. 34, 43, 58

[76] Pert, G. 'Inverse bremsstrahlung in strong radiation fields at low temperatures'. *Physical Review E*, **vol. 51**(5), 4778, 1995, URL http://link.aps.org/doi/10.1103/PhysRevE.51.4778. 35

[77] Ginzburg, V. *The propagation of electromagnetic waves in plasmas.* Pergammon Press, 1964. 36

[78] Brunel, F. 'Not-so-resonant, resonant absorption'. *Physical Review Letters*, **vol. 59**(1), 52, 1987, URL http://link.aps.org/doi/10.1103/PhysRevLett.59.52. 36, 42

[79] Gibbon, P. 'Efficient production of fast electrons from femtosecond laser interaction with solid targets'. *Physical Review Letters*, **vol. 73**(5), 664, 1994, URL http://link.aps.org/doi/10.1103/PhysRevLett.73.664. 37, 41, 42, 44

[80] Mulser, P., Bauer, D., and Ruhl, H. 'Collisionless Laser-Energy Conversion by Anharmonic Resonance'. *Physical Review Letters*, **vol. 101**(22), 225002, 2008, URL http://link.aps.org/doi/10.1103/PhysRevLett.101.225002. 37

[81] Cerchez, M., Jung, R., Osterholz, J. *et al.* 'Absorption of Ultrashort Laser Pulses in Strongly Overdense Targets'. *Physical Review Letters*, **vol. 100**(24), 245001, 2008, URL http://link.aps.org/doi/10.1103/PhysRevLett.100.245001. 37

[82] Malka, G. and Miquel, J. 'Experimental Confirmation of Ponderomotive-Force Electrons Produced by an Ultrarelativistic Laser Pulse on a Solid Target.' *Physical review letters*, **vol. 77**(1), 75, 1996, URL http://www.ncbi.nlm.nih.gov/pubmed/10061775. 37

[83] Kruer, W. L. and Estabrook, K. 'JxB heating by very intense laser light'. *Physics of Fluids*, **vol. 28**(1), 430, 1985, URL http://link.aip.org/link/PFLDAS/v28/i1/p430/s1&Agg=doi. 37, 38

[84] Wilks, S. C. and Kruer, W. 'Absorption of ultrashort, ultra-intense laser light by solids and overdense plasmas'. *IEEE Journal of Quantum Electronics*, **vol. 33**(11), 1954, 1997, URL http://ieeexplore.ieee.org/lpdocs/epic03/wrapper.htm?arnumber=641310. 38, 41, 82, 113

[85] Santala, M., Zepf, M., Watts, I. *et al.* 'Effect of the Plasma Density Scale Length on the Direction of Fast Electrons in Relativistic Laser-Solid Interactions'. *Physical Review Letters*, **vol. 84**(7), 1459, 2000, URL http://link.aps.org/doi/10.1103/PhysRevLett.84.1459. 38, 41, 47

[86] Lefebvre, E. and Bonnaud, G. 'Nonlinear electron heating in ultrahigh-intensity-laser-plasma interaction'. *Physical Review E*, **vol. 55**(1), 1011, 1997. 38, 40

[87] Chen, H., Wilks, S. C., Kruer, W. L. *et al.* 'Hot electron energy distributions from ultraintense laser solid interactions'. *Physics of Plasmas*, **vol. 16**(2), 020705, 2009, URL http://link.aip.org/link/PHPAEN/v16/i2/p020705/s1&Agg=doi. 39, 45

[88] Yabuuchi, T., Adumi, K., Habara, H. *et al.* 'On the behavior of ultraintense laser produced hot electrons in self-excited fields'. *Physics of Plasmas*, **vol. 14**(4), 040706, 2007, URL http://link.aip.org/link/PHPAEN/v14/i4/p040706/s1&Agg=doi. 39, 45

[89] Key, M. H., Cable, M. D., Cowan, T. E. *et al.* 'Hot electron production and heating by hot electrons in fast ignitor research'. *Physics of Plasmas*, **vol. 5**(5), 1966, 1998, URL http://link.aip.org/link/PHPAEN/v5/i5/p1966/s1&Agg=doi. 39

[90] Town, R., Chen, C., Cottrill, L. *et al.* 'Simulations of electron transport for fast ignition using LSP'. *Nuclear Instruments and Methods in Physics Research Section A: Accelerators, Spectrometers, Detectors and Associated Equipment*, **vol. 544**(1-2), 61, 2005, URL `http://linkinghub.elsevier.com/retrieve/pii/S0168900205003001`. 39

[91] Wharton, K. B., Hatchett, S. P., Wilks, S. C. *et al.* 'Experimental Measurements of Hot Electrons Generated by Ultraintense (10^{19}W/cm^2) Laser-Plasma Interactions on Solid-Density Targets'. *Physical Review Letters*, **vol. 81**(4), 822, 1998, URL `http://link.aps.org/doi/10.1103/PhysRevLett.81.822`. 39, 65

[92] Bell, A. R., Davies, J. R., Guerin, S. *et al.* 'Fast-electron transport in high-intensity short-pulse laser-solid experiments'. *Plasma Physics and Controlled Fusion*, **vol. 39**(5), 653, 1997, URL `http://iopscience.iop.org/0741-3335/39/5/001`. 39, 49, 50, 146

[93] Pisani, F., Bernardinello, A., Batani, D. *et al.* 'Experimental evidence of electric inhibition in fast electron penetration and of electric-field-limited fast electron transport in dense matter'. *Physical Review E*, **vol. 62**(5), R5927, 2000, URL `http://link.aps.org/doi/10.1103/PhysRevE.62.R5927`. 39

[94] Bell, A. R. and Kingham, R. J. 'Resistive Collimation of Electron Beams in Laser-Produced Plasmas'. *Physical Review Letters*, **vol. 91**(3), 035003, 2003, URL `http://link.aps.org/doi/10.1103/PhysRevLett.91.035003`. 39, 54, 109, 119, 124, 131, 138, 157

[95] Yuan, X. H., Robinson, A. P. L., Quinn, M. N. *et al.* 'Effect of self-generated magnetic fields on fast-electron beam divergence in solid targets'. *New Journal of Physics*, **vol. 12**(6), 063018, 2010, URL `http://stacks.iop.org/1367-2630/12/i=6/a=063018?key=crossref.80a0ccfe1f712cb9c60bc2ccfb3aa29d`. 39, 131, 155

[96] Quinn, M. N., Yuan, X. H., Lin, X. X. *et al.* 'Refluxing of fast electrons in solid targets irradiated by intense, picosecond laser pulses'. *Plasma Physics and Controlled Fusion*, **vol. 53**(2), 025007, 2011, URL `http://stacks.iop.org/0741-3335/53/i=2/a=025007?key=crossref.fc0888512d2ab6f4080e80934ee33476`. 39, 119, 129

[97] Myatt, J., Theobald, W., Delettrez, J. A. *et al.* 'High-intensity laser interactions with mass-limited solid targets and implications for fast-ignition experiments on OMEGA EP'. *Physics of Plasmas*, **vol. 14**(5), 056301, 2007, URL `http://link.aip.org/link/PHPAEN/v14/i5/p056301/s1&Agg=doi`. 39, 74, 141, 145, 146

[98] Nilson, P. M., Theobald, W., Myatt, J. *et al.* 'Bulk heating of solid-density plasmas during high-intensity-laser plasma interactions'. *Physical Review E*, **vol. 79**(1), 016406, 2009, URL `http://link.aps.org/doi/10.1103/PhysRevE.79.016406`. 39, 72, 141

[99] Chen, C. D., Patel, P. K., Hey, D. S. *et al.* 'Bremsstrahlung and Kα fluorescence measurements for inferring conversion efficiencies into fast ignition relevant hot electrons'. *Physics of Plasmas*, **vol. 16**(8), 082705, 2009, URL `http://link.aip.org/link/PHPAEN/v16/i8/p082705/s1&Agg=doi`. 40, 42

[100] Davies, J. R. 'Laser absorption by overdense plasmas in the relativistic regime'. *Plasma Physics and Controlled Fusion*, **vol. 51**(1), 014006, 2009, URL `http://stacks.iop.org/0741-3335/51/i=1/a=014006?key=crossref.c3675425a4381cd7bf392fdc828dbff1`. 40

[101] Haines, M., Wei, M. S., Beg, F. N. *et al.* 'Hot-Electron Temperature and Laser-Light Absorption in Fast Ignition'. *Physical Review Letters*, **vol. 102**(4), 045008, 2009, URL `http://link.aps.org/doi/10.1103/PhysRevLett.102.045008`. 41, 42

[102] Forslund, D., Kindel, J., and Lee, K. 'Theory of Hot-Electron Spectra at High Laser Intensity'. *Physical Review Letters*, **vol. 39**(5), 284, 1977, URL `http://link.aps.org/doi/10.1103/PhysRevLett.39.284`. 41, 42

[103] Gibbon, P. and Bell, A. R. 'Collisionless absorption in sharp-edged plasmas'. *Physical Review Letters*, **vol. 68**(10), 1535, 1992, URL `http://link.aps.org/doi/10.1103/PhysRevLett.68.1535`. 41

[104] Beg, F. N., Bell, A. R., Dangor, A. E. *et al.* 'A study of picosecond laser-solid interactions up to 10^{19} W/cm^2'. *Physics of Plasmas*, **vol. 4**(2), 447, 1997, URL `http://link.aip.org/link/PHPAEN/v4/i2/p447/s1&Agg=doi`. 41, 42, 108

[105] Brandl, F., Pretzler, G., Habs, D. *et al.* 'Čerenkov radiation diagnostics of hot electrons generated by fs-laser interaction with solid targets'. *Europhysics Letters*, **vol. 61**(5), 632, 2003, URL `http://stacks.iop.org/0295-5075/61/i=5/a=632?key=crossref.e027ec291d7b3b535e17d1753869a4af`. 41, 47

[106] Schollmeier, M. S. *Optimization and control of laser-accelerated proton beams*. Phd, Technischen Universität Darmstadt, 2008. 42, 80

[107] Tanimoto, T., Habara, H., Kodama, R. *et al.* 'Measurements of fast electron scaling generated by petawatt laser systems'. *Physics of Plasmas*, **vol. 16**(6), 062703, 2009, URL `http://link.aip.org/link/PHPAEN/v16/i6/p062703/s1&Agg=doi`. 42

[108] Sprangle, P., Tang, C.-M., and Esarey, E. 'Relativistic Self-Focusing of Short-Pulse Radiation Beams in Plasmas'. *IEEE Transactions on Plasma Science*, **vol. 15**(2), 145, 1987, URL `http://ieeexplore.ieee.org/lpdocs/epic03/wrapper.htm?arnumber=4316677`. 42

[109] Bezzerides, B., Gitomer, S., and Forslund, D. 'Randomness, Maxwellian Distributions, and Resonance Absorption'. *Physical Review Letters*, **vol. 44**(10), 651, 1980, URL `http://link.aps.org/doi/10.1103/PhysRevLett.44.651`. 43

[110] Chen, L. M., Zhang, J., Dong, Q. L. *et al.* 'Hot electron generation via vacuum heating process in femtosecond laser-solid interactions'. *Physics of Plasmas*, **vol. 8**(6), 2925, 2001, URL `http://link.aip.org/link/PHPAEN/v8/i6/p2925/s1&Agg=doi`. 44

[111] Jüttner, F. 'Das Maxwellsche Gesetz der Geschwindigkeitsverteilung in der Relativtheorie'. *Annalen der Physik*, **vol. 339**(5), 856, 1911, URL `http://doi.wiley.com/10.1002/andp.19113390503`. 44

[112] Moore, C., Knauer, J., and Meyerhofer, D. 'Observation of the Transition from Thomson to Compton Scattering in Multiphoton Interactions with Low-Energy Electrons'. *Physical Review Letters*, **vol. 74**(13), 2439, 1995, URL `http://link.aps.org/doi/10.1103/PhysRevLett.74.2439`. 45

[113] Yu, W., Bychenkov, V., Sentoku, Y. *et al.* 'Electron Acceleration by a Short Relativistic Laser Pulse at the Front of Solid Targets'. *Physical Review Letters*, **vol. 85**(3), 570, 2000, URL `http://link.aps.org/doi/10.1103/PhysRevLett.85.570`. 46

[114] Sheng, Z. M., Sentoku, Y., Mima, K. *et al.* 'Angular Distributions of Fast Electrons, Ions, and Bremsstrahlung x/γ-Rays in Intense Laser Interaction with Solid Targets'. *Physical Review Letters*, **vol. 85**(25), 5340, 2000, URL `http://link.aps.org/doi/10.1103/PhysRevLett.85.5340`. 46

[115] Wei, M. S., Solodov, A. A., Pasley, J. *et al.* 'Study of relativistic electron beam production and transport in high-intensity laser interaction with a wire target by integrated LSP modeling'. *Physics of Plasmas*, **vol. 15**(8), 083101, 2008, URL `http://link.aip.org/link/PHPAEN/v15/i8/p083101/s1&Agg=doi`. 46

[116] Adam, J. C., Héron, A., and Laval, G. 'Dispersion and Transport of Energetic Particles due to the Interaction of Intense Laser Pulses with Overdense Plasmas'. *Physical Review Letters*, **vol. 97**(20), 205006, 2006, URL `http://link.aps.org/doi/10.1103/PhysRevLett.97.205006`. 47, 58, 62, 63, 66, 110, 161

[117] Bennett, W. H. 'Magnetically Self-Focussing Streams'. *Physical Review*, **vol. 45**(12), 890, 1934, URL http://link.aps.org/doi/10.1103/PhysRev.45.890. 49, 58

[118] Alfvén, H. 'On the Motion of Cosmic Rays in Interstellar Space'. *Physical Review*, **vol. 55**(5), 425, 1939, URL http://link.aps.org/doi/10.1103/PhysRev.55.425. 49

[119] Lawson, J. D. 'On the classification of electron streams'. *Journal of Nuclear Energy. Part C*, **vol. 1**(1), 31, 1959, URL http://stacks.iop.org/0368-3281/1/i=1/a=305?key=crossref.3acd33a61f81e2d0b630aae559ae1164. 49

[120] Hammer, D. A. and Rostoker, N. 'Propagation of High Current Relativistic Electron Beams'. *Physics of Fluids*, **vol. 13**(7), 1831, 1970, URL http://link.aip.org/link/PFLDAS/v13/i7/p1831/s1&Agg=doi. 50

[121] Bell, A. R., Robinson, A. P. L., Sherlock, M. *et al.* 'Fast electron transport in laser-produced plasmas and the KALOS code for solution of the Vlasov-Fokker-Planck equation'. *Plasma Physics and Controlled Fusion*, **vol. 48**(3), R37, 2006, URL http://stacks.iop.org/0741-3335/48/i=3/a=R01?key=crossref.ab0ba53f8162ac23b354c6b27212081c. 50, 107, 150

[122] Bell, A. R., Davies, J. R., and Guerin, S. 'Magnetic field in short-pulse high-intensity laser-solid experiments'. *Physical Review E*, **vol. 58**(2), 2471, 1998, URL http://link.aps.org/doi/10.1103/PhysRevE.58.2471. 51

[123] Davies, J. R., Green, J. S., and Norreys, P. A. 'Electron beam hollowing in laser-solid interactions'. *Plasma Physics and Controlled Fusion*, **vol. 48**(8), 1181, 2006, URL http://stacks.iop.org/0741-3335/48/i=8/a=010?key=crossref.fb97d6d8e524f9422927d0a417fdc43f. 52, 53

[124] Norreys, P. A., Green, J. S., Davies, J. R. *et al.* 'Observation of annular electron beam transport in multi-TeraWatt laser-solid interactions'. *Plasma Physics and Controlled Fusion*, **vol. 48**(2), L11, 2006, URL http://stacks.iop.org/0741-3335/48/i=2/a=L01?key=crossref.7f6f5b20d17369ada2477fa56ef2d041. 53

[125] Weibel, E. 'Spontaneously Growing Transverse Waves in a Plasma Due to an Anisotropic Velocity Distribution'. *Physical Review Letters*, **vol. 2**(3), 83, 1959, URL http://link.aps.org/doi/10.1103/PhysRevLett.2.83. 55, 125

[126] Jung, R., Osterholz, J., Löwenbrück, K. *et al.* 'Study of Electron-Beam Propagation through Preionized Dense Foam Plasmas'. *Physical Review Letters*, **vol. 94**(19), 195001, 2005, URL http://link.aps.org/doi/10.1103/PhysRevLett.94.195001. 56, 60, 66, 67

[127] Evans, R. G. 'Modelling electron transport for fast ignition'. *Plasma Physics and Controlled Fusion*, **vol. 49**(12B), B87, 2007, URL http://stacks.iop.org/0741-3335/49/i=12B/a=S07?key=crossref.54f8df21da906798ebe40e45e9a7b59f. 56, 57, 125, 134, 158

[128] Silva, L. O., Fonseca, R. A., Tonge, J. W. *et al.* 'On the role of the purely transverse Weibel instability in fast ignitor scenarios'. *Physics of Plasmas*, **vol. 9**(6), 2458, 2002, URL http://link.aip.org/link/PHPAEN/v9/i6/p2458/s1&Agg=doi. 56

[129] Evans, R. G. 'Effects of target Z in ultra-high intensity laser solid interactions'. *CLF Annual Report*, 2007, URL www.clf.rl.ac.uk/resources/PDF/ar06-07_s3_effectsoftargetz.pdf. 56, 125

[130] Honda, M., Meyer-Ter-Vehn, J., and Pukhov, A. 'Collective stopping and ion heating in relativistic-electron-beam transport for fast ignition'. *Physical review letters*, **vol. 85**(10), 2128, 2000, URL http://www.ncbi.nlm.nih.gov/pubmed/10970479. 57, 58, 125, 161

[131] Sentoku, Y., Mima, K., Kojima, S. *et al.* 'Magnetic instability by the relativistic laser pulses in overdense plasmas'. *Physics of Plasmas*, **vol. 7**(2), 689, 2000, URL http://link.aip.org/link/PHPAEN/v7/i2/p689/s1&Agg=doi.

[132] Sentoku, Y., Mima, K., Sheng, Z. *et al.* 'Three-dimensional particle-in-cell simulations of energetic electron generation and transport with relativistic laser pulses in overdense plasmas'. *Physical Review E*, **vol. 65**(4), 046408, 2002, URL http://link.aps.org/doi/10.1103/PhysRevE.65.046408.

[133] Shvets, G., Polomarov, O., Khudik, V. *et al.* 'Nonlinear evolution of the Weibel instability of relativistic electron beams'. *Physics of Plasmas*, **vol. 16**(5), 056303, 2009, URL http://link.aip.org/link/PHPAEN/v16/i5/p056303/s1&Agg=doi. 58

[134] Gremillet, L., Bonnaud, G., and Amiranoff, F. 'Filamented transport of laser-generated relativistic electrons penetrating a solid target'. *Physics of Plasmas*, **vol. 9**(3), 941, 2002, URL http://link.aip.org/link/PHPAEN/v9/i3/p941/s1&Agg=doi. 58, 125, 129, 139

[135] Robinson, A. P. L., Kingham, R. J., Ridgers, C. P. *et al.* 'Effect of transverse density modulations on fast electron transport in

dense plasmas'. *Plasma Physics and Controlled Fusion*, **vol. 50**(6), 065019, 2008, URL http://stacks.iop.org/0741-3335/50/i=6/a=065019?key=crossref.255fdb89802d8a85ea3b5d62b23fac8b. 58, 73

[136] Storm, M., Solodov, A., Myatt, J. *et al.* 'High-Current, Relativistic Electron-Beam Transport in Metals and the Role of Magnetic Collimation'. *Physical Review Letters*, **vol. 102**(23), 23500, 2009, URL http://link.aps.org/doi/10.1103/PhysRevLett.102.235004. 59, 60, 61, 66, 67, 112, 157

[137] Krasheninnikov, S. I., Kim, a. V., Frolov, B. K. *et al.* 'Intense electron beam propagation through insulators: Ionization front structure and stability'. *Physics of Plasmas*, **vol. 12**(7), 073105, 2005, URL http://link.aip.org/link/PHPAEN/v12/i7/p073105/s1&Agg=doi. 59, 125

[138] Debayle, A. and Tikhonchuk, V. T. 'Filamentation instability of a fast electron beam in a dielectric target'. *Physical Review E*, **vol. 78**(6), 066404, 2008, URL http://link.aps.org/doi/10.1103/PhysRevE.78.066404. 59

[139] Robinson, A. P. L., Bell, A. R., and Kingham, R. J. 'Fast electron transport and ionization in a target irradiated by a high power laser'. *Plasma Physics and Controlled Fusion*, **vol. 48**(8), 1063, 2006, URL http://stacks.iop.org/0741-3335/48/i=8/a=002?key=crossref.0163e1785384cbff14935cf66c02f3af. 60

[140] Fuchs, J., Cowan, T. E., Audebert, P. *et al.* 'Spatial Uniformity of Laser-Accelerated Ultrahigh-Current MeV Electron Propagation in Metals and Insulators'. *Physical Review Letters*, **vol. 91**(25), 255002, 2003, URL http://link.aps.org/doi/10.1103/PhysRevLett.91.255002. 60, 125, 126, 128, 140, 158

[141] Stephens, R. B., Snavely, R., Aglitskiy, Y. *et al.* 'K_α fluorescence measurement of relativistic electron transport in the context of fast ignition'. *Physical Review E*, **vol. 69**(6), 066414, 2004, URL http://link.aps.org/doi/10.1103/PhysRevE.69.066414. 60, 61, 65, 66, 67, 115

[142] Debayle, A., Honrubia, J. J., D'Humières, E. *et al.* 'Divergence of laser-driven relativistic electron beams'. *Physical Review E*, **vol. 82**(3), 036405, 2010, URL http://link.aps.org/doi/10.1103/PhysRevE.82.036405. 62, 63, 110

[143] Tatarakis, M., Davies, J. R., Lee, P. *et al.* 'Plasma Formation on the Front and Rear of Plastic Targets due to High-Intensity Laser-Generated Fast Electrons'. *Physical Review Letters*, **vol. 81**(5), 999, 1998, URL http://link.aps.org/doi/10.1103/PhysRevLett.81.999. 63

[144] Gremillet, L., Amiranoff, F., Baton, S. *et al.* 'Time-Resolved Observation of Ultrahigh Intensity Laser-Produced Electron Jets Propagating through Transparent Solid Targets'. *Physical Review Letters*, **vol. 83**(24), 5015, 1999, URL `http://link.aps.org/doi/10.1103/PhysRevLett.83.5015`. 64, 65, 66, 110

[145] Teng, H., Zhang, J., Chen, Z. *et al.* 'Propagation of hot electrons through high-density plasmas'. *Physical Review E*, **vol. 67**(2), 026408, 2003, URL `http://link.aps.org/doi/10.1103/PhysRevE.67.026408`. 64

[146] Green, J. S., Ovchinnikov, V. M., Evans, R. G. *et al.* 'Effect of Laser Intensity on Fast-Electron-Beam Divergence in Solid-Density Plasmas'. *Physical Review Letters*, **vol. 100**(1), 015003, 2008, URL `http://link.aps.org/doi/10.1103/PhysRevLett.100.015003`. 64, 65, 110, 112, 131, 157

[147] Lancaster, K. L., Green, J. S., Hey, D. S. *et al.* 'Measurements of Energy Transport Patterns in Solid Density Laser Plasma Interactions at Intensities of $5 \times 10^{20}\mathrm{Wcm}^{-2}$'. *Physical Review Letters*, **vol. 98**, 125002, 2007, URL `http://link.aps.org/doi/10.1103/PhysRevLett.98.125002`. 64, 65, 110, 115, 157

[148] Ovchinnikov, V. M., Kemp, G. E., Schumacher, D. W. *et al.* 'How well do time-integrated K_α images represent hot electron spatial distributions?' *Physics of Plasmas*, **vol. 18**(7), 072704, 2011, URL `http://link.aip.org/link/PHPAEN/v18/i7/p072704/s1&Agg=doi`. 65, 164

[149] Santos, J. J., Amiranoff, F., Baton, S. D. *et al.* 'Fast Electron Transport in Ultraintense Laser Pulse Interaction with Solid Targets by Rear-Side Self-Radiation Diagnostics'. *Physical Review Letters*, **vol. 89**(2), 025001, 2002, URL `http://link.aps.org/doi/10.1103/PhysRevLett.89.025001`. 66, 67

[150] Jung, R. *Laser-plasma interaction with ultra-short laser pulses.* Phd thesis, Heinrich-Heine-Universitat Dusseldorf, 2007. 66

[151] Honrubia, J. J., Kaluza, M. C., Schreiber, J. *et al.* 'Laser-driven fast-electron transport in preheated foil targets'. *Physics of Plasmas*, **vol. 12**(5), 052708, 2005, URL `http://link.aip.org/link/PHPAEN/v12/i5/p052708/s1&Agg=doi`. 66

[152] Berger, M., Coursey, J., Zucker, M. *et al.* 'Stopping-Power and Range Tables for Electrons, Protons, and Helium Ions', 2010. URL `http://physics.nist.gov/PhysRefData/Star/Text/contents.html`. 68, 114, 146

[153] Bethe, H. 'Zur Theorie des Durchgangs schneller Korpuskularstrahlen durch Materie'. *Annalen der Physik*, **vol. 397**(3), 325, 1930, URL `http://doi.wiley.com/10.1002/andp.19303970303`. 68

[154] Bethe, H. 'Bremsformel für Elektronen relativistischer Geschwindigkeit'. *Z. Phys.*, **vol. 76**(5-6), 293, 1932, URL http://www.springerlink.com/content/p2l14k04v7681813/. 68

[155] Sternheimer, R., Seltzer, S., and Berger, M. 'Density effect for the ionization loss of charged particles in various substances'. *Physical Review B*, **vol. 26**(11), 6067, 1982, URL http://link.aps.org/doi/10.1103/PhysRevB.26.6067. 68

[156] Seltzer, S. and Berger, M. 'Bremsstrahlung spectra from electron interactions with screened atomic nuclei and orbital electrons'. *Nuclear Instruments and Methods in Physics Research Section B: Beam Interactions with Materials and Atoms*, **vol. 12**(1), 95, 1985, URL http://dx.doi.org/10.1016/0168-583X(85)90707-4. 68

[157] Pratt, R. H., Lee, H. K., Tseng, C. M. *et al.* 'Bremsstrahlung energy spectra from electrons of kinetic energy 1 keV < T1 < 2000 keV incident on neutral atoms 2 < Z < 92'. *Atomic Data and Nuclear Data Tables*, **vol. 20**(2), 175, 1977, URL http://linkinghub.elsevier.com/retrieve/pii/0092640X77900456. 68

[158] More, R. 'Pressure ionization, resonances, and the continuity of bound and free states'. **vol. 21**, 305 , 1985, URL http://www.sciencedirect.com/science/article/B94TB-4S934V6-B/2/023a9bbba41916acef7dc3797929482f. 69, 70

[159] Popescu, H. *Génération et transport des électrons rapides dans l'interaction laser-matière à haut flux.* Phd thesis, Ecole Polytechnique, 2005. URL http://www.luli.polytechnique.fr/pages/PHARE/PHARE_theses.html. 70, 71

[160] Gremillet, L. *Etude theorique et experimentale du transport des electrons rapides dans l'interaction laser-solide a tres haut flux.* Phd thesis, Ecole Polytechnique, 2001. URL http://www.luli.polytechnique.fr/pages/PHARE/PHARE_theses.html. 70, 71, 72

[161] Lovelace, R. and Sudan, R. 'Plasma Heating by High-Current Relativistic Electron Beams'. *Physical Review Letters*, **vol. 27**(19), 1256, 1971, URL http://link.aps.org/doi/10.1103/PhysRevLett.27.1256. 70, 163

[162] Bush, I. A., Robinson, A. P. L., Kingham, R. J. *et al.* 'Cavitation and shock wave formation in dense plasmas by relativistic electron beams'. *Plasma Physics and Controlled Fusion*, **vol. 52**(12), 125007, 2010, URL http://stacks.iop.org/0741-3335/52/i=12/a=125007?key=crossref.cc74ae27aff0732e2bb3f6d39cf14e98. 73

[163] Kingham, R. J., Sherlock, M., Ridgers, C. P. *et al.* 'Vlasov-Fokker-Planck simulations of fast-electron transport with hydrodynamic plasma response'. *Journal of Physics: Conference Series*, **vol. 244**(2), 022042, 2010, URL `http://stacks.iop.org/1742-6596/244/i=2/a=022042?key=crossref.f6b8d2443a574ebf41871afb5b7492fe`. 73, 106

[164] Davies, J. R. 'How wrong is collisional Monte Carlo modeling of fast electron transport in high-intensity laser-solid interactions?' *Physical Review E*, **vol. 65**(2), 026407, 2002, URL `http://link.aps.org/doi/10.1103/PhysRevE.65.026407`. 73, 106, 107, 136, 150

[165] Pukhov, A. 'Three-Dimensional Simulations of Ion Acceleration from a Foil Irradiated by a Short-Pulse Laser'. *Physical Review Letters*, **vol. 86**(16), 3562, 2001, URL `http://link.aps.org/doi/10.1103/PhysRevLett.86.3562`. 74

[166] Sentoku, Y., Kemp, A. J., Presura, R. *et al.* 'Isochoric heating in heterogeneous solid targets with ultrashort laser pulses'. *Physics of Plasmas*, **vol. 14**(12), 122701, 2007, URL `http://link.aip.org/link/PHPAEN/v14/i12/p122701/s1&Agg=doi`. 74

[167] McKenna, P., Carroll, D. C., Clarke, R. J. *et al.* 'Lateral Electron Transport in High-Intensity Laser-Irradiated Foils Diagnosed by Ion Emission'. *Physical Review Letters*, **vol. 98**(14), 145001, 2007, URL `http://link.aps.org/doi/10.1103/PhysRevLett.98.145001`. 74, 82, 115, 116, 131, 144

[168] Cottrill, L., Kemp, A. J., Tabak, M. *et al.* 'Characterization of escaping electrons from simulations of hot electron transport for intense femtosecond laser-target scenarios'. *Nuclear Fusion*, **vol. 50**(9), 095002, 2010, URL `http://stacks.iop.org/0029-5515/50/i=9/a=095002?key=crossref.fae235c4872cb5e300931b12a1fe9306`. 74, 141

[169] Fuchs, J., Antici, P., D'Humières, E. *et al.* 'Laser-driven proton scaling laws and new paths towards energy increase'. *Nature Physics*, **vol. 2**(1), 48, 2006, URL `http://www.nature.com/doifinder/10.1038/nphys199`. 76, 80, 111, 112, 113, 153, 155

[170] Carroll, D. C. *Laser Driven Ion Acceleration: Source optimisation and optical control.* Phd, University of Strathclyde, 2008. 78

[171] Romagnani, L., Fuchs, J., Borghesi, M. *et al.* 'Dynamics of Electric Fields Driving the Laser Acceleration of Multi-MeV Protons'. *Physical Review Letters*, **vol. 95**(19), 195001, 2005, URL `http://link.aps.org/doi/10.1103/PhysRevLett.95.195001`. 78, 80

[172] Robson, L., Simpson, P. T., Clarke, R. J. *et al.* 'Scaling of proton acceleration driven by petawatt-laser-plasma interactions'. *Nature Physics*, **vol. 3**(1), 58, 2006, URL http://www.nature.com/doifinder/10.1038/nphys476. 80, 112, 155

[173] Cowan, T. E., Fuchs, J., Ruhl, H. *et al.* 'Ultralow Emittance, Multi-MeV Proton Beams from a Laser Virtual-Cathode Plasma Accelerator'. *Physical Review Letters*, **vol. 92**(20), 204801, 2004, URL http://link.aps.org/doi/10.1103/PhysRevLett.92.204801. 82, 83

[174] Nürnberg, F., Schollmeier, M., Brambrink, E. *et al.* 'Radiochromic film imaging spectroscopy of laser-accelerated proton beams.' *The Review of scientific instruments*, **vol. 80**(3), 033301, 2009, URL http://www.ncbi.nlm.nih.gov/pubmed/19334914. 82, 83, 117, 128

[175] Quinn, K., Wilson, P. A., Cecchetti, C. *et al.* 'Laser-Driven Ultrafast Field Propagation on Solid Surfaces'. *Physical Review Letters*, **vol. 102**(19), 194801, 2009, URL http://link.aps.org/doi/10.1103/PhysRevLett.102.194801. 82, 83, 116, 131

[176] Schollmeier, M., Harres, K., Nürnberg, F. *et al.* 'Laser beam-profile impression and target thickness impact on laser-accelerated protons'. *Physics of Plasmas*, **vol. 15**(5), 053101, 2008, URL http://link.aip.org/link/PHPAEN/v15/i5/p053101/s1&Agg=doi. 83, 126

[177] Borghesi, M., Mackinnon, A. J., Campbell, D. H. *et al.* 'Multi-MeV Proton Source Investigations in Ultraintense Laser-Foil Interactions'. *Physical Review Letters*, **vol. 92**(5), 055003, 2004, URL http://link.aps.org/doi/10.1103/PhysRevLett.92.055003. 83

[178] Baumgartner, R. and Byer, R. 'Optical parametric amplification'. *IEEE Journal of Quantum Electronics*, **vol. 15**(6), 432, 1979, URL http://ieeexplore.ieee.org/lpdocs/epic03/wrapper.htm?arnumber=1070043. 88

[179] Danson, C., Brummitt, P. A., Clarke, R. *et al.* 'Vulcan petawatt: Design, operation and interactions at $5 \times 10^{20}\ Wcm^{-2}$'. *Laser and Particle Beams*, **vol. 23**(01), 87, 2005, URL http://www.journals.cambridge.org/abstract_S0263034605050159. 89

[180] Blažević, A., Bagnoud, V., Borneis, S. *et al.* 'Phelix at Z6 - Extended possibilities for combined ion-laser experiments'. *GSI Scientific Report*, 2008, URL http://www.gsi.de/informationen/wti/library/scientificreport2008/PAPERS/PLASMA-PHYSICS-02.pdf. 90

[181] Bagnoud, V., Aurand, B., Blazevic, A. *et al.* 'Commissioning and early experiments of the PHELIX facility'. *Applied Physics B*, **vol. 100**(1), 137, 2009, URL http://www.springerlink.com/index/10.1007/s00340-009-3855-7. 90

[182] Schollmeier, M., Rousse, A., Schaumann, G. *et al.* 'Plasma physics experiments at GSI'. *Journal of Physics: Conference Series*, **vol. 112**(4), 042068, 2008, URL http://stacks.iop.org/1742-6596/112/i=4/a=042068?key=crossref.d21013a0770b4752f52b3f308581cde0. 90

[183] Harres, K., Alber, I., Tauschwitz, A. *et al.* 'Beam collimation and transport of quasineutral laser-accelerated protons by a solenoid field'. *Physics of Plasmas*, **vol. 17**(2), 023107, 2010, URL http://link.aip.org/link/PHPAEN/v17/i2/p023107/s1&Agg=doi. 91

[184] Butson, M. J., Yu, P. K., Cheung, T. *et al.* 'Radiochromic film for medical radiation dosimetry'. *Materials Science and Engineering: R: Reports*, **vol. 41**(3-5), 61, 2003, URL http://linkinghub.elsevier.com/retrieve/pii/S0927796X03000342. 94

[185] Vatnitsky, S. M., Schulte, R. W. M., Galindo, R. *et al.* 'Radiochromic film dosimetry for verification of dose distributions delivered with proton-beam radiosurgery'. *Physics in Medicine and Biology*, **vol. 42**(10), 1887, 1997, URL http://stacks.iop.org/0031-9155/42/i=10/a=003?key=crossref.b0c13f53ce22f2cb59d580f9e08e3690.

[186] Niroomand-Rad, A., Blackwell, C. R., Coursey, B. M. *et al.* 'Radiochromic film dosimetry: Recommendations of AAPM Radiation Therapy Committee Task Group 55'. *Medical Physics*, **vol. 25**(11), 2093, 1998, URL http://link.aip.org/link/MPHYA6/v25/i11/p2093/s1&Agg=doi. 94

[187] Borghesi, M., Campbell, D. H., Schiavi, A. *et al.* 'Electric field detection in laser-plasma interaction experiments via the proton imaging technique'. *Physics of Plasmas*, **vol. 9**(5), 2214, 2002, URL http://link.aip.org/link/PHPAEN/v9/i5/p2214/s1&Agg=doi. 94

[188] Carroll, D. C., Brummitt, P. A., Neely, D. *et al.* 'A modified Thomson parabola spectrometer for high resolution multi-MeV ion measurements-Application to laser-driven ion acceleration'. *Nuclear Instruments and Methods in Physics Research Section A*, **vol. 620**(1), 23, 2010, URL http://linkinghub.elsevier.com/retrieve/pii/S0168900210001221. 97, 98

[189] Sakai, K., Labrado Abella, D., Khan, Y. *et al.* 'Theoretical and experimental studies for spherical ifree-conducting particle behavior between non-parallel

plane electrodes with ac voltages in air'. *Trans. Diele. Elect. Insul.*, **vol. 10**(3), 404, 2003, URL `http://ieeexplore.ieee.org/lpdocs/epic03/wrapper.htm?arnumber=1207466`. 97

[190] Markey, K. *Development of laser accelerated MeV ion sources.* Phd thesis, Queen's University Belfast, 2009. 98

[191] Mancić, A., Fuchs, J., Antici, P. *et al.* 'Absolute calibration of photostimulable image plate detectors used as (0.5-20 MeV) high-energy proton detectors.' *The Review of scientific instruments*, **vol. 79**(7), 073301, 2008, URL `http://www.ncbi.nlm.nih.gov/pubmed/18681694`. 98

[192] Akli, K. U., Key, M. H., Chung, H. K. *et al.* 'Temperature sensitivity of Cu K_α imaging efficiency using a spherical Bragg reflecting crystal'. *Physics of Plasmas*, **vol. 14**(2), 023102, 2007, URL `http://link.aip.org/link/PHPAEN/v14/i2/p023102/s1&Agg=doi`. 99, 141, 153

[193] Chung, H. K., Chen, M. H., Morgan, W. L. *et al.* 'FLYCHK: Generalized population kinetics and spectral model for rapid spectroscopic analysis for all elements'. *High Energy Density Physics*, **vol. 1**, 3, 2005, URL `http://linkinghub.elsevier.com/retrieve/pii/S1574181805000029`. 100, 153

[194] Agostinelli, S. 'GEANT4 - a simulation toolkit'. *Nuclear Instruments and Methods in Physics Research Section A: Accelerators, Spectrometers, Detectors and Associated Equipment*, **vol. 506**(3), 250, 2003, URL `http://linkinghub.elsevier.com/retrieve/pii/S0168900203013688`. 103, 113, 144

[195] Bell, A. R., Evans, R. G., and Nicholas, D. J. 'Elecron Energy Transport in Steep Temperature Gradients in Laser-Produced Plasmas'. *Phys. Rev. Lett*, **vol. 46**(4), 243, 1981, URL `http://link.aps.org/doi/10.1103/PhysRevLett.46.243`. 105

[196] Evans, R. G., Bennett, A. J., and Pert, G. J. 'Two-dimensional fluid simulations of non-uniformly irradiated targets for inertial confinement fusion'. *Journal of Physics D: Applied Physics*, **vol. 15**(9), 1673, 1982, URL `http://stacks.iop.org/0022-3727/15/i=9/a=011`. 106

[197] Pert, G. J. 'Algorithms for the self-consistent generation of magnetic fields in plasmas'. *Journal of Computational Physics*, **vol. 43**, 111, 1981, URL `http://linkinghub.elsevier.com/retrieve/pii/0021999181901145`. 106

[198] Robinson, A. P. L. and Sherlock, M. 'Magnetic collimation of fast electrons produced by ultraintense laser irradiation by structuring the target composition'. *Physics of Plasmas*, **vol. 14**, 083105, 2007. 107

[199] Sandhu, A. S., Dharmadhikari, A. K., and Kumar, G. R. 'Time resolved evolution of structural, electrical, and thermal properties of copper irradiated by an intense ultrashort laser pulse'. *Journal of Applied Physics*, **vol. 97**(2), 023526, 2005, URL `http://link.aip.org/link/JAPIAU/v97/i2/p023526/s1&Agg=doi`. 107, 150

[200] Honrubia, J. J. and Meyer-ter Vehn, J. 'Fast ignition of fusion targets by laser-driven electrons'. *Plasma Physics and Controlled Fusion*, **vol. 51**(1), 014008, 2009, URL `http://stacks.iop.org/0741-3335/51/i=1/a=014008?key=crossref.dd3bf030fd2fb7e005b10c0607c83691`. 109, 124, 161

[201] Kar, S., Robinson, A. P. L., Carroll, D. C. *et al.* 'Guiding of Relativistic Electron Beams in Solid Targets by Resistively Controlled Magnetic Fields'. *Physical Review Letters*, **vol. 102**(5), 055001, 2009, URL `http://link.aps.org/doi/10.1103/PhysRevLett.102.055001`. 110, 135, 163

[202] Kaluza, M., Schreiber, J., Santala, M. *et al.* 'Influence of the Laser Prepulse on Proton Acceleration in Thin-Foil Experiments'. *Physical Review Letters*, **vol. 93**(4), 045003, 2004, URL `http://link.aps.org/doi/10.1103/PhysRevLett.93.045003`. 111, 112

[203] Honrubia, J. J., Antonicci, A., and Moreno, D. 'Hybrid simulations of fast electron transport in conducting media'. *Laser and Particle Beams*, **vol. 22**(02), 129, 2004, URL `http://www.journals.cambridge.org/abstract_S0263034604222078`. 114

[204] Honrubia, J. J., Alfonsín, C., Alonso, L. *et al.* 'Simulations of heating of solid targets by fast electrons'. *Laser and Particle Beams*, **vol. 24**(02), 217, 2006, URL `http://www.journals.cambridge.org/abstract_S0263034606060319`. 115

[205] Brambrink, E., Roth, M., Blazevic, A. *et al.* 'Modeling of the electrostatic sheath shape on the rear target surface in short-pulse laser-driven proton acceleration'. *Laser and Particle Beams*, **vol. 24**(01), 061301, 2006, URL `http://www.journals.cambridge.org/abstract_S026303460606023X`. 116

[206] Antici, P. *Laser-acceleration of high-energy short proton beams and applications.* Phd thesis, Ecole Polytechnique, 2007. 116, 131

[207] Kar, S., Markey, K., Simpson, P. *et al.* 'Dynamic Control of Laser-Produced Proton Beams'. *Physical Review Letters*, **vol. 100**(10), 105004, 2008, URL `http://link.aps.org/doi/10.1103/PhysRevLett.100.105004`. 116, 131

[208] Sentoku, Y., Cowan, T. E., Kemp, A. J. *et al.* 'High energy proton acceleration in interaction of short laser pulse with dense plasma target'. *Physics of Plasmas*,

vol. 10(5), 2009, 2003, URL http://link.aip.org/link/?PHPAEN/10/2009/1. 119, 125, 141

[209] Wei, M. S., Beg, F. N., Clark, E. L. *et al.* 'Observations of the filamentation of high-intensity laser-produced electron beams'. *Physical Review E*, **vol. 70**(5), 056412, 2004, URL http://link.aps.org/doi/10.1103/PhysRevE.70.056412. 125

[210] Hao, B., Sheng, Z.-M., Ren, C. *et al.* 'Relativistic collisional current-filamentation instability and two-stream instability in dense plasma'. *Physical Review E*, **vol. 79**(4), 046409, 2009, URL http://link.aps.org/doi/10.1103/PhysRevE.79.046409. 125

[211] Karmakar, A., Kumar, N., Shvets, G. *et al.* 'Collision-Driven Negative-Energy Waves and the Weibel Instability of a Relativistic Electron Beam in a Quasineutral Plasma'. *Physical Review Letters*, **vol. 101**(25), 255001, 2008, URL http://link.aps.org/doi/10.1103/PhysRevLett.101.255001. 126

[212] Karmakar, A., Kumar, N., Pukhov, A. *et al.* 'Detailed particle-in-cell simulations on the transport of a relativistic electron beam in plasmas'. *Physical Review E*, **vol. 80**(1), 016401, 2009, URL http://link.aps.org/doi/10.1103/PhysRevE.80.016401. 126

[213] Roth, M., Blazevic, A., Geissel, M. *et al.* 'Energetic ions generated by laser pulses: A detailed study on target properties'. *Physical Review Special Topics - Accelerators and Beams*, **vol. 5**(6), 061301, 2002, URL http://link.aps.org/doi/10.1103/PhysRevSTAB.5.061301. 127

[214] Sherlock, M., Bell, A. R., Kingham, R. J. *et al.* 'Non-Spitzer return currents in intense laser-plasma interactions'. *Physics of Plasmas*, **vol. 14**(10), 102708, 2007, URL http://link.aip.org/link/PHPAEN/v14/i10/p102708/s1&Agg=doi. 134

[215] Desjarlais, M., Kress, J., and Collins, L. 'Electrical conductivity for warm, dense aluminum plasmas and liquids'. *Physical Review E*, **vol. 66**(2), 025401, 2002, URL http://link.aps.org/doi/10.1103/PhysRevE.66.025401. 136

[216] Kresse, G. and Hafner, J. 'Ab initio molecular dynamics for liquid metals'. *Physical Review B*, **vol. 47**(1), 558, 1993, URL http://link.aps.org/doi/10.1103/PhysRevB.47.558. 136

[217] Kresse, G. and Furthmüller, J. 'Efficient iterative schemes for ab initio total-energy calculations using a plane-wave basis set.' *Physical review. B, Condensed matter*, **vol. 54**(16), 11169, 1996, URL http://www.ncbi.nlm.nih.gov/pubmed/9984901. 136

[218] Desjarlais, M. 'Practical Improvements to the Lee-More Conductivity Near the Metal-Insulator Transition'. *Contributions to Plasma Physics*, **vol. 41**(2-3), 267, 2001, URL http://dx.doi.org/10.1002/1521-3986(200103)41:2/3<267::AID-CTPP267>3.0.CO;2-P. 136

[219] Molvig, K. 'Filamentary Instability of a Relativistic Electron Beam'. *Physical Review Letters*, **vol. 35**(22), 1504, 1975, URL http://link.aps.org/doi/10.1103/PhysRevLett.35.1504. 139, 163

[220] Martinolli, E., Koenig, M., Baton, S. D. *et al.* 'Fast-electron transport and heating of solid targets in high-intensity laser interactions measured by Kα fluorescence'. *Physical Review E*, **vol. 73**, 046402, 2006, URL http://link.aps.org/doi/10.1103/PhysRevE.73.046402. 141

[221] Santos, J. J., Batani, D., McKenna, P. *et al.* 'Fast electron propagation in high density plasmas created by shock wave compression'. *Plasma Physics and Controlled Fusion*, **vol. 51**(1), 014005, 2009, URL http://stacks.iop.org/0741-3335/51/i=1/a=014005?key=crossref.d7e5293c64f449de9479792240dbe9eb. 141, 156, 164

[222] Theobald, W., Akli, K., Clarke, R. *et al.* 'Hot surface ionic line emission and cold K-inner shell emission from petawatt-laser-irradiated Cu foil targets'. *Physics of Plasmas*, **vol. 13**, 043102, 2006, URL http://link.aip.org/link/PHPAEN/v13/i4/p043102/s1&Agg=doi. 141

[223] Park, H.-S., Chambers, D. M., Chung, H.-K. *et al.* 'High-energy Kα radiography using high-intensity, short-pulse lasers'. *Physics of Plasmas*, **vol. 13**(5), 056309, 2006, URL http://link.aip.org/link/PHPAEN/v13/i5/p056309/s1&Agg=doi.

[224] Nilson, P. M., Theobald, W., Myatt, J. *et al.* 'High-intensity laser-plasma interactions in the refluxing limit'. *Physics of Plasmas*, **vol. 15**(5), 056308, 2008, URL http://link.aip.org/link/PHPAEN/v15/i5/p056308/s1&Agg=doi. 141, 146

[225] Mackinnon, A., Sentoku, Y., Patel, P. K. *et al.* 'Enhancement of Proton Acceleration by Hot-Electron Recirculation in Thin Foils Irradiated by Ultraintense Laser Pulses'. *Physical Review Letters*, **vol. 88**(21), 215006, 2002, URL http://link.aps.org/doi/10.1103/PhysRevLett.88.215006. 141

[226] Hubbell, J. H. 'Photon mass attenuation and energy-absorption coefficients'. *Journal of Applied Radiation and Isotopes*, **vol. 33**(11), 1269, 1982, URL http://dx.doi.org/10.1016/0020-708X(82)90248-4. 143

[227] Paterson, I. J., Clarke, R. J., Woolsey, N. C. *et al.* 'Image plate response for conditions relevant to laser-plasma interaction experiments'. *Measurement Science and*

Technology, **vol. 19**(9), 095301, 2008, URL http://stacks.iop.org/0957-0233/19/i=9/a=095301?key=crossref.97596e8c3eca5590828cf3a4b8083c30. 143

[228] Tanaka, K. A., Yamanaka, T., Sato, T. *et al.* 'Calibration of imaging plate for high energy electron spectrometer'. *Review of Scientific Instruments*, **vol. 76**(1), 013507, 2005, URL http://link.aip.org/link/RSINAK/v76/i1/p013507/s1&Agg=doi. 143

[229] Bambynek, W., Crasemann, B., Fink, R. *et al.* 'X-Ray Fluorescence Yields, Auger, and Coster-Kronig Transition Probabilities'. *Reviews of Modern Physics*, **vol. 44**(4), 716, 1972, URL http://link.aps.org/doi/10.1103/RevModPhys.44.716. 146

[230] Quarles, C. A. 'Semiempirical analysis of electron-induced K-shell ionization'. *Physical Review A*, **vol. 13**(3), 1278, 1976, URL http://link.aps.org/doi/10.1103/PhysRevA.13.1278. 146

[231] Robinson, A. P. L. and Sherlock, M. 'Magnetic collimation of fast electrons produced by ultraintense laser irradiation by structuring the target composition'. *Physics of Plasmas*, **vol. 14**, 083105, 2007, URL http://link.aip.org/link/PHPAEN/v14/i8/p083105/s1&Agg=doi. 150

[232] Huang, Y.-s., Lan, X.-f., Duan, X.-j. *et al.* 'Hot-electron recirculation in ultraintense laser pulse interactions with thin foils'. *Physics of Plasmas*, **vol. 14**(10), 103106, 2007, URL http://link.aip.org/link/PHPAEN/v14/i10/p103106/s1&Agg=doi. 155

[233] Ridgers, C. P., Sherlock, M., Evans, R. G. *et al.* 'Superluminal sheath-field expansion and fast-electron-beam divergence measurements in laser-solid interactions'. *Physical Review E*, **vol. 83**(3), 036404, 2011, URL http://link.aps.org/doi/10.1103/PhysRevE.83.036404. 155

[234] Santos, J. J., Batani, D., McKenna, P. *et al.* 'Fast electron propagation in high-density plasmas created by 1D shock wave compression: Experiments and simulations'. *Journal of Physics: Conference Series*, **vol. 244**(2), 022060, 2010, URL http://stacks.iop.org/1742-6596/244/i=2/a=022060?key=crossref.f1523ecf5ad8788a5671c529e7cdcf87. 156

[235] Ramakrishna, B., Wilson, P. A., Quinn, K. *et al.* 'Propagation of relativistic electrons in low density foam targets'. *Astrophysics and Space Science*, **vol. 322**(1-4), 161, 2008, URL http://www.springerlink.com/index/10.1007/s10509-008-9950-0. 160

[236] Moses, E. I., Boyd, R. N., Remington, B. A. *et al.* 'The National Ignition Facility: Ushering in a new age for high energy density science'. *Physics of Plasmas*, **vol. 16**(4), 041006, 2009, URL http://link.aip.org/link/PHPAEN/v16/i4/p041006/s1&Agg=doi. 160, 198

[237] Boehly, T. R., McCrory, R. L., Verdon, C. P. *et al.* 'Inertial confinement fusion experiments with OMEGA-A 30-kJ, 60-beam UV laser'. *Fusion Engineering and Design*, **vol. 44**(1-4), 35, 1999, URL http://linkinghub.elsevier.com/retrieve/pii/S0920379698002762. 160

[238] Maywar, D. N., Kelly, J. H., Waxer, L. J. *et al.* 'OMEGA EP high-energy petawatt laser: progress and prospects'. *Journal of Physics: Conference Series*, **vol. 112**(3), 032007, 2008, URL http://stacks.iop.org/1742-6596/112/i=3/a=032007?key=crossref.c4d5f0a2d4aea0edda645dfc49292e00. 160

[239] Azechi, H. 'Present status of the FIREX programme for the demonstration of ignition and burn'. *Plasma Physics and Controlled Fusion*, **vol. 48**(12B), B267, 2006, URL http://stacks.iop.org/0741-3335/48/i=12B/a=S26?key=crossref.17b678ae4536296b5d93241d52db8bfa. 160

[240] Koga, M., Arikawa, Y., Azechi, H. *et al.* 'Present states and future prospect of fast ignition realization experiment (FIREX) with Gekko and LFEX Lasers at ILE'. *Nuclear Instruments and Methods in Physics Research Section A*, **vol. In Press**, 2011, URL http://linkinghub.elsevier.com/retrieve/pii/S0168900211001872. 160

[241] Lindl, J. 'Development of the indirect-drive approach to inertial confinement fusion and the target physics basis for ignition and gain'. *Physics of Plasmas*, **vol. 2**(11), 3933, 1995, URL http://link.aip.org/link/PHPAEN/v2/i11/p3933/s1&Agg=doi. 160, 197

[242] Betti, R., Zhou, C., Anderson, K. *et al.* 'Shock Ignition of Thermonuclear Fuel with High Areal Density'. *Physical Review Letters*, **vol. 98**(15), 155001, 2007, URL http://link.aps.org/doi/10.1103/PhysRevLett.98.155001. 160, 198

[243] Nilson, P. M., Solodov, A. A., Myatt, J. F. *et al.* 'Scaling Hot-Electron Generation to High-Power, Kilojoule-Class Laser-Solid Interactions'. *Physical Review Letters*, **vol. 105**(23), 235001, 2010, URL http://link.aps.org/doi/10.1103/PhysRevLett.105.235001. 160

[244] Lee, R. and Lampe, M. 'Electromagnetic Instabilities, Filamentation, and Focusing of Relativistic Electron Beams'. *Physical Review Letters*, **vol. 31**(23), 1390, 1973, URL http://link.aps.org/doi/10.1103/PhysRevLett.31.1390. 163

[245] Benford, G. 'Electron-Beam Filamentation in Strong Magnetic Fields'. *Physical Review Letters*, **vol. 28**(19), 1242, 1972, URL http://link.aps.org/doi/10.1103/PhysRevLett.28.1242. 163

[246] Perez, F., Gizzi, L. A., MacKinnon, A. J. *et al.* 'Fast-electron transport in cylindrically laser-compressed matter'. *Plasma Physics and Controlled Fusion*, **vol. 51**(12), 124035, 2009, URL http://stacks.iop.org/0741-3335/51/i=12/a=124035?key=crossref.d8ed55c6423461425a90bb5498f936d0. 164

[247] Einstein, A. 'Does the Inertia of a Body Depend Upon Its Energy Content?' *Annalen der Physik*, **vol. 323**(13), 639, 1905. 193

[248] Atzeni, S. and Meyer-ter Vehn, J. *The Physics of Inertial Fusion: Beam Plasma Interaction, Hydrodynamics, Hot Dense Matter*. Oxford University Press, Oxford, 2004. 194, 196

[249] Bosch, H.-S. and Hale, G. 'Improved formulas for fusion cross-sections and thermal reactivities'. *Nuclear Fusion*, **vol. 32**(4), 611, 1992, URL http://stacks.iop.org/0029-5515/32/i=4/a=I07?key=crossref.499a5e49f8dde53d266bf4090e2da6c1. 195

[250] Lawson, J. D. 'Some Criteria for a Power Producing Thermonuclear Reactor'. *Proceedings of the Physical Society. Section B*, **vol. 70**(1), 6, 1957, URL http://stacks.iop.org/0370-1301/70/i=1/a=303?key=crossref.e1697fd64b8a71aa295438657a972463. 195

[251] Nuckolls, L. T. A. Z. G., J; Wood. 'Laser compression of matter to super-high densities: Thermonuclear applications'. *Nature*, **vol. 239**, 139, 1972, URL http://www.nature.com/nature/journal/v239/n5368/abs/239139a0.html. 197

Appendix A

Notes on Laser-induced Fusion

A.1 Fusion energy

Achieving a controlled release of energy by nuclear fusion is a significant motivation in plasma physics research. This process offers a potentially limitless supply of energy via the equivalence of energy and matter, famously identified by Einstein's equation [247]:

$$E = mc^2 \tag{A.1}$$

The formation of matter, from elementary particles to atoms and molecules, provides an organised storage of energy. The release of this energy underpins the activity and survival of all life-forms. Extraction is predominately inefficient with just a tiny fraction of the matter transformed into energy. For example, in terms of energy density, the metabolism of sugar can release $\approx 35\,\mathrm{MJ/kg}$ similar to the burning of petrol which $\approx 46\,\mathrm{MJ/kg}$. Compare this to nuclear fusion which can yield $\approx 10^7\,\mathrm{MJ/kg}$. The opposite of this process - the breakup or fission of nuclear matter is another, albeit less effective, approach which yields $\approx 10^6\,\mathrm{MJ/kg}$.

Evidently fusion and fission are the most dense energy sources possible[1]. The matter in these two processes involve the constituents at the centre of each atom - the nucleus - comprised of protons and neutrons bound together by the strong nuclear force. The negative potential energy of a bound state corresponds to negative mass. Therefore, a bound nucleus has less mass than the sum of individual particles. This mass difference, Δm, is equivalent to the binding energy of the nucleus. It is this binging energy, Δmc^2, that is released during the fusion or fission processes. For a net energy release, the end products need to have a higher binding energy than the initial reactants. This is

[1] This is true if excluding the energy density of matter/anti-matter

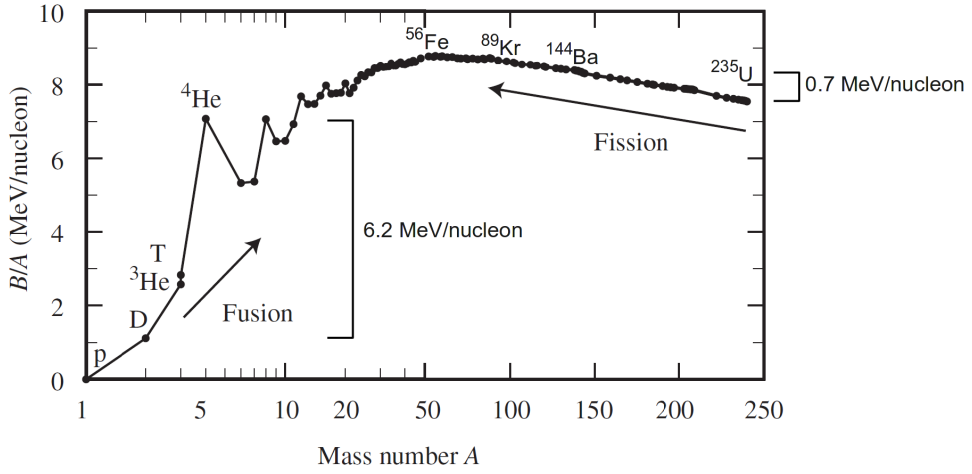

FIGURE A.1: Binding energy per nucleon versus mass number A [248]. Higher binding energy yields a more stable nucleus. The starting points for fusion and fission reactions are indicated.

shown in Figure A.1 using the average binding energy per nucleon (B/A). Heavy atoms such as uranium, with mass number $A = 238$, provide the starting point for fission. The converse is true for fusion, with the light atoms providing the most likely starting point. As a simple estimate, the change in binding energy per nucleon is 0.7 MeV for fission and 6.2 MeV for fusion. Due to the larger number of nucleons, fissioning a single uranium-235 nucleus yields far more energy than creating a single helium-4 nucleus by fusion. However, for a given mass of fuel the energy released by fusion is up to 4-5 times greater than the energy released by fission.

The probability of fusion reactions occurring is zero at room temperature. This probability or cross-section increases to meaningful magnitudes at temperatures of $10 - 100\,\text{keV}$. At such temperatures the atoms are stripped of their electrons and exist in the state of a plasma of nuclei and electrons. The equivalent velocities of the nuclei are such that the electrostatic or coulomb repulsion between them can be overcome - the nuclei can then approach sufficiently close into the range of the strong nuclear force. This short range force brings the reactant nuclei together into a larger nucleus.

The product of Maxwellian-averaged velocity (v) and cross-section (σ) is termed the reactivity ($\langle \sigma v \rangle$) with units of [cm^3/s]. Curves of the reactivity as a function of plasma temperature are shown in Figure A.2. The highest reactivity is for isotopes of hydrogen specifically deuterium (D = ^{2}H) and tritium (T = ^{3}H). [2] The DT reactivity has a broad maximum at about 64 keV which is a 100 times larger than that of any other reaction at 10–20 keV. The combination of DT in such fusion reactions yields $\approx 17.6\,\text{MeV}$ in kinetic

[2]Both isotopes constitute a fraction of sea water : $\approx 10^{-2}$% D, $\approx 10^{-15}$% T. The less abundant tritium can be 'bred' by capturing the fast neutrons, produced in the fusion reaction, within a lithium medium.

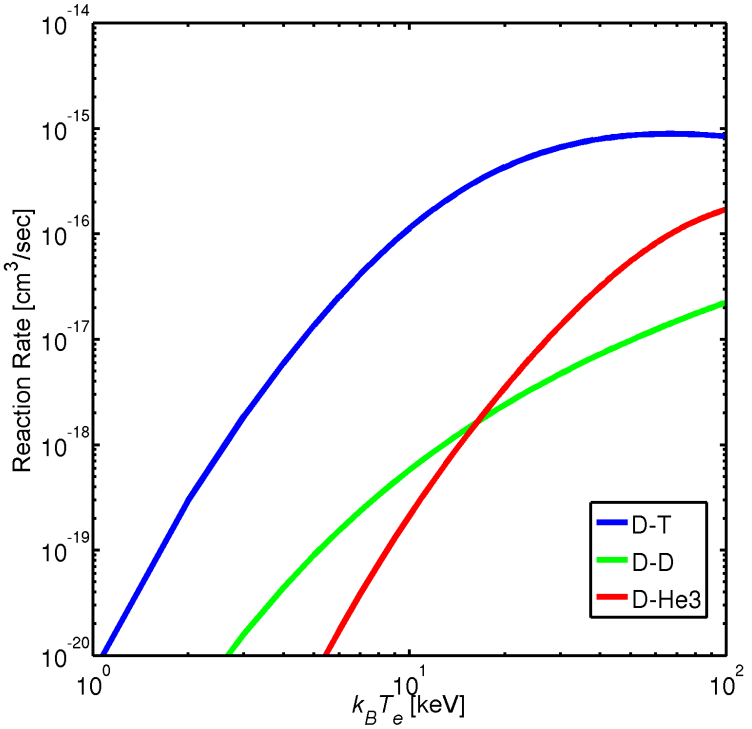

FIGURE A.2: The fusion reaction rate for reactants involving deuterium (D) and tritium (T) calculated using the Bosch-Hale formulae [249].

energy shared between the neutron and a bare helium nucleus i.e. an alpha particle:

$$\mathrm{D} + \mathrm{T} = {}^{4}\mathrm{He}\,[3.5\,\mathrm{MeV}] + \mathrm{n}^{+}\,[14.1\,\mathrm{MeV}] \tag{A.2}$$

Confinement of the hot plasma is the necessary requirement for a self-sustaining fusion energy source. Once fusion ignition occurs the stopping of the alpha-particles is instrumental in providing the heating of the surrounding fuel to fusion temperatures. Such a self-sustaining reaction, or **fusion burn**, is essential to achieve **break even** where the output energy matches the driver to give a **gain** of 1 ($Q = 1$). Confining such energetic particles long enough is the fundamental obstacle to fusion energy. The confinement time must be sufficiently long to ensure that enough fusion reactions occur to replace the input heating energy and other energy losses. The **Lawson criteria [250]** define how much time (τ) the plasma at a given density (n_e) must be confined for in order to achieve a sustained fusion reaction. For a DT reaction at temperature of 20 keV the Lawson criteria requires:

$$n_e\tau > 10^{20}\,\mathrm{s/m^3} \tag{A.3}$$

The process of gravitational confinement occurs naturally in stars which have sufficient stellar mass to confine the plasma for billions of year. On Earth, there are two main

candidates for achieving fusion: magnetic confinement, where the confinement time is large (seconds), and inertial confinement fusion (ICF), where the plasma density is large. The large density is achieved by compression, the fuels own inertia then acts as the confinement mechanism within some small interval of time.

A.2 Inertial Confinement Fusion (ICF)

To begin defining the requirements of ICF, in terms of driver energy, it is useful to realise how much fuel will be involved. The significant amount of energy released by an efficient fusion burn places a restriction on the amount of fuel used in the fusion reaction. Complete fusion of 1 mg of D-T releases 337 MJ of fusion energy. The possibility of damaging the reaction chamber by such micro explosions limits the energy yield to a few GJ, even when operated with a few shots per second. The fraction of fuel that undergoes fusion is a defining factor in the mass of fuel used (M_{fuel}). Assuming that this fraction is $\eta_{fuel} = 30\%$ the fuel mass should be restricted to a few 10 mg [248].

This small amount of fuel is enclosed within a smooth spherical capsule. The compression, confinement and subsequent expansion occurs over a few billionths of a second. The density must be sufficiently high that for such nano-second confinement times the number of fusion reactions burn a significant fraction of the D-T fuel. The necessary density can be estimated by considering how much fuel must undergo fusion - the **burn efficiency** [248]:

$$\eta_{fuel} = \frac{\rho R_{fuel}}{H_B + \rho R_{fuel}} \tag{A.4}$$

which is defined using the burn parameter $H_B \approx 7\,\mathrm{g/cm^3}$ and areal density ρR_{fuel}. For $\eta_{fuel} = 30\%$ the **areal density** is then $\rho R_{fuel} = 3\,\mathrm{g/cm^2}$. The required density is then estimated by considering the fuel mass within a spherical volume [248]:

$$M_{fuel} = \frac{4\pi}{3}\rho R_{fuel}^3 = \frac{4\pi}{3}\frac{(\rho R_{fuel})^3}{\rho^2} \tag{A.5}$$

$$\rho = \sqrt{\frac{4\pi}{3}\frac{(\rho R_{fuel})^3}{M_{fuel}}} \tag{A.6}$$

For a fuel mass of 1 mg the compressed fuel density for a 30% burn efficiency should be $\rho = 336\,\mathrm{g/cm^3}$. The initial density of the D-T fuel is $0.225\,\mathrm{g/cm^3}$ - so the required compression factor is:

$$\text{Compression} = \frac{\rho}{\rho_{DT}} = 1500 \tag{A.7}$$

The challenge of ICF is to provide smooth uniform compression of a milli-metre fuel capsule to over 1000 times solid density. Such a feat was quickly seen as a possible application for the laser in providing a non-thermal source of heat. Nuckolls and co-workers [251] published the first description of laser induced implosion of fuel capsules to achieve the necessary compression and heating for ICF. The beams act to deliver the driver energy over a few nano-seconds. The physical picture is then one of hydrodynamics, describing energy absorption, compression, shock waves and heating of the fuel.

1. **Surface Ablation:** Compression is instigated by laser induced ablation of the capsule surface. The energy needed to drive this compression is currently understood to be a few million Joules or 10^{15} W of total laser power. If the laser beams are focused directly onto the pellet, it is called **direct drive**, which can in principle be very efficient although it is difficult to achieve the required uniformity. An alternative approach is **indirect drive** [241], in which the laser beams enter and heat a cavity surrounding the fuel creating x-rays which drive a smoother implosion of the pellet. Either way, the compression of the fuel by heating of the outer surface must be such that energy is delivered to the target uniformly.

2. **Shock wave compression:** As the outer surface then expands, or ablates, outward, an inward, equal but opposite force drives the fuel towards the center in order to conserve momentum. As the fuel travels inward and the remaining fuel is compressed, shock waves act to equalise the pressure (**isobaric compression**) throughout the target. In the final stage of compression, the fuel consists of two distinct regions, a central hot spot region containing $2-5\%$ of the fuel mass surrounded by the remaining cooler but higher density fuel.

3. **Ignition:** Instead of igniting the entire fuel pellet by compression alone it is more efficient to create a self-sustained fusion burn. This is referred to as **hot spot ignition**. Calculations predict a significant higher gain with respect to volume ignition, but still mega-joules of driver energy are required. For hot-spot ignition to occur, the Lawson criteria and temperature for inertial confinement must be reached: a central hot spot with an areal density of $\rho R_{spot} = 0.3 - 0.5\,\mathrm{g/cm^2}$ and a temperature of $5 - 10\,\mathrm{keV}$.

4. **Burn:** Once initiated, the 3.6 MeV alpha particles produced from the D-T fusion ignition are stopped within the hot spot. This absorption rises the surrounding fuel temperature and triggers a burn wave to propagate into the outer regions igniting the remaining fuel. The neutrons are then the primary energy carrier to escape the plasma.

Even with the necessary driver energy, achieving smooth spherical compression of the DT capsule to > 1000 times solid density is not a trivial task. The past 30 years have provided many hard lessons on the road to achieving ignition. The symmetry requirements of the compression beams are very high - both in terms of temporal synchronisation ($< 10\,\text{ps}$) and energy balance ($< 3\%$). The capsule surface roughness must be $< 1\,\mu\text{m}$ on the inside surface, and at the nano-metre level on the outer surface. Even with perfect compression the fuel can still be disrupted by a number of undesirable hydrodynamic instabilities. As the shell implodes, the low density plasma at the outer surface is accelerated against the high density shell, triggering the **Rayleigh-Taylor instability** on the external surface which can lead to shell breakup. The instability is seeded by the capsule surface roughness and by imprinting of the driver nonuniformity on the shell. As the shell is decelerated by the internal pressure buildup, it experiences the Rayleigh Taylor instability on the interior surface, this time seeded by the inner D-T ice roughness. The shell can again break up and a mixing of the cold DT ice with the heated gas can occur, disrupting the fusion burn.

Demonstrating ICF: The National Ignition Facility (NIF)

The subtleties of compression and ICF scale physics are currently being investigated with a purpose built National Ignition Facility at the Livermore lab in the USA [236]. The NIF carries on from its predecessor, NOVA, and is capable of delivering laser beams and MJ energies with increased uniformity onto target capsules. The 192 beams provide 4 MJ of infared radiation which is frequency tripled to 1.8 MJ of ultra-violet radiation before entering a gold cylinder, known as a **hohlraum**[3] for the purpose of indirect-drive ICF. The NIF facility will also be used to investigate alternative schemes for ICF such as Shock Ignition [242] and Fast Ignition [7].

[3] German for 'hollow room', or cavity

Appendix B

Analytical Models

A number of analytical models were created for the investigations of this thesis. These were written using the standard version of MATLAB R2010. The code for a selection of these models is listed here for the application or interest of the reader.

B.1 Degree of ionisation Z^*

```
% Analytic formulae to calculate the degree of ionisation
%using the More Model via expressions from Azenti
% Any temperature (eV) and density (g/cm3)
% Sources:
% More R M
% "Pressure ionization, resonances, and the continuity of bound and free states"
% Advances in atomic and molecular physics    volume: 21    pages: 305-356
% 1985
% Atzeni S
% "The physics of inertial fusion:
% beam plasma interaction, hydrodynamics, hot dense matter"
% Oxford University Press,
% 2004
function Zion = Ionisation_MoreModel_MNQ(Z,rho,A,T);
alpha= 14.3139; Beta = 0.6624;
a1 = 0.003323;a2 = 0.9718;a3 = 9.26148e-5;a4 = 3.10165;
b0 = -1.7630;b1 = 1.43175;b2 = 0.31546;
c1 = -0.366667;c2 = 0.983333;
rho1 = rho/(A*Z);
T1 = T/Z^(4/3);
Tf = T1/(1+T1);
```

```
A = a1*T1^a2 + a3*T1^a4;
B = -1*exp(b0 + b1*Tf + b2*Tf^7);
C = c1*Tf + c2;
Q1 = A*rho1^B;
Q = (rho1^C + Q1^C)^(1/C);
x = alpha*Q^Beta;
Zion = Z*x/(1 + x + sqrt(1 + 2*x));
```

B.2 Refluxing efficiency

```
% Refluxing efficiency obtained from the Myatt capacitance model.
% Myatt, J. et al., 2007.
%   Physics of Plasmas, 14, p.056301.
%   Available at:
%    http://link.aip.org/link/PHPAEN/v14/i5/p056301/s1&Agg=doi.
% Use Fixed Laser energy
% Vary Intensity:
clear all;
close all
clc
font=30;linew=8;markerS=24;fullscreen = get(0,'ScreenSize');

%% PHYSICAL CONSTANTS
me = 9.109e-31;
mi=1.67E-27; %proton energy
e=1.6e-19;%electron charge
c=3e8;% light velocity in vacuum
epson=8.854e-12;%electric constant
Eme=511e3; %Electron Rest Mass [eV]
me = 9.109e-31; %Electron Mass [kg]
mi=1.67E-27; %proton Mass [kg]
h=6.626e-34;    %Planck constant
h_bar=h/(2*pi); %h-bar
a_b = 5.29e-11; %Bohr radius [m]
mu0 = pi.*4e-7; %mu0 (Permeability of free space Wb/Am)
e0 = 1/(mu0.*(c.^2)); %e0 (Permittivity of free space C^2/Nm^2)
Ea=e/(4.*pi.*e0.*(a_b.^2)); %Atomic E-field [V/m]
JH = 13.6; %ionisation potential for Hydrogen (eV)
omega_a= 2*JH*e/h_bar; % Atomic Freq [/s]
rc= 2.8179e-15;% Electron Radius [m]
%% Laser
EL=300;
```

```
TL=1e-12; %Laser pulse duration           [s]
Dx=5e-6; %Laser focus spot in long axis  [m]
Dy=5e-6; %Laser focus spot in short axis [m]
lambda=1.064; %Laser wavelength           [um]
eta=0.20; %Laser energy -> electrons conversion efficiency
Intensity=linspace(1e18,1e21,200); %laser intensity on target

%% Calculate Refluxing efficiency for different target radii
r= [0.1 1 2]; % Target radius [mm]
col=['r','b','k'];
for i=1:length(r),
    for l=1:length(Intensity),
        if Intensity(l) > 1e18,
% Haines Scaling [eV]
            %kTe=(sqrt(1+sqrt(2)*a0)-1)* me*c^2/e;
% Wilks Scaling [eV]
            kTe=0.511e6*(sqrt(1+(Intensity(l)/1e18*(lambda^2)/1.37))-1);
        else
% Use Beg's Scaling [eV]
            %  kTe = 1e5*(Intensity(l)/1e17)^(1/3);
% Use Beg Scaling [eV]
           kTe =215*(Intensity(l)/1e18 * lambda^2)^(1/3)*1e3;
% Use Gibbon Scaling [eV]
           % kTe = 1e6*0.05*(Intensity(l)/1e18*lambda^2)^(1/3);
        end
        %FAST ELECTRON DENSITY
        Ne=eta*EL/(kTe*e); % Total electron number
        kTe=kTe/1e6;
        k=7.08e-2*r(i)*kTe^2/(eta*EL);
        k = round(k*10^4)/10^4; %Round to 3 decimal places
        for V=1e-3:1e-4:50, % Potenial difference V [MV]
            phi=(V/kTe);
            ratio=exp(-phi)./phi;
            ratio = round(ratio*10^4)/10^4; %Round to 3 decimal places
            if ratio==k,
                eta_R(l)=1-exp(-phi);
                break
            end
        end
    end
    Nl=4.42e11*r(i)*V;
    H(i)=semilogx(Intensity,eta_R) ;
    set(H(i),'LineStyle','-','Color',col(i),'Marker','none','LineWidth',linew)
```

```
    hold on
end
axis tight
box on
ylim([0.2 1.099])
xlabel('Laser Intensity [W/cm^2]','fontsize',font,'FontName','Arial');
ylabel('Refluxing Efficiency','fontsize',font,'FontName','Arial')
set(gca,'FontSize',font,'LineWidth',4,'FontName','Arial')
set(gcf,'Position',[0 -50 fullscreen(3) fullscreen(4)]);
legend(H,'radius=0.1mm','radius=1mm','radius=2mm')
```

B.3 K-shell ionisation cross section

```
% Computes Ionisation Cross Section using Quarles Method
% C. A. Quarles.
%    Phys. Rev. A, 13 1278 (1976)
% 3 Inputs: Quarles(Electron Energy, Ionisation Energy, Print to Screen (1 or 0))
function CS=Quarles(EeV,IeV,P)
Eme=511e3; %Electron Rest Mass [eV]
%Rest Mass Units
E=EeV./Eme; %Electron Energy
I=IeV/Eme; %Cu K-shell Ionisation
U=E./I; % Ratio

%Relativistic Correction Factor
R=((2+I)./(2+E)).*((1+E)./(1+I)).^2.*((I+E).*(2+E).*(1+I)^2 ...
    ./ (E.*(2+E)*(1+I)^2 + (I*(2+I)))).^(3/2);
CS=(828e-16).*(R./(IeV.^2)).*(log(U)/U);

if P==1,
    fprintf('\n#################################\n')
    fprintf('Quarles Kalpha Cross Section [CS]:\n')
    fprintf('#################################\n')
    fprintf('Electron Energy:%2.2e eV\n K-shell:%2.2e eV\nCS: %4.2f Barn',...
    EeV,IeV,CS./1e-24);
    fprintf('\n#################################\n')
end
```